Models for the Formation of Highland Regions on Venus

Thesis by
Walter Scott Kiefer

In Partial Fulfillment of the Requirements
for the Degree of
Doctor of Philosophy

California Institute of Technology
Pasadena, California

1991
(Submitted July 16, 1990)

Acknowledgements

My foremost thanks go to my thesis adviser, Brad Hager. I am grateful to Brad both for his patience in allowing me to pursue a variety of subjects as they became of interest to me, as well as for his willingness to provide useful suggestions whenever I got stuck.

I am grateful to Dave Stevenson for many enlightening discussions. I have always learned something from our talks, and his skepticism has helped me to better understand the limitations of my models. I thank Bruce Murray both for supporting one of my early research projects and for providing continuous "encouragement" as I attempted to complete this thesis. Jim Westphal's enthusiasm is infectious. He was even able to make being a teaching assistant fun.

I owe a very special thanks to Bob Sharp. His field trips were always both fun and educational, and it was a pleasure to be able to participate in so many of them. I am particularly grateful for the opportunity to go to Hawaii as part of Project Pahoehoe 1989, which is surely among the most memorable of all my Caltech experiences.

My interest in the geophysics of Venus was initially inspired by Bruce Bills of the Lunar and Planetary Institute. I thank Bruce for helping me to understand the Venus gravity and topography data sets and for listening to many of my ideas over the years. I am grateful to Bill Graham and Arthur Ehlmann of Texas Christian University, whose inspirational teaching gave me a good foundation in both physics and geology.

It has been my good fortune to have shared my time at Caltech with many other friendly and enthusiastic grad students. I particularly thank Tim Dowling, Bridget Landry, Rich Achterberg, Julie Moses, and Michelle Santee. My office mates, Bill Anderson, Mark Hofstadter, and Bruce Betts, did their best to guarantee that there was never a boring moment in our office. I thank them for keeping the noise level down to a dull roar (at least some of the time) and for

allowing me to stay out of the cross-fire most of the time. I am also grateful to the other students and post-docs who have been a part of Brad Hager's research group, Mark Richards, Scott King, Andrea Donnellan, Leslie Sonder, Mike Gurnis, and Louise Kellogg, whose assistance and suggestions have been quite valuable.

I am grateful to Arthur Raefsky for providing the finite element code used in most of the work described in this thesis. I also thank Richard Stead and Doug Neuhauser for their help with the Seismo Lab computing facilities.

I thank Kay Campbell, Lorna Griffith, Donna Lathrop, Nancy Durland, Dorothy Coy, and Priscilla Piano for their help in dealing with a multitude of administrative details.

Finally, I thank my parents, Walter and Betty Kiefer. Without their love and encouragement, this thesis would never have been possible. I dedicate this work to them.

Abstract

The unifying theme of this thesis is an attempt to understand the origin of several major highland units on Venus. Chapters 1 and 2 develop numerical models of mantle plumes. In Chapter 1, I discuss the numerical methods used in calculating the geoid anomalies, topographic uplifts, and heatflow associated with upwelling plumes. Because plumes are a likely cause of at least some terrestrial hotspot swells, Chapter 1 also examines how the numerical models compare with observations of terrestrial hotspots. In Chapter 2, I compare the plume model results with observations of geoid anomalies and topography from the Equatorial Highlands of Venus. Chapter 3 examines another model, in which parts of the Equatorial Highlands are interpreted as spreading centers analogous to terrestrial mid-ocean ridges. Chapter 4 develops a crustal convergence and mantle downwelling model for the Ishtar Terra region of Venus.

Terrestrial hotspot swells are regions of elevated topography and high rates of volcanism. A variety of evidence suggests that at least some hotspots, such as Hawaii, are formed by quasi-cylindrical mantle plumes upwelling from deep in the mantle. I model such plumes using a finite element code in cylindrical, axisymmetric geometry with a depth-dependent Newtonian viscosity. Many previous workers have modeled plumes using a sheet-like, Cartesian geometry, but I find that cylindrical and sheet-like upwellings have significantly different geoid and topography signatures. However, Rayleigh number-Nusselt number systematics in the two geometries are quite similar. Increasing the Rayleigh number or including a low-viscosity asthenosphere decrease the geoid anomaly and the topographic uplift of a plume. For comparison with observations, the models are scaled with the assumptions of whole-mantle convection and a temperature contrast of about 300 °C between the center of a plume and normal mantle. The models are able to explain the amplitudes of the observed geoid anomalies and topographic uplifts at Cape Verde and Hawaii, provided that the Earth's mantle has a low viscosity zone in the asthenosphere and upper mantle similar to that

previously inferred by Hager and colleagues on the basis of long-wavelength geoid modeling. However, for aspect ratio 1, the models predict swell widths that are about twice as wide as observed. This discrepancy may be due in part to terrestrial plumes having aspect ratios of less than 1. Alternatively, inclusion of temperature-dependent rheology may lead to narrower swells.

The Equatorial Highlands of Venus consist of four main structures, Atla, Beta, Ovda, and Thetis Regiones. Each of these features has a circular to oval-shaped planform and rises 4 to 6 km above the mean planetary radius. These highland units are also long-wavelength geoid highs, with amplitudes ranging from 35 meters at Ovda to 120 meters at Atla. These features also contain topographic valleys, interpreted as extensional rift zones, and Beta is known to contain shield volcanoes. These characteristics are all consistent with the Equatorial Highlands being formed by upwelling mantle plumes. In order to compare results for Venus and Earth, I assume that the two planets have similar mantle heat flows. With this assumption, I find that in order to satisfy the observed geoid and topography for the Equatorial Highlands, the asthenosphere and upper mantle viscosity must be higher on Venus than on Earth. This conclusion is consistent with modeling of the long-wavelength admittance spectrum of Venus and with the observed differences in the slopes of the geoid spectra of the two planets. One possible explanation for the different viscosity structures of the two planets is that the mantle of Venus is drier than the Earth's mantle.

An alternative model for Ovda and Thetis Regiones, proposed by Crumpler, Head, and colleagues, is that these features are terrestrial-type spreading centers. The strong positive correlation between the geoid and topography observed in Ovda and Thetis is unlike that observed for terrestrial spreading centers. The maximum elevation expected for spreading centers on Venus is 1.5 km, and a cooling plate thermal model predicts a maximum geoid anomaly of 8 meters, both much less than observed. Thus, even if a spreading center is operative in Ovda and Thetis, most of the geoid and topography must be due to other mechanisms. Crumpler et al. also proposed the existence of "cross-strike

discontinuities," which they interpreted as transform fault zones, but the evidence for these structures is not conclusive.

The Ishtar Terra region of Venus contains the highest topography known on the planet, over 10 km above the mean planetary radius, as well as abundant tectonic features, many of which are apparently compressional in origin. These characteristics suggest that Ishtar is a crustal convergence zone overlying a region of downwelling mantle. In order to explore quantitatively the implications of this hypothesis for Ishtar's origin, I present models of the viscous crustal flow driven by gradients in lithostatic pressure. For reasonable bounds on the mantle convective velocity, I find that if the crustal convergence hypothesis is correct, then the crustal thickness in the plains surrounding Ishtar can be no more than about 25 km thick. This result is in good agreement with several independent estimates of crustal thickness on Venus based on modeling of the spacing of tectonic features and of impact crater relaxation, but is much less than the estimated crustal thickness derived from an Airy isostasy model of Ishtar's gravity anomaly. Much of the observed gravity anomaly must be due to density anomalies in the mantle beneath Ishtar. Although I treat Ishtar as a crustal convergence zone, the crustal flow model results show that under some circumstances near-surface material may actually flow away from Ishtar, providing a possible explanation for graben-like structures in Fortuna Tessera.

Table of Contents

Chapter 1

Geoid Anomalies and Dynamic Topography from Convection in Cylindrical Geometry: Applications to Mantle Plumes on Earth and Venus

Walter S. Kiefer and Bradford H. Hager[1]

Division of Geological and Planetary Sciences
California Institute of Technology
Pasadena, CA 91125

[1]Now at: Department of Earth, Atmospheric, and Planetary Science
Massachusetts Institute of Technology
Cambridge, MA 02139

To be submitted to Geophysical Journal International

anomalies. Observations of heat flow anomalies at several hotspot swells in the range of 8 to 16 mW m^{-2} are also consistent with the existence of substantial thermal anomalies in the lithosphere (Von Herzen et al., 1982; Detrick et al., 1986; Courtney and White, 1986), although there is some controversy surrounding the magnitude of these heat flow anomalies (Louden et al., 1987; Von Herzen et al., 1989).

Long-wavelength geoid anomalies and seismic tomography provide tools for probing the deeper structure of hotspot swells. There is a strong positive correlation between the global distribution of terrestrial hotspots and the longest wavelength components of the geoid (Crough and Jurdy, 1980; Richards et al., 1988). At somewhat shorter wavelengths, individual hotspots also tend to be geoid highs, although the size and shape of these more localized geoid highs depends on how the long-wavelength geoid components are filtered. For example, Crough (1982) estimated a regional geoid anomaly of 8 meters for the Cape Verde Rise, whereas McNutt (1988) estimated a geoid anomaly of 12 meters. A similar range in geoid amplitudes has been reported for the Hawaiian Swell (Sandwell and Poehls, 1980; McNutt and Shure, 1986; Richards et al., 1988). Although geoid anomalies of this amplitude can be interpreted in terms of compensation within the lithosphere, this does not preclude the existence of density anomalies deeper within the mantle. Kiefer et al. (1986), Robinson et al. (1987), and Ceuleneer et al. (1988) have all shown that inclusion of a low-viscosity asthenosphere can lead to apparent compensation depths in convection models that are arbitrarily small. Richards et al. (1988) analyzed the spectral content of the geoid anomalies associated with hotspots globally and with the Hawaiian Swell in particular and concluded that density anomalies are required at substantial depths in the mantle beneath hotspots in order to explain the observed spectral slope.

Seismic tomography provides another tool to probe the deep structure of hotspot swells. Richards et al. (1988) showed that there is a strong correlation between the global distribution of hotspots and seismically slow regions in both the upper and lower mantles. The slow seismic velocities are assumed to be due to hotter than normal mantle. Higher resolution images of individual hotspots can be obtained using regional scale studies. Zhang and Tanimoto (1989)

inverted surface wave data for the Pacific Ocean region. In their Love wave velocity anomaly maps, they found a circular low velocity region near Hawaii that extends from the surface down to a depth of 200 km, the largest depth for which they inverted the Love wave structure. Tryggvason et al. (1983) examined P-wave travel time data for the Iceland region and inverted for velocity anomalies down to a depth of 375 km. Their results show a pipe-like low velocity anomaly that extends to the base of their inversion region. This low velocity anomaly is clearly distinguishable from adjacent parts of the Mid-Atlantic Ridge.

Geochemical data can also be used to constraint hotspot models. The basalts produced at hotspots can be distinguished from mid-ocean ridge basalts in several ways. In this paper, we consider only one type of data, the isotopic ratio $^3He / ^4He$. In basaltic glasses from the Mid-Atlantic Ridge, the helium isotopic ratio is observed to be between 6.5 and 11 R, with most samples clustering near 8 R, where R is the atmospheric value of the $^3He / ^4He$ ratio (Kurz et al., 1982). In contrast, several hotspots show evidence for elevated He isotope ratios. For example, basaltic glasses from the Loihi seamount near Hawaii have helium isotope ratios of 20 to 32 R (Kurz et al., 1983). Basaltic glasses from Iceland have values as high as 26 R (Kurz et al., 1985). Olivine phenocrysts from basalts produced by the Reunion hotspot have helium isotope ratios in the range 13 to 15 R (Kaneoka et al., 1986). However, not all hotspots have elevated levels of ^3He. The helium isotope ratio of the Azores hotspot, for example, is indistinguishable from adjacent parts of the Mid-Atlantic Ridge (Kurz et al., 1982).

As a noble gas, helium is likely to behave as an incompatible element and thus to preferentially partition into the melt phase whenever a parcel of mantle material undergoes partial melting. Much of this He is then likely to be outgassed to the atmosphere. Because ^3He is primordial, whereas ^4He is produced by radioactive decay of U and Th, mantle material that has experienced partial melting and degassing should have a low $^3He / ^4He$ ratio. Thus, samples with high He isotope ratios are generally interpreted as coming from mantle material that has not been previously outgassed. Assuming that the helium isotope ratios measured at mid-ocean ridges are typical of material in the upper part of

the mantle, then material with high He isotope ratios are likely to come from greater depths, such the lower mantle, the D" layer, or the core. The evidence for high He isotope ratios therefore suggests that at least some hotspots have deep sources, a conclusion that is consistent with the inferences based on geoid anomalies and seismic tomography data that were described above. For a more detailed discussion of the possible role that mantle plumes play in transporting He within the mantle, see Kellogg and Wasserburg (1990).

The volcanic activity and the topography data described above clearly require the existence of thermal anomalies within the lithosphere or mantle at hotspots. A variety of models have been proposed. Wilson (1963) and Morgan (1972 a,b) proposed that hotspot swells and their associated volcanic island chains are formed by cylindrical convective upwellings, or mantle plumes, that rise from deep within the mantle. Such upwellings can form as the result of convective instability of a thermal boundary layer within the mantle, for example at the core-mantle boundary (e.g., Yuen and Peltier, 1980; Christensen, 1984; Olson et al., 1987). Hofmann and White (1982) favored a somewhat different plume model, in which hotspot volcanism is due to recycling of oceanic crust, with old subducted slabs being reheated at depth and ascending again as thermo-chemical plumes. McKenzie et al. (1980) and Watts et al. (1985) suggested a different type of convective model, in which hotspot swells form over the upwelling limbs of elongated convective cells. Turcotte and Oxburgh (1978) and Sleep (1984) suggested that hotspot volcanism is due to magma erupting through propagating lithospheric cracks.

The foregoing observations place significant constraints on plausible hotspot models. For example, in the propagating crack or delamination model, material from the uppermost mantle should be emplaced in the crack, but this fails to explain the high $^{3}He / ^{4}He$ ratios observed at some hotspots. Also, the geoid spectrum expected for a pure propagating crack model is much flatter than the observed spectrum (Richards et al., 1988).

The elongated convective upwelling model has a number of difficulties. In such a model, we would expect adiabatic decompression to lead to partial melting and volcanism along the entire length of the upwelling. In fact, the

Hawaiian Swell and some other hotspot swells have well defined age versus distance progressions in their volcanic histories (Duncan and Clague, 1985), with active volcanism confined to one end of the swell. This is consistent with a cylindrical, plume-like upwelling but not with an elongated upwelling. On the other hand, more complex distributions of volcanic activity, as in the Cook-Austral chain (Okal and Batiza, 1987) or the Easter Island "hot line" (Bonatti et al., 1977), could conceivably be related to elongated convective upwellings. In the case of the Hawaiian Swell, an elongated upwelling is also inconsistent with the observed shape of the seismic low velocity anomaly (Zhang and Tanimoto, 1989). The elongated upwelling model also has difficulties explaining several aspects of hotspot topography. The square-root of age subsidence behavior of hotspot swell topography is readily understood in terms of conductive cooling of the lithosphere. On the other hand, if a swell is supported convectively along its entire length, it is not obvious why such a pattern should arise. Also, the sharp bends in the trends of hotspot tracks such as the Hawaiian-Emperor swell and other Pacific hotspot swells would require equally sharp bends in the geometry of convective upwellings, but there is no obvious mechanism for producing such distorted upwelling geometries.

The mantle plume hypothesis appears to be consistent with the various constraints outlined above. The existence of deep upwellings can explain the geoid and seismic tomography data and the high $^3He/^4He$ ratios observed at some hotspots. The restriction of the upwelling to a narrow, cylindrical region can explain the observation that active volcanism is typically concentrated at only one end of a swell. The elongated topographic swell simply reflects the thermal heating of the lithosphere as it passes over a plume. This thermally elevated region is then carried away from the plume by the motion of the plate. Thus, the topographic planform of the swell does not necessarily reflect the convective planform of the underlying convective upwelling. We therefore believe that mantle plumes are the most likely cause of many terrestrial hotspots, a conclusion that is consistent with the opinions advanced by many other workers in recent years (e.g., Courtney and White, 1986; Robinson et al., 1987; Davies, 1988; Richards et al., 1988; Sleep, 1990). However, this does not

preclude the possibility that some hotspots may be produced by other mechanisms.

Numerical Modeling Procedures

The foregoing discussion suggests that hot, upwelling mantle plumes are a likely cause of at least some hotspot swells. This paper focuses on numerical modeling of the topographic uplift, geoid anomalies, and heat flow anomalies associated with mantle plumes. In this section, we describe the numerical modeling procedures which we use. In subsequent sections, we describe how our plume models are influenced by the model geometry and by various mantle parameters, such as the Rayleigh number, the variation of viscosity with depth, and the aspect ratio. We then discuss how our models compare with observations of possible plume swells on Earth and Venus.

Finite Element Calculations

We use a finite element code to solve the coupled system of differential equations that govern mantle convection. We non-dimensionalize the governing equations by scaling distance according to the cylinder depth d, temperature according to the temperature contrast ΔT across the cylinder depth, and time according to $\frac{d^2}{\kappa}$, where κ is the thermal diffusivity. In some models, we use a flux boundary condition rather than a temperature boundary condition at the base of the convecting layer. In this case, we define $\Delta T = \frac{(F + Hd)d}{k}$, where F is the applied basal flux, H is the volumetric heating rate, and k is the thermal conductivity. In non-dimensional form, the governing equations are the incompressible continuity equation (conservation of mass),

$$\nabla \cdot V = 0, \tag{1}$$

conservation of momentum,

$$-\nabla P + \nabla \cdot \tau + Ra\, T\, \hat{k} = 0, \tag{2}$$

and conservation of energy,

$$\frac{\partial T}{\partial t} + V \cdot \nabla T = \nabla^2 T + \mu. \tag{3}$$

In equations 1 to 3, P is the pressure, T is the temperature, t is time, and $\hat{k}$ is a unit vector in the vertical direction. τ is the stress tensor, whose elements are given by

$$\tau_{rr} = 2\eta \frac{\partial V_r}{\partial r} \tag{4a}$$

$$\tau_{zz} = 2\eta \frac{\partial V_z}{\partial z} \tag{4b}$$

$$\tau_{\phi\phi} = 2\eta \frac{V_r}{r} \tag{4c}$$

$$\tau_{rz} = \eta \left(\frac{\partial V_r}{\partial z} + \frac{\partial V_z}{\partial r} \right). \tag{4d}$$

For axisymmetry, $\tau_{r\phi} = \tau_{z\phi} = 0$. V_r and V_z are the radial and vertical components of the velocity field and η is the viscosity. These governing equations are solved using the finite element code of Daly and Raefsky (1985).

In writing the momentum equation, we have neglected inertial terms, which is appropriate because the Prandtl number, $Pr = \frac{\eta}{\rho\kappa}$, is in excess of 10^{20} for the mantles of Earth and Venus. The solutions to equations 1 to 3 are controlled by two dimensionless parameters. One is the Rayleigh number,

$$Ra = \frac{\rho g \alpha \Delta T d^3}{\eta \kappa}, \tag{5a}$$

which governs the vigor of the convection. In equation 5, ρ is the density, g is the gravitational acceleration, α is the thermal expansion coefficient, and the other variables are as defined above. In models with an applied basal flux, we can rewrite Ra as a flux Rayleigh number,

$$Ra_F = \frac{\rho g \alpha (F + Hd) d^4}{\eta \kappa k}. \tag{5b}$$

The second dimensionless parameter is the internal heating parameter (McKenzie et al., 1974),

$$\mu = \frac{H d}{F + H d}. \tag{6}$$

μ governs the relative strength of basal and internal heating, with $\mu = 0$

corresponding to heating entirely from below and $\mu = 1$ to purely internal heating.

Although some workers have recently begun reporting results of three-dimensional numerical mantle convection models (Houseman, 1988, 1990; Glatzmaier, 1988; Baumgardner, 1988; Bercovici et al., 1989a,b), we have chosen to work with two-dimensional models. By restricting our models to two dimensions, we are able to perform calculations at higher grid resolution than is possible for 3D modeling with current computers. As a result, we are able to calculate well-resolved models at Rayleigh numbers that approach those believed to exist in the mantles of Earth and Venus.

Our models are calculated in cylindrical axisymmetric geometry, which reflects our belief that mantle plumes are quasi-cylindrical structures. Our use of cylindrical geometry distinguishes our plume models from many existing studies of mantle plumes in Cartesian geometry (Parsons and Daly, 1983; Detrick et al., 1986; Robinson et al., 1987; Robinson and Parsons, 1988; Ceuleneer et al., 1988). As we show later, the choice of model geometry has a strong effect on calculations of topographic uplift and geoid anomalies. Only a few studies exist in the literature on geoid and topography for axisymmetric convection. Courtney and White (1986) calculated a limited suite of cylindrical axisymmetric models and compared their results with observations of the Cape Verde Rise. Their models were restricted to an isoviscous mantle with a conductive lid to simulate the lithosphere. Richards et al. (1988) examined the effects of temperature-dependent rheology on plume geoid and topography. Their study assumed a fixed temperature field and solved only the incompressible equations of motion. Bercovici et al. (1988) examined geoid and topographic uplift for spherical axisymmetric convection, but they restricted their study only to isoviscous convection at Rayleigh numbers less than 27 times critical, well below the range relevant to Earth, Venus, and Mars.

Our calculations have been done using the cylindrical axisymmetric convection code of Daly and Raefsky (1985). This code solves the incompressible equations of motion using a penalty function formulation (Hughes, 1987, Section 4.4) and bilinear shape functions. In the penalty function formulation, the

incompressible continuity equation is not explicitly solved. Rather, a slightly compressible form of the continuity equation is imposed as a Lagrangian multiplier type constraint on the solution to the equations of motion. This constraint is parameterized by the choice of the penalty parameter, λ; incompressibility is achieved in the limit $\frac{\lambda}{\eta} \rightarrow \infty$. λ must be chosen large enough to make the solution approach incompressibility and yet small enough to avoid numerical difficulties. Following Daly and Raefsky (1985) and Hughes (1987), we use $\frac{\lambda}{\eta} = 10^7$. In this formulation, it is not necessary to directly solve for the pressure, which is obtained instead from the relationship $P = -\lambda \nabla \cdot V$. The energy equation is solved using a streamline-upwind Petrov-Galerkin formulation (Brooks and Hughes, 1982). This method is more accurate than either the Galerkin method or normal upwind methods for advection-dominated flows.

The code steps between solutions of the energy equation and of the equation of motion. For a given temperature field, it calculates the corresponding velocity field, which is then used to update the temperature equation for the next timestep. The code uses an implicit time-stepping routine which allows us to efficiently obtain steady-state solutions (Hughes, 1987). We discuss time-dependent solutions in a subsequent section. Daly and Raefsky (1985) reported a number of comparisons between their code results and laboratory convection experiments and analytic boundary layer models. These comparisons provide a good check on the accuracy of the code.

For mechanical boundary conditions, we assume zero vertical velocity and free-slip (zero shear stress) on the top and bottom of the cylinder,

$$V_z = \frac{\partial V_r}{\partial z} = 0. \tag{7a}$$

Similarly, along the axis and outer rim, we have

$$V_r = \frac{\partial V_z}{\partial r} = 0. \tag{7b}$$

For thermal boundary conditions, we apply an insulating sidewall condition along the axis and outer rim of the cylinder,

$$\frac{\partial T}{\partial r} = 0. \tag{8a}$$

In models which are heated entirely from below, we assume constant temperature boundaries, T=0 on top and T=1 on the bottom. For models that are partially heated from within, we still apply T=0 on the top but find it convenient to impose a flux boundary condition on the bottom,

$$\frac{\partial T}{\partial z} = \frac{F}{k}, \tag{8b}$$

where F is the specified basal heat flux and k is the thermal conductivity.

Scaling Parameters

The various scaling parameters that we have used to dimensionalize our calculations are identified in Table 1, along with the specific numerical values that we have assumed. Comments on several of these numerical values are in order. We assume that the convective layer thickness, d, is that for whole mantle convection. For Earth, this is 2900 km, or somewhat less if part of the D" layer is a chemically distinct region. Because Venus is about 300 km smaller in radius than Earth, its mantle is probably 100 to 150 km thinner than Earth's mantle (Basaltic Volcanism Study Project, 1981, pp. 682-685). We have therefore adopted d=2800 km for use in our models. The value of ΔT given in Table 1 does not represent the entire temperature change that occurs vertically through the mantle. For example, because we assume incompressible convection, it is inappropriate to include temperature differences associated with the adiabatic gradient or with phase transitions. For the purpose of modeling geoid anomalies, topographic uplift, and heat flow anomalies, the more critical parameter is actually the horizontal variations of temperature within the mantle. As we discuss in more detail in a later section, our choice of ΔT leads to a temperature contrast between the plume center and the mean mantle of about 300 °C, a value which agrees with several lines of observational constraints.

Several of the parameters in Table 1, particularly ρ, α, and κ, are expected to vary with depth in the mantle (Anderson, 1987). In our models, these parameters are assumed to have constant values. Because the geophysical observables of interest are most sensitive to the upper part of the plume's thermal structure, we have chosen values of these parameters which are

representative of upper mantle conditions. Viscosity is also expected to be a strong function of depth. As discussed in a later section, we have explicitly included this in our models.

Calculation of Topographic Uplift and Geoid Anomalies

Having obtained the temperature and velocity fields for a given convection model, we can calculate various quantities, such as topographic uplift and geoid anomalies, for comparison with observational data. We calculate topographic uplift from the vertical normal stress,

$$\tau_{zz} = 2\eta \frac{\partial V_z}{\partial z} - P \,. \tag{9}$$

For each element in the top two rows of elements, we calculate an element average value of τ_{zz} which is assigned to the element center. We convert the non-dimensional τ_{zz} to dimensional units by multiplying by $\frac{\eta_o \kappa}{d^2}$, or equivalently by $\frac{\rho g \alpha \Delta T d}{Ra}$. Here η_o is the viscosity used to normalize the depth-dependent viscosity profile (See Figure 9). We project these values to the surface nodes using a modified version of the pressure-smoothing algorithm of Hughes (1987, Section 4.4.1) and then calculate the horizontally averaged value of the vertical stress at the surface, $\overline{\tau}_{zz}$.

Once we have obtained τ_{zz} and $\overline{\tau}_{zz}$ at the surface, we calculate surface topography, δh, from the relationship

$$\delta h = \frac{(\overline{\tau}_{zz} - \tau_{zz})}{\rho_s g} \,. \tag{10}$$

ρ_s is the density of the surface layer that is uplifted. For continental hotspots, ρ_s is the same as ρ_m because both crust and mantle material is uplifted. For oceanic hotspots, $\rho_s = \rho_m - \rho_w$, where ρ_w is the density of seawater. In the results given in this paper, we have set $\rho_s = \rho_m - \rho_w$; thus, for continental hotspots it is necessary to multiply our results for topography by

$$\frac{\rho_m - \rho_w}{\rho_m} = 0.70. \tag{11}$$

We use a similar procedure to calculate the topography at the base of the

convecting layer. Although we are not directly interested in this quantity as an observational test of our models, it is necessary to include the effects of density anomalies at this interface in calculating geoid anomalies.

Because the geoid is a surface of constant gravitational potential, U, we must first calculate U before calculating the geoid anomaly. At or above the surface of a planet, the potential must satisfy Laplace's equation, $\nabla^2 U = 0$. In cylindrical geometry, Laplace's equation is most readily solved by expanding the radial variations of temperature and of topographic uplift in terms of a series of Bessel functions of the form $J_0(k_n r)$, where k_n is a horizontal wavenumber. With such a series expansion, the external potential varies vertically as $\exp(-k_n z)$. At the surface (z=0), the potential is therefore given by

$$\delta U = \frac{2\pi G}{g} \sum_n \frac{J_0(k_n r)}{k_n} \left(\rho_s \delta h_s^n + (\rho_c - \rho_m) \delta h_c^n \exp(-k_n d) - \rho_m \alpha \int_0^d T^n(z) \exp(-k_n z)\, dz \right). \qquad (12)$$

In equation 12, δh_s^n and δh_c^n are the n-th harmonics of the surface topographic uplift and the core-mantle boundary uplift. Similarly, $T^n(z)$ is the n-th harmonic of the temperature field at depth z. G is the gravitational constant. We do not consider the zero-th order gravitational potential and instead begin the sum at n=1, so that δU represents the anomalous potential. For models with 33 horizontal nodes, the Nyquist condition shows that we can resolve harmonics up to $n = 16$. Based on the shape of the potential spectrum, essentially all of the power in the spectrum occurs for $n \leq 10$. In order to determine the values of the harmonic coefficients and the depth integral in equation 12 as accurately as possible, we use the finite element shape functions to interpolate the temperature fields onto 129 x 129 node meshes. The integrations are then done using a midpoint rule. We have experimented with interpolating the solutions onto even finer grids, but find that this does not significantly alter the integration results.

Although equation 12 formally includes the core density, ρ_c, in practice it is not necessary to specify a value for ρ_c. This is because, by analogy with

equation 10, the density contrast and the topographic uplift are inversely related, with a constant product, namely $(\rho_c - \rho_m)\,\delta h_c^n = \frac{(\tau_{zz} - \overline{\tau}_{zz})}{g}$. Similarly, the value of the potential does not depend on whether or not an ocean is present.

The geoid anomaly is related to the potential by the expression $\delta N = \frac{\delta U}{g}$. Equation 12 shows that there are three contributions to the geoid anomaly. The first two terms in the braces are the contributions of the mass anomalies created by uplift of the top and bottom surfaces of the convecting layer. The third term represents the contributions of mass anomalies due to thermal expansion of material within the convecting layer. For a convective upwelling, the first two contributions are positive and the third contribution is negative. The sign of the potential, and hence of the geoid anomaly, depends on the relative balance of the three terms. For the models described in this paper, the topographic mass anomalies dominate, so that the geoid is positive over the upwellings.

In the work that follows, we present both geoid anomalies and topographic uplift in dimensional form, based on the scaling parameters of Table 1. In Table 2, we have tabulated the peak values of the geoid and topography (along the axis of the cylinder) in non-dimensional form. Table 2 also identifies the model parameters that define each model calculation. The non-dimensional geoid and topography results given in Table 2 are related to the dimensional values by the relationships

$$\delta N = \frac{G\,\rho_m\,\alpha\,\Delta T\,d^2}{g}\,\delta N' \tag{13a}$$

and

$$\delta h = \left(\frac{\rho_m}{\rho_s}\right)\alpha\,\Delta T\,d\,\delta h' \ . \tag{13b}$$

In equations 13a and 13b, δN and δh are the dimensional geoid and topography along the plume axis and the primed values are the corresponding non-dimensional values. The other variables are as defined above.

Calculation of Nusselt Number and Heat Flow Anomalies

In addition to the geoid and topography of a plume, we are also interested in the heat transported by plumes. The non-dimensional heat flux is simply

$$Q = V_z T - \frac{\partial T}{\partial z} . \tag{14}$$

Following Ho-Liu et al. (1987), for each element, we calculate Q at the 2x2 Gaussian quadrature points and sum the values at the four quadrature points to determine an average flux for the element. The Nusselt number, Nu, is determined by integrating over all elements in order to determine a volume-averaged heat flux.

The surface heat flow anomaly is calculated by taking Q(r) along the surface and removing the average Q in order to determine the anomalous heat flow. The surface heat flow anomaly is converted to dimensional form by multiplying by $\frac{k \Delta T}{d}$, where k is the thermal conductivity.

Grid Resolution Requirements

In any numerical convection study, it is important to demonstrate that the numerical grids used have fine-enough spacing to resolve the non-linear physics. We have carried out an extensive series of resolution checks on our plume models using two different grid types. In one, the nodes are uniformly spaced in both the radial and vertical directions. In the second, nodes are uniformly spaced in the radial direction but non-uniformly spaced in the vertical direction, with spacing in the upper boundary layer being four times higher than it is with the uniform grid, as shown in Figure 1.

A representative set of results are shown in Figure 2, which examines the effect of varying grid resolution on a constant viscosity, $Ra=10^5$ cylinder. This figure presents the results of geoid anomaly, topographic uplift, and Nusselt number when calculated on grids with 17 x 17, 33 x 33, and 65 x 65 nodes. In Figure 2, the peak geoid and topography at the center of the upwelling and the globally averaged Nusselt number are shown as a percent deviation from the results for the 65 x 65 uniform grid model. The symbols represent calculated values, which are connected with line segments to illustrate the trends in the

data. The triangles and solid lines represent results from the uniform grid models. The squares and dashed lines represent results from the non-uniform grid models. For calculations of Nusselt number (Figure 2c), the two grid types give results that differ negligibly, so only one curve is shown. Based on the behavior of the curves in Figure 2, it is clear that the model results would change by only a small amount if carried out on grids larger than 65 x 65 nodes. Somewhat surprisingly, Figures 2a and b indicate that the convergence as a function of grid size is somewhat more rapid on the uniform grid than on the non-uniform grid. Both grids do eventually converge to the same values, however. In spite of the more rapid convergence of the uniform grid, in this study we have generally made use of a non-uniform grid such as that shown in Figure 1. We have done so because, as described in a later section, the high vertical resolution (11-22 km) in the upper boundary layer of the non-uniform grid enables us to mimic the variation of viscosity with depth expected in a thermal boundary layer.

In the results which follow, our calculations are generally carried out on 33 x 33 and 65 x 65 grids. All models with $Ra > 10^5$ were calculated using both grids to check convergence. Models with lower Rayleigh numbers were calculated on the 33 x 33 grid, with a selected set of these models checked for convergence using the 65 x 65 grid. Based on the resolution tests in Figure 2 and our other resolution tests, we believe that the calculations reported here are typically within $\pm$ 2 to 3% of their true values if calculated on a grid of infinite resolution. One exception to this is the geoid anomalies calculated for models which include an asthenosphere (Viscosity Model 3 of Figure 9). For these calculations, our resolution tests suggest that our highest resolution results may be as much as 5 to 10% higher than their true values at infinite grid resolution.

The other area of problematic resolution is the heat flow anomaly in models with constant viscosity. Because the thermal boundary layer is thinnest along the axis of the upwelling, our ability to resolve the boundary layer structure is poorest in this region. Our resolution studies show that for constant viscosity models, even our highest resolution grids do not accurately determine the heat flow anomaly near the plume axis, and for this reason, we do not show heat flow anomaly results for the constant viscosity case in this paper.

However, because the Nusselt number is defined in terms of a volume-averaged heat flux, we are able to accurately determine Nu in these models, as shown in Figure 2c. In most of the models described in this paper, we have used a high viscosity near-surface layer to mimic the effects of temperature-dependent viscosity. The inclusion of such a layer tends to thicken the thermal boundary layer, so that our heat flow anomaly results are well-resolved in these cases.

Basal versus Internal Heating

In terrestrial planets, mantle convection is driven by a combination of basal heating, due to heat flowing from the core into the mantle, and internal heating, due to radioactive decay and secular cooling of the mantle. In most of the models presented in this paper, we assume an internal heating parameter of $\mu = 0.0$, and as noted earlier, we scale our models with a value of d appropriate for whole mantle convection. We recognize that for whole mantle convection models of the Earth, μ must be closer to 1 than to 0. Nevertheless, we believe that our models actually do provide a reasonable model for the thermal structure of mantle plumes. As we see it, there two key questions which must be considered. Do plumes form if μ is close to 1? If plumes do form, what is the temperature contrast between a plume and the surrounding mantle? We address these issues in turn.

Do Plumes Form in a Mostly Internally Heated Mantle?

The value of μ is important because it determines whether or not plumes can form. As shown in Figure 3a, if $\mu=1$, no bottom boundary layer forms and consequently no plume can form. This is true whether or not viscosity is assumed to be temperature-dependent (Parmentier et al., 1975). However, if there is some basal heating ($\mu<1$), then a bottom boundary layer must form. In a medium whose rheology is temperature-dependent, boundary layer instabilities can then lead to the formation of narrow upwellings in a geologically short period of time (e.g., Olson et al., 1987). Plumes will therefore form even when μ is large. An example of this is shown in Figure 3b, where we show a

calculation at $\mu = 0.8$ and $Ra_F = 1 \cdot 10^6$. A rising plume is clearly visible in this model. For comparison, Figure 4 shows a model with μ=0.0.

In spherical geometry, the heat flow out of the core is concentrated into an area that is only about 25 % of the area of the Earth's surface. Thus, for a given μ, a model calculated in spherical geometry will have a basal heat flux per unit area which is nearly 4 times that of our cylindrical models. Thus, plumes at large μ in spherical geometry will be even more pronounced than indicated in Figure 3b. We therefore believe that our assumption of μ=0 does not significantly affect our results.

The Temperature Contrast between Plumes and the Surrounding Mantle

The second key issue is the magnitude of the temperature contrast, δT, which exists between the plume and the surrounding mantle. (Note that δT is a different quantity than ΔT, which we used earlier to denote the variation of temperature with depth. See Figure 4.) The value of δT is important because the geoid anomaly, topographic uplift, and heat flow anomaly all scale linearly with the size of the temperature contrast.

For ΔT=1000 °C as given in Table 1, Figure 4 shows that δT is about 300 °C. Several lines of observational evidence suggest that this is in fact a reasonable estimate of the temperature contrast between plumes and normal mantle. One type of constraint on the magnitude of δT comes from petrology. Wyllie (1988) showed that δT of up to 300 °C is consistent with the petrology of Hawaiian basalts. McKenzie and Bickle (1988) estimated that a temperature contrast of about 200 °C is necessary to produce the excess crustal thickness observed at hotspots such as Iceland. This estimate presumably refers to the average thermal contrast in a plume, so that the peak value must be somewhat larger than 200 °C.

Geophysical arguments can also help constrain δT. Richards et al. (1988) developed a kinematic model of the interaction between the radial outflow of material away from a plume and the flow driven by plate motions. They concluded that the stagnation line between the two flow regimes is consistent with the observed shape of the southeastern end of the Hawaiian swell, provided that δT is around 300 °C. In principle, observations of heat flow anomalies can

also help constrain δT. Our choice of thermal scaling predicts heat flow anomalies that are consistent with observations, although as discussed in greater detail in a later section, our heat flow results do not tightly constrain the allowed value of δT.

As Figure 4 shows, δT is essentially the same as the temperature difference which occurs vertically in the lower thermal boundary layer. We can therefore obtain an independent estimate of δT from the relationship

$$F = k\frac{\delta T}{\delta z} \quad , \tag{15}$$

where k is the thermal conductivity and δz is the thickness of the lower thermal boundary layer. As before, F is the heat flux into the base of the convecting layer.

Gubbins et al. (1979) estimated a total core heat flow of $2.5-5.0 \cdot 10^{12}$ W is needed to drive the Earth's magnetic dynamo. This corresponds to a value of F between 16 and 33 mW m^{-2}. On the basis of thermal history models, Stevenson et al. (1983) estimated F for the Earth between 17 and 25 mW m^{-2}. Melchior (1986) gave an estimated lower bound on F of 20 mW m^{-2}. Brown (1986) estimated that k varies between 12 and 18 W m^{-1} K^{-1} at conditions near the core-mantle boundary. He noted, however, that there is little experimental constraint on this value and also gave several models with substantially smaller k. δz can be estimated from models of the seismic structure of the D" layer. Young and Lay (1987) gave seismic velocity versus depth profiles that indicate D" thicknesses of 200 to 280 km. If we adopt as representative values F=25 mW m^{-2}, k=15 W m^{-1} K^{-1}, and δz=200 km, Equation 15 leads to δT=330 °C.

Obviously, each of these methods for estimating δT has uncertainties associated with it. Taken together, the various constraints suggest that δT is likely to be in the range 200 to 300 °C for at least some plumes, with a preference towards values at the upper end of the range. Sleep (1990) has recently reached a similar conclusion. For Venus, the lack of a magnetic field has been interpreted as indicating that F for Venus might be a only 50 to 80% of the heat flux from Earth's core (Stevenson et al., 1983). A straightforward

application of Equation 15 would then suggest that δT is also a up to a factor of 2 lower on Venus than on Earth. However, the smaller value of F will also lead to a thicker lower thermal boundary layer on Venus (larger δz). Jeanloz and Richter (1979) used a boundary layer analysis and showed that the temperature contrast across a boundary layer should be proportional to $F^{0.75}$. As a result, δT for Venus should be similar to, but somewhat less than, its value on Earth. Given the uncertainties in the precise value of δT, we will use the same thermal scaling for both planets.

Cylindrical versus Cartesian Geometry

Figure 5 illustrates the differences between the thermal structures for Cartesian convection (Figure 5a) and cylindrical axisymmetric convection (Figure 5b). Both models are isoviscous, heated entirely from below, and have $Ra = 10^5$. In the Cartesian model, the upwellings and downwellings exhibit a 180° rotation symmetry. In the cylindrical model, the temperature contrast across the upwelling plume is much larger than the temperature contrast across the downwelling. Because of the cylindrical geometry, the upwelling flow along the axis of the cylinder is confined to a narrow area and hence must be quite vigorous in order to transport the required amount of heat. On the other hand, the downwelling return flow on the outer rim of the cylinder occurs in a larger total area. Consequently, the thermal anomalies and flow velocities must be less in the downwelling than in the upwelling, producing the asymmetric thermal structure shown in Figure 5b.

In Figure 6, we compare the geoid anomalies and topographic uplifts as a function of distance from the upwelling for the two thermal models of Figure 5. The cylindrical results are shown as solid lines and the Cartesian results are shown as dashed lines. The Cartesian results are calculated in a manner analogous to that described above for the cylindrical models, except that the wavenumber expansion is in terms of $\cos(k_n x)$ rather than Bessel functions. The Cartesian results are approximately symmetric about the center plane of the convection cell, with the lows over the downwellings having 10 to 20% larger amplitudes than the highs over the upwellings. The symmetry about the

midplane is not exact because the thermal anomalies have a rotation symmetry rather than a reflection symmetry.

In contrast, the results for the cylindrical model are noticeably asymmetric, with the amplitudes of the highs being 2.5 to 3 times the amplitudes of the lows. This reflects the asymmetry in the underlying thermal structure. Notice also that the amplitudes of the geoid and topography highs in the cylindrical case are about twice as large as in the Cartesian case. This reflects the more concentrated upwelling flow in the cylindrical case. Figure 6 clearly shows that it is important to choose the correct geometry when modeling the geoid and topography of mantle plumes. Given the evidence cited above for quasi-cylindrical upwellings under hotspots such as Hawaii, we believe that our models are more realistic than previously published models that used Cartesian geometry.

Although the geoid and topography are distinctly different for cylindrical and Cartesian geometries, the heat transport properties of the two geometries are quite similar. For isoviscous cylindrical models, we find $Nu = 10.42$ at $Ra = 10^5$ (Table 2, Model 6) and $Nu = 21.73$ at $Ra = 10^6$ (Table 2, Model 10). Blankenbach et al. (1989) recently published a benchmark comparison of ten different Cartesian convection codes. They gave consensus estimates of $Nu = 10.53$ and 21.97 for the cases $Ra = 10^5$ and 10^6 in Cartesian geometry. These results differ from our cylindrical results by only about 1%. Nusselt numbers for axisymmetric, isoviscous convection were previously published by Jones et al. (1976). Although our models do not correspond exactly to any of the models in Jones et al., their Nusselt number when the Rayleigh number is 100 times the critical value is about 10% less than expected from our Ra-Nu curve in Figure 13c.

Parameterization of Viscosity in the Upper Thermal Boundary Layer

Because viscosity is a strong function of temperature, it is expected to vary by many orders of magnitude between the surface of a planet and the convecting interior. Although our models do not include temperature-dependent

rheology, we have attempted to mimic the effect of temperature on boundary layer rheology by imposing a vertical variation of the form

$$\eta(z) = 10^{S\cdot(1 - \frac{z}{\gamma})}, \quad z \leq \gamma. \tag{16}$$

Equation 16 defines a viscosity profile which is normalized relative to a mantle viscosity of 1.0. The surface viscosity (at $z=0$) is 10^S, and the viscosity decreases exponentially with depth, reaching $\eta=1$ at $z=\gamma$, which defines the base of the high viscosity zone. Our parameterization of $\eta(z)$ within the mantle ($z \geq \gamma$) is discussed in the next section. In practice, equation 16 is approximated by a sequence of 3 to 7 step function changes in η, depending on the choice of γ. For our normal choices of $S=3$ and $\gamma=0.0469$, six steps are used, with the viscosity changing by a factor of $\sqrt{10}$ at each step.

We have investigated the effects of various values of S and γ via two sets of model calculations. In the first, illustrated in Figure 7, we vary S and hold γ fixed at a non-dimensional value of 0.0469, which corresponds to a dimensional depth of 130 km. This value of γ is chosen to correspond to the thickness of the lithosphere in old oceanic regions. In these calculations, the viscosity within the mantle (below the upper boundary layer) is independent of depth and the Rayleigh number is 10^5. We vary S between 0, corresponding to a constant viscosity model, and 5, corresponding to a surface viscosity that is 10^5 times the interior viscosity.

The effects that variations in S have on the geoid anomaly, topographic uplift, Nusselt number, and heat flow anomaly are shown in Figures 7a, b, c, and d, respectively. The geoid anomaly, topographic uplift, and heat flow anomaly are all evaluated at the plume axis. In each graph, the triangles represent the calculated model points, which are connected by line segments for ease of perceiving trends in the results. Each of the curves in Figure 7 drops sharply as the surface viscosity increases from 1 to 10^3 and changes much more gradually with further increases in surface viscosity. The sharp drop in Nu and heat flow anomaly with increasing S is easy to understand, because increasing the surface viscosity forces a thickening of the upper boundary layer and leads to smaller heat flows. The decrease in geoid and topography with increasing S may seem

more surprising, because a high viscosity surface layer enhances the coupling between the convecting layer and the surface, which might be expected to lead to larger topographic uplifts and geoid anomalies. Although this coupling effect certainly occurs, it is more than offset by changes in the thermal structure that are induced by changes in S. As an examination of the isotherm contours in Figures 4 and 5b shows, the horizontal variations in temperature within the mantle are much larger in isoviscous models (Figure 5b) than in models that include a high viscosity surface layer (Figure 4). The larger temperature contrasts in the isoviscous case lead to the larger geoid and topography shown in Figures 7a and b.

In a second series of model calculations, we hold the surface viscosity fixed using S=3 and vary γ over the range 0.0234 to 0.0547, which corresponds to dimensional lid thicknesses of 65 to 150 km. The effects of varying γ over this range are shown in Figure 8, which shows how geoid anomaly, topographic uplift, Nusselt number, and heat flow anomaly vary with γ. The triangles represent calculated points and the connecting line segments are least squares fit to the model results. Figure 8 shows that over the range of lid thicknesses that we have investigated, the geoid anomaly, topographic uplift, and Nusselt number only vary by 5 to 10%. The variations in heat flow anomaly are much larger, about 40%.

In the work that follows, we have adopted S=3 (surface viscosity = 10^3) and γ=0.0469 (Lid thickness = 130 km) as the parameters that define the lid viscosity in our models. Although the viscosity in the boundary layer of real planets clearly varies by much more than the 3 orders of magnitude assumed here, the results of Figure 7 make it clear that results obtained using a viscosity contrast of 10^3 will not differ significantly from models with much larger viscosity contrasts. Our nominal lid thickness of 130 km is comparable to the lithospheric thickness in the old parts of oceanic plates. This is a reasonable choice, because several of the hotspots of greatest interest, such as Hawaii, Cape Verde, and Bermuda, are located on oceanic lithosphere of age 90 million years or greater. Of course, some other hotspots, such as Iceland and the Azores, are located on spreading centers, where the lithospheric thickness is nearly 0. On Venus, the high surface temperature implies that the boundary

layer thickness should be somewhat less than on Earth. Kaula and Phillips (1981) estimated a thermal boundary layer thickness of slightly less than 100 km for Venus. Figure 8 shows that the difference between lid thicknesses of 100 and 130 km is slight for both the geoid and the topography. In recent years, a number of numerical models have used a conductive lid, in which both the vertical and horizontal velocity components are set to zero, as a means of simulating the thermal boundary layer structure (Courtney and White, 1986; Detrick et al., 1986; Robinson et al., 1987; Ceuleneer et al., 1988). We believe that our models, in which the viscosity varies continuously with depth, are somewhat more realistic than models in which there is a discrete change between conduction and convection. In practice, however, the difference between the two approaches is likely to be small.

Effects of Variation in Mantle Viscosity with Depth

The effects of depth variation of viscosity have been widely recognized both in studies of long-wavelength geoid anomalies (Richards and Hager, 1984; Ricard et al., 1984; Kiefer et al., 1986; Hager and Clayton, 1989; Hager and Richards, 1989) and in studies of the topographic uplift and geoid anomalies of individual mantle plumes (Robinson et al., 1987; Richards et al., 1988; Robinson and Parsons, 1988; Ceuleneer et al., 1988). Within the mantles of silicate planets, the viscosity may vary continuously with depth due to the effects of pressure on rheology. The viscosity may also undergo discrete jumps at phase changes. In this paper, we consider the effects of three layers of constant viscosity. The transition depths between the layers are at non-dimensional depths of $\gamma = 0.143$ and $\gamma = 0.25$, corresponding to dimensional depths of 400 and 700 km. This choice of parameterization was made both because it provides a convenient way of parameterizing $\eta(z)$ with a minimum number of parameters and also because it enables a straight forward comparison with results obtained by Hager and Clayton (1989) and Hager and Richards (1989) on the depth variation of mantle viscosity on Earth. In the following discussion, we refer to the layer between 130 and 400 km as the asthenosphere, the layer between 400 and 700 km as the upper mantle, and the layer below 700 km as the lower mantle.

Figure 9 shows the three standard viscosity models used in this study. The viscosity profiles are all normalized relative to the lower mantle viscosity. All three models have a high viscosity lid defined by the parameters $\gamma = 0.0469$ and $S = 3$, as described in the previous section. Viscosity model 1 (Figure 9a) has a high viscosity lid and an isoviscous mantle. In viscosity model 2 (Figure 9b), the asthenosphere and upper mantle layers have a viscosity that is 0.1 times the lower mantle viscosity. In viscosity model 3 (Figure 9c), the asthenosphere viscosity is 0.01 times that of the lower mantle and the upper mantle viscosity is 0.1 times the lower mantle viscosity.

In models in which viscosity varies with depth, one must choose which viscosity to use in defining the Rayleigh number. One possibility is to attempt to define a vertically averaged viscosity. An alternative method, followed here, is to choose one of the layer viscosities to define Ra. We use the lower mantle viscosity to define Ra. This is a reasonable choice because the lower mantle layer always occupies at least 75% of our model cylinder. Robinson et al. (1987) and Ceuleneer et al. (1988) used a similar procedure in their calculations.

Figure 10 shows profiles of geoid anomaly, topographic uplift, and heat flow for our three viscosity models at $Ra = 10^6$. The results for viscosity model 1 are shown in solid lines, viscosity model 2 results are in dashed lines, and viscosity model 3 results are in dot-dashed lines. These models correspond to models 23, 26, and 29 of Table 2. The presence of a low-viscosity asthenosphere reduces the efficiency with which deep convective stresses are able to couple with the surface. Thus, viscosity model 3 produces a weaker topographic uplift than is produced by the other models. As shown in Figure 10b, the peak topographic uplift is 7.4 km for viscosity model 1 and 3.6 km for viscosity model 3.

The geoid anomaly depends on contributions both from the mass anomalies at the uplifted surface and on thermally induced density anomalies within the convecting mantle. As Figure 11 shows, changing the viscosity model at fixed Ra does have some effect on the thermal structure. The most pronounced effect is in the region of the low viscosity zone. In this region, the plume is significantly narrower than in models without a low viscosity zone. As

noted by Richards et al. (1988), when a parcel of material enters the low viscosity zone, its velocity increases, so conservation of mass requires that the plume become narrower. Also, in models with a low viscosity zone (Figure 11b), the near-surface outflow of material away from the plume is confined to the low viscosity layer, whereas in models without a low viscosity zone (Figure 11a), the outflow occurs over a broader depth range. The decreased positive mass anomaly at the uplifted surface in models with a low viscosity zone is more important than the decreased negative mass anomalies within the mantle, so that inclusion of a low viscosity zone leads to significant decreases in the geoid anomaly. As shown in Figure 10a, the peak geoid anomaly decreases from 165 meters for viscosity model 1 to only 25 meters for viscosity model 3. If the asthenosphere viscosity were decreased below 0.01, then the additional decrease in topographic uplift could lead to a geoid anomaly that is negative over the upwelling.

Heat flow profiles are shown in Figure 10c. This figure suggests that the surface heat flow is relatively insensitive to the choice of viscosity model. However, as discussed in the next section, this result may be incorrect. It seems likely that the surface heat flow should actually be somewhat higher for viscosity model 3 than for the other two models.

Effects of Variation in Rayleigh Number

In Figures 12 and 13, we examine how varying the Rayleigh number effects the geoid, topographic uplift, and heat flow associated with a mantle plume. In Figure 12, we show profiles of these quantities as a function of distance from the center of the plume for $Ra = 10^5$ (solid line), $Ra = 3 \cdot 10^5$ (dashed line), and $Ra = 10^6$ (dot-dashed line). The results are for our viscosity model 3 and correspond to Models 27, 28, and 29 of Table 2.

Figures 12a and b show that both the geoid anomaly and the topographic uplift are decreasing functions of Ra. Using the scaling parameters of Table 1, the peak geoid anomaly over the upwelling decreases from 30 meters at $Ra = 10^5$ to 25 meters at $Ra = 10^6$. As we show in Figure 13a, the geoid

anomalies of our other viscosity models are much more sensitive to variations in Ra. The peak topographic uplift over the upwelling also decreases in amplitude, from 5.6 km at $Ra = 10^5$ to 3.6 km at $Ra = 10^6$.

In performing the calculations shown in Figure 12, we have held the quantity $\frac{\rho g \alpha \Delta T d^3}{\kappa}$ fixed, so that increasing Ra is equivalent to decreasing η. As shown in our earlier discussion of the calculation of topographic uplifts, this assumption implies that the dimensional normal stress, τ_{zz}, and hence the topographic uplift, is a decreasing function of Ra. The physical reasons that cause the topographic uplift to decrease with increasing Ra are readily understood. The surface topography produced by mantle convection receives contributions both from thermal anomalies in the near-surface thermal boundary layer and from thermal anomalies in the upwelling and downwelling limbs of the convection cell. As one proceeds to higher Ra, the upwellings, downwellings, and thermal boundary layers all become narrower. (Compare Figures 4 and 11a.) Density anomalies within the thermal boundary layer produce topography in a manner which is essentially equivalent to Pratt compensation, so that as the boundary layer is thinned, the amount of topographic uplift that it can support is decreased. The narrowing of the upwellings and downwellings with increasing Ra implies that in the spectral domain, there is an increasing amount of power at short wavelengths. These short wavelengths do not couple as efficiently to the surface as longer wavelengths do, and hence they produce less topographic uplift. Together, these two effects produce the observed decrease in topographic uplift with increasing Ra.

In contrast with our assumption, Davies (1986) increased Ra by increasing ΔT, which implies that that topographic uplift increases with increasing Ra. Although controlling the value of Ra by varying the value of ΔT is a fluid dynamically acceptable choice, it produces misleading results when applied to real planets. Because viscosity is a strong function of temperature, small increases in ΔT will lead to large decreases in η. Thus, we prefer to hold ΔT constant and vary Ra by varying η.

The geoid anomaly over a mantle plume is the sum of positive contributions from topographic uplift of the surface and of the core-mantle boundary

and a negative contribution from hot, low density material in the upwelling plume. As shown above, the surface topographic uplift is a decreasing function of Ra, and in the same manner, the core-mantle boundary uplift is also a decreasing function of Ra. The narrowing of the upwellings and downwellings with increasing Ra implies that their contribution to the geoid anomaly is also a decreasing function of Ra. The net sum of these contributions leads to an overall decrease in the geoid anomaly with increasing Ra, as shown in Figure 12a.

Figure 12c shows profiles of the surface heat flow anomaly versus distance from the upwelling plume for three different values of Ra. The line patterns are the same as used in Figures 12a and b. As one proceeds to higher Ra, the thinner thermal boundary layer will of course lead to higher average heat flow, and hence to higher Nusselt numbers. As Figure 12c shows, increasing Ra also leads to increasing values of the surface heat flow anomaly.

In Cartesian geometry, it is well known that if the Rayleigh number is high enough that well developed boundary layers form, then the Nusselt number can be written as a power law function of Ra. A similar relationship between Ra and Nu also exists in cylindrical geometry, and relationships can also be found between Ra and the geoid, the topographic uplift, and the peak heat flow. In Figure 13, we show the relationships that we find between Ra and the other quantities. These results are plotted as log-log figures, so that a power law relationship follows a straight line. The triangles are results for constant viscosity, the squares are for viscosity model 1, the pentagons for viscosity model 2, and the stars for viscosity model 3. In each case, the lines represent least squares best fitting lines. The least squares fits were calculated using only points with $Ra \geq 10^5$. For the constant viscosity model, the derived power laws also provide a good fit to model results with Ra as low as $Ra = 3 \cdot 10^4$. For viscosity model 1, the results for $Ra = 10^4$ begin to deviate from the power law relationship. This reflects the absence of well developed boundary layers at this relatively low Ra.

Table 3 shows the derived power law parameters. They are expressed in terms of $f(Ra) = a \cdot (Ra)^b$, where a and b are constants and f(Ra) is a quantity

such as geoid or Nu. The geoid, topography, and heat flow results refer to the peak values of these quantities along the axis of the upwelling. They are dimensionalized using the values in Table 1 and are in units of meters (geoid), kilometers (topographic uplift), and mW m^{-2} (heat flow).

Figure 13a shows that the geoid anomalies for viscosity model 3 are a much weaker function of Ra than is observed for the other viscosity models. We find a power law exponent of only $b = -0.084$ for viscosity model 3, whereas the other viscosity models have exponents in the range -0.27 to -0.29. There is also some suggestion of curvature in the Ra-geoid relationship for viscosity model 3, but we can not fully define this on the basis of only 3 model points. In the Cartesian geometry results of Robinson and Parsons (1988, Figure 10), the geoid anomaly also appears to be a weaker function of Ra in models with a low viscosity layer than in models without a low viscosity layer. However, this flattening of the Ra-geoid relationship does not appear to be as strong in the work of Robinson and Parsons (1988) as it is in our results. A quantitative comparison can not be made because they did not tabulate power law parameters for their results.

We noted earlier that for our constant viscosity models, our values for Nu agree closely with those observed in Cartesian geometry. Consequently, the power law parameters for the two geometries are also quite similar. For example, Ho-Liu et al. (1987) gave $b = 0.326$ for the isoviscous Cartesian case. Using the same volume averaging technique as used by Ho-Liu et al., we find $b = 0.319$ for our isoviscous cylindrical models.

Although all of the models reported in this paper use a free-slip top boundary, the models with a high viscosity lid have very low flow velocities at the top surface and behave as if the top surface were nearly rigid. In Cartesian geometry, both analytic and numerical studies of convection with rigid boundaries show that the power law exponent in the Ra-Nu relationship is about 0.2 (Roberts, 1979; Mitrovica and Jarvis, 1987). Our high viscosity lid models produce similar results, with b in the range 0.17 to 0.20 for our three viscosity models. For a given lower mantle viscosity, viscosity model 3 has a smaller vertically-averaged viscosity than the other two viscosity models. Consequently,

at a given Ra, viscosity model 3 has a higher Nu than the other two viscosity models (Figure 13c).

The heat flow anomaly results for the three models with high viscosity lids show vastly different slopes when plotted as a function of Ra. The three models give virtually the same heat flow at $Ra = 10^6$. If projected to still higher Ra, viscosity model 1 would predict a higher peak heat flow than the other models. Given that the overall heat flow is highest for viscosity model 3, it seems surprising that viscosity model 1 could ever have a higher peak heat flow than viscosity model 3. This suggests that the heat flow systematics given in Figure 13d may not provide a useful basis for projecting the behavior of the peak heat flow at higher Ra.

Effects of Variation in Aspect Ratio

The aspect ratio of a convection cell is defined as the distance from the upwelling to the downwelling, divided by the depth of the cell. Until now, we have assumed an aspect ratio of 1. This is consistent with the experimental results of Nataf and Richter (1982). On the other hand, Christensen and Yuen (1988) numerically studied a two-dimensional Cartesian box of aspect ratio 12. The individual convection cells that developed within the larger box typically had an aspect ratio of about 1.5, with some variation about the mean. Hotspots in the Pacific Ocean, such as Hawaii, might seem to provide evidence for plume aspect ratios exceeding 2. Although material that comes up through the Hawaiian plume is eventually subducted in the western Pacific, we argue that this is not an appropriate measure of the horizontal scale of mantle plume flow. For the purpose of understanding the thermal structure of an upwelling plume, we are actually more interested in the area at the base of the convecting layer that feeds each upwelling. Judging from the spacing between hotspots, an average aspect ratio for terrestrial mantle plumes is about 0.5, although there is likely to be some variation about this value. For example, vigorous plumes such as Hawaii may have "feeding zones" in the lower thermal boundary layer that are larger than normal, implying aspect ratios that are also larger than

normal. In this section, we examine how varying the aspect ratio over the range 0.5 to 1.4 affects a plume's structure.

Figure 14 illustrates how varying the aspect ratio affects the thermal structure of a plume. Figure 14a shows a cylindrical model with a high viscosity lid (viscosity model 1), $Ra = 10^5$, and an aspect ratio of 1.4. In comparison with a similar model of aspect ratio 1.0 (Figure 4), the upwelling plume in Figure 14a is significantly broadened. This broadening is necessary to transport the additional heat introduced at the base of the cylinder when the aspect ratio is increased. A similar broadening is also observed with increasing aspect ratio for isoviscous cylindrical models. Figure 14b shows an isoviscous Cartesian model with $Ra = 10^5$ and aspect ratio 1.4. Comparing Figures 5a and 14b, we see that very little broadening of the upwellings and downwellings occur in the large aspect ratio Cartesian case.

Figure 15 shows how varying the aspect ratio affects the geoid anomaly, topographic uplift, and Nusselt number for cylindrical geometry plumes. The models shown in Figure 15 have $Ra = 10^5$, use viscosity model 1, and vary the aspect ratio. The geoid anomaly and topographic uplifts refer to the peak values on the axis of the cylinder, while the Nusselt number is a volume-average.

As shown in Figures 15a and b, both the geoid and the topography are approximately linear functions of the aspect ratio. The solid lines are least squares best fits and the triangles are model results. These fits can be expressed as

$$\frac{\delta N}{\delta N_1} = 1.3\,A - 0.3 \tag{17a}$$

and

$$\frac{\delta h}{\delta h_1} = 0.89\,A + 0.07\ . \tag{17b}$$

In equation 17a, δN is the geoid anomaly, δN_1 is the geoid anomaly at aspect ratio 1.0, and A is the aspect ratio. Similarly, in equation 17b, δh is the topographic uplift and δh_1 is the topographic uplift at aspect ratio 1.0. Although the formal linear correlation is good for the topography results ($r^2 = 0.99$), there

is clearly also some concave downward curvature in the results shown in Figure 15b. The broadening of the plume with increasing aspect ratio implies an increased amount of long-wavelength loading. Because long wavelengths couple more efficiently to the surface than short wavelengths, this implies an increasing topographic uplift with increasing aspect ratio. The increased mass anomalies due to the higher topography leads to a larger geoid.

Figure 15c shows that Nu has a maximum value between aspect ratios 0.8 and 1.0. In Cartesian geometry, both Hansen and Ebel (1984) and Olson (1987) found Nu maxima at aspect ratios slightly less than 1.0.

Time-Dependent Convection

As noted earlier, our finite element calculations use an implicit time stepping routine. This allows us to use time steps that are significantly larger than allowed by the Courant condition in explicit time stepping routines. As a result, we are able to obtain steady-state solutions efficiently whenever such solutions exist. Using this technique, we have found steady solutions for all of the models listed in Table 2, where steady-state is defined as no change in either the heat flux or kinetic energy of the flow at the level of 1 part in 10^5 for 100 or more time steps. However, use of large time steps with an implicit technique may produce an apparently steady solution that would actually be time-dependent if calculated using the Courant condition time-step. We have therefore examined several of our models using the Courant time-step and running the calculation for the equivalent of several over-turn times in order to determine if the solutions are truly steady-state.

Several parameters are believed to affect the development of time-dependent convection. Jarvis (1984) suggested that high Rayleigh numbers should favor time-dependent convection. Ceuleneer et al. (1988) found that pronounced contrasts between upper and lower mantle viscosities also favors the development of time-dependence. Based on these considerations, we have tested our model 29 for possible time-dependence. This model uses $Ra = 10^6$ and viscosity model 3 (asthenosphere viscosity = 0.01·lower mantle viscosity).

When calculated on a 65 x 65 grid using a Courant time-step, we find that this model is weakly time-dependent. Specifically, we observe the formation of instabilities in the upper thermal boundary layer that detach from the top boundary layer and descend along the outer side wall as discrete blobs. The upwelling plume, in contrast, appears to be steady. Over the course of several over-turn times, we observed variations in the peak geoid and peak topographic uplift of 3 to 4% and variations of 2% in the volume-averaged Nusselt number. Because of the relatively weak time-dependence observed for this model, we have not tested our other $Ra = 10^6$ models for time-dependence. At higher values of Ra, however, it seems possible that all three of our standard viscosity models will become time-dependent. Inclusion of temperature-dependent rheology would probably also enhance the development of time-dependent flow.

Several recent studies have shown that large aspect ratios can lead to time-dependent convective flow (Christensen, 1987; Hansen and Ebel, 1988; Weinstein et al., 1989). We have therefore tested our model 34 for possible time-dependence. This model was calculated on a 33 x 33 grid. It has $Ra = 10^5$ and an aspect ratio of 1.4 and uses viscosity model 1. When calculated for 1000 Courant time-steps, we find no evidence for time-dependent behavior in this model. We have not tested our models that use internal heating for possible time dependence.

Comparison of Model Results and Observations

In this section, we compare the results of our plume models with observations. We consider two terrestrial hotspots, Hawaii and Cape Verde. Hawaii is chosen because it is the archetypal hotspot. Cape Verde is chosen because it is a well studied hotspot on a slow moving plate. We also briefly discuss the applications of our models to Beta Regio, a highland structure on Venus.

Based on modeling of the Earth's long-wavelength geoid, Hager and colleagues have estimated the variation of viscosity as a function of depth in the Earth's mantle (Hager and Richards, 1989; Hager and Clayton, 1989). Their preferred Earth model most nearly resembles our viscosity model 3. The main

difference between their preferred model and our model 3 is in the asthenosphere viscosity. Hager and colleagues preferred an asthenosphere viscosity that is 0.003 times the lower mantle viscosity, a factor of 3 less than the asthenosphere viscosity used in our model 3. As Figure 10 shows, using a smaller asthenosphere viscosity will decrease the amplitude of both the geoid and the topographic uplift. Our parameterization of the viscosity within the upper boundary layer also differs from that used by Hager and colleagues, but this is unlikely to significantly affect the geoid and topography results.

Hager and Clayton (1989) used their estimated viscosity profile, estimates of mantle density anomalies inferred from seismic tomography, and the Earth's observed heat flow to place bounds on the lower mantle viscosity. They estimated a lower mantle viscosity of at least $3 \cdot 10^{23}$ Poise is necessary in order to prevent the heat flow out of the mantle from exceeding the observed value. Using this value of η along with the parameter values from Table 1 implies that Ra is about $7 \cdot 10^5$. On this basis, we calculated models with Ra up to 10^6. More recently, Hager (1989) has lowered this estimate to $3 \cdot 10^{22}$ Poise. In the earlier work of Hager and Clayton (1989), tomographic data on the density heterogeneity spectrum was used only out to spherical harmonic degree 6, and the density heterogeneity spectrum was assumed to be relatively flat at shorter wavelengths. However, Gudmundsson et al. (1990) recently found that in the Earth's lower mantle, the heterogeneity spectrum is strongly dominated by the longest wavelengths. Hager (1989) incorporated this effect into his new model, and also considered the effects of a low-viscosity zone in the D" layer. With these two effects included in the model, he finds that a lower mantle viscosity of $3 \cdot 10^{22}$ Poise is consistent both with the observed heat flow and with the observed plate velocities. This new viscosity estimate implies that Ra is about $7 \cdot 10^6$ for the Earth. Because of the computational expense of calculating properly resolved convection models at high Ra, we have not calculated models beyond $\mathrm{Ra} = 10^6$. However, we can use the power law relationships derived above to estimate what the geoid, topographic uplift, and heat flow should be at higher Ra and can then compare these projections with observations. Table 4 shows the results of these power law projections. For each viscosity model, the results at $\mathrm{Ra} = 10^6$ are based on our model calculations and the values at

$Ra = 5 \cdot 10^6$ and 10^7 represent power law projections. The two higher values of Ra were chosen to bracket the estimate of $7 \cdot 10^6$ derived using Hager's (1989) lower mantle viscosity.

Table 4 shows that for viscosity model 3 and Ra between $5 \cdot 10^6$ and 10^7, Nu should be between 15 and 17. An estimate of Nu for the Earth can be derived from the average boundary layer thickness. For isoviscous Rayleigh-Benard convection in Cartesian geometry, the temperature contrasts across the upper and lower boundary layers are the same (Figure 5a). One can therefore estimate Nu from the ratio of half the depth of convecting layer to the boundary layer thickness,

$$Nu = \frac{(d/2)}{\delta} , \tag{18}$$

where d is the convecting layer thickness and δ is the thickness of the boundary layer. Inclusion of temperature-dependent rheology, spherical geometry, and the depth-dependence of the thermal diffusivity will alter the relative values of the temperature contrasts across the two boundary layers, but Equation 18 is still useful as a means of estimating an approximate value of Nu. Oceanic plates on Earth have a maximum thickness of 125 km and average about 90 to 100 km thick. Assuming whole mantle convection, Equation 18 then implies Nu in the range 14.5 to 16, consistent with our viscosity model 3 results and our preferred range for Ra. Given that mantle plumes probably transport only a small fraction of the Earth's mantle heat flow (e.g., Davies, 1988; Sleep, 1990), it may seem inappropriate to compare the Nusselt numbers from our single cell plume models with estimates of the Earth's Nu. However, in a series of models at fixed Ra_F and variable μ, we find that Nu varies by only about 10 % as μ varies from 0 to 1. We therefore believe that it is reasonable to compare our model Nusselt numbers with the Earth's Nusselt number.

The Cape Verde Rise

The Cape Verde Rise is a hotspot swell on the African plate. Extensive volcanic activity extends back to 20 million years ago, although Courtney and White (1986) summarize evidence suggesting that some volcanic activity extends back to 50 million years ago, or possibly to even earlier dates. The

velocity of the African plate in the vicinity of Cape Verde is quite low, although the precise value depends on the choice of location for the pole of rotation. Davies (1988) suggests a velocity of less than 0.5 cm $year^{-1}$, while Sleep (1990) suggests a velocity of 1.2 to 1.8 cm $year^{-1}$. These velocities are sufficiently low that the lithosphere should be able to reach thermal equilibrium with the underlying plume.

Courtney and White (1986) estimated a peak geoid anomaly of 7.6 $\pm$ 0.3 meters. Crough (1982) estimated a peak geoid anomaly of 8 meters, and McNutt (1988) estimated a peak geoid anomaly of 12 meters. The peak topographic uplift was estimated to be 1.9 $\pm$ 0.2 km by Courtney and White (1986), 2 km by Crough (1982), and 2.4 km by McNutt (1988). The different estimates are apparently due to different methods of filtering the data. Crough (1982) estimated a swell width of 1600 km. Courtney and White (1986) measured the heat flow at 7 points on the Cape Verde Rise and estimated that the peak heat flow anomaly is 16 $\pm$ 4 mW m^{-2} higher than it should be for 125 million year old oceanic crust. Von Herzen et al. (1989) reexamined Courtney and White's heat flow data and suggested that the peak heat flow anomaly might be only 5 to 10 mW m^{-2}.

In comparing the Cape Verde Rise geoid anomaly and topographic uplift with the model results in Table 4, it is clear that viscosity models 1 and 2 can not satisfy the observations for reasonable values of Ra. Viscosity model 2 would require $Ra \approx 10^8$ and viscosity model 1 would require an even larger Ra to predict geoid and topography values comparable to those observed. On the other hand, viscosity model 3 predicts a peak geoid anomaly of 22 meters and a peak topography uplift of 2.3 to 2.7 km if Ra is in the range $5 \cdot 10^6$ to 10^7. The predicted range of uplifts overlaps the observational estimates of 1.9 to 2.4 km, but the predicted geoid is a factor of of 2 to 3 higher than observed. If the asthenosphere viscosity is reduced by a factor of about 2 from its value in viscosity model 3, then the predicted uplift would be reduced by a few hundred meters and the predicted geoid would be reduced into the observed range of 8 to 12 meters. We conclude that a viscosity structure similar to that favored by Hager and Clayton (1989) and Hager and Richards (1989) is consistent with the geoid anomalies and topographic uplifts observed on the Cape Verde Rise.

One possible difficulty with our models is in the width of the topographic swell. As noted above, the Cape Verde Rise is about 1600 km wide, and many other terrestrial hotspots have comparable dimensions. Our models, on the other hand, predict elevated regions that are about twice this size. One way to reduce the model swell width would be to assume an aspect ratio of less than 1. Temperature-dependent viscosity should also tend to make plumes narrower and may help to explain the difference between the model results and the observed swell widths. Further study will be necessary to assess this.

Table 4 shows that viscosity model 3 predicts a peak heat flow anomaly of about 9 mW m^{-2}. This is nearly two standard deviations less than Courtney and White's (1986) heat flow estimate but is within the range of values estimated by Von Herzen et al. (1989). There are several difficulties in comparing our models with observations. As noted above, our power law slope for the viscosity model 3 heat flow seems anomalously low. At $Ra = 10^5$, viscosity model 3 produces a heat flow anomaly of 7.3 mW m^{-2}. Assuming that this value is correct and that viscosity model 3 should really have the same power law slope as viscosity model 1 (b = 0.258), then this projects to a peak heat flow of 24 mW m^{-2} at $Ra = 10^7$. These two estimates (9 and 24 mWm^{-2}) probably bound the true heat flow anomaly of viscosity model 3 at $Ra = 10^7$. Although these bounds encompass Courtney and White's (1986) observations, the uncertainties in the model results are too large for the heat flow data to provide useful constraints.

Two further difficulties also exist. We have used an imposed high-viscosity lid to mimic the effects of temperature-dependent viscosity. In our models, the lid is of constant thickness, whereas in the temperature-dependent viscosity case, the high viscosity layer would be thinner near the plume axis than elsewhere. This should lead an increased heat flow anomaly near the plume axis in the temperature-dependent viscosity case. This problem might also affect the heat flow results of Courtney and White (1986) and of Robinson and Parsons (1988), who used a constant thickness conductive lid in their modeling. On the other hand, the formation of magma will tend to buffer the temperature, and hence the heat flow anomaly, in the upwelling plume. This buffering effect could be quite large, with Courtney and White (1986) estimating a decrease in

the heat flow of as much as 15 mW m^{-2}. Presumably, these two effects at least partially offset one another, but the quantitative balance between the two has not yet been assessed.

The Hawaiian Swell

The Hawaiian Swell is generally believed to be the most vigorous hotspot on Earth (Davies, 1988; Sleep, 1990). Volcanic activity in the Emperor seamounts extends back to at least 75 million years ago (Duncan and Clague, 1985). Evidence for any earlier volcanic activity that may have been produced by the Hawaiian hotspot has been subducted into the Aleutian trench.

Estimates of the geoid anomaly at Hawaii range between 8 meters (Sandwell and Poehls, 1980; McNutt and Shure, 1986) and 13 meters (Richards et al., 1988). This is similar to the range of geoid anomalies reported for the Cape Verde Rise. On the other hand, estimates of the topographic uplift of the Hawaiian Swell in regions away from shield volcanoes is slightly more than 1 km (Sandwell and Poehls, 1980; Crough, 1983), much less than that observed for Cape Verde. One possible explanation for this difference is that the asthenosphere beneath Hawaii is either thicker or less viscous than it is beneath Cape Verde. This could account for the lower topographic uplift at Hawaii, but would also have a large effect on the geoid. Alternatively, because the Pacific plate is moving over the Hawaiian hotspot at nearly 10 cm $year^{-1}$ (Davies, 1988), the lithosphere may not reach thermal equilibrium with the underlying plume. This would imply that the actual topographic uplift should be less than predicted by our steady-state models. The effect on the geoid anomaly in this case could be relatively small.

There is currently some uncertainty about the magnitude of the heat flow anomaly on the Hawaiian Swell. Von Herzen et al. (1982) obtained data for 8 sites along the strike of the swell between Hawaii and Midway. This data set shows a peak heat flow anomaly of about 8 mW m^{-2}. More recently, Von Herzen et al. (1989) measured the heat flow at 8 sites on a survey line perpendicular to the strike of the swell. The new survey results suggest that the heat flow on the swell may not be significantly higher than for points off of the swell. Von Herzen et al. (1989) suggested that the lack of a detectable heat flow

anomaly may be due to magmatic buffering of the plume's thermal structure. Given the uncertainties in both the observations and in our model heat flow results, a detailed comparison is unwarranted at the present time.

Beta Regio, Venus

Beta Regio is one of several prominent highland regions on Venus that are sometimes collectively referred to as the Equatorial Highlands. Beta reaches a peak elevation of about 4.5 km and has a quasi-circular planform, with a diameter of 2500 to 3000 km (U. S. Geological Survey, 1984). The peak geoid anomaly, based on spherical harmonic degrees 2 to 18, is 90 meters and is strongly correlated with the topography (Bills et al., 1987). Airy isostasy models of Beta's gravity anomaly require compensation depths in excess of 300 km (e.g., Esposito et al., 1982; Phillips and Malin, 1983). This is implausibly large, implying that most of the geoid and topography are related to density anomalies within the convecting mantle. Radar observations indicate the presence of shield volcanoes and rift zones (Campbell et al., 1989). All of these observations are consistent with the presence of an upwelling plume.

The results in Table 4 must be modified in two ways before applying them to Venus. Because Venus lacks an ocean, the topographic uplifts given in Table 4 must be multiplied by a factor 0.7 (Equation 11). The geoid anomalies in Table 4 must be multiplied by the factor $\frac{980}{887} = 1.10$, which is the ratio of the gravitational accelerations on the two planets. Venus and Earth are similar in size and presumably also in total heat flow. Assuming that the two planets have similar Ra, it is clear that viscosity model 3 can not account for the observed geoid and topography at Beta. On the other hand, viscosity model 1 at $Ra = 10^7$ does satisfy the observations reasonably well. This implies that Venus lacks an Earth-like low viscosity zone in its asthenosphere and upper mantle, a conclusion that is consistent with our earlier modeling of Venus's long-wavelength admittance spectrum (Kiefer et al., 1986). Our models predict swell widths that are consistent with the observed widths of Beta Regio and of other highland regions on Venus. It is not clear what causes plume swells to be nearly twice as broad on Venus as they are on Earth. A more complete

discussion of the application of our plume models to Beta Regio and other highland regions on Venus may be found in Kiefer and Hager (1990; Chapter 2).

Summary and Conclusions

Observations of geoid anomalies, topographic uplift, heat flow, distribution of volcanism, and seismic velocity anomalies suggest that at least some terrestrial hotspots, including several of the most prominent ones, are due to convective upwellings that extend from deep in the mantle to the surface and have an approximately cylindrical geometry. In this paper, we have examined the geoid anomalies, topography, and heat flow associated with mantle convection in cylindrical axisymmetric geometry. Most previous numerical models of mantle plumes have used a sheet-like, two-dimensional Cartesian upwelling. We find, however, that sheet-like and cylindrical upwellings produce significantly different geoid and topography signatures. Our models do not include the effects of spherical geometry or temperature-dependent viscosity, although both factors deserve consideration in future studies.

In dimensionalizing our results, we assume that convection extends throughout the mantle and that the temperature contrast between the upwelling plume and normal mantle is about 300 °C. This choice of δT is consistent with several geophysical and petrological constraints. For reasonable values of Ra, our models can explain the observed geoid and topography of the Hawaiian Swell and the Cape Verde Rise, provided that the asthenosphere's viscosity is at least a factor of 100 less than the lower mantle's viscosity. This viscosity profile is in good agreement with that derived from modeling of Earth's long-wavelength geoid done by Hager and Richards (1989). Our models are also broadly consistent with existing heat flow observations, but this does not provide a strong constraint because of uncertainties in the model results. One difficulty with our aspect ratio 1 models is that they predict swell widths that are about a factor of two broader than observed for terrestrial hotspots. This may be due in part to terrestrial plumes having aspect ratios of less than 1 and in part to our neglect of temperature-dependent viscosity.

We have also applied our models to observations of Beta Regio on Venus. The geoid anomaly and dynamic uplift at Beta are both significantly larger than for any terrestrial hotspot. Assuming that Venus and Earth have similar heat flows and hence similar Ra, our model results indicate that Venus must lack an Earth-like low viscosity asthenosphere, a conclusion that is consistent with our earlier modeling of Venus's long-wavelength admittance spectrum (Kiefer et al., 1986).

References

Anderson, D. L., A Seismic Equation of State: II. Shear Properties and Thermodynamics of the Lower Mantle, *Phys. Earth Planet. Int., 45,* 307-323, 1987.

Basaltic Volcanism Study Project, *Basaltic Volcanism on the Terrestrial Planets,* Pergamon Press, Elmsford, NY, 1981.

Baumgardner, J. R., Application of Supercomputers to 3-D Mantle Convection, in *The Physics of The Planets,* edited by S.K. Runcorn, pp. 199-231, John Wiley and Sons, 1988.

Bercovici, D., G. Schubert, and A. Zebib, Geoid and Topography for Infinite Prandtl Number Convection in a Spherical Shell, *J. Geophys. Res., 93,* 6430-6436, 1988.

Bercovici, D., G. Schubert, and G. A. Glatzmaier, Influence of Heating Mode on Three-Dimensional Mantle Convection, *Geophys. Res. Lett., 16,* 617-620, 1989a.

Bercovici, D., G. Schubert, and G. A. Glatzmaier, Three-Dimensional Spherical Models of Convection in the Earth's Mantle, *Science, 244,* 950-955, 1989b.

Bills, B. G., W. S. Kiefer, and R. L. Jones, Venus Gravity: A Harmonic Analysis, *J. Geophys. Res., 92,* 10,335-10,351, 1987.

Blankenbach, B., F. Busse, U. Christensen, L. Cserepes, D. Gunkel, U. Hansen, H. Harders, G. Jarvis, M. Koch, G. Marquart, D. Moore, P. Olson, H. Schmeling, and T. Schnaubelt, A Benchmark Comparison for Mantle

Convection Codes, *Geophys. J. Int., 98,* 23-38, 1989.

Bonatti, E., C. G. A. Harrison, D. E. Fisher, J. Honnorez, J.-G. Schilling, J. J. Stipp, and M. Zentilli, Easter Volcanic Chain (Southeast Pacific): A Mantle Hot Line, *J. Geophys. Res., 82,* 2457-2478, 1977.

Brooks, A. N., and T. J. R. Hughes, Streamline Upwind/Petrov-Galerkin Formulations for Convection Dominated Flows with Particular Emphasis on the Incompressible Navier-Stokes Equations, *Computer Methods in Applied Mechanics and Engineering, 32,* 199-259, 1982.

Brown, J. M., Interpretation of the D" Zone at the Base of the Mantle: Dependence on Assumed Values of Thermal Conductivity, *Geophys. Res. Lett., 13,* 1509-1512, 1986.

Campbell, D. B., J. W. Head, A. A. Hine, J. K. Harmon, D. A. Senske, and P. C. Fisher, Styles of Volcanism on Venus: New Arecibo High Resolution Radar Data, *Science, 246,* 373-377, 1989.

Ceuleneer, G., M. Rabinowicz, M. Monnereau, A. Cazenave, and C. Rosemberg, Viscosity and Thickness of the Sub-Lithospheric Low-Viscosity Zone: Constraints from Geoid and Depth over Oceanic Swells, *Earth Planet. Sci. Lett., 89,* 84-102, 1988.

Christensen, U., Instability of a Hot Boundary Layer and Initiation of Thermo-chemical Plumes, *Annales Geophysicae, 2,* 311-320, 1984.

Christensen, U. R., Time-Dependent Convection in Elongated Rayleigh-Benard Cells, *Geophys. Res. Lett., 14,* 220-223, 1987.

Christensen, U., and D. Yuen, On the Aspect Ratio of Rayleigh-Benard Convection Cells, *Geophys. Res. Lett., 15,* 597-600, 1988.

Clague, D. A., and G. B. Dalrymple, The Hawaiian-Emperor Volcanic Chain: Geologic Evolution, *U. S. Geological Survey Professional Paper 1350,* 5-54, 1987.

Courtney, R. C., and R. S. White, Anomalous Heat Flow and Geoid Across the Cape Verde Rise: Evidence for Dynamic Support from a Thermal Plume in the Mantle, *Geophys. J. R. Astr. Soc., 87,* 815-867, 1986.

Crough, S. T., Thermal Origin of Mid-Plate Hotspot Swells, *Geophys. J. R. Astr. Soc., 55,* 451-469, 1978.

Crough, S. T., Geoid Height Anomalies over the Cape Verde Rise, *Marine Geophys. Res., 5,* 263-271, 1982.

Crough, S. T., Hotspot Swells, *Ann. Rev. Earth Planet. Sci., 11,* 165-193, 1983.

Crough, S. T., and D. M. Jurdy, Subducted Lithosphere, Hotspots, and the Geoid, *Earth Planet. Sci. Lett., 48,* 15-22, 1980.

Daly, S. F., and A. Raefsky, On the Penetration of a Hot Diapir Through a Strongly Temperature-Dependent Viscosity Medium, *Geophys. J. R. Astr. Soc., 83,* 657-681, 1985.

Davies, G. F., Mantle Convection Under Simulated Plates: Effects of Heating Modes and Ridge and Trench Migration, and Implications for the Core-Mantle Boundary, Bathymetry, and the Geoid and Benioff Zones, *Geophys. J. R. Astr. Soc., 84,* 153-183, 1986.

Davies, G. F., Ocean Bathymetry and Mantle Convection: 1. Large-Scale Flow and Hotspots, *J. Geophys. Res., 93,* 10,467-10,480, 1988.

Detrick, R. S., and S. T. Crough, Island Subsidence, Hotspots, and Lithospheric Thinning, *J. Geophys. Res., 83,* 1236-1244, 1978.

Detrick, R. S., R. P. Von Herzen, B. Parsons, D. Sandwell, and M. Dougherty, Heat Flow Observations on the Bermuda Rise and Thermal Models of Midplate Swells, *J. Geophys. Res., 91,* 3701-3723, 1986.

Duncan, R. A., and D. A. Clague, Pacific Plate Motion Recorded by Linear Volcanic Chains, in *The Ocean Basins and Margins, Vol. 7A, The Pacific Ocean,* edited by A. E. M. Nairn, F. G. Stehli, and S. Uyeda, pp. 89-121, Plenum Press, 1985.

Esposito, P. B., W. L. Sjogren, N. A. Mottinger, B. G. Bills, and E. Abbott, Venus Gravity: Analysis of Beta Regio, *Icarus, 51,* 448-459, 1982.

Glatzmaier, G. A., Numerical Simulations of Mantle Convection: Time-Dependent, Three-Dimensional, Compressible, Spherical Shell, *Geophys. Astrophys. Fluid Dynamics, 43,* 223-264, 1988.

Gubbins, D., T. G. Masters, and J. A. Jacobs, Thermal Evolution of the Earth's Core, *Geophys. J. R. Astr. Soc., 59,* 57-99, 1979.

Gudmundsson, O., J. H. Davies, and R. W. Clayton, Stochastic Analysis of Global Traveltime Data: Mantle Heterogeneity and Random Errors in the ISC Data, *Geophys. J. Int., 102,* 25-43, 1990.

Hager, B. H., Dynamics and Constitution of the Earth's Interior (abstract), *EOS, 70,* 1334, 1989.

Hager, B. H. and R. W. Clayton, Constraints on the Structure of Mantle Convection using Seismic Observations, Flow Models, and the Geoid, in *Mantle Convection: Plate Tectonics and Global Dynamics,* edited by W. R. Peltier, pp. 657-763, John Wiley and Sons, 1989.

Hager, B. H., and M. A. Richards, Long-Wavelength Variations in Earth's Geoid: Physical Models and Dynamical Implications, *Phil. Trans. R. Soc. London A, 328,* 309-327, 1989.

Hansen, U., and A. Ebel, Experiments with a Numerical Model Related to Mantle Convection: Boundary Layer Behavior and Small- and Large Scale Flows, *Phys. Earth Planet. Int., 36,* 374-390, 1984.

Hansen, U., and A. Ebel, Time-Dependent Thermal Convection - A Possible Explanation for a Multi-scale Flow in the Earth's Mantle, *Geophys. J., 94,* 181-191, 1988.

Hofmann, A. W., and W. M. White, Mantle Plumes from Ancient Oceanic Crust, *Earth Planet. Sci. Lett., 57,* 421-436, 1982.

Ho-Liu, P., B. H. Hager, and A. Raefsky, An Improved Method of Nusselt Number Calculation, *Geophys. J. R. Astr. Soc., 88,* 205-215, 1987.

Houseman, G., The Dependence of Convection Planform on Mode of Heating, *Nature, 332,* 346-349, 1988.

Houseman, G. A., The Thermal Structure of Mantle Plumes: Axisymmetric or Triple-Junction?, *Geophys. J. Int., 102,* 15-24, 1990.

Hughes, T. J. R., *The Finite Element Method,* Prentice-Hall, Englewood Cliffs, NJ, 1987.

Jarvis, G. T., Time-Dependent Convection in the Earth's Mantle, *Phys. Earth Planet. Int., 36,* 305-327, 1984.

Jeanloz, R., and F. M. Richter, Convection, Composition, and the Thermal State of the Lower Mantle, *J. Geophys. Res., 84,* 5497-5504, 1979.

Jones, C. A., D. R. Moore, and N. O. Weiss, Axisymmetric Convection in a Cylinder, *J. Fluid Mech., 73,* 353-388, 1976.

Kaneoka, I., N. Takaoka, and B.G.J. Upton, Noble Gas Systematics in Basalts and and a Dunite Nodule from Reunion and Grand Comore Islands, Indian Ocean, *Chemical Geology, 59,* 35-42, 1986.

Kaula, W. M., and R. J. Phillips, Quantitative Tests for Plate Tectonics on Venus, *Geophys. Res. Lett., 8,* 1187-1190, 1981.

Kellogg, L. H., and G. J. Wasserburg, The Role of Plumes in Mantle Helium Fluxes, *Earth Planet. Sci. Lett.,* in press, 1990.

Kiefer, W. S., M. A. Richards, B. H. Hager, and B. G. Bills, A Dynamic Model of Venus's Gravity Field, *Geophys. Res. Lett., 13,* 14-17, 1986.

Kiefer, W. S., and B. H. Hager, The Role of Mantle Convection in the Origin of the Tharsis and Elysium Provinces of Mars (abstract), *MEVTV-LPI Workshop: Early Tectonic and Volcanic Evolution of Mars, LPI Technical Report 89-04,* 48-50, 1989.

Kiefer, W. S., and B. H. Hager, A Mantle Plume Model for the Equatorial Highlands of Venus, to be submitted to *J. Geophys. Res.,* 1990.

Kurz, M. D., W. J. Jenkins, J. G. Schilling, and S. R. Hart, Helium Isotopic Variations in the Mantle Beneath the Central North Atlantic Ocean, *Earth Planet. Sci. Lett., 58,* 1-14, 1982.

Kurz, M. D., W. J. Jenkins, S. R. Hart, and D. Clague, Helium Isotopic Variations in Volcanic Rocks from Loihi Seamount and the Island of Hawaii, *Earth Planet. Sci. Lett., 66,* 388-406, 1983.

Kurz, M. D., P. S. Meyer, and H. Sigurdsson, Helium Isotopic Systematics within the Neovolcanic Zones of Iceland, *Earth Planet. Sci. Lett., 74,* 291-305, 1985.

Louden, K. E., D. O. Wallace, and R. C. Courtney, Heat Flow and Depth Versus Age for the Mesozoic Northwest Atlantic Ocean: Results from the Sohm Abyssal Plain and Implications for the Bermuda Rise, *Earth Planet. Sci. Lett., 83,* 109-122, 1987.

McKenzie, D. P., J. M. Roberts, and N. O. Weiss, Convection in the Earth's Mantle: Towards a Numerical Simulation, *J. Fluid Mech., 62,* 465-538, 1974.

McKenzie, D., A. Watts, B. Parsons, and M. Roufosse, Planform of Mantle Convection beneath the Pacific Ocean, *Nature, 288,* 442-446, 1980.

McKenzie, D., and M. J. Bickle, The Volume and Composition of Melt Generated by Extension of the Lithosphere, *J. Petrology, 29,* 625-679, 1988.

McNutt, M., Thermal and Mechanical Properties of the Cape Verde Rise, *J. Geophys. Res., 93,* 2784-2794, 1988.

McNutt, M., and L. Shure, Estimating the Compensation Depth of the Hawaiian Swell with Linear Filters, *J. Geophys. Res., 91,* 13,915-13,923, 1986.

Melchior, P., *The Physics of The Earth's Core,* Pergamon Press, Elmsford, NY, 1986.

Mitrovica, J. X., and G. T. Jarvis, A Numerical Study of Thermal Convection Between Rigid Horizontal Boundaries, *Geophys. Astrophys. Fluid Dynamics, 38,* 193-224, 1987.

Morgan, W. J., Deep Mantle Convection Plumes and Plate Motions, *Am. Assoc. Petroleum Geol. Bull., 56,* 203-213, 1972a.

Morgan, W. J., Plate Motions and Deep Mantle Convection, *Geol. Soc. Am. Memoir 132,* 7-22, 1972b.

Nataf, H. C., and F. M. Richter, Convection Experiments in Fluids with Highly Temperature-Dependent Viscosity and the Thermal Evolution of the Planets, *Phys. Earth Planet. Int., 29,* 320-329, 1982.

Okal, E. A., and R. Batiza, Hotspots: The First 25 Years, in *Seamounts, Islands, and Atolls, Geophysical Monograph 43,* edited by B. H. Keating, P. Fryer, R. Batiza, and G. W. Boehlert, pp. 1-11, American Geophysical Union, Washington D. C., 1987.

Olson, P., A Comparison of Heat Transfer Laws for Mantle Convection at Very High Rayleigh Numbers, *Phys. Earth Planet. Int., 48,* 153-160, 1987.

Olson, P., G. Schubert, and C. Anderson, Plume Formation in the D" Layer and the Roughness of the Core-mantle Boundary, *Nature, 327,* 409-413, 1987.

Parmentier, E. M., D. L. Turcotte, and K. E. Torrance, Numerical Experiments on the Structure of Mantle Plumes, *J. Geophys. Res., 80,* 4417-4424, 1975.

Parsons, B., and S. Daly, The Relationship Between Surface Topography, Gravity Anomalies, and Temperature Structure of Convection, *J. Geophys. Res., 88,* 1129-1144, 1983.

Phillips, R. J., and M. C. Malin, The Interior of Venus and Tectonic Implications, in *Venus,* edited by D. M. Hunten, L. Colin, T. M. Donahue, and V. I. Moroz, pp. 159-214, Univ. of Arizona Press, Tucson, 1983.

Ricard, Y., L. Fleitout, and C. Froidevaux, Geoid Heights and Lithospheric Stresses for a Dynamic Earth, *Annales Geophysicae, 2,* 267-286, 1984.

Richards, M. A., and B. H. Hager, Geoid Anomalies in a Dynamic Earth, *J. Geophys. Res., 89,* 5987-6002, 1984.

Richards, M. A., B. H. Hager, and N. H. Sleep, Dynamically Supported Geoid Highs over Hotspots: Observations and Theory, *J. Geophys. Res., 93,* 7690-7708, 1988.

Roberts, G. O., Fast Viscous Benard Convection, *Geophys. Astrophys. Fluid Dynamics, 12,* 235-272, 1979.

Robinson, E. M., B. Parsons, and S. F. Daly, The Effect of a Shallow Low Viscosity Zone on the Apparent Compensation of Mid-Plate Swells, *Earth*

Planet. Sci. Lett., 82, 335-348, 1987.

Robinson, E. M., and B. Parsons, Effect of a Shallow Low-Viscosity Zone on the Formation of Midplate Swells, *J. Geophys. Res., 93,* 3144-3156, 1988.

Sandwell, D. T., and K. A. Poehls, A Compensation Mechanism for the Central Pacific, *J. Geophys. Res., 85,* 3751-3758, 1980.

Sleep, N. H., Tapping of Magmas from Ubiquitous Mantle Heterogeneities: An Alternative to Mantle Plumes?, *J. Geophys. Res., 89,* 10,029-10,041, 1984.

Sleep, N. H., Hotspots and Mantle Plumes: Some Phenomonology, *J. Geophys. Res., 95,* 6715-6736, 1990.

Stevenson, D. J., T. Spohn, and G. Schubert, Magnetism and Thermal Evolution of the Terrestrial Planets, *Icarus, 54,* 466-489, 1983.

Tryggvason, K., E. S. Husebye, and R. Stefansson, Seismic Image of the Hypothesized Icelandic Hotspot, *Tectonophysics, 100,* 97-118, 1983.

Turcotte, D. L., and E. R. Oxburgh, Intra-plate Volcanism, *Phil. Trans. R. Soc. London, A288,* 561-579, 1978.

U. S. Geological Survey, Topographic and Shaded Relief Maps of Venus, Miscellaneous Investigations Series Map I-1562, 1984.

Von Herzen, R. P., R. S. Detrick, S. T. Crough, D. Epp, and U. Fehn, Thermal Origin of the Hawaiian Swell: Heat Flow Evidence and Thermal Models, *J. Geophys. Res., 87,* 6711-6723, 1982.

Von Herzen, R. P., M. J. Cordery, R. S. Detrick, and C. Fang, Heat Flow and the Thermal Origin of Hot Spot Swells: The Hawaiian Swell Revisited, *J. Geophys. Res., 94,* 13,783-13,799, 1989.

Watts, A. B., D. P. McKenzie, B. E. Parsons, and M. Roufosse, The Relationship Between Gravity and Bathymetry in the Pacific Ocean, *Geophys. J. R. Astr. Soc., 83,* 263-298, 1985.

Weinstein, S. A., P. L. Olson, and D. A. Yuen, Time-Dependent Large Aspect-Ratio Thermal Convection in the Earth's Mantle, *Geophys. Astrophys. Fluid Dynamics, 47,* 157-197, 1989.

Wilson, J. T., A Possible Origin of the Hawaiian Islands, *Canadian J. of Physics, 41,* 863-870, 1963.

Wyllie, P. J., Solidus Curves, Mantle Plumes, and Magma Generation Beneath Hawaii, *J. Geophys. Res., 93,* 4171-4181, 1988.

Young, C. J., and T. Lay, The Core-Mantle Boundary, *Ann. Rev. Earth Planet. Sci., 15,* 25-46, 1987.

Yuen, D. A., and W. R. Peltier, Mantle Plumes and the Thermal Stability of the D" Layer, *Geophys. Res. Lett., 7,* 625-628, 1980.

Zhang, Y. S., and T. Tanimoto, Three-Dimensional Modelling of Upper Mantle Structure Under the Pacific Ocean and Surrounding Area, *Geophys. J. Int., 98,* 255-269, 1989.

Table 1. Scaling Parameters

ρ_m	Mantle Density	3.3 gm cm^{-3}
g	Gravitational Acceleration	980 cm s^{-2} (Earth)
		887 cm s^{-2} (Venus)
α	Thermal Expansion Coefficient	$3 \cdot 10^{-5}$ $°C^{-1}$
ΔT	Vertical Temperature Contrast	1000 °C
d	Depth of Convecting Layer	2800 km
κ	Thermal Diffusivity	10^{-2} cm^2 sec^{-1}
k	Thermal Conductivity	3 W m^{-1} K^{-1}

Table 2. Model Parameters and Results

Model #	Ra	S	γ	η_a	η_{um}	AR	Grid	G	T	Nu
1	10^5	0	0.0000	1	1	1	17	0.0708	0.1289	11.24
2	10^5	0	0.0000	1	1	1	33	0.0722	0.1374	10.62
3	10^5	0	0.0000	1	1	1	65	0.0733	0.1365	10.42
4	10^5	0	0.0000	1	1	1	17	0.0795	0.1449	11.24
5	10^5	0	0.0000	1	1	1	33	0.0757	0.1414	10.62
6	10^5	0	0.0000	1	1	1	65	0.0742	0.1373	10.42
7	$3*10^4$	0	0.0000	1	1	1	33	0.1000	0.1570	7.03
8	$6*10^4$	0	0.0000	1	1	1	33	0.0855	0.1485	8.94
9	$3*10^5$	0	0.0000	1	1	1	65	0.0557	0.1214	14.85
10	10^6	0	0.0000	1	1	1	65	0.0399	0.1038	21.73
11	10^5	1	0.0469	1	1	1	33	0.0762	0.1317	8.86
12	10^5	2	0.0469	1	1	1	33	0.0667	0.1046	6.28
13	10^5	3	0.0469	1	1	1	33	0.0608	0.0911	5.40
14	10^5	4	0.0469	1	1	1	33	0.0588	0.0873	5.24
15	10^5	5	0.0469	1	1	1	33	0.0578	0.0856	5.20
16	10^5	3	0.0234	1	1	1	33	0.0633	0.0991	6.09
17	10^5	3	0.0313	1	1	1	33	0.0624	0.0962	5.84
18	10^5	3	0.0391	1	1	1	33	0.0616	0.0935	5.61
19	10^5	3	0.0547	1	1	1	33	0.0600	0.0889	5.21
20	10^4	3	0.0469	1	1	1	33	0.1019	0.1185	2.99
21	10^5	3	0.0469	1	1	1	65	0.0609	0.0895	5.29
22	$3*10^5$	3	0.0469	1	1	1	65	0.0447	0.0754	6.66
23	10^6	3	0.0469	1	1	1	65	0.0312	0.0615	8.45
24	10^5	3	0.0469	0.1	0.1	1	65	0.0259	0.0627	6.49
25	$3*10^5$	3	0.0469	0.1	0.1	1	65	0.0192	0.0519	7.95
26	10^6	3	0.0469	0.1	0.1	1	65	0.0138	0.0417	9.73
27	10^5	3	0.0469	0.01	0.1	1	65	0.0057	0.0464	7.51
28	$3*10^5$	3	0.0469	0.01	0.1	1	65	0.0054	0.0377	9.08
29	10^6	3	0.0469	0.01	0.1	1	65	0.0047	0.0299	11.22
30	10^5	3	0.0469	1	1	0.5	33	0.0194	0.0430	5.06
31	10^5	3	0.0469	1	1	0.65	33	0.0315	0.0598	5.30
32	10^5	3	0.0469	1	1	0.8	33	0.0442	0.0747	5.41
33	10^5	3	0.0469	1	1	1.2	33	0.0765	0.1048	5.30
34	10^5	3	0.0469	1	1	1.4	33	0.0916	0.1166	5.17

Notes on Table 2

(1) S and γ are parameters which define the variation of viscosity with depth in the upper boundary layer. See Equation 16. Note that where S=γ=0 in Table 2, the boundary layer viscosity is independent of depth.

(2) η_a and η_{um} are the viscosities of the asthenosphere and upper mantle layers, normalized relative to a lower mantle viscosity of 1.0. The asthenosphere is defined to be the region between non-dimensional depths z=0.0469 and z=0.1406. The upper mantle is defined as the region between z=0.1406 and z=0.2578. See Figure 9.

(3) AR is the aspect ratio of the convection cell, defined as the distance from upwelling to downwelling divided by the cell depth.

(4) Grid indicates the number of nodes used in each direction. Models 1-3 used a grid that is uniformly space in both dimensions. The remaining models used a grid with uniform radial spacing and non-uniform vertical spacing, with high vertical resolution in the upper boundary layer and lower vertical resolution elsewhere. See Figure 1.

(5) G and T are the non-dimensional geoid anomaly and topographic uplift along the axis of the plume, defined by Equations 13a and 13b.

Table 3. Power Law Parameters

	Geoid		Topography	
	a	b	a	b
Constant Viscosity	$8.7 \cdot 10^3$	-0.269	66	-0.121
Viscosity Model 1	$9.1 \cdot 10^3$	-0.290	72	-0.164
Viscosity Model 2	$3.2 \cdot 10^3$	-0.273	62	-0.182
Viscosity Model 3	$8.1 \cdot 10^1$	-0.084	51	-0.192

	Nusselt Number		Heat Flow	
	a	b	a	b
Constant Viscosity	0.27	0.319	---	---
Viscosity Model 1	0.51	0.203	0.22	0.258
Viscosity Model 2	0.86	0.176	1.06	0.147
Viscosity Model 3	1.01	0.174	4.13	0.050

Table 4. Projection of Results to Higher Ra

	$Ra=10^6$	$5 \cdot 10^6$	10^7
Viscosity Model 1			
Geoid	165	104	85
Topography	7.4	5.8	5.1
Nusselt Number	8.5	11.7	13.5
Heatflow Anomaly	7.8	11.8	14.1
Viscosity Model 2			
Geoid	73	47	39
Topography	5.0	3.7	3.3
Nusselt Number	9.7	13.0	14.7
Heatflow Anomaly	8.0	10.2	11.3
Viscosity Model 3			
Geoid	25	22	21
Topography	3.6	2.7	2.3
Nusselt Number	11.2	14.8	16.7
Heatflow Anomaly	8.2	8.9	9.2

Results are scaled using quantities in Table 1. Geoid results are in meters, topographic uplift in kilometers, and heatflow anomaly in milliwatts per square meter. All three quantities are values at the surface along the axis of the upwelling plume. Nusselt numbers are nondimensional and are averaged over the entire convection cell.

Figure 1. Element distribution in the 33 x 33 node non-uniform grid. Vertical grid resolution is high in the top boundary layer (between non-dimensional heights 0.9375 and 1.0) and lower elsewhere. Radial resolution is uniform.

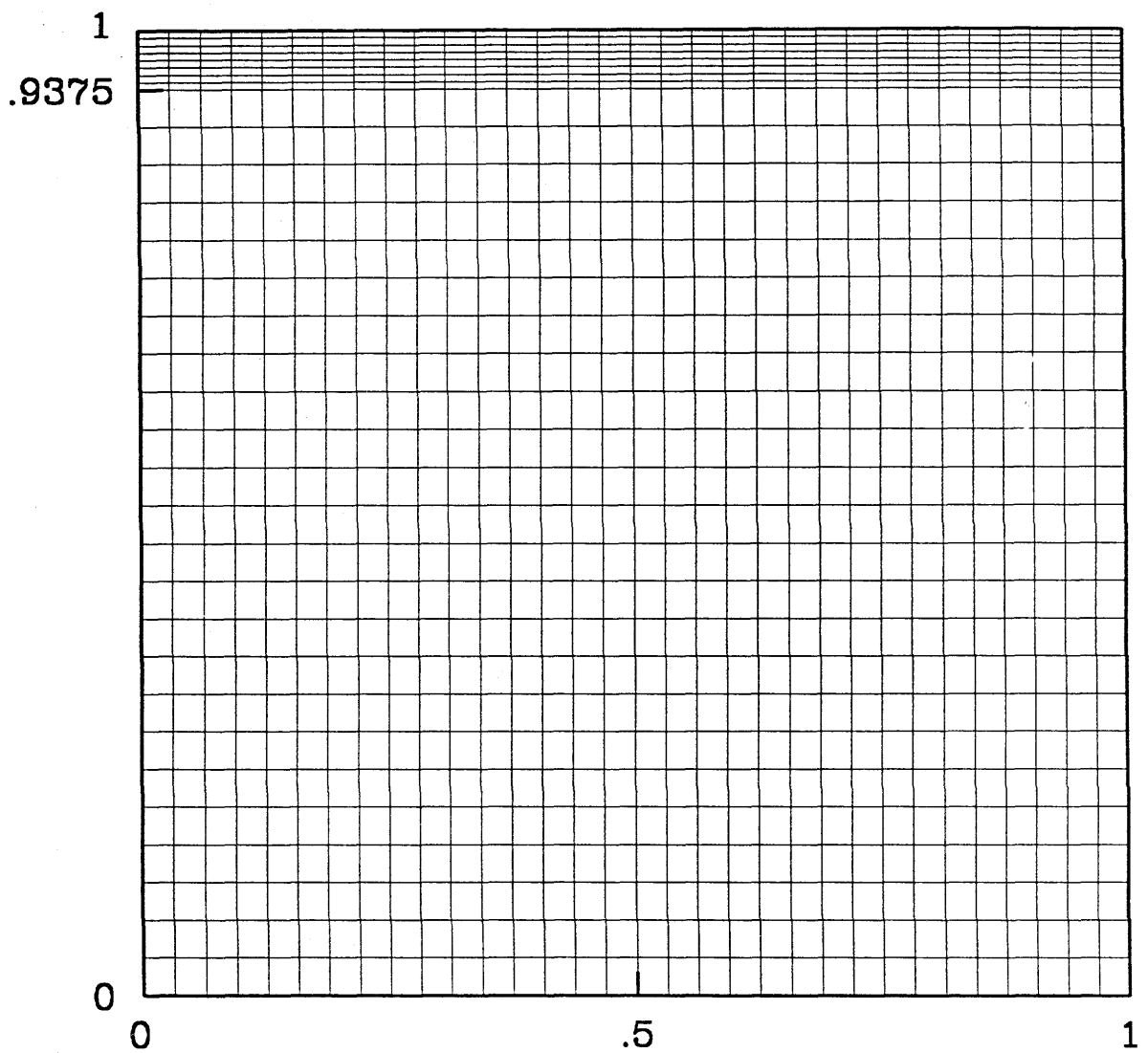
1
.9375
0
0
.5
1

Figure 2. Convergence behavior versus grid size for models 1-6. Triangles are calculated results for uniform grid, squares are calculated results for non-uniform grid. Results are all expressed as percent differences relative to highest resolution uniform grid case. a) Peak Geoid Anomaly, b) Peak Topographic Uplift, and c) Nusselt Number.

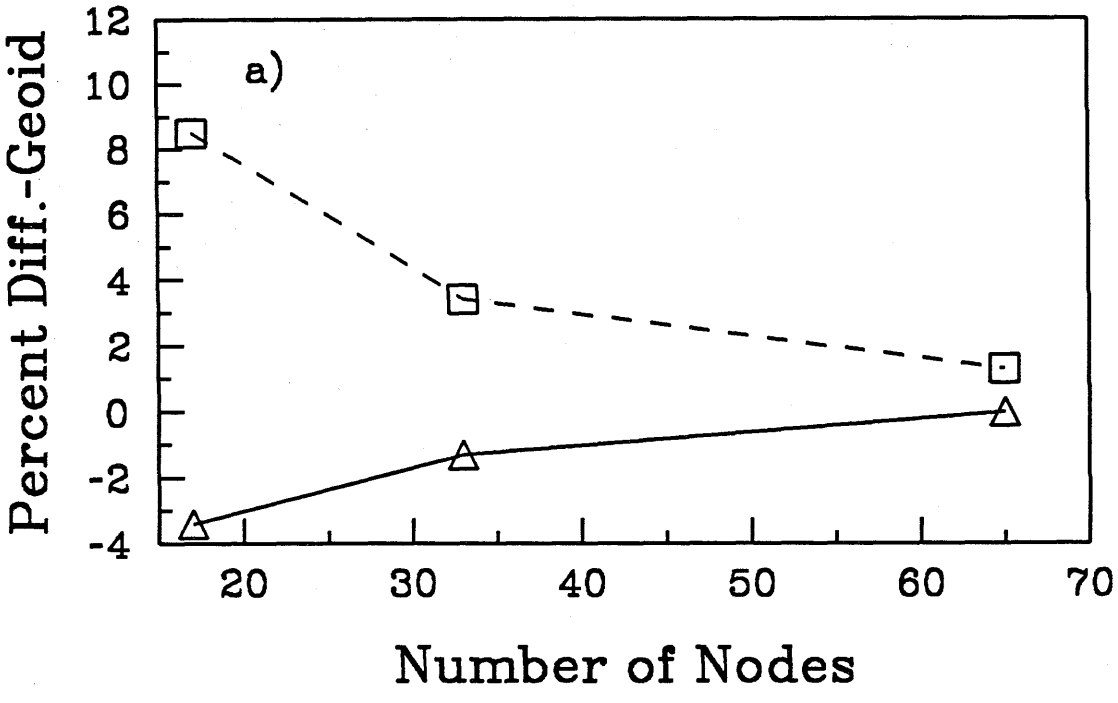
a)
Percent Diff.-Geoid
12
10
8
6
4
2
0
-2
-4
20
30
40
50
60
70
Number of Nodes

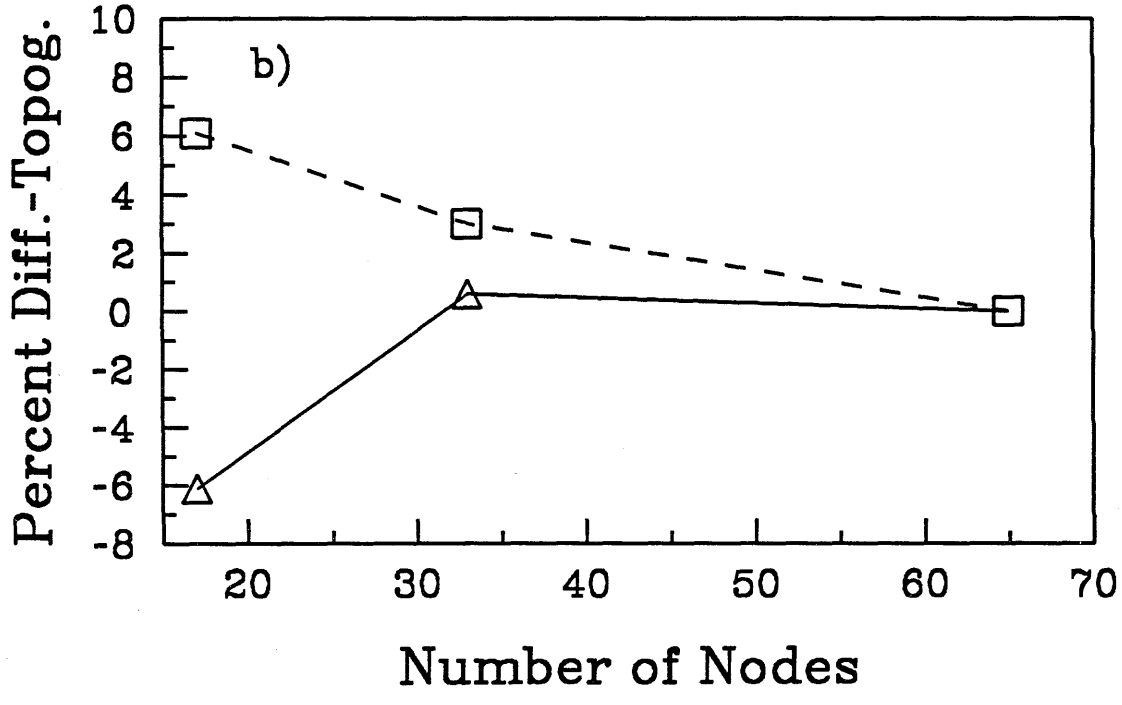
b)
Percent Diff.-Topog.
10
8
6
4
2
0
-2
-4
-6
-8
20
30
40
50
60
70
Number of Nodes

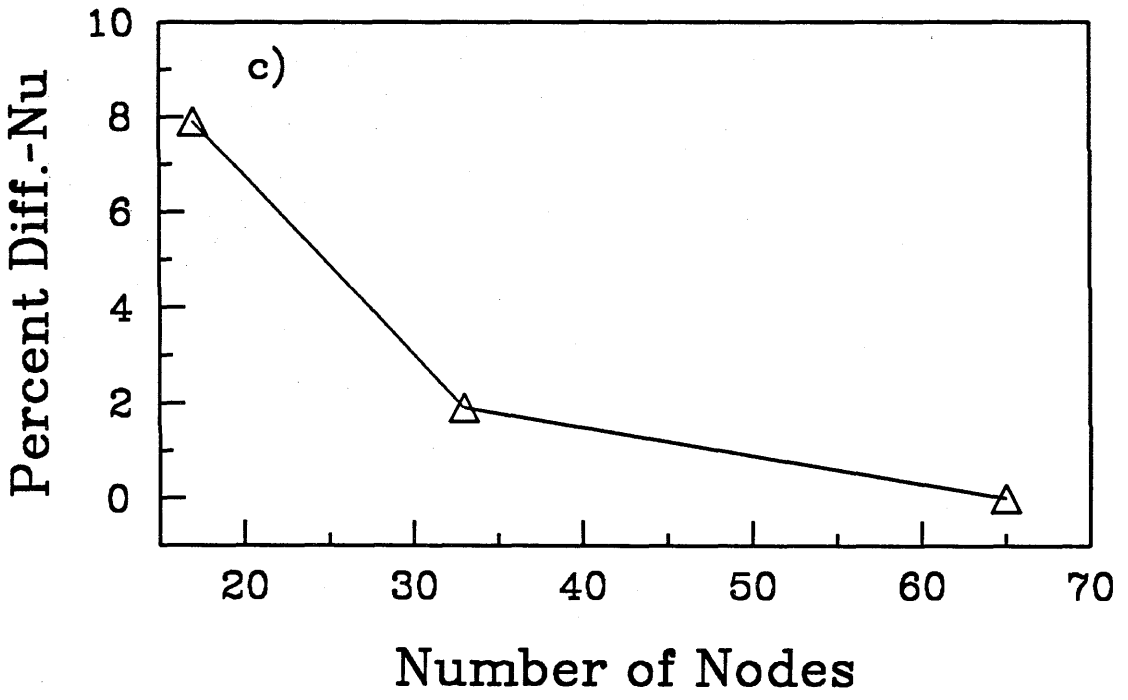
c)
Percent Diff.-Nu
10
8
6
4
2
0
20
30
40
50
60
70
Number of Nodes

Figure 3. Temperature contours for internally heated models at $Ra_F = 1 \cdot 10^6$. a) μ=1.0 and b) μ=0.8 . In both cases, the central axis of the cylinder is at the left. The contour interval is 0.1 of the temperature variation in the cylinder.

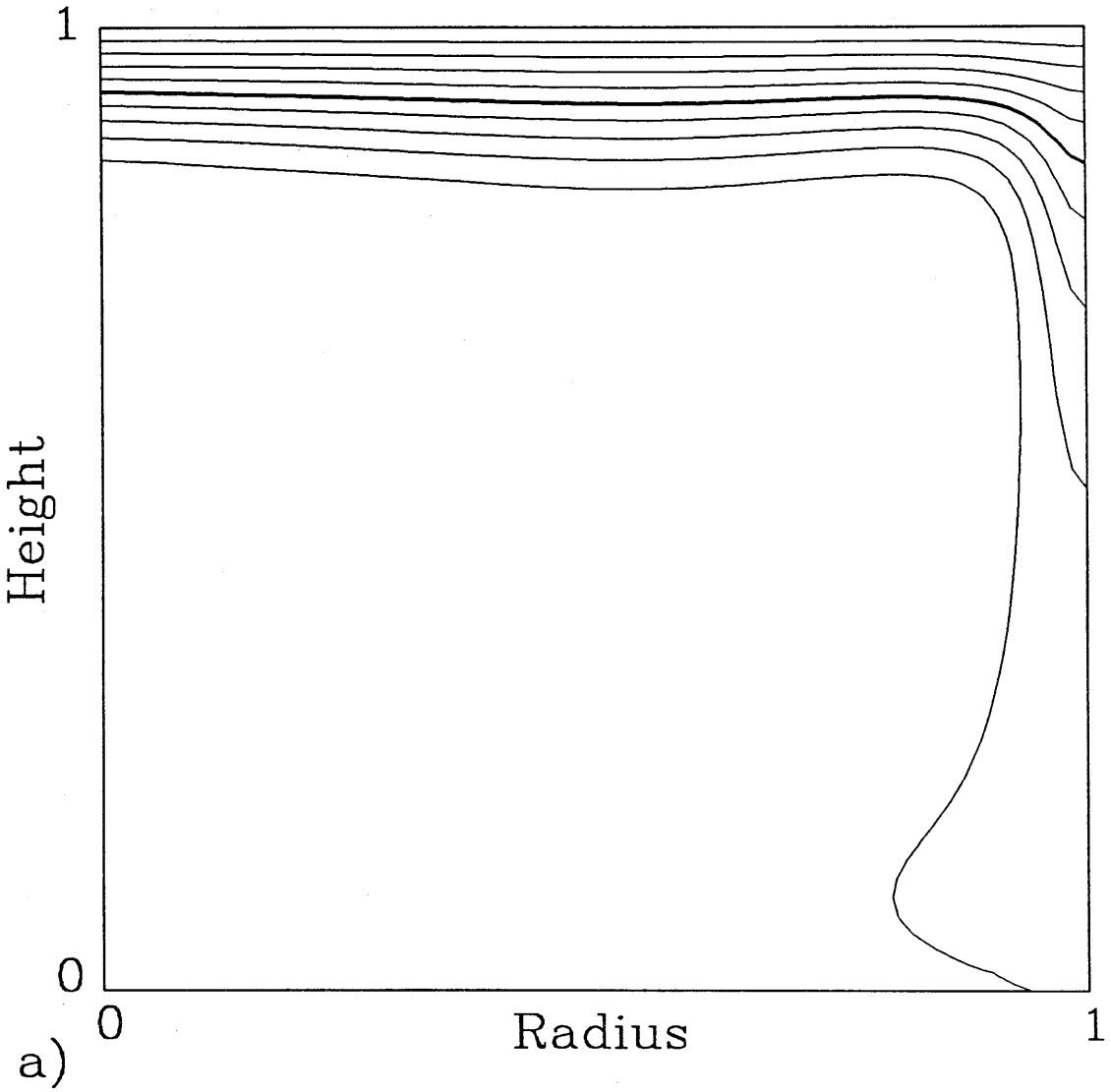
1
Height
0
0
Radius
1
a)

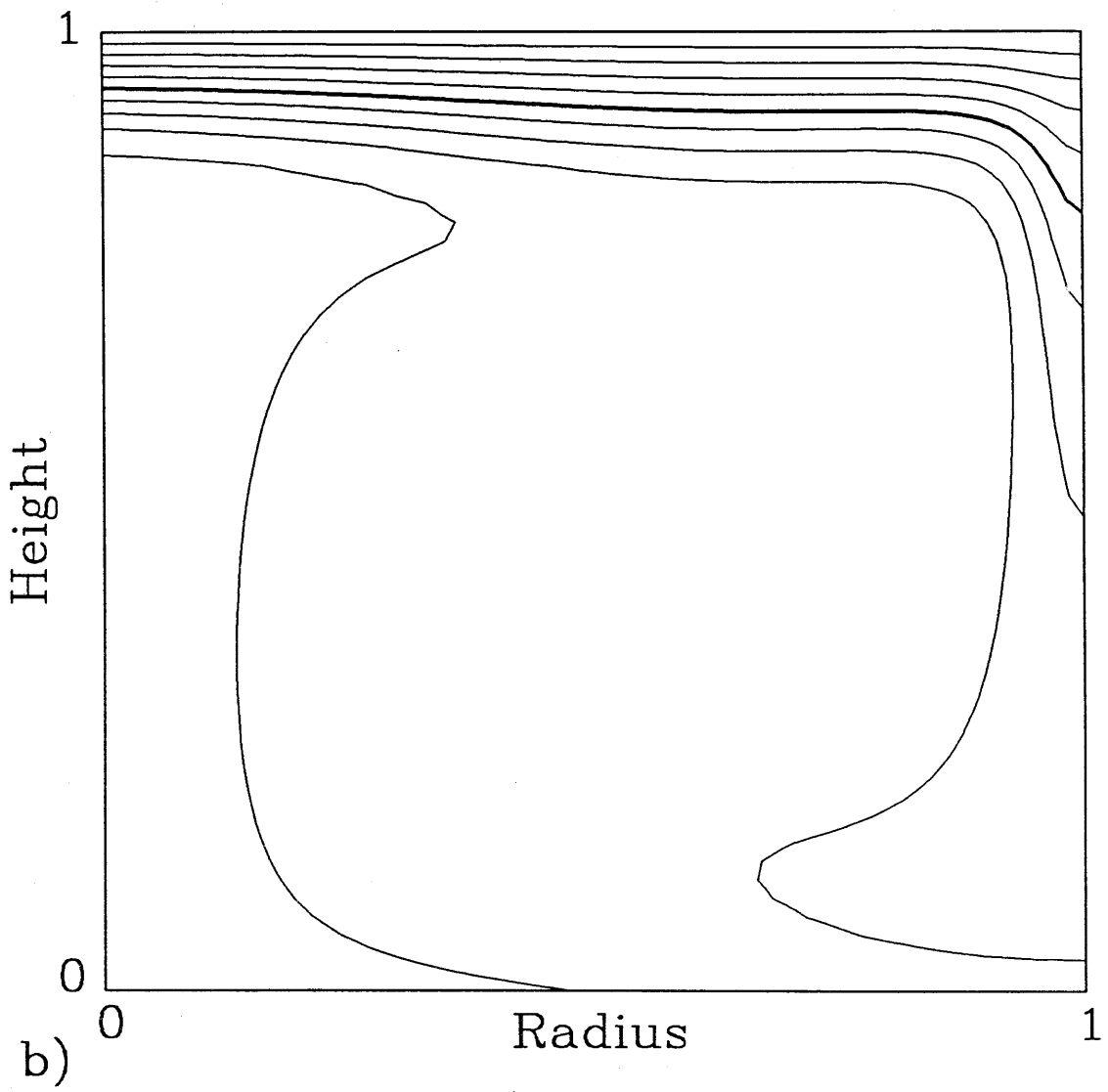
1
Height
0
0
Radius
1
b)

Figure 4. Isotherms for bottom-heated convection at $Ra=10^5$ (Model number 21). ΔT is the temperature contrast across the depth of the cylinder. δT is the temperature contrast across the lower thermal boundary layer and the rising plume. δz is the thickness of the lower thermal boundary layer. Contour interval is 0.10 .

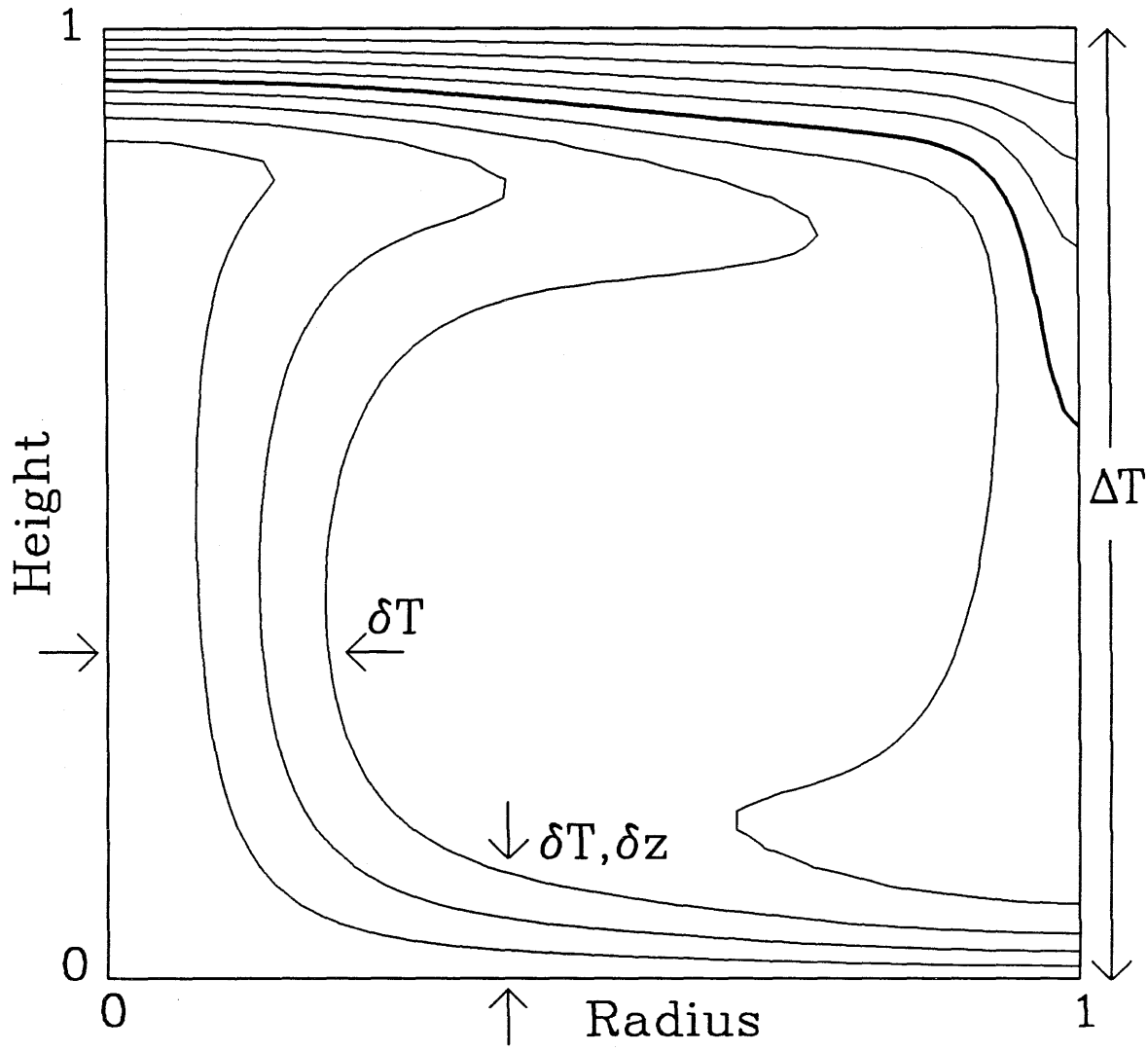
1
Height
0
0
Radius
1
ΔT
δT
δT,δz

Figure 5. Isotherms for isoviscous, bottom-heated convection at $Ra=10^5$ for (a) Cartesian geometry and (b) cylindrical axisymmetric geometry (Model 3). Contour interval is 0.10.

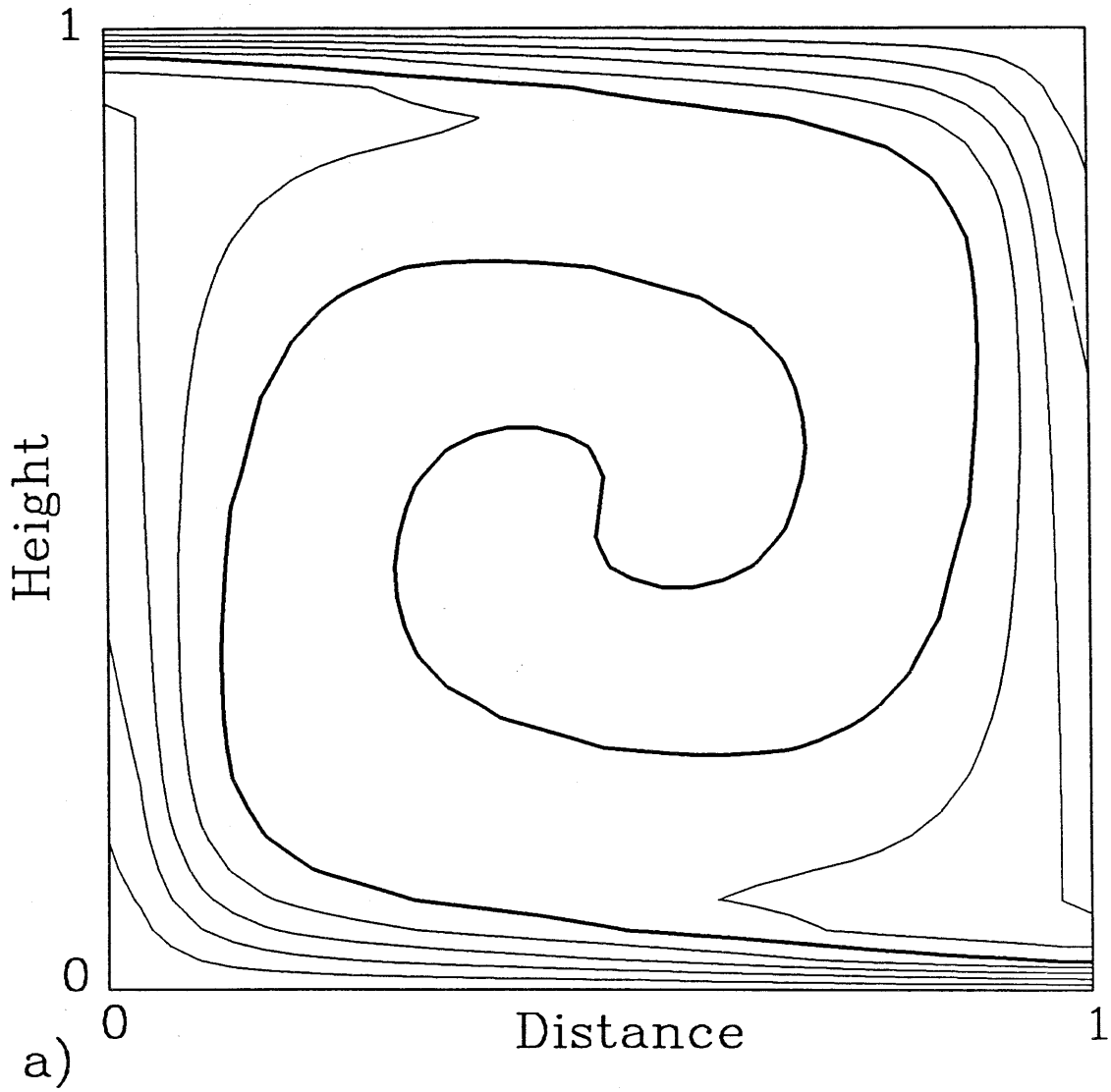

a)

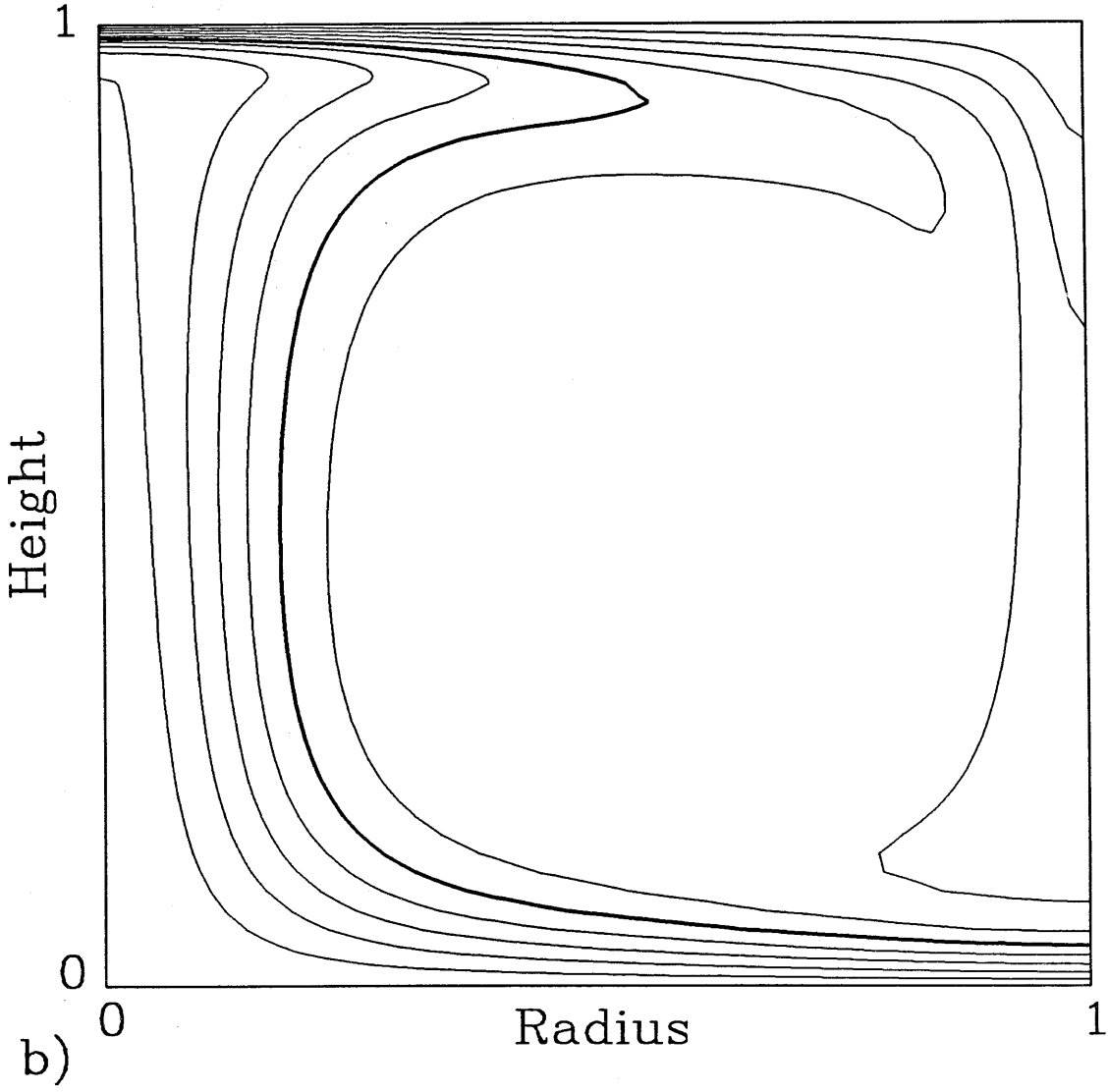
1
Height
0
0
Radius
1
b)

Figure 6. Profiles of geophysical observables versus distance from plume center for cylindrical geometry (solid lines, Model 3) and Cartesian geometry (dashed lines). a) Geoid anomaly and b) Topographic uplift.

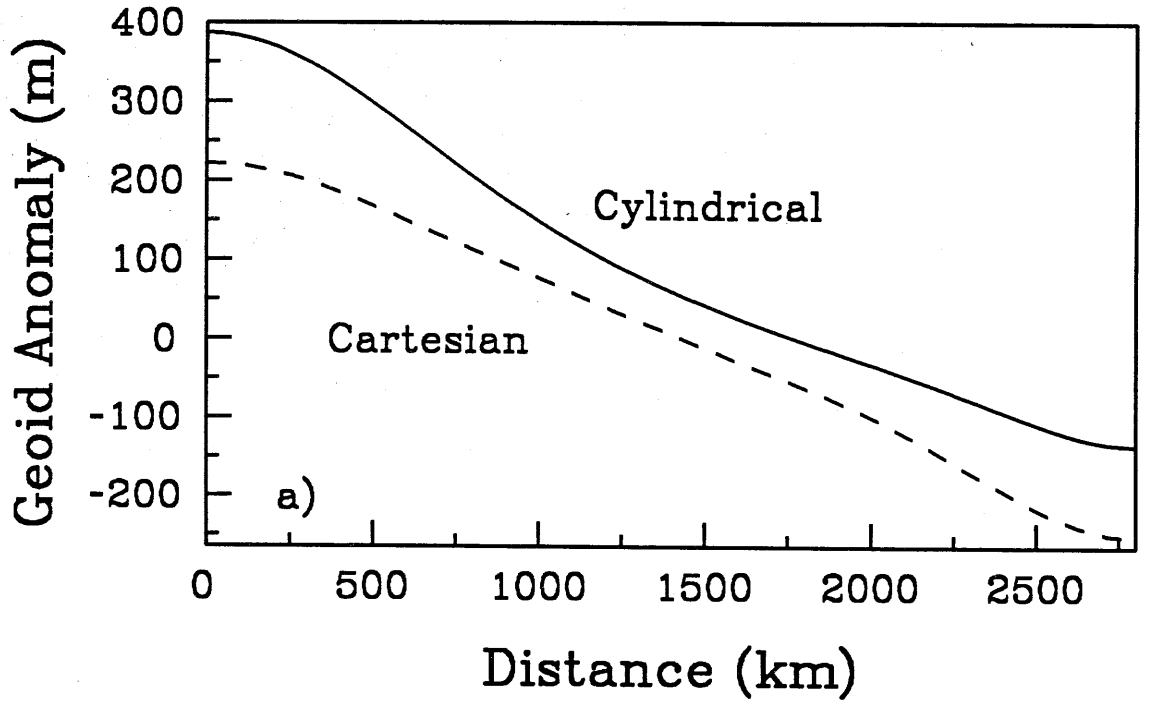
Geoid Anomaly (m)
400
300
200
100
0
-100
-200
Cylindrical
Cartesian
a)
0
500
1000
1500
2000
2500
Distance (km)

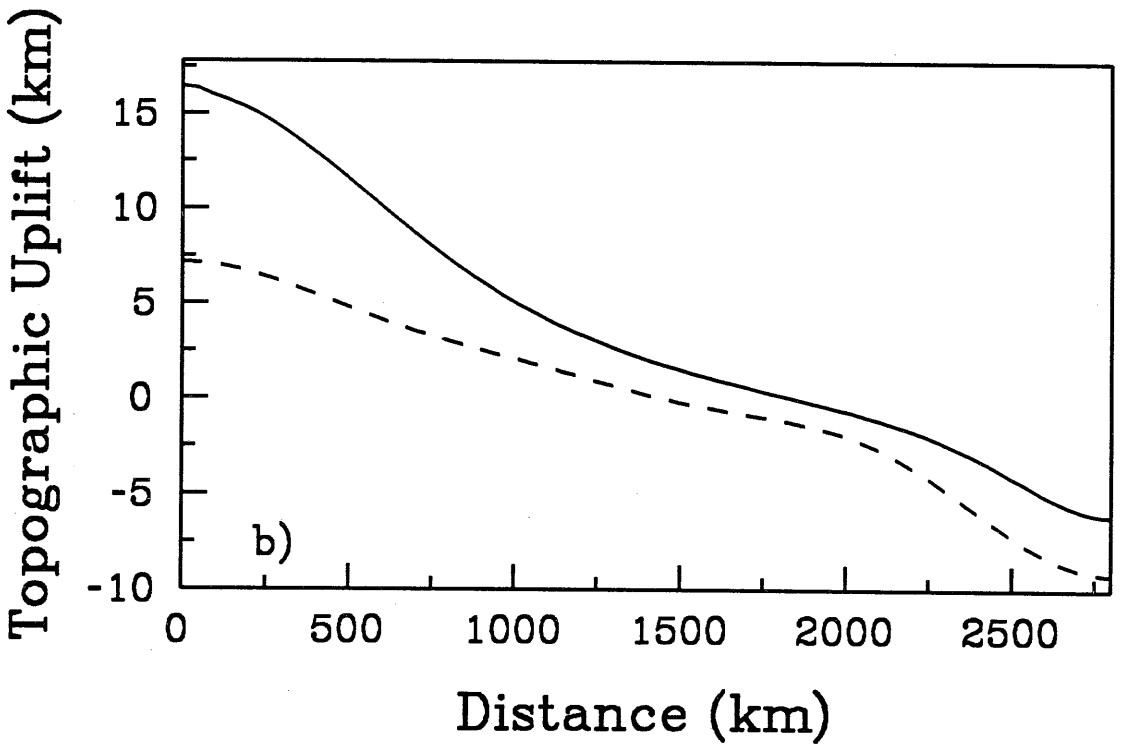
Topographic Uplift (km)
15
10
5
0
-5
-10
b)
0
500
1000
1500
2000
2500
Distance (km)

Figure 7. Effects of varying surface viscosity on a) Peak Geoid Anomaly, b) Peak Topographic Uplift, c) Nusselt Number, and d) Peak Heatflow anomaly. Surface viscosity is shown normalized relative to a mantle viscosity of 1.0 . Lid thickness is 130 km ($\gamma = 0.0469$). Models 5 and 11-15.

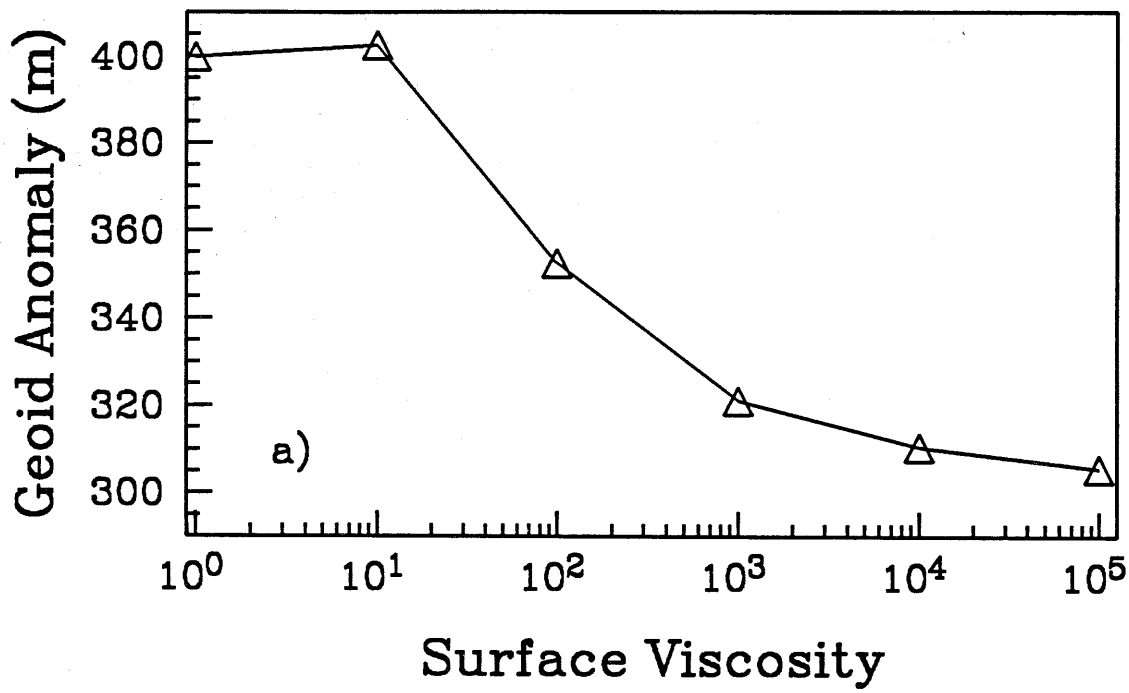
Geoid Anomaly (m)
400
380
360
340
320
300
a)
10^0
10^1
10^2
10^3
10^4
10^5
Surface Viscosity

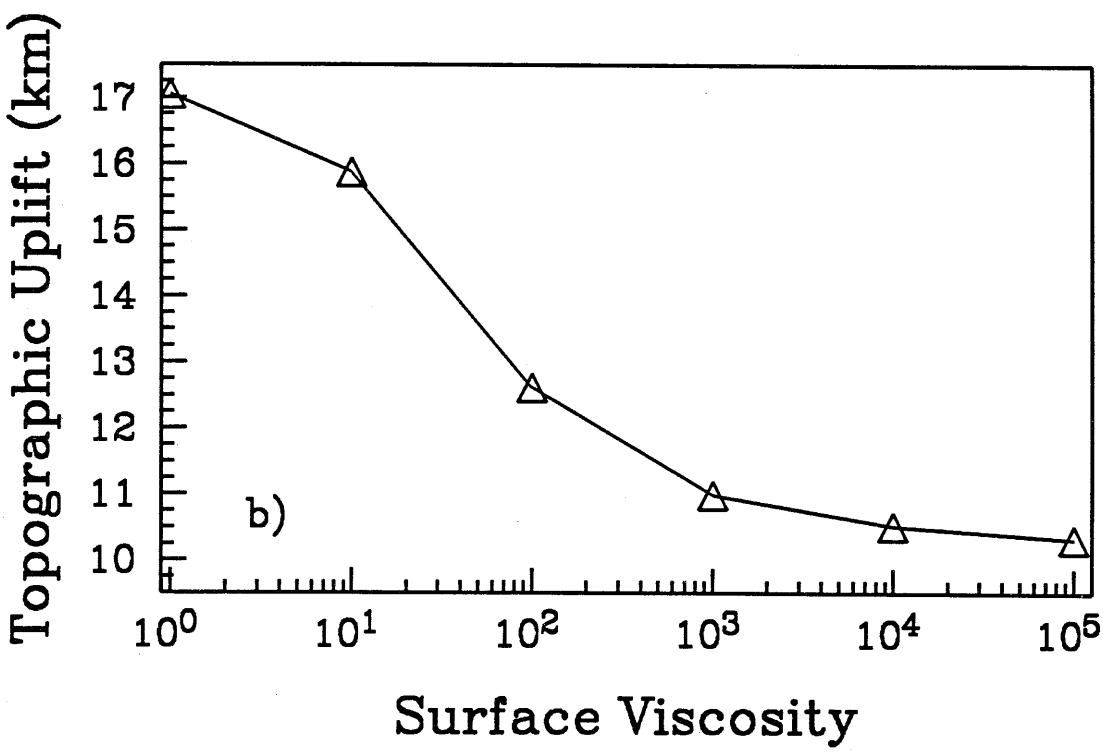
Topographic Uplift (km)
17
16
15
14
13
12
11
10
b)
10^0
10^1
10^2
10^3
10^4
10^5
Surface Viscosity

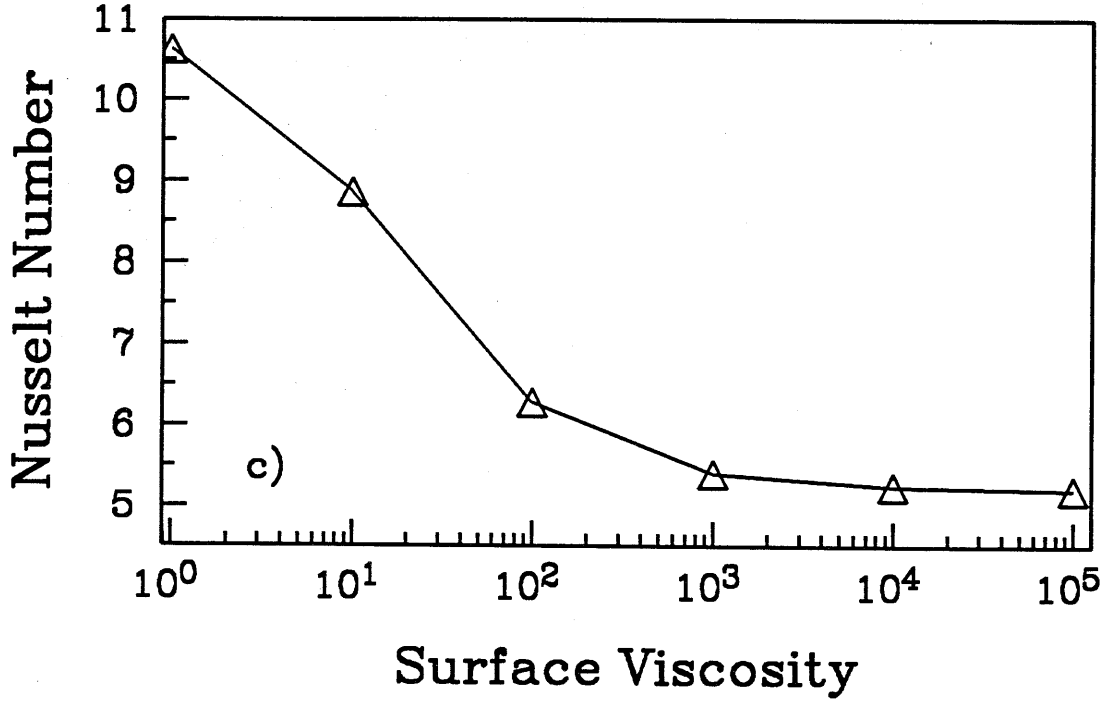
Nusselt Number
11
10
9
8
7
6
5
c)
10^0
10^1
10^2
10^3
10^4
10^5
Surface Viscosity

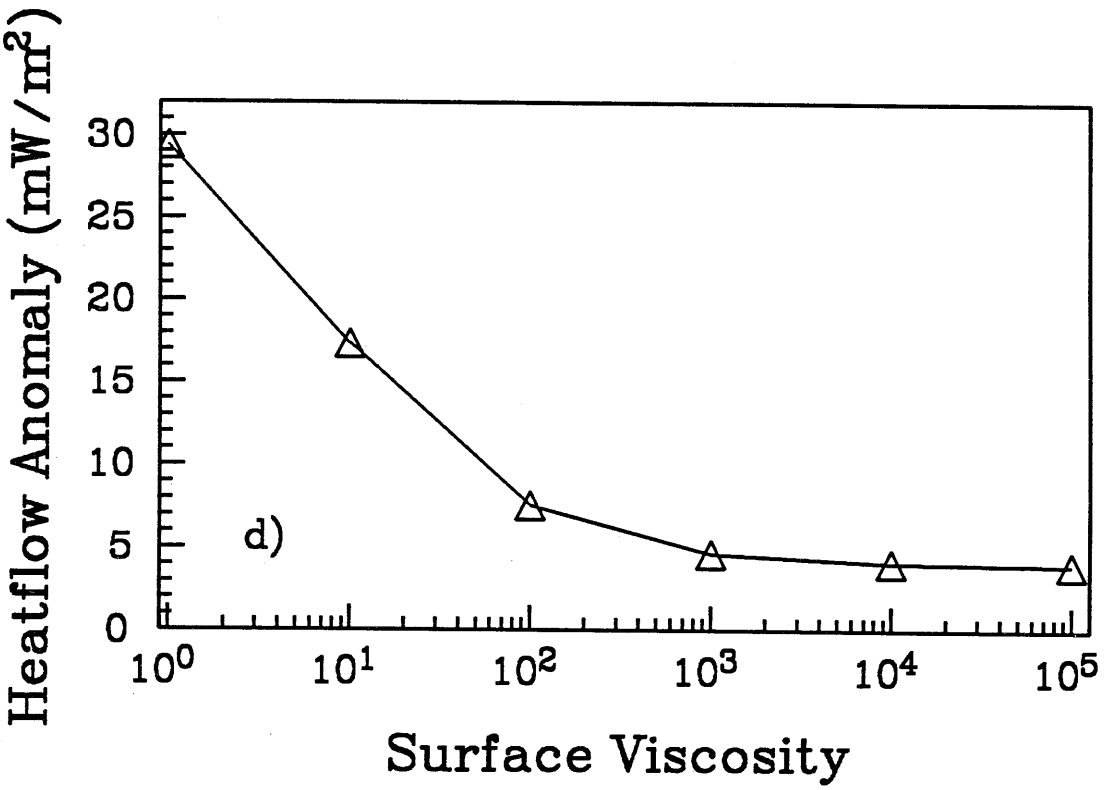
Heatflow Anomaly (mW/m^2)
30
25
20
15
10
5
0
d)
10^0
10^1
10^2
10^3
10^4
10^5
Surface Viscosity

Figure 8. Effects of varying high-viscosity lid thickness on a) Peak Geoid Anomaly, b) Peak Topographic Uplift, c) Nusselt Number and d) Peak Heatflow Anomaly. Surface viscosity=10^3 (S=3). Models 13 and 16-19. Triangles are model results, solid lines are best fit least-squares lines.

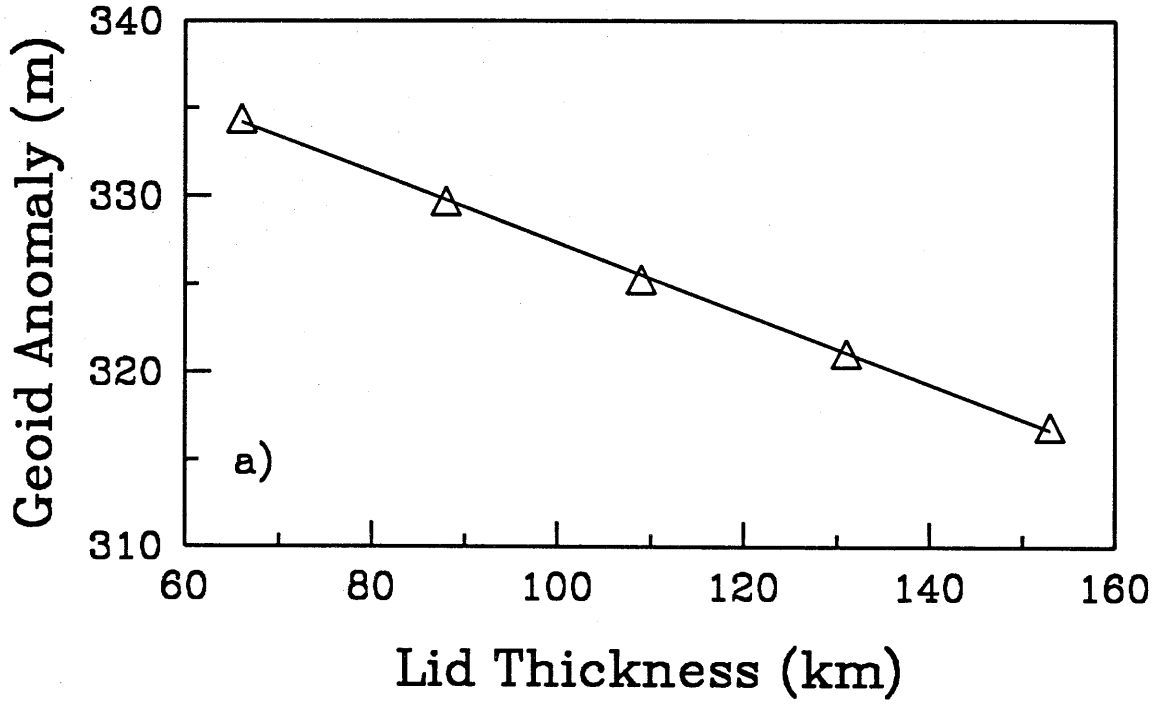
Geoid Anomaly (m)
340
330
320
310
a)
60
80
100
120
140
160
Lid Thickness (km)

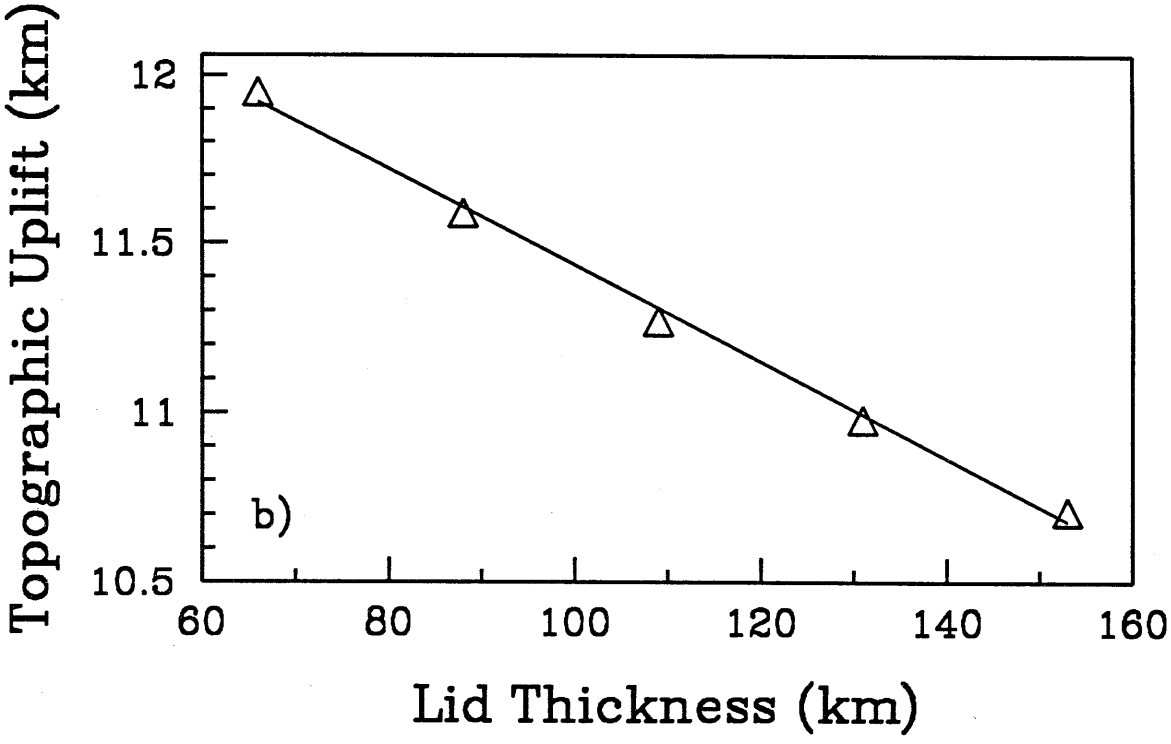
Topographic Uplift (km)
12
11.5
11
10.5
b)
60
80
100
120
140
160
Lid Thickness (km)

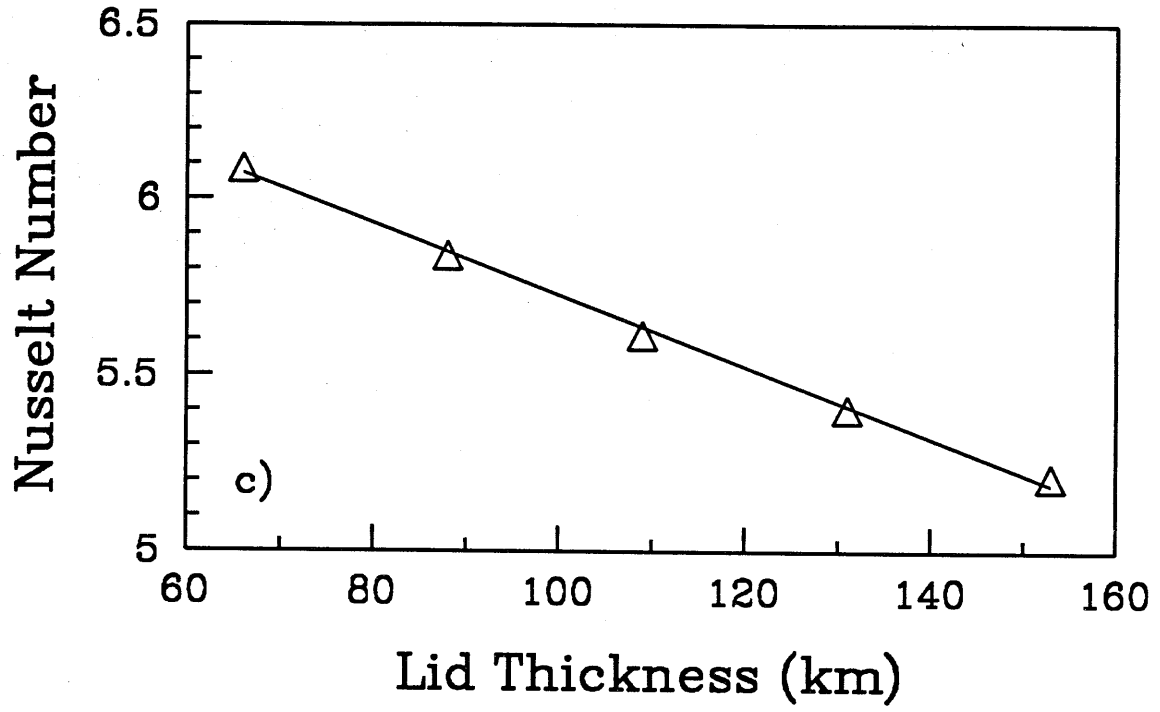
Nusselt Number
6.5
6
5.5
5
c)
60
80
100
120
140
160
Lid Thickness (km)

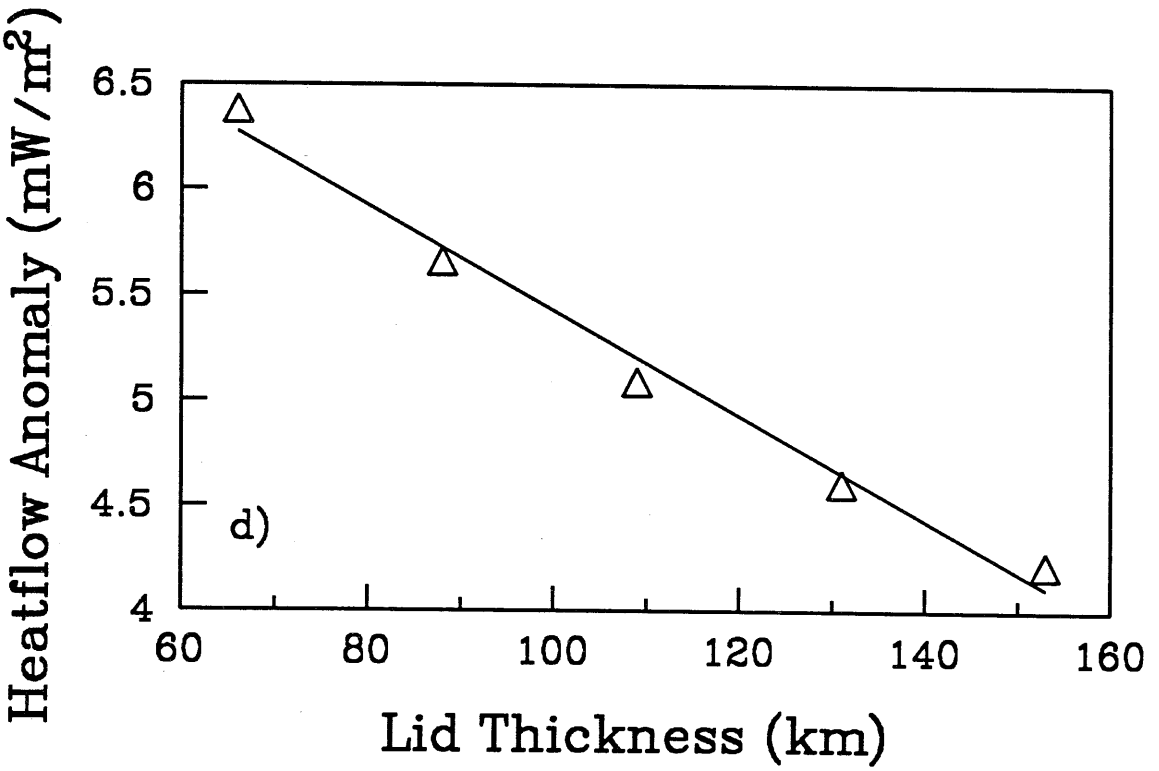
Heatflow Anomaly (mW/m²)
6.5
6
5.5
5
4.5
4
d)
60
80
100
120
140
160
Lid Thickness (km)

Figure 9. Viscosity versus depth profiles for three standard viscosity models used in this study. Viscosity profiles are normalized relative to a lower mantle viscosity of 1.0. All three models have high viscosity lids defined by S=3 and γ=0.0469. a) Viscosity model 1 has an isoviscous mantle. b) Viscosity model 2 has an upper mantle viscosity 0.1 times the lower mantle viscosity. c) Viscosity model 3 includes an asthenosphere with viscosity 0.01 times the lower mantle viscosity.

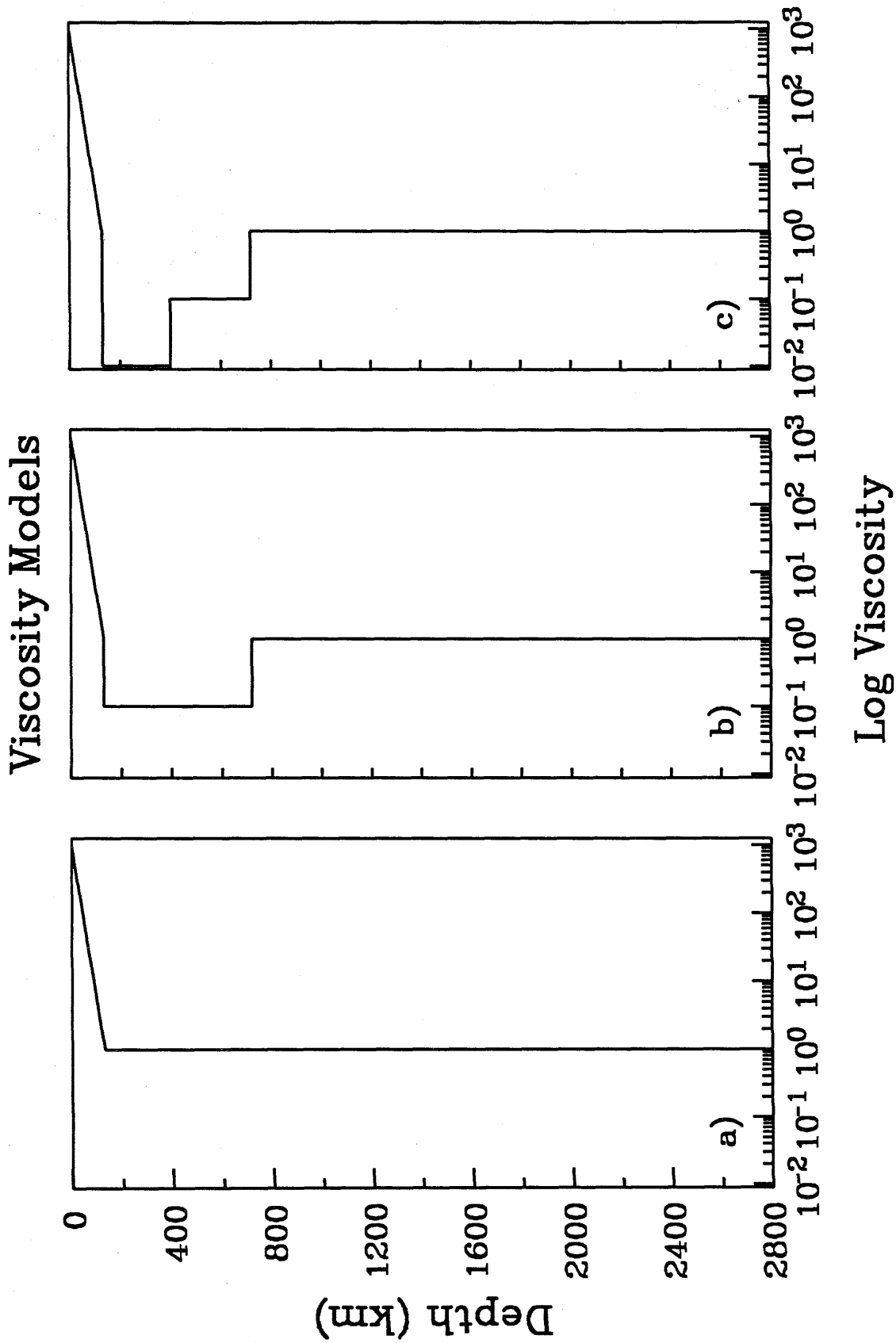
Viscosity Models
Depth (km)
0
400
800
1200
1600
2000
2400
2800
a)
b)
c)
10^{-2} 10^{-1} 10^{0} 10^{1} 10^{2} 10^{3}
Log Viscosity

Figure 10. Profiles versus distance from plume center of (a) Geoid anomaly, (b) Topographic uplift, and (c) Heatflow anomaly for viscosity models 1 (solid line), 2 (dashed line) and 3 (dot-dash line). Ra=10^6. (Models 23, 26, and 29).

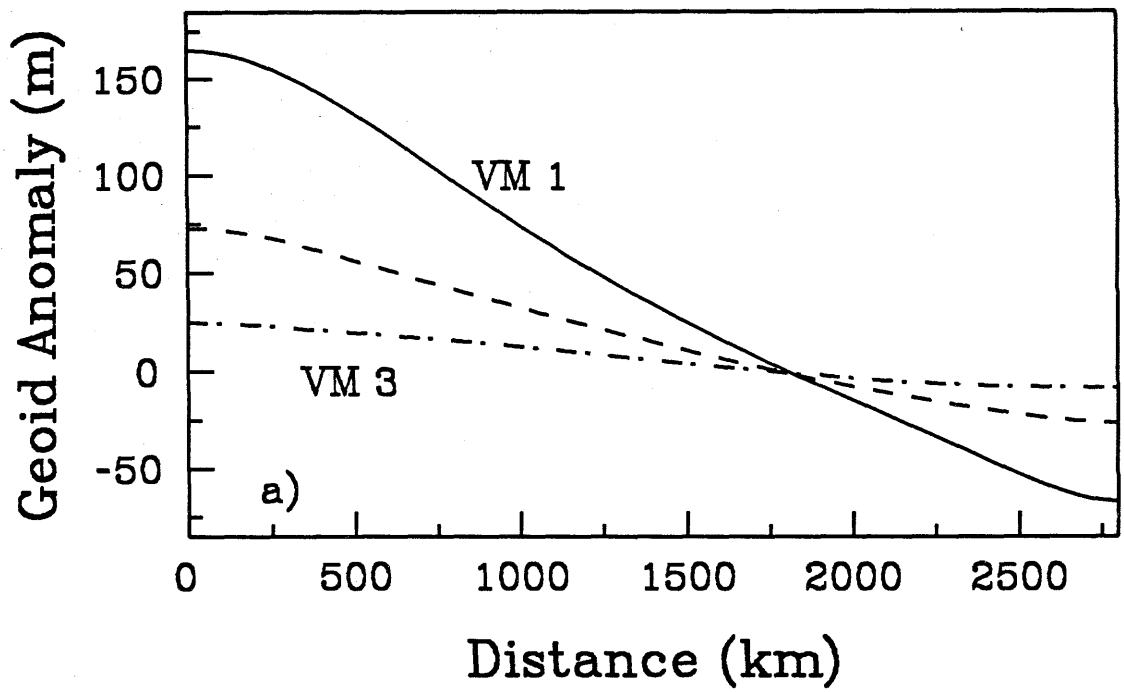
Geoid Anomaly (m)
150
100
50
0
-50
VM 1
VM 3
a)
0
500
1000
1500
2000
2500
Distance (km)

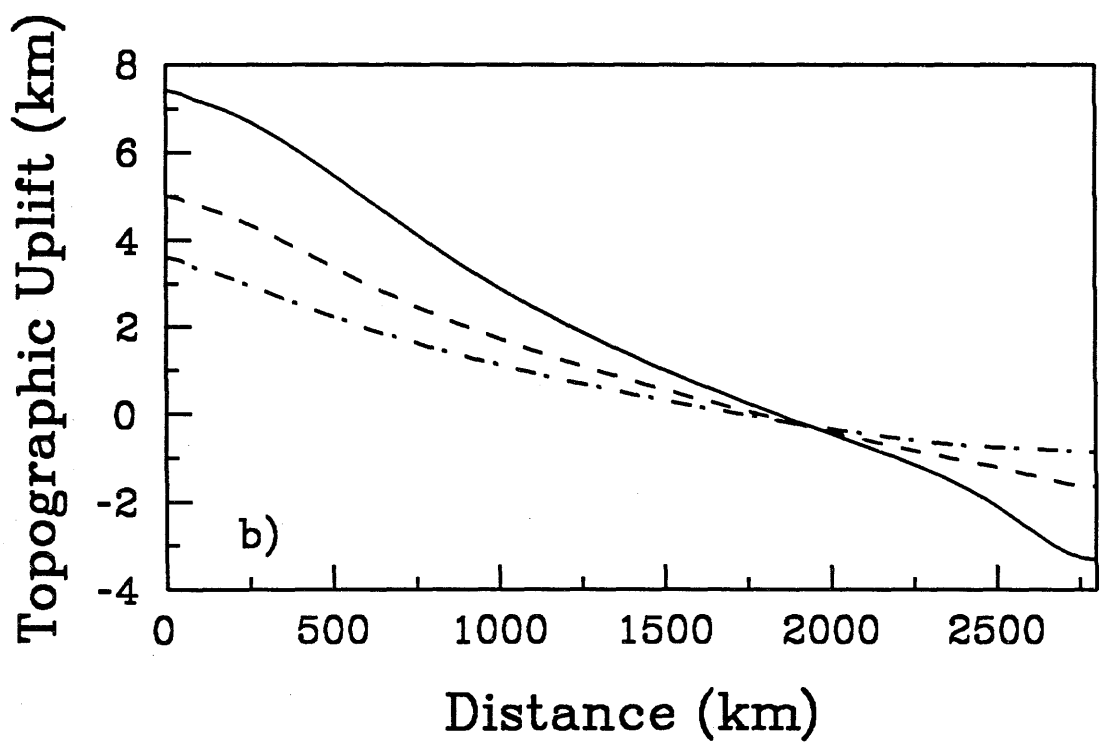
Topographic Uplift (km)
8
6
4
2
0
-2
-4
b)
0
500
1000
1500
2000
2500
Distance (km)

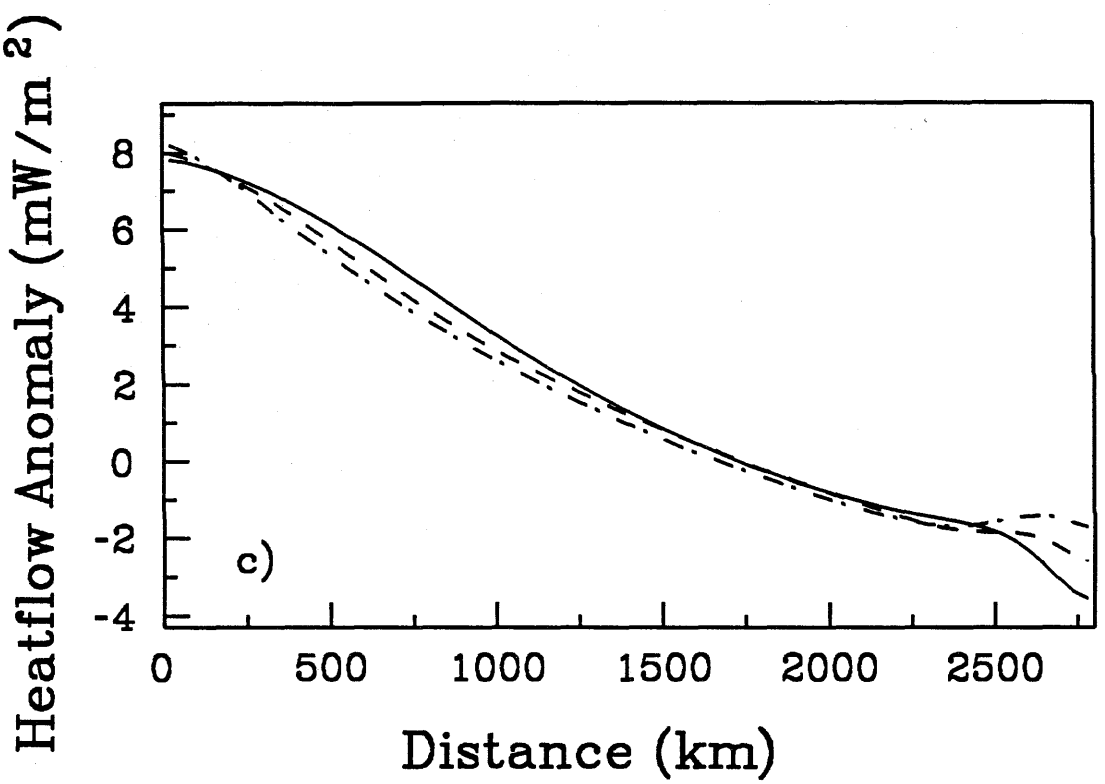
Heatflow Anomaly (mW/m 2)
8
6
4
2
0
-2
-4
c)
0
500
1000
1500
2000
2500
Distance (km)

Figure 11. Isotherms as a function of viscosity model at $Ra = 10^6$. a) Viscosity model 1 (Model 23). b) Viscosity model 3 (Model 29).

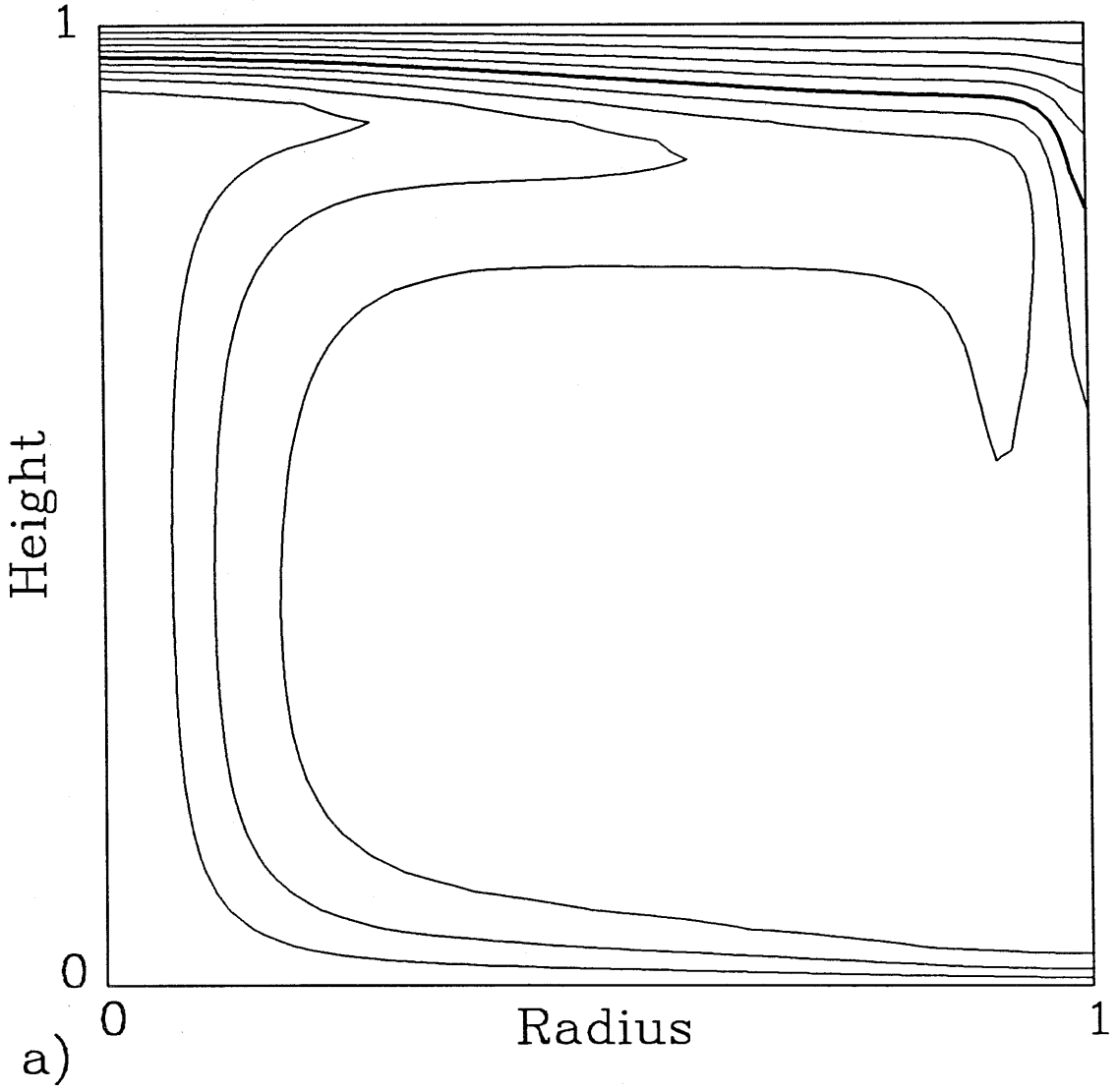
1
Height
0
0
Radius
1
a)

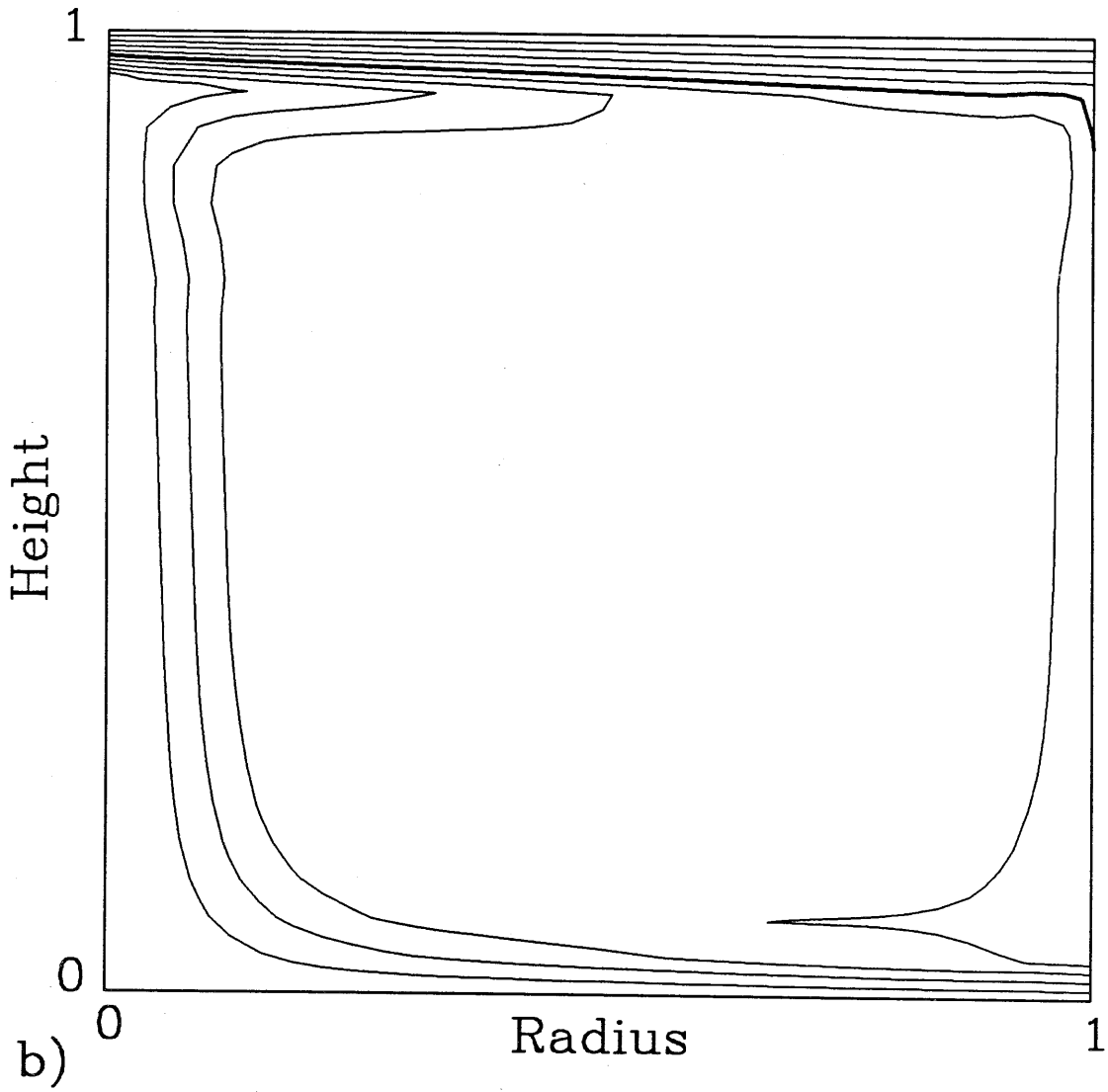
1
Height
0
0
Radius
1
b)

Figure 12. Profiles versus distance from plume center of (a) Geoid anomaly, (b) Topographic uplift, and (c) Heatflow anomaly for $Ra=10^5$ (solid line), $Ra=3\cdot10^5$ (dashed line), and $Ra=10^6$ (dot-dash line). All three models use viscosity model 3. (Models 27, 28, and 29).

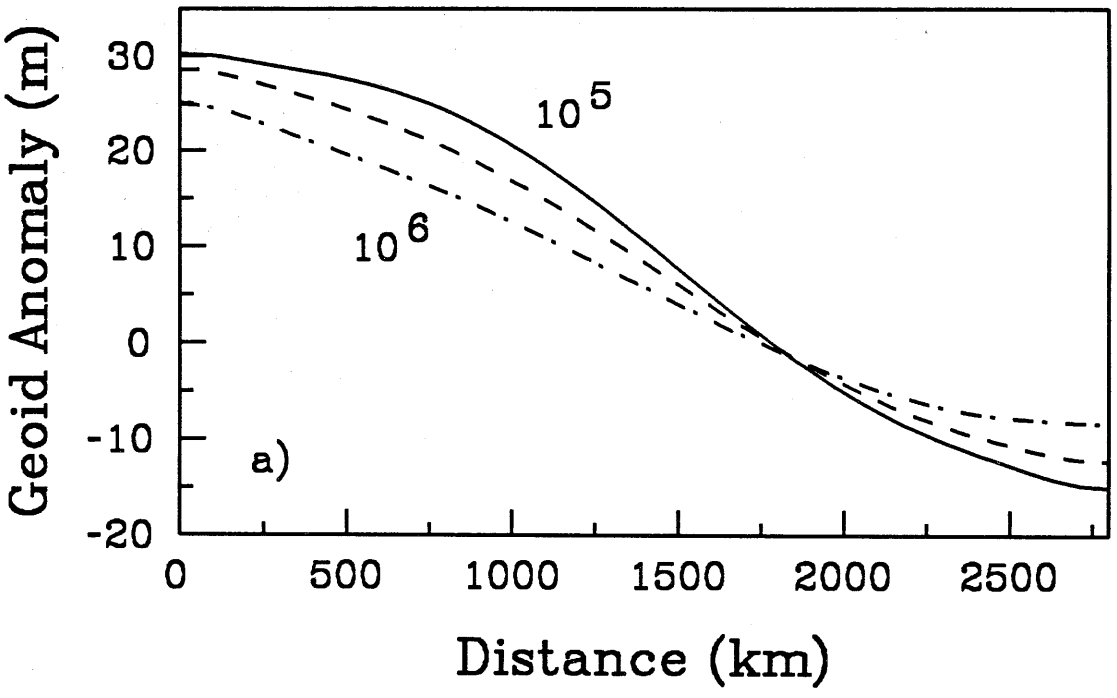
Geoid Anomaly (m)
30
20
10
0
-10
-20
10^5
10^6
a)
0
500
1000
1500
2000
2500
Distance (km)

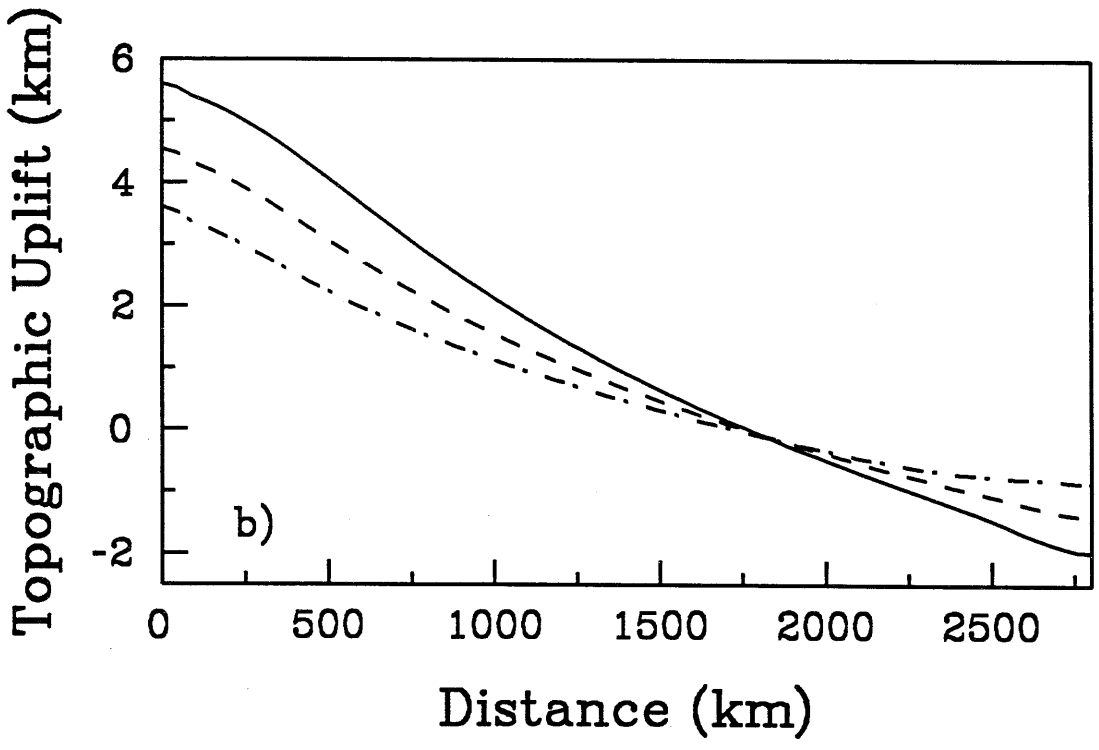
Topographic Uplift (km)
6
4
2
0
-2
b)
0
500
1000
1500
2000
2500
Distance (km)

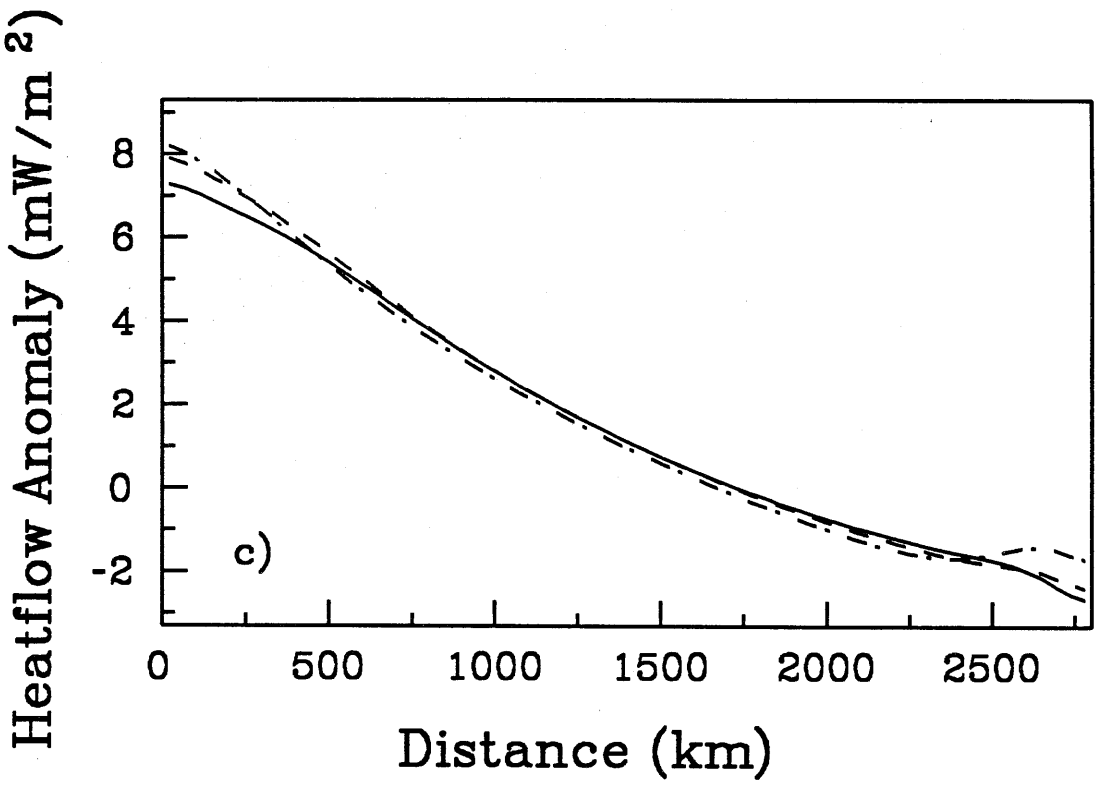
Heatflow Anomaly (mW/m 2)
8
6
4
2
0
-2
c)
0
500
1000
1500
2000
2500
Distance (km)

Figure 13. The lines are power-law fits to model results as discussed in the text. Triangles are models with constant viscosity (Models 6-10), squares are models using viscosity model 1 (Models 20-23), pentagons are models using viscosity model 2 (Models 24-26), and stars are models using viscosity model 3 (Models 27-29). a) Log Rayleigh Number versus Log Geoid. b) Log Ra versus Log Topography. c) Log Ra versus Log Nusselt Number. d) Log Ra versus Log Heat Flow Anomaly.

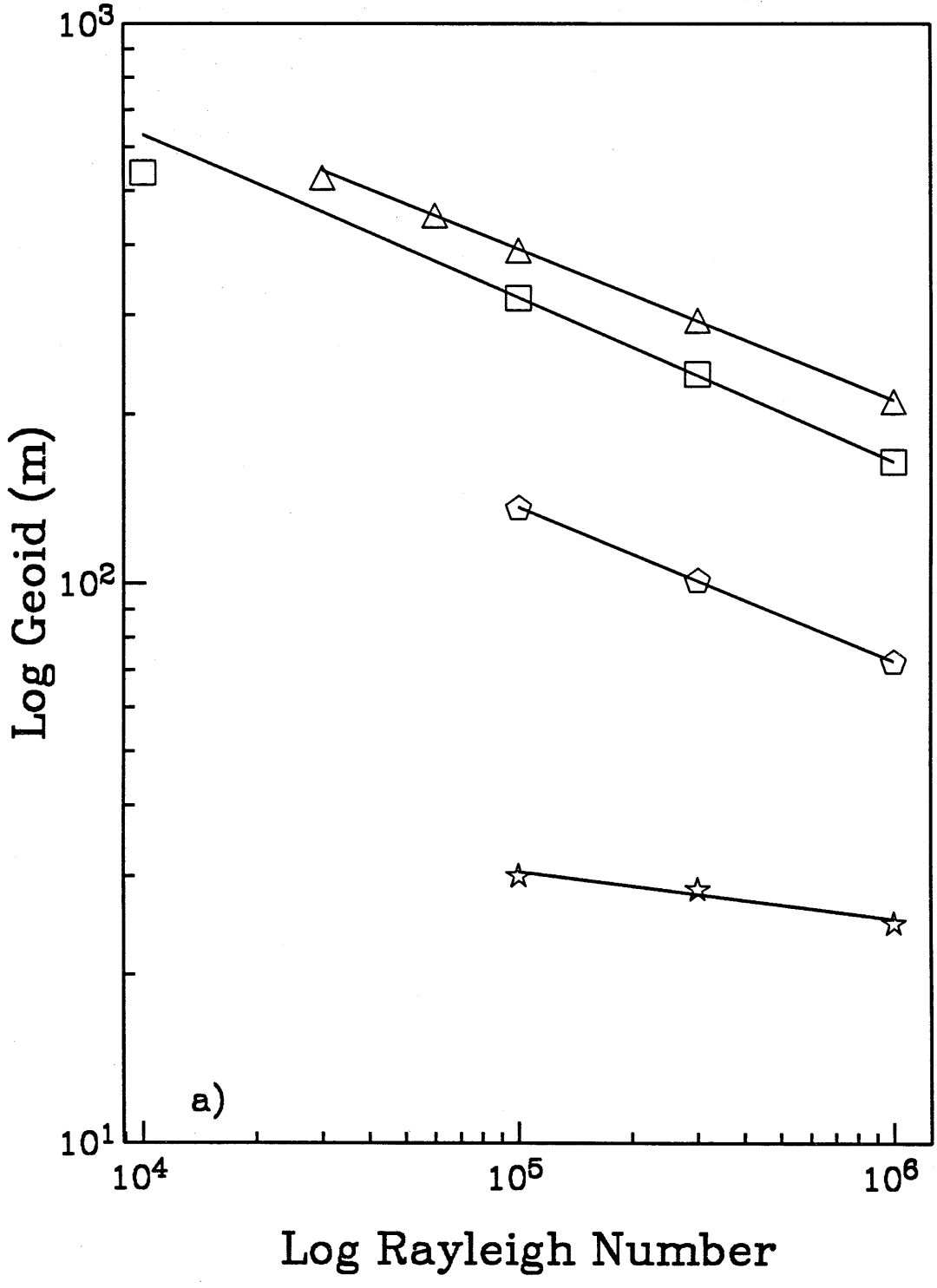
10^3
10^2
10^1
Log Geoid (m)
a)
10^4
10^5
10^6
Log Rayleigh Number

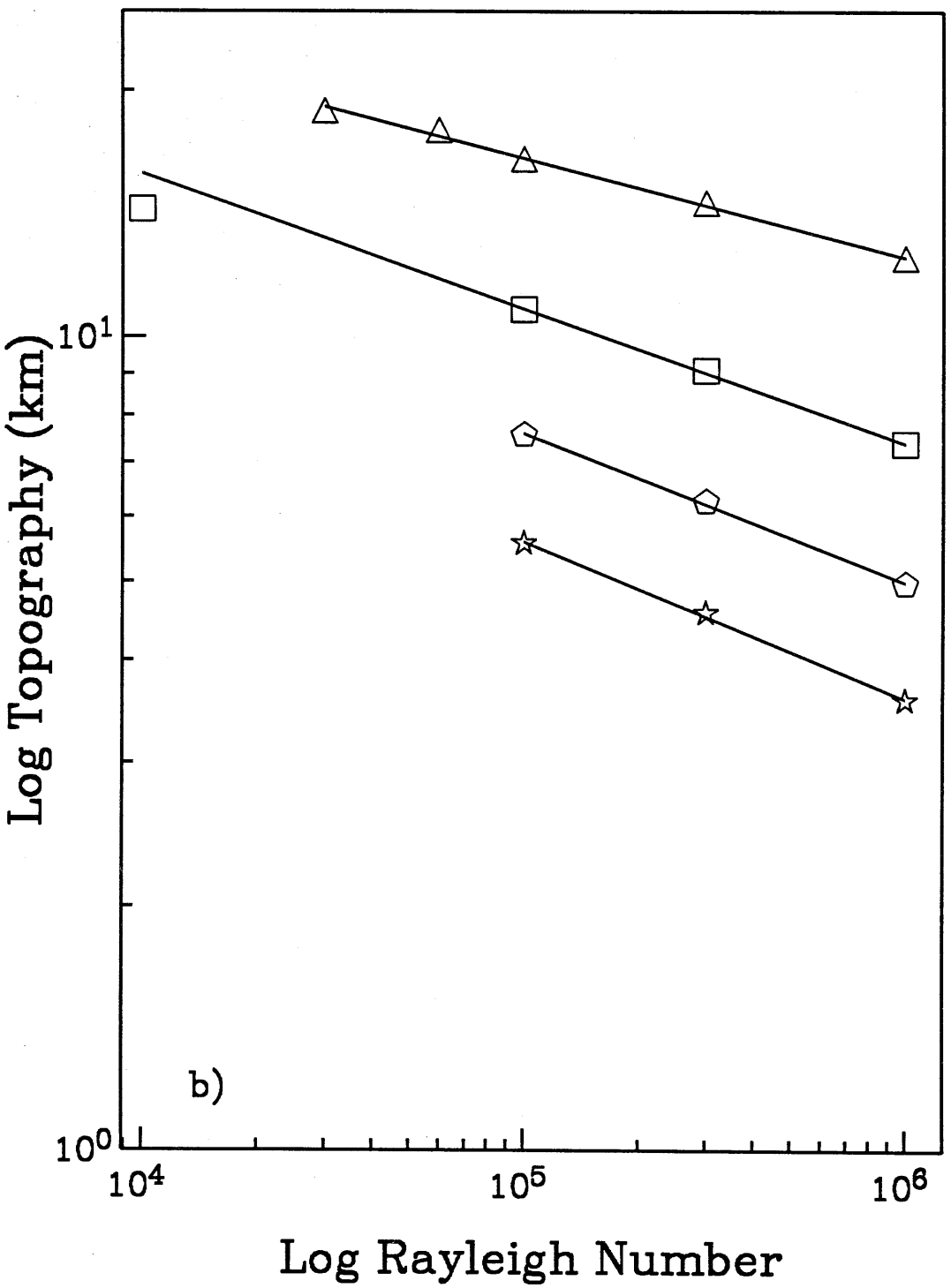
Log Topography (km)
10^1
10^0
b)
10^4
10^5
10^6
Log Rayleigh Number

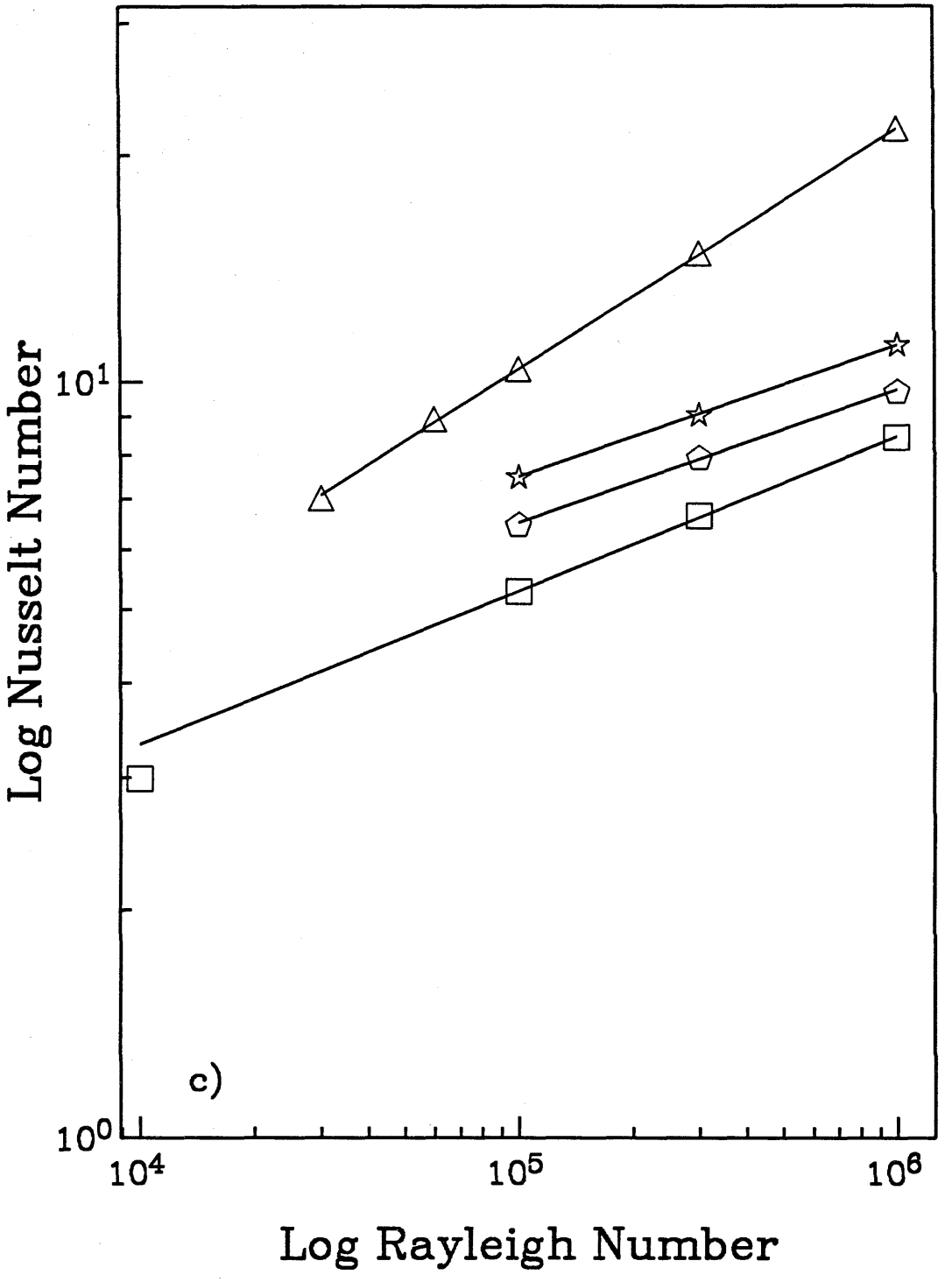
Log Nusselt Number
10^1
10^0
c)
10^4
10^5
10^6
Log Rayleigh Number

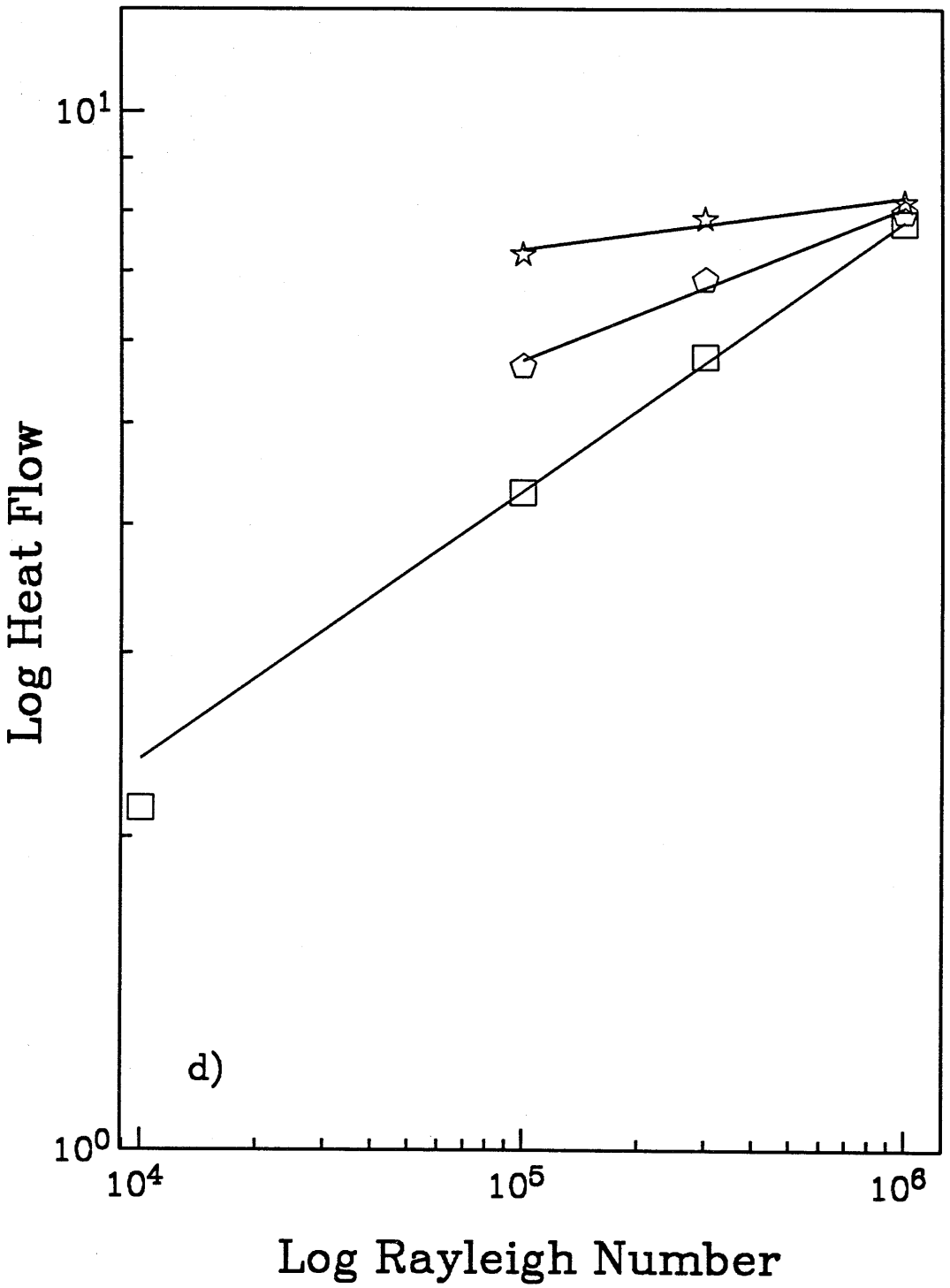
10^1
10^0
Log Heat Flow
d)
10^4
10^5
10^6
Log Rayleigh Number

Figure 14. Isotherms for bottom heated convection at Ra=10^5 and aspect ratio 1.4. a) Cylindrical geometry (Model 34). b) Cartesian geometry. Contour interval is 0.10.

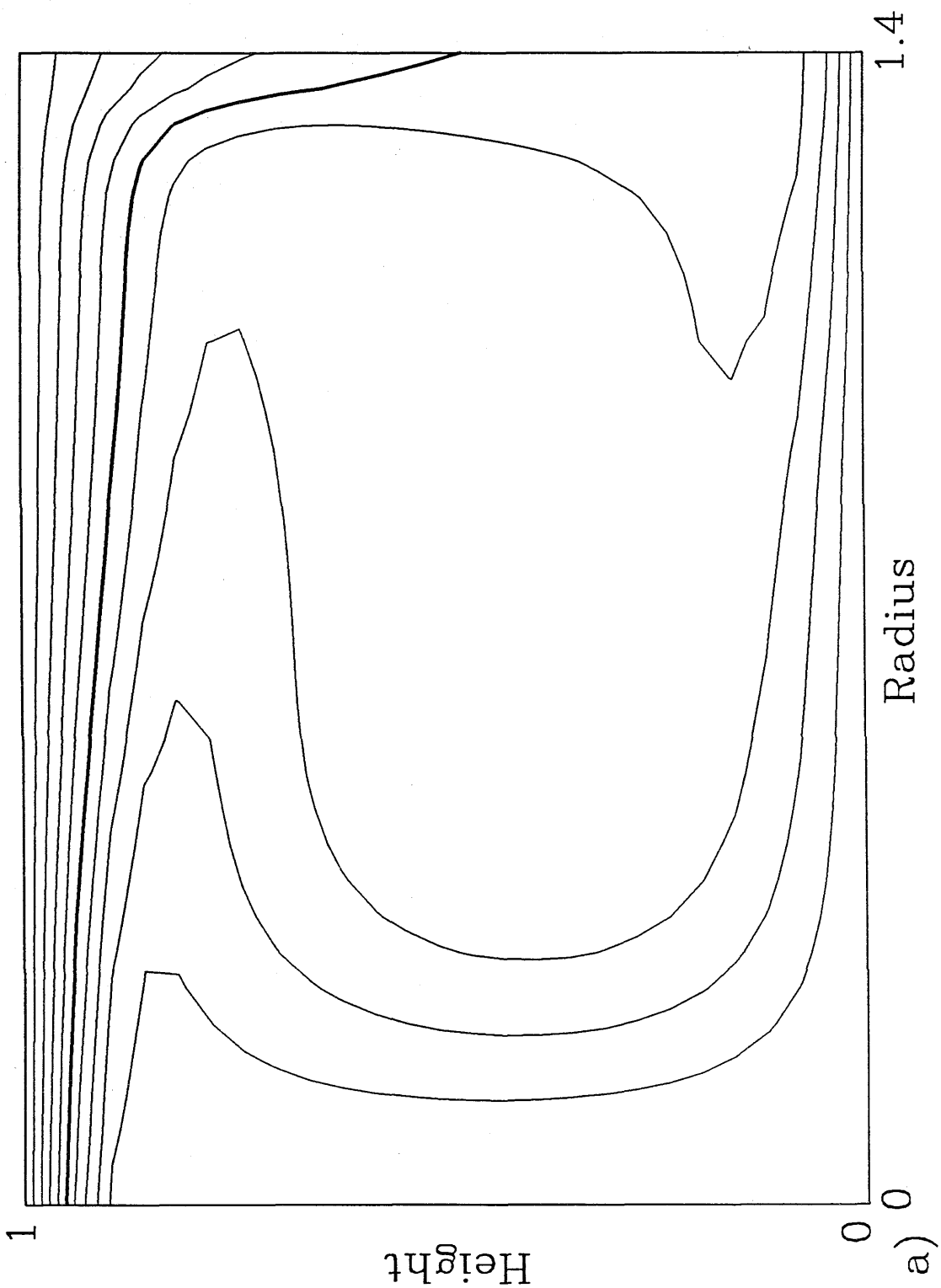
1
0
Height
0
1.4
Radius
a)

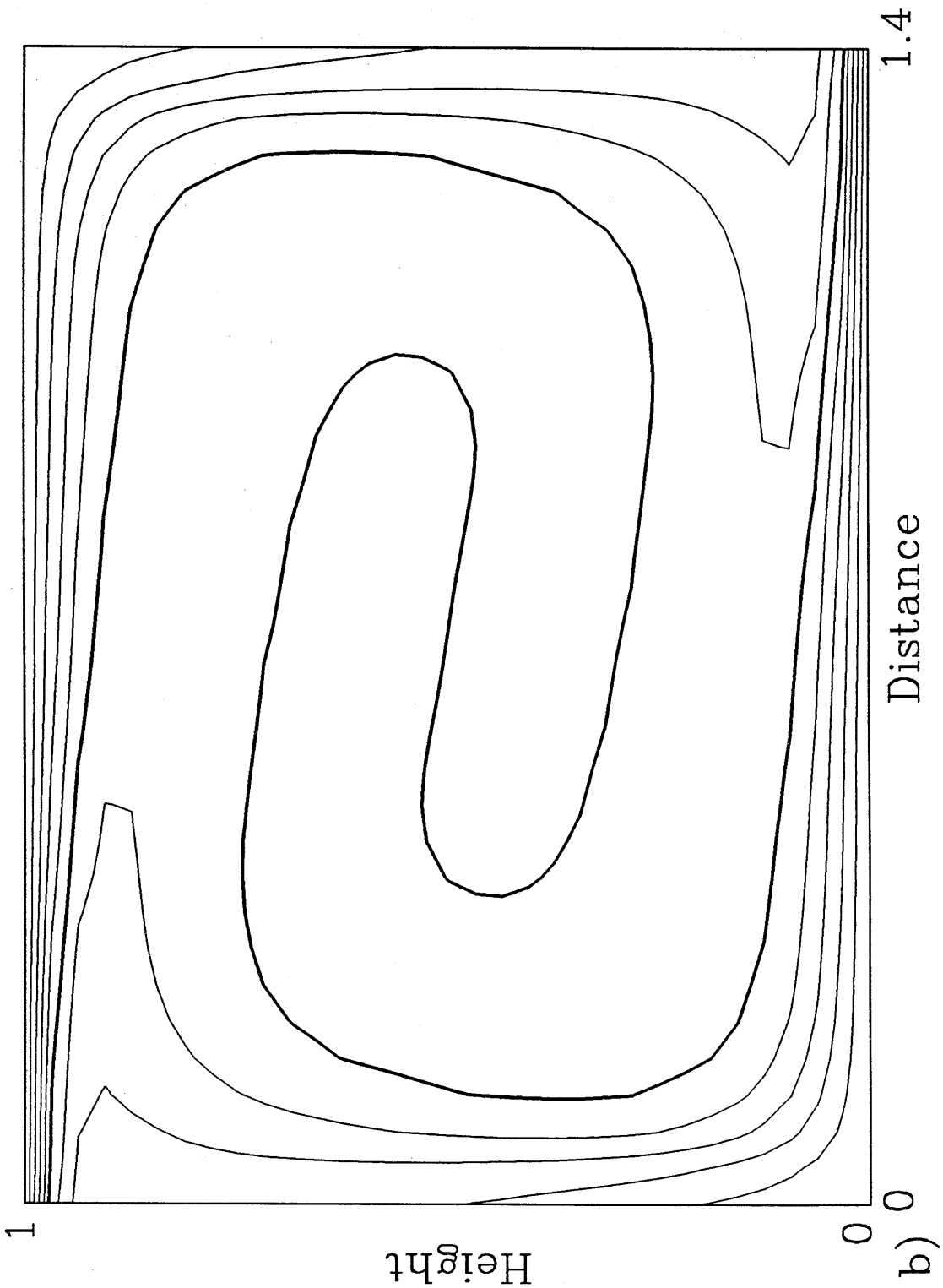
b)
1
0
Height
0
1.4
Distance

Figure 15. Effects of varying aspect ratio on a) Geoid anomaly at plume center, b) Topographic uplift at plume center, and c) Nusselt number. The triangles are the model results for Models 13 and 30-34. The lines in panels a and b are best fit straight lines to the model results, as discussed in the text.

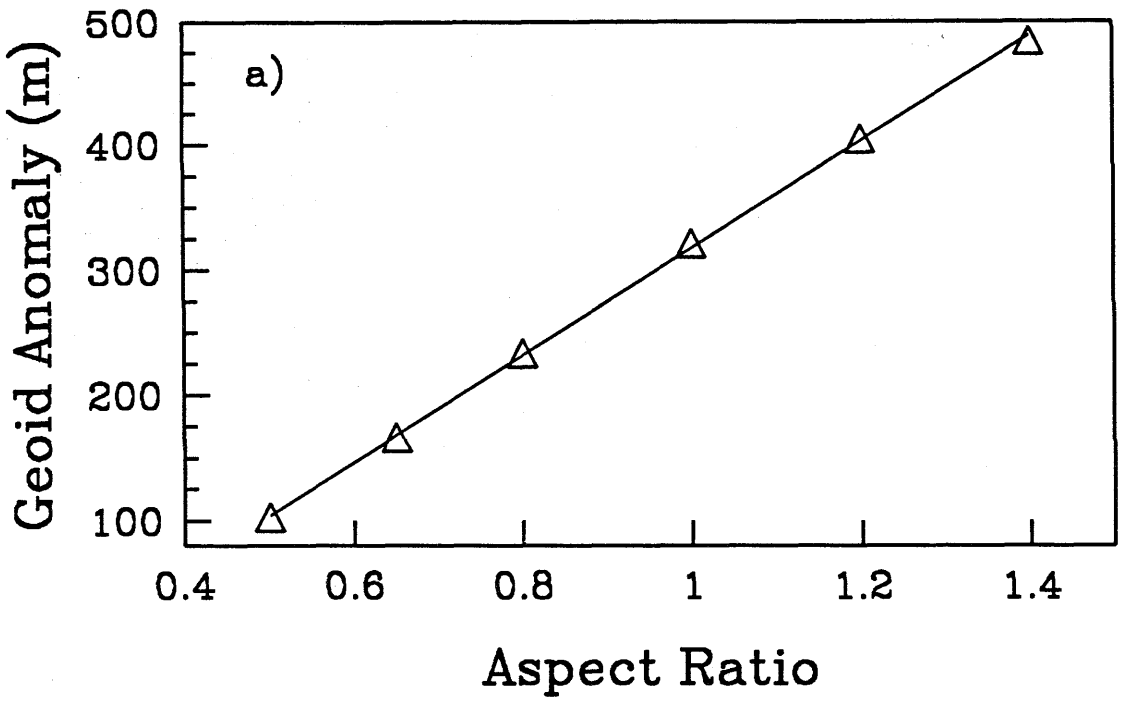
a)
Geoid Anomaly (m)
500
400
300
200
100
0.4
0.6
0.8
1
1.2
1.4
Aspect Ratio

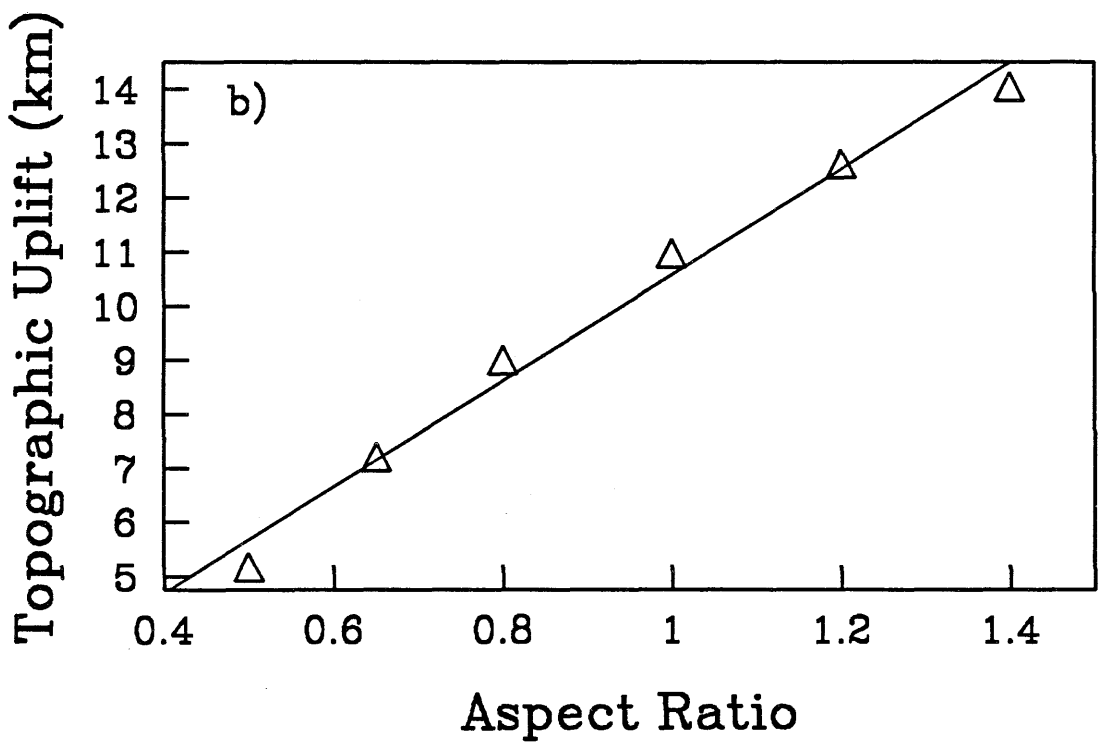
b)
Topographic Uplift (km)
14
13
12
11
10
9
8
7
6
5
0.4
0.6
0.8
1
1.2
1.4
Aspect Ratio

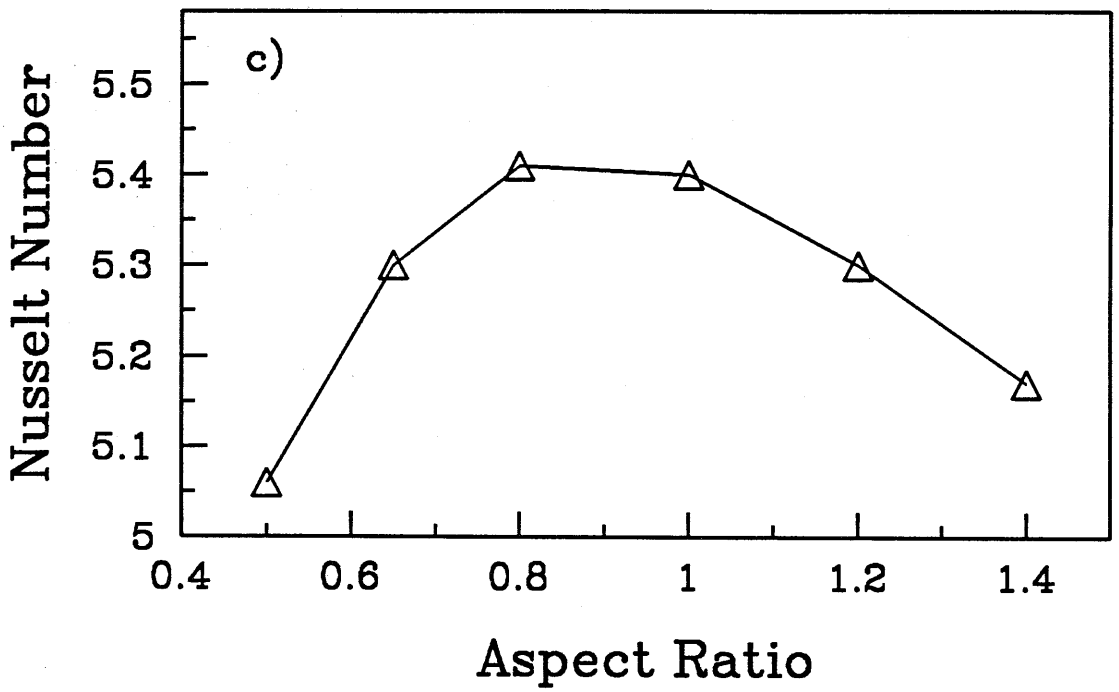
c)
Nusselt Number
5.5
5.4
5.3
5.2
5.1
5
0.4
0.6
0.8
1
1.2
1.4
Aspect Ratio

Chapter 2

A Mantle Plume Model for the Equatorial Highlands of Venus

Walter S. Kiefer and Bradford H. Hager[1]
Division of Geological and Planetary Sciences
California Institute of Technology
Pasadena, CA 91125

[1]Now at: Department of Earth, Atmospheric, and Planetary Science
Massachusetts Institute of Technology
Cambridge, MA 02139

To be submitted to J. Geophys. Res.

Introduction

For the most part, topography on Venus is rather flat. Altimetry data obtained by the Pioneer Venus Orbiter (PVO) indicate that only 5 per cent of the mapped surface of Venus differs from the mean planetary radius by more than 2 km. Indeed, 60 per cent of the surface lies within only 500 meters of the modal radius (Pettengill et al., 1980). Most regions of substantial topography on Venus are highlands; the deepest basin on Venus, Atalanta Planitia, is only 1.5 to 2 km below mean planetary radius (MPR). In contrast, the Equatorial Highlands rise 4 to 6 km above MPR and the mountain belts of Ishtar Terra rise 6 to 10 km above MPR (U.S. Geological Survey, 1981, 1984). An understanding of the origin of the highland regions of Venus is fundamental to our understanding of the geology and tectonics of Venus as a whole. We have presented models of Ishtar Terra elsewhere (Kiefer and Hager, 1990b; Chapter 4); in this manuscript we focus on the Equatorial Highlands and show that they are probably the result of rising mantle plumes.

The Equatorial Highlands of Venus consists of four main regions: Atla Regio, Beta Regio, Ovda Regio, and Thetis Regio. Each of these structures has a circular to oval-shaped surface planform with a characteristic size of 2000 to 3000 km. The geographic relationships among the various parts of the Equatorial Highlands are illustrated in Figure 1. This map shows the topography of Venus expanded in spherical harmonics out to degree and order 18 (Bills and Kobrick, 1985). The map is in cylindrical projection and has a horizontal resolution of 2100 km. The contour level is 500 meters, with regions below MPR shaded in gray. We show the topography in this form to facilitate comparison with the geoid data shown in Figure 2. Higher resolution topography maps have been published by the U. S. Geological Survey (1981, 1984).

Ovda and Thetis have sometimes been referred to collectively as Aphrodite Terra. This nomenclature derives from the work of Masursky et al. (1980), who arbitrarily distinguished between rolling plains, defined as regions with elevations between 0 and 2 km, and highlands, defined as regions with elevations greater than 2 km above MPR. This choice of nomenclature has contributed to the perception that Ovda and Thetis are parts of a single, linear

highland unit and may have influenced some later tectonic interpretations, such as the spreading center hypothesis of Head and Crumpler (1987). We note, however, that Ovda reaches a peak elevation of 4.5 to 5 km above MPR and that Thetis reaches a peak elevation of 3.5 to 4 km, whereas the topographic saddle between Ovda and Thetis has an elevation of only 2 km. The regions of peak elevation in Ovda and Thetis are separated by about 3500 km. We therefore believe that Ovda and Thetis are best interpreted as distinct, quasi-circular highland units.

Figure 2 shows a map of Venus's geoid based on the degree 18 spherical harmonic expansion of Bills, Kiefer, and Jones (1987). Figures 1 and 2 clearly show the strong positive correlation between geoid and topography on Venus (Sjogren et al., 1980; Kiefer et al., 1986a; Bills et al., 1987). Atla Regio has a peak geoid anomaly of 120 meters, the largest observed on the planet. Beta and Thetis also have large geoid anomalies of 92 meters and 73 meters, respectively. The peak geoid anomaly at Ovda is about 35 meters. For comparison with the Venus data, in Figure 3 we show Earth's geoid for spherical harmonic degrees 2 to 18 (Lerch et al., 1985). It is readily apparent that Earth's long-wavelength geoid is essentially uncorrelated with the positions both of continents and of spreading centers. This conclusion has been statistically verified by Richards and Hager (1988).

PVO altimetry data shows that all four of the main structures in the Equatorial Highlands contain interconnected topographic valleys or chasmata (U.S. Geological Survey, 1981, 1984; Schaber, 1982). These troughs sometimes exceed 2 km in depth (see, for example, Figure 11b) and have typical widths of 75 to 100 km. However, because of averaging over the PVO altimeter's measurement footprint and because of the spacing between measurements, the troughs may be both narrower and deeper than indicated by PVO data. On the basis of PVO data, McGill et al. (1981) and Schaber (1982) both suggested that the troughs are extensional rift zones. The geology of Devana Chasma, the trough that runs through Beta Regio, can be studied in greater detail using radar imagery from the Arecibo Observatory (Campbell et al., 1984; Stofan et al., 1989). The Arecibo observations are also consistent with a rift zone interpretation for Devana Chasma. The Arecibo imagery also reveal the

presence of two prominent shield volcanoes in Beta Regio, Rhea Mons and Theia Mons (Campbell et al., 1984, 1989; Stofan et al., 1989). The limited data available on the chemical composition of the surface are consistent with the presence of basalt (Surkov et al., 1984, 1986, 1987).

Models for the Formation of the Equatorial Highlands

A variety of models have been suggested for the formation of the Equatorial Highlands. One class of models proposes that the Highlands are regions of thickened crust, formed either by volcanic activity or by crustal convergence over a region of downwelling mantle. Other models propose that the Highlands are spreading centers or are due to uplift by hot, upwelling mantle plumes. We consider these various types of models in turn.

Crustal Thickening Models

A conceptually simple model for supporting high topography is to have a region of thickened crust compensated by means of Airy isostasy. This type of model for the Equatorial Highlands has been tested by various workers using gravity data obtained by the PVO spacecraft. If modeled in terms of Airy isostasy, Atla, Beta, and Thetis would all require compensation depths of several hundred kilometers (Esposito et al., 1982; Phillips and Malin, 1983; Kiefer and Bills, 1984; Herrick et al., 1988). Numerous workers have suggested that the crustal thickness in the plains of Venus is no more than 25 to 30 km (Zuber, 1987; Banerdt and Golombek, 1988; Grimm and Solomon, 1988; Zuber and Parmentier, 1990; Kiefer and Hager, 1990b; Chapter 4). If the Equatorial Highlands are supported by Airy isostasy, then the crust beneath the highlands should be 20 to 30 km thicker than in the plains. This implies a crustal thickness in the Highlands of less than about 60 km, much less than required to satisfy the gravity data.

Even if one were to assume that the crustal thickness in the plains is more than 25 km, the base of the crustal roots in the highlands must not extend below the base of the thermal lithosphere or else the highlands could not be supported for geologically long periods of time. Kaula and Phillips (1981)

estimated that the thermal boundary layer thickness on Venus should be less than 100 km. Turcotte (1989a) suggested that if most heat transport in the lithosphere of Venus occurs magmatically in "heat pipes," then the lithosphere could reach a thickness of 150 km or more. However, Turcotte's model requires a magma flux of 200 $km^3\ year^{-1}$, an order of magnitude higher than on Earth. The observed density of impact craters sets an upper limit of about 2 $km^3\ year^{-1}$ on the extrusive volcanism rate (Grimm and Solomon, 1987), so that if Turcotte's model is correct, 99% of all magmatic activity on Venus must be intrusive, with no more than 1% occurring as extrusive flows. On Earth, extrusive activity is typically 10 to 20% of all magmatic activity (Crisp, 1984). Although it may be possible to satisfy the conditions required by the heat pipe model, we think that it is preferable to explore other models.

We therefore conclude that the Airy model can not plausibly explain the geoid anomalies observed at Atla, Beta, and Thetis. This does not preclude the existence of Airy-compensated crustal thickness variations in these regions, but it does require that significant density anomalies exist within the mantle. This implies that mantle convection plays a significant role in supporting these features. The geoid anomaly at Ovda is substantially smaller than in the other parts of the Equatorial Highlands. In principle, Ovda's geoid anomaly could be explained entirely by density anomalies within the lithosphere (e.g., Herrick et al., 1988; Sotin et al., 1989; Kiefer, 1990). However, as shown later in this paper, mantle convection models can also explain Ovda's geoid anomaly.

Banerdt (1986) suggested that Ovda is a region of thickened crust overlying mantle material which is denser than normal. The dense, downwelling mantle material could entrain crustal material into the convergence zone, producing the hypothesized crustal thickening. Bindschadler and Parmentier (1989) have suggested that this type of model may apply to both Ovda and Thetis. This crustal convergence/mantle downwelling model is similar to a model preferred by many workers for Ishtar Terra (e.g., Morgan and Phillips, 1983; Banerdt, 1986; Kiefer and Hager, 1990b; Chapter 4). Because this model contains density anomalies in the mantle as well as the lithosphere, it can in principle satisfy the observed geoid anomalies. However, this model predicts that the Ovda and Thetis should be in compression (Banerdt, 1986), whereas the apparent rift

zones suggest that they are actually undergoing extension. Bindschadler and Parmentier (1989) suggested that downwelling under Ovda and Thetis may have ceased, so that the highland topography may currently be undergoing viscous relaxation. In this model, the observed chasmata would be relaxation features. If the crustal convergence model is correct, then we would expect the formation of mountain belts flanking a high plateau, as is observed both at Ishtar Terra on Venus and at the Tibetan Plateau on Earth. However, no such mountain belts are obvious in the PVO altimetry for Ovda and Thetis. Such mountain belts may have formed and later relaxed away, but in that case they may have left behind a signature in the form of compressive folds and thrust faults on the margins of Ovda and Thetis. Magellan imagery should be examined for such features.

Spreading Center Models

In a series of papers, Crumpler, Head, and their colleagues have proposed that Ovda and Thetis are spreading centers, analogous to terrestrial mid-ocean ridges (Crumpler et al., 1987; Crumpler and Head, 1988a,b; Head and Crumpler, 1987, 1989; Sotin et al., 1989). Both geological and geophysical observations have been suggested as tests of this model. As noted above, the long-wavelength geoid and topography are strongly correlated on Venus, a situation that is quite different from that observed at terrestrial spreading centers. This suggests that Ovda and Thetis are not similar to terrestrial spreading centers. Sotin et al. (1989) recently argued that the geoid and topography are also strongly correlated at spreading centers on Earth. However, as discussed by Kiefer (1990; Chapter 3), the conclusions of Sotin et al. refer only to wavelengths that are not detectable in the existing Venus gravity dataset.

The amplitudes of the geoid anomalies and topography also provide clues to the mechanisms that produced the highlands. Using a cooling plate thermal model, Kiefer (1990) showed that spreading centers on Venus would produce geoid anomalies of only 8 meters, much less than that observed at either Ovda or Thetis. Similarly, spreading centers on Venus should produce topographic uplifts of no more than 1.5 km (Kaula and Phillips, 1981), which is also much less than the observed values. Moreover, Grimm and Solomon (1988) and Black

et al. (1990) both found that the observed topography does not follow the square-root of distance subsidence profile expected if Ovda and Thetis are spreading centers with approximately constant spreading velocities. The only good fit to the expected subsidence profile occurs near longitude 180° (see Profile LL' in Figure 5 of Head and Crumpler, 1987). Although these observations do not rule out the existence of spreading centers in Ovda and Thetis, they do require that both the geoid and topography of these regions must be dominated by processes other than the hypothesized spreading centers.

Geological observations have also been used to argue for the spreading center model. For example, Crumpler et al. (1987) argued for the existence of a series of seven parallel linear structures, which they termed "cross-strike discontinuities," or CSDs. Crumpler et al. interpreted these features as analogous to terrestrial transform faults. However, Kiefer (1990) reexamined the evidence for the CSDs and concluded that existing (pre-Magellan) data does not require the existence of CSDs. If any CSDs exist in this region, Magellan radar imagery will be necessary to verify the existence of the CSDs and to characterize their structure.

Crumpler and Head (1988a) suggested that a symmetry axis could be defined in Ovda and Thetis. The proposed symmetry axis is orthogonal to the orientation of Crumpler et al.'s (1987) CSDs. Crumpler and Head (1988a) proposed that the topography to the north and south of this axis shows a bilateral symmetry pattern. They further suggested that the bilateral symmetry supports their spreading center model. They proposed that topographic plateaus formed at the spreading center axis during episodes of high volcanic activity. These plateaus later rifted apart and spread to their present locations, producing bilaterally symmetric topography (Crumpler and Head, 1988b). However, Grimm and Solomon (1989) found that no statistically significant bilateral symmetry pattern is detectable in the PVO altimetry for Ovda and Thetis.

Head and Crumpler (1989) recently argued that impact cratering statistics require that the equatorial region of Venus is on average somewhat younger than regions further north. They also noted that the equatorial region seems to be dominated by extensional tectonism, whereas at least some parts of the

northern latitudes are dominantly compressional. Although both observations are consistent with their spreading center model, neither observation uniquely requires a spreading center interpretation.

We conclude that none of the existing data requires the existence of spreading centers in Ovda and Thetis. Although the existence of spreading centers in these areas can not be completely excluded at present, both the geoid and topography in these areas clearly must be dominated by processes other than spreading centers.

Mantle Plume Models

Upwelling mantle plumes have been widely suggested as an explanation for Beta Regio and possibly for other parts of the Equatorial Highlands (McGill et al., 1981; Morgan and Phillips, 1983; Phillips and Malin, 1983; Campbell et al., 1984; Kiefer et al., 1986a; Banerdt, 1986; Kiefer and Hager, 1988; Stofan et al., 1989). The mantle plume model is consistent with the observations cited above of basaltic shield volcanism and extensional tectonism in the Equatorial Highlands, and is also consistent with the observed quasi-circular planforms of the highlands. As we show in this paper, the plume model can also quantitatively explain much of the observed geoid anomalies and topography. For these reasons, we favor the plume model as an explanation for the origin of the Equatorial Highlands.

Initial attempts to quantify the geoid and topography signatures expected for convective upwellings on Venus were made by Kiefer et al. (1986a) and Kiefer and Hager (1988). The material presented in this manuscript represents a more detailed treatment of the material presented in abstract form by Kiefer and Hager (1988). We begin by describing the numerical procedures that we have used to model mantle plumes and then examine how our model results compare with observations of geoid anomalies and topography in the Equatorial Highlands. On the basis of these models, we conclude that Venus's asthenosphere is more viscous than Earth's asthenosphere and suggest that this may be due to Venus's mantle being drier than Earth's mantle.

Numerical Modeling of Mantle Plumes

In this section, we briefly discuss the numerical procedures that we have used in our plume modeling. For a more detailed description, see Kiefer and Hager (1990a, hereafter referred to as KH; Chapter 1). We have used a finite element code developed by Daly and Raefsky (1985) to solve the conservation laws for mass, momentum, and energy in a cylindrical, axisymmetric geometry. Courtney and White (1986) have previously presented some cylindrical axisymmetry plume models for the Earth. By assuming axisymmetry, the convection problem is reduced to two dimensions, enabling us to do well-resolved calculations at Rayleigh numbers that approach those expected for Venus and Earth. In contrast, existing three-dimensional spherical geometry models have generally been restricted to very low Ra (Machetel et al., 1986) or are substantially underresolved in the horizontal dimensions (Baumgardner, 1988; Glatzmaier, 1988; Bercovici et al., 1989). Although such studies may provide useful qualitative results on convective planforms, they can not be used for quantitative studies of the topographic uplift and geoid anomalies created by high Rayleigh number convection.

An alternative type of two-dimensional model uses Cartesian geometry and treats plumes as infinitely long, sheet-like upwellings. This type of model has been used in many recent studies of terrestrial mantle plumes (e.g., Robinson et al., 1987; Robinson and Parsons, 1988; Ceuleneer et al., 1988). However, in KH we showed that the Cartesian and cylindrical geometry models produce significantly different geoid anomalies and topographic uplifts. We favor the cylindrical geometry because it provides a better representation of the overall shape of the various portions of the Equatorial Highlands. This is most clearly true for Beta Regio and Atla Regio. Even for the most elongated part of the Equatorial Highlands, Ovda Regio, the cylindrical geometry model is probably at least as good an approximation as the the infinitely long Cartesian sheet model. Our models neglect the possible effects of sphericity on plume structure. We expect that the differences in the geoid and topography signatures calculated for plumes in cylindrical and spherical geometries should be much smaller

than the differences shown in KH between cylindrical and Cartesian geometries, but this certainly merits further study.

For mechanical boundary conditions, we apply $V_z = 0$ and $\frac{\partial V_r}{\partial z} = 0$ on the top and bottom of the cylinder, where V_r and V_z are the radial and vertical components of the velocity. The condition $\frac{\partial V_r}{\partial z} = 0$ is the free-slip (zero shear stress) condition. We have also examined several test cases in which we applied a no-slip ($V_r = 0$) condition on the top surface and find that the resulting geoid and topography profiles differ by only a few percent from their values in the free-slip top case. This is because the high viscosity surface layer in our models (see Figure 6) cause low flow velocities, so that the surface behaves as if it were nearly rigid. On the side walls, we apply $V_r = 0$ and $\frac{\partial V_z}{\partial r} = 0$. For thermal boundary conditions, we apply a constant temperature condition on the top and bottom and an insulating condition (no heat flux, $\frac{\partial T}{\partial r} = 0$) on the sidewalls.

The calculations presented in this paper are all calculated on a 65 x 65 grid. This grid uses uniform spacing in the radial direction and has enhanced resolution in the vertical dimension of the upper boundary layer (see Figure 1 of KH). Based on the resolution tests described in KH, we believe that the geoid anomalies and topographic uplifts given here are typically within 2 to 3% of the true values of these quantities if calculated on a grid of infinite resolution. The models that include a low viscosity asthenosphere (viscosity model 3 of Figure 6) may be somewhat less accurate than this, but as shown below, these models are not applicable to Venus anyway.

For various combinations of mantle parameters, we have used the finite element code to calculate steady-state temperature and stress fields. An example temperature field is shown in Figure 4, which shows an isotherm diagram for a representative solution. The contour interval is 0.1 of the total temperature contrast across the cylinder. This figure shows a rising plume along the symmetry axis of the cylinder ($r = 0$) and a downwelling ring of material along the outer wall of the cylinder. All of the models described in this paper are

heated entirely from below and neglect the contribution of radioactive heating within the convecting layer. For whole mantle convection, it is likely that internal heating dominates over basal heating, but we nevertheless believe that our models provide a good representation of the thermal structure of a mantle plume. Provided that there is at least some flow of heat from the core into the base of the mantle, a thermal boundary layer must form at the base of the mantle, and instabilities in this boundary layer will insure that plume-like upwellings form. Indeed, in KH we showed an example of a cylinder that is 80% internally heated and which has an upwelling plume along the axis of the cylinder. Inclusion of spherical geometry will concentrate the core's heat flow into a smaller area, thus enhancing the formation of a lower thermal boundary layer and rising plumes. The key issue, therefore, is not whether or not plumes will form in Venus's mantle, but rather the magnitude of the temperature contrast between the rising plumes and the surrounding mantle. We return to this issue when we discuss scaling parameters below.

Once we have obtained the temperature and stress fields for a given model, we can calculate the expected topographic uplift and geoid anomaly associated with the model. By comparing the results of various models with observations, we can place constraints on the allowed range of mantle parameters on Venus. The topographic uplift, δh, can be calculated from the total vertical normal stress, τ_{zz}, by the relationship

$$\delta h = \frac{\tau_{zz}}{\rho_m g}, \tag{1}$$

where ρ_m is the mantle density and g is the gravitational acceleration. Even though a low density crust is likely to be present in most regions of Venus, it is still appropriate to use the mantle density in Equation 1 because both crust and mantle material are uplifted by the plume. For sub-oceanic hotspot swells on Earth, ρ_m must be replaced by $(\rho_m - \rho_w)$ in Equation 1, where ρ_w is the density of seawater. Thus, for a given thermal and viscosity structure, the topographic uplift over a mantle plume will be less on Venus than for sub-oceanic regions on Earth. Because of the high surface temperature on Venus, the elastic

lithosphere must be thin, implying that flexural resistance to uplift will be negligible at the long wavelengths of interest in this paper.

The geoid is a surface of constant gravitational potential, so in order to calculate the geoid anomaly associated with a mantle plume, we must first calculate the gravitational potential, U. At or above the surface of a planet, the gravitational potential must satisfy Laplace's equation, $\nabla^2 U = 0$. This equation is most readily solved by expanding the radial variations of temperature and of topographic uplift in terms of a series of Bessel functions of the form $J_0(k_n r)$, where k_n is a horizontal wavenumber. With this series expansion, the external potential must vary vertically as $\exp(-k_n z)$. One can therefore show that the potential at the surface ($z = 0$) is given by

$$\delta U(r) = \frac{2\pi G}{g} \sum_n \frac{J_0(k_n r)}{k_n} \left(\rho_m \delta h_s^n + (\rho_c - \rho_m) \delta h_c^n \exp(-k_n d) - \rho_m \alpha \int_0^d T^n(z) \exp(-k_n z)\, dz \right). \quad (2)$$

In equation 2, ρ_m and ρ_c are the densities of the mantle and core, G is the gravitational constant, α is the thermal expansion coefficient, and d is the thickness of the convecting layer. δh_s^n and δh_c^n are the n-th harmonics of the surface topographic uplift and the core-mantle boundary uplift. Similarly, $T^n(z)$ is the n-th harmonic of the temperature field at depth z. The first term within the braces is the contribution to the potential of the mass anomaly at the uplifted surface, the second term represents the contribution of mass anomalies associated with convectively-induced topography on the lower boundary of the convecting layer, and the final term represents the contributions of mass anomalies due to thermal expansion of material within the convecting layer. For a convective upwelling, the first two terms are positive and the third term is negative. The sign of the potential, and hence of the geoid, depends on the relative balance of the three terms; for the models shown here, the geoid is always positive over the upwelling plume. In writing equation 2, we have left out the zero-th order gravitational potential, $U = \frac{GM}{R}$, where M is the

planetary mass and R is the planetary radius. Equation 2 therefore represents the anomalous gravitational potential, δU, associated with the convecting system.

Note that although equation 2 includes the core density, in practice it is not necessary to actually specify a value of ρ_c because by analogy with equation 1, the topographic uplift at the top or bottom of the convecting layer is inversely proportional to the density contrast at the boundary, i.e., $(\rho_c - \rho_m)\,\delta h_c = \frac{\tau_{zz}}{g}$. Similarly, the value of the potential does not depend on the presence or absence of an ocean, contrary to a recent assertion by Phillips (1990).

Once we have obtained δU, we can evaluate both the geoid anomaly, $\delta N = \frac{\delta U}{g}$, and the gravity anomaly, $\delta g = -\frac{\partial U}{\partial z}$. Because the gravity anomaly is the derivative of the potential, it enhances the value of short-wavelength components relative to longer wavelength features. We are interested in structures that may extend deep into the mantle and which are therefore sensed only by the long-wavelength part of the potential. We therefore prefer to work with geoid anomalies rather than gravity anomalies. In this paper, we compare our plume model geoids with the eighteenth degree spherical harmonic geoid model of Bills et al. (1987) (Figure 2), which has a horizontal resolution of 2100 km. It is not possible to exactly match the wavelengths in our models with those of the Bills et al. geoid. In the work presented here, we include only the first three harmonics in our model geoid calculations, corresponding to wavelengths longer than 1850 km. In KH, we present results for the first 16 harmonics of the model cylinder, which corresponds to essentially 100% of the power in the geoid spectrum. The results given here contain at least 90% of the power present in the more complete geoid spectra.

In order to facilitate comparisons between models and data, all of the model results presented here are expressed in dimensional form. Non-dimensional results are tabulated in KH. The scaling constants that we use are given in Table 1. Our choice of d=2800 km for the convecting layer thickness corresponds to whole mantle convection. The value $\Delta T = 1000\,^{\circ}C$ does not

represent the entire change in temperature between the top and bottom of the mantle. Because we assume incompressible convection, it is inappropriate to include temperature changes associated either with the adiabatic gradient or with phase transitions in our estimate of ΔT. For $\Delta T = 1000\,^{\circ}C$, Figure 4 shows that there should be about a 300 °C difference in temperature between the center of a plume and the surrounding average mantle. This choice of ΔT gives a temperature contrast of about 700 °C across the upper thermal boundary layer, which is somewhat less than the 1000 °C temperature contrast predicted by the boundary layer model of Kaula and Phillips (1981).

The relative temperature contrasts across the upper and lower boundary layers depend on a number of parameters, including the ratio of internal heating to basal heating and the temperature dependence of the rheology, as well as the choice of spherical or planar geometry. The models presented here do not incorporate some of these factors and therefore do not simultaneously produce the correct temperature contrasts across both boundary layers. Because we are primarily interested in the geophysical signatures of upwelling plumes, we have chosen a thermal scaling that is reasonable for mantle plumes. In KH, we argued that a 300 °C temperature contrast between the center of an upwelling plume and the average mantle is consistent with the petrology of basalts produced by hotspots, with estimates of the core heat flow needed to power the Earth's geodynamo, and with observations of heat flow anomalies at terrestrial hotspots. Sleep (1990) recently reached a similar conclusion. We assume that a similar temperature contrast can also be applied to upwelling plumes on Venus. This choice of ΔT underestimates the likely temperature contrasts in downwelling regions on Venus, so the geoid and topography that we predict for downwellings are probably underestimates.

In the past, Pratt compensation has sometimes been used to calculate the geoid and topography expected from density anomalies within the convecting mantle (e.g., Banerdt, 1986). Although thermal density anomalies exist both in convecting systems and in the Pratt isostasy model, in the Pratt model the density anomalies have fixed positions, whereas in mantle convection the density anomalies drive viscous flow. The two models predict significantly different relationships between geoid and topography. In Figure 5, we compare the

admittance, which is the ratio of geoid anomaly to topographic uplift as a function of wavelength, for Pratt and convection models. The lines are for models that are uniformly Pratt compensated over depth ranges of 100, 200, and 400 km. The triangles are the admittance values calculated for the plume model of Figure 4 and can only be defined for wavelengths that are harmonics of the model cylinder. It is clear that the convection model differs significantly from the Pratt models, a result which is consistent with the conclusions of Kiefer et al. (1986a) and of Robinson et al. (1987).

Model Results

In this section, we describe how various mantle parameters affect the geoid and topography signatures of a mantle plume. We focus here on two particular issues, the effects of varying viscosity with depth in the mantle and of varying the Rayleigh number. A more complete discussion of the effects that these and other parameters have on plume structure can be found in KH. In the following section, we apply these models to observations of the Equatorial Highlands.

We have performed calculations using three standard viscosity models, shown in Figure 6. All viscosities shown in this figure are normalized relative to a lower mantle viscosity of 1. All three models use a high viscosity near-surface layer (the "lid") to mimic the effects of temperature-dependent viscosity on the rheology of the thermal boundary layer. This layer is 130 km thick, within which the viscosity decreases by 3 orders of magnitude from the surface to the base of the lid. The viscosity contrast between the surface and the base of the lid on Venus is undoubtedly much larger than 3 orders of magnitude, but as we showed in KH, increasing the viscosity contrast beyond 3 orders of magnitude has a very small effect on either the geoid anomaly or the topographic uplift associated with a plume. The lid thickness of 130 km corresponds to the lithospheric thickness of old oceanic plates on Earth (Parsons and Sclater, 1977). Because of the high surface temperature on Venus, the lid is probably somewhat thinner on Venus than it is on Earth, but as shown in KH, decreasing the lid thickness by a factor of 2 has only a 5 to 10% effect on the geoid and topography.

Within the mantle, viscosity may vary continuously with depth due to the effect of pressure on rheology and may also undergo discrete jumps at phase transitions. We have parameterized the mantle viscosity into 3 layers of constant viscosity: an asthenosphere from 130 to 400 km depth, an upper mantle layer from 400 to 700 km depth, and a lower mantle from 700 to 2800 km depth. We use this parameterization both for simplicity and to facilitate comparison of our results with the viscosity profile derived by Hager and Clayton (1989) and Hager and Richards (1989) for the Earth. The layer depths at 400 and 700 km correspond approximately to the two major phase transitions known to occur in the mantle. Viscosity model 1 (Figure 6a) has a uniform viscosity mantle. In viscosity model 2 (Figure 6b), the asthenosphere and upper mantle layers have a viscosity of 0.1 times the lower mantle viscosity. In viscosity model 3 (Figure 6c), the asthenosphere viscosity is 0.01 times the lower mantle viscosity. Model 3 is similar to the viscosity profile favored by Hager and Clayton (1989) and Hager and Richards (1989) for the Earth. The main difference is that Hager and colleagues prefer an asthenosphere viscosity which is a factor of 3 less than that used in our viscosity model 3.

The depth-dependence of viscosity is well known to affect both the geoid and the topography associated with convective upwellings and downwellings (e.g., Richards and Hager, 1984; Kiefer et al., 1986a; Robinson et al., 1987; Ceuleener et al., 1988). This is illustrated in Figure 7. The three models shown all have a Rayleigh number of 10^6. Inclusion of a low viscosity asthenosphere prevents convective stresses in the interior from coupling efficiently to the surface. Consequently, the peak topographic uplift is reduced in models with low viscosity layers in the upper mantle. As Figure 7b shows, going from viscosity model 1 to viscosity model 3 decreases the peak uplift by a factor of 2. As we noted above, the geoid anomaly over a plume depends on contributions both from density anomalies at the uplifted surface and from density anomalies associated with temperature anomalies in the plume. These contributions are similar in magnitude but opposite in sign, so small changes in the amplitude of the topographic uplift can lead to large changes in the associated geoid anomaly. In Figure 7a, we see that going from viscosity model 1 to viscosity model 3 changes the peak geoid anomaly by a factor of 7. If the asthenosphere

viscosity were reduced to a value even less than that used in viscosity model 3, the topographic uplift could be reduced to such an extent that the geoid anomaly over the upwelling plume would be negative.

The vigor of convection is controlled by the Rayleigh number,

$$\mathrm{Ra} = \frac{\rho\, g\, \alpha\, \Delta T\, d^3}{\eta\, \kappa}\,, \tag{3}$$

with larger values of Ra indicating more vigorous convection. In equation 3, η is the viscosity and the other variables are identified in Table 1. Because η varies with depth in our models, we have used the lower mantle viscosity to define the value of Ra. This is an appropriate choice because the lower mantle constitutes at least 75% of the volume of our model cylinders. Robinson et al. (1987) and Ceuleneer et al. (1988) used a similar procedure to define Ra in their calculations that used depth-dependent rheology.

Figure 8 shows that increasing Ra causes both the geoid anomaly and the topographic uplift of a plume to decrease. Increasing Ra causes the upwelling plumes and downwelling sheets to become thinner, which in the spectral domain implies that there is an increasing amount of power at short wavelengths. However, short wavelengths do not couple efficiently from the interior to the surface, so that for fixed buoyancy ($\rho g \alpha \Delta T$), the surface uplift produced by a plume must decrease as Ra increases. The thinner upwellings and downwellings and the decreased amount of topographic uplift imply that all of the terms which contribute to the geoid anomaly decrease with increasing Ra. The net result is that the geoid decreases in amplitude as Ra increases.

Comparisons of Models and Observations

In this section, we compare the results of our plume models with observations of geoid anomalies and topography in the Equatorial Highlands of Venus. We focus in turn on each of the four main parts of the Equatorial Highlands, Beta, Atla, Thetis, and Ovda. For each region, we compare our models with North-South and East-West profiles of topography and of geoid anomalies. The topography data was obtained from a digital database that is a part of the

Lunar and Planetary Institute's Geophysical Data Facility. The geoid profiles are based on the Bills et al. (1987) spherical harmonic model. In each figure, the heavy solid line represents the observations and the other lines are our models. The model lines use the same pattern as in Figure 7, with viscosity model 1 using the short-dashed line, viscosity model 2 using the long-dashed line, and viscosity model 3 using the dot-dashed line. These models are all calculated at $Ra = 10^6$. The mantle of Venus probably has a Rayleigh number that is about an order of magnitude larger than this, but because the computational cost is a strongly increasing function of Ra, we have not attempted models larger than $Ra = 10^6$. At the end of this section, we discuss how our conclusions are likely to be affected by a larger Ra.

In studies of terrestrial hotspot swells, it is common practice to filter the long-wavelength geoid by subtracting the spherical harmonic degrees 2 to 10 geoid from the total geoid and then analyzing only the residual geoid. This filtering has sometimes been done using an untapered filter (e.g., McKenzie et al., 1980). In other cases, it has been done using a tapered filter to avoid "ringing" in the spatial domain results (Sandwell and Renkin, 1988). The rationale usually presented for this long-wavelength filtering is that terrestrial hotspot swells are typically less than 2000 km in width and are therefore assumed to be unrelated to geoid anomalies of much longer wavelength. However, Richards et al. (1988) showed that the Earth's degree 2 geoid is strongly correlated with the distribution of hotspots. This correlation may simply mean that both the degree 2 geoid and the distribution of hotspots are controlled by long-wavelength convective structures in the Earth's mantle. However, it seems likely that the thermal structures that produce hotspots must make some contribution to even the very long-wavelength geoid. Therefore, in the following discussion, the geoid anomalies include all of the terms from degree 2 to degree 18 in the Bills et al. (1987) spherical harmonic model. As we will show, our plume models can explain a substantial fraction of the geoid in the the Equatorial Highlands. However, our models should not be expected to explain all of the observed geoid anomalies. For example, regional variations in crustal thickness may arise from volcanic activity, leading to topographic variations. Such variations would also produce some geoid anomalies, although they would be

small if the crust is only a few tens of kilometers thick. More importantly, there are likely to be convective structures within the mantle of Venus that are unrelated to the mantle plumes that we have modeled. These other structures will also contribute to the long-wavelength geoid.

As Figures 7 and 8 show, our models predict that the geoid anomaly and the topographic depression over downwellings will have amplitudes that are about 40% of the amplitudes of the corresponding quantities over the upwellings. The basins surrounding the Equatorial Highlands typically have depths of 1 to 1.5 km below MPR, while the highlands reach elevations of about 4 km above MPR. Similarly, the geoid lows in the flanking basins have smaller amplitudes than the geoid highs in the highlands. These observations are broadly consistent with our model predictions. However, as noted above, the thermal scaling that we use probably underestimates the amplitudes of the geoid and topography in the downwellings. Because of this, in the comparisons that follow, we focus only on the upwelling portion of the model profiles and cut off the comparisons at a distance of about 2000 km from the center of the upwelling.

Beta Regio

Beta Regio rises to a peak elevation of about 4 km above MPR. It is approximately circular in planform, with a North-South size of about 2400 km and an East-West size of about 2200 km (U.S. Geological Survey, 1984). Beta has a peak geoid anomaly of 92 meters (Figure 2). Because of the availability of Arecibo radar imagery, Beta is the best studied of the four main parts of the Equatorial Highlands. Beta contains two distinct topographic peaks, Rhea Mons and Theia Mons, that are separated by about 800 km. On the basis of their dome shaped topography and the presence of lobate, flow-like structures that radiate away from the topographic peaks, Rhea and Theia are generally regarded as shield volcanoes (Campbell et al., 1984, 1989; Stofan et al., 1989).

A major topographic depression, Devana Chasma, runs North-South through Beta and extends southward towards Phoebe Regio. Devana varies in width from 100 km to 300 km and in depth from less than 1 km to more than 2 km. It is generally regarded as a rift zone, perhaps analogous to the East

African rift zone system on Earth (McGill et al., 1981; Schaber, 1982; Campbell et al., 1984; Stofan et al., 1989). Numerous radar bright lineaments exist within Devana and typically parallel the trend of the topographic valley. These lineaments may represent the traces of individual faults or fault zones (Campbell et al., 1984; Stofan et al., 1989). A second topographic valley, Hecate Chasma, runs away from Beta to the southwest, through Asteria Regio, and towards Atla Regio. Hecate may be another rift zone.

In Figure 9, we compare our plume model results with observations of topography (Figure 9a) and geoid anomalies (Figure 9b) in Beta Regio. The East-West profiles are taken along Latitude 28° N, and the North-South profiles are taken along Longitude 283°. The two profiles intersect in the approximate center of Beta. The origin for the horizontal distance scale is the intersection of the two profiles. Figure 9a shows that viscosity model 2 (long-dashed line) gives the best overall fit to Beta's topography. On the East-West profile, the two main discrepancies between viscosity model 2 and the data are near -1000 km and +800 km, where the data falls significantly below the model. These locations correspond to the locations of Hecate Chasma and Devana Chasma. Rifting in these locations may have locally thinned the crust, leading to lower than predicted elevations. On the North-South profile, viscosity model 2 is a good match to the broad shape of topography on the southern part of the profile. Between +250 km and +750 km, the observations are substantially higher than model 2 predicts. This corresponds to the location of Rhea Mons. Volcanic activity at Rhea has presumably produced local thickening of the crust, leading to topography that is higher than predicted by our plume thermal model. Further to the north, the observed topography falls off more rapidly with distance than predicted by any of our models.

Geoid results are shown in Figure 9b. On the East-West profile, viscosity model 2 gives the best fit to the shape of the observed anomaly, but it underestimates the peak geoid amplitude by about 15 meters. Of course, there are a continuum of possible model parameters. For example, the fit between the model and the data could be improved by slightly increasing the upper mantle viscosity, producing a model intermeditate between viscosity models 1 and 2. However, given the simplifying assumptions that have gone into the modeling,

an effort to more precisely "tune" the viscosity model is unwarranted. Model 2 is also clearly the best fit to the North-South geoid profile, although the fit is not as good as on the East-West profile. As was the case for the topography, the data falls off more rapidly to the north than predicted by the model.

Atla Regio

Atla Regio is about 2000 km across and reaches a peak elevation of about 5 km above MPR. It is somewhat less circular in planform than Beta, with the long axis striking Northeast. Atla contains two distinct topographic peaks, Ozza Mons and Maat Mons (U.S. Geological Survey, 1984). These may be volcanic shields analogous to Rhea and Theia Mons in Beta Regio. Atla lies near the intersection of several chasmata, Ganis Chasma, Parga Chasm, and Dali Chasma (Schaber, 1982; U.S. Geological Survey, 1984). These features may be rift zones analogous to Devana Chasma. Atla has not yet been studied with high resolution radar imagery. Magellan imagery will be needed to assess the detailed tectonic and volcanic processes that have operated in Atla. The peak geoid anomaly in Atla is about 120 meters (Figure 2).

Figure 10 compares topography and geoid anomaly data for Atla with our plume model results. The figure format is identical to that used in Figure 9. The East-West profiles are taken along 3° N Latitude, and the North-South profiles are taken along Longitude 198°. On the North-South topography profile (Figure 10a), viscosity model 2 provides the best overall fit, particularly on the southern half of the profile. The broad valley between +250 km and +750 km may be a part of a rift system that connects to Ganis Chasma. The topography highs further north (+1000 to +1500 km) are part of a small, isolated highland structure that might be the result of volcanic activity. On the East-West profile, the observed topography lies significantly above model 2 between 0 and +800 km. This is in the vicinity of Ozza Mons. We assume that volcanic construction contributes to the topography in this area. Further east, near +1500 km, the topography lies about 1 km below our model predictions. This trough is near the intersection of Ganis Chasma and Parga Chasma. On the western side of the profile, between -2000 and -500 km, the observations lie consistently about 1 km below model 2 and actually provide a closer match to

viscosity model 3. However, if we had centered our model profiles 200 to 300 km further east, near Longitude 200 to 201°, then viscosity model 2 would provide a better fit to the profile as a whole. We have chosen to center our models at 198° Longitude because this is the location that best fits the geoid profiles.

Geoid results for Atla Regio are shown in Figures 10b and c. Figure 10b shows that the observed peak geoid anomaly lies half-way between the results for our viscosity models 1 and 2. Although we could adjust the viscosity structure to match the peak amplitude, such intermediate models would not provide a good fit to the overall shape of the geoid profiles. In Figure 10c, we have added a constant offset of 35 meters to our model geoids. We interpret this offset as arising from long-wavelength convective structures within the mantle of Venus that are not included in our aspect ratio 1 models. With the inclusion of this offset, viscosity model 2 provides an extremely good fit to the East-West geoid profile, although the observed profile is slightly narrower than the model. Neither viscosity model 1 nor model 3 can be adjusted to fit the data using just a constant offset. Model 3 is too flat to fit the curvature in the data, while model 1 varies too rapidly with distance to fit the observed profile. The offset model 2 also provides an adequate fit to the North-South geoid profile, although there is some discrepancy on the northern part of the profile. If we had used a slightly sloping offset that dipped to the south, there would be even better agreement between model 2 and the observations.

Thetis Regio

Thetis Regio is about 3000 to 3500 km across in the East-West direction and 2500 to 3000 km across in the North-South direction. Thetis reaches a peak elevation of about 4 km above MPR (U.S. Geological Survey, 1984). The peak geoid anomaly is 73 meters (Figure 2). On the south side of Thetis, the topographic valley Virava Chasma runs approximately East-West and may be a rift structure (Schaber, 1982; U.S. Geological Survey, 1984). In places, Virava is more than 2 km lower than the surrounding terrain (Figure 11a). Unlike Atla and Beta, Thetis does not contain distinct, circular topographic peaks that might be interpreted as shield volcanoes. However, Senske and Head (1989) have reported the presence of several circular radar-bright spots in low

resolution PVO radar images of Thetis Regio. They believed that these features may be volcanic, but a detailed assessment of the morphology of these features must await Magellan imagery.

In Figure 11, we compare our plume models with observations of topography and geoid anomalies in Thetis. The figure format is the same as in Figures 9 and 10. The East-West profiles are taken along 9° South Latitude, and the North-South profiles are taken along 131° Longitude. On the East-West topography profile (Figure 11a), viscosity model 2 provides a good fit to the eastern two-thirds of the profile. On the western end of the profile, from -700 km westward, the observed topography is up to 3 km higher than predicted by model 2 and is even significantly higher than predicted by viscosity model 1. This topographic peak, centered near -1500 km on the East-West profile, might be the result of volcanically thickened crust. This possibility can be addressed using Magellan radar imagery by looking for evidence of volcanic activity in the vicinity of 115° Longitude and 9° South Latitude. An alternative possibility is that the upwelling beneath Thetis is somewhat elongated in the East-West direction, so that the topographic peak near -1500 km would have a significant dynamic uplift component. On the North-South profile, viscosity model 2 provides the best overall fit to the data, although the actual topography is somewhat broader and has a flatter top than the model predicts. The prominent valley in the observed profile near -700 km is Virava Chasma. We assume that rifting in this area has led to local thinning of the crust, producing the low topography.

Figure 11b compares our models with the observed geoid anomaly in Thetis. Although viscosity model 2 provides the best match to the observed peak amplitude, it does not do a good job in reproducing the shapes of the observed profiles. Indeed, on the East-West profile, an offset viscosity model 3 would provide a better match to the total profile. On the North-South profile, model 2 is the best fit to the northern half of the profile, but the fit is not as good as those shown previously for Atla and Beta.

The Thetis geoid anomaly is somewhat broader than the region of high topography, and the peak geoid anomaly is offset to the southeast of the peak

topography. Comparing Figures 1 and 2, we see that Thetis is the only one of the four main Equatorial Highlands for which the peak geoid and the peak topography are noticeably offset. The topography to the south of Thetis is moderately elevated, typically lying between 1 and 1.5 km above MPR (U.S. Geological Survey, 1984). This elevated region extends as much as 2000 km south of Thetis Regio. Two topographic valleys, Artemis Chasma and Quilla Chasma, exist in this area and might be rift zones (Schaber, 1982; U.S. Geological Survey, 1984). The geoid high, topographic elevation, and possible rift zones are all consistent with the possibility that a broad thermal upwelling exists in the region south of Thetis Regio. This upwelling might be distinct from the plume that we have inferred to exist beneath Thetis. Alternatively, the Thetis Regio plume might be embedded within a broader upwelling that extends to the south. Magellan imagery should provide information on the tectonic and volcanic styles of Thetis Regio and the area to the south of Thetis. This data may help to better define the relationships between the convective structures hypothesized here.

Ovda Regio

Ovda Regio is the most elongated part of the Equatorial Highlands. It is 4000 to 4500 km across in the East-West direction and 2000 to 2500 km across in the North-South direction. Ovda reaches a peak elevation of slightly more than 4 km above MPR (U.S. Geological Survey, 1984). The peak geoid anomaly is 35 meters (Figure 2). On the southern side of Ovda, two topographic valleys, Ix Chel Chasma and Kuanja Chasma, might be rift features (Schaber, 1982; U.S. Geological Survey, 1984). Senske and Head (1989) reported the presence of several circular, radar-bright spots in PVO radar imagery. They suggested that these may be volcanic features, although the morphology of these features is not yet well known.

In Figure 12, we compare our plume model results with observations of topography and geoid anomalies in Ovda. The figure format is the same as before, with the North-South profiles taken along 91° Longitude and the East-West profiles taken along 6° South Latitude. Figure 12a shows that viscosity model 2 provides the best match to the peak amplitude of the topography, but

none of the models adequately fit the shapes of the observed profiles. Our assumption of axisymmetry clearly breaks down here, although we nevertheless believe that the axisymmetric models are at least as good an approximation as the alternative two-dimensional model of infinitely long Cartesian sheets.

Figure 12b shows geoid results. In contrast with the three regions analyzed above, viscosity model 3 provides the best fit to the peak amplitude and the overall shape of the geoid anomaly profiles in Ovda. Model 3 is a good fit to much of the East-West profile, except in the eastern-most part of the profile, where the observed anomaly begins to rise into Thetis Regio. Model 3 is also a good fit to the North-South profile, except south of -1000 km, where the data amplitude decreases more rapidly than predicted by the model.

In KH, we showed that a two-dimensional, Cartesian geometry convection model produces geoid anomalies and topographic uplifts that are about a factor of two less than for a cylindrical axisymmetric model using the same model parameters. Given that the topographic planform of Ovda suggests a convective upwelling whose geometry is intermediate between the end member models of axisymmetry and Cartesian geometry, it seems reasonable to believe that the geoid anomaly associated with the upwelling is also intermediate in amplitude between the two end member models. This might partially explain why Ovda's geoid anomaly is so much less than at the other parts of the Equatorial Highlands, but it is unlikely to be a complete explanation. It therefore may be necessary to invoke an asthenospheric viscosity that is lower in the Ovda region than elsewhere in order to explain the observed geoid.

Considerations of the possible effects of time-dependent convection and temperature-dependent rheology may provide an explanation for regional variations in the asthenospheric viscosity. As discussed in KH, our plume models typically reach steady-state, but if temperature-dependent viscosity were included, the thermal structures might be time-dependent. Such time-dependence might take the form of hot blobs of material that travel up the plume as solitary waves (Olson et al., 1987; Schubert et al., 1989). When such a blob is discharged from the plume, it should spread laterally at the base of the thermal boundary layer. The sudden addition of a large volume of hot material

to the asthenosphere could produce a local decrease in the asthenosphere's viscosity. This could decrease the geoid anomaly associated with the plume. If such a blob has recently ascended the Ovda plume, it could explain the relatively low amplitude geoid anomaly observed in Ovda.

However, decreasing the asthenosphere's viscosity also decreases the topographic uplift of a plume (Figure 7b), so we must find another mechanism for producing the observed topography. If a large, hot blob has recently reached the near-surface in Ovda, we can reasonably expect that this hot material will produce an enhanced rate of volcanic activity. Volcanic construction might therefore play a significant role in producing the observed topography in Ovda. Assuming that the volcanically-induced crustal thickening is Airy compensated at shallow depths, it could produce several kilometers of topographic relief with little effect on the long-wavelength geoid. If this hypothesis is correct, then we would expect to find evidence for recent volcanic activity in Magellan imagery of Ovda Regio. On the other hand, if Magellan imagery shows that Ovda is old, with many impact craters and little or no recent volcanic activity, then the time-dependent hot blob model would not be a viable explanation for Ovda's geoid and topography.

Scaling Model Results to Larger Ra

In the foregoing discussion, we compared observations with models calculated at a Rayleigh number of 10^6. In this section, we examine how our conclusions would be affected by other choices of Ra. The main results described in this section are summarized in Table 2, where we show results for the peak geoid anomaly and peak topographic uplift for our three viscosity models at four different values of Ra. Table 2 also includes results for the Nusselt number, Nu, which is a dimensionless measure of the heat transporting ability of a convective structure. We calculate Nu using the volume-averaging technique of Ho-Liu et al. (1987). In Table 2, the results for $Ra = 10^6$ are based on the finite element calculations shown in Figure 7. The results for larger values of Ra are based on power-law projections of the form $f(Ra) = a \cdot (Ra)^b$, where f(Ra) is geoid, topography, or Nu, and a and b are power law parameters given in Table 3 of KH.

Hager (1989; see also discussion in KH) estimated that a lower mantle viscosity of $3 \cdot 10^{22}$ Poise is consistent with both the Earth's overall heat flow and the observed plate velocities. Assuming whole mantle convection, this choice of lower mantle viscosity implies a Rayleigh number of about $7 \cdot 10^6$. For the Earth-like viscosity model 3, our calculations imply a Nusselt number for the Earth of about 15, which is consistent with the observed average thickness of oceanic plates.

In comparing models for Venus and Earth, we follow Solomon and Head (1982) in assuming that the two planets have similar heat sources per unit mass and hence similar total heat flows. Because we have defined the Rayleigh number in terms of the lower mantle viscosity rather than a vertically-averaged viscosity, for fixed Ra the various viscosity models will have different values of Nu. Our assumption of similar heat flows is equivalent to assuming that Earth and Venus have similar Nu. This statement implicitly assumes that essentially all of Venus's heat flow comes from sources in the mantle and core. If radioactive elements were strongly concentrated into the crust of Venus, as suggested by Turcotte (1989b), then the heat flow out of the mantle of Venus could be much less than out of Earth's mantle, and yet the two planets could have similar total heat flows. In this case, Nu could be less on Venus than on Earth. However, given the available data on the radioactive element concentrations obtained by Soviet landers (Surkov et al., 1984, 1986, 1987) and estimates that the crust on Venus is typically less than 30 km thick (Zuber, 1987; Banerdt and Golombek, 1988; Grimm and Solomon, 1988; Zuber and Parmentier, 1990; Kiefer and Hager, 1990b), it seems likely that the contribution of crustal heat sources to the total heat flow is small. For example, in the thermal models of Kiefer and Hager (1990b; Chapter 4), the crust typically contributes less than 10 mW m^{-2}, which is less than 14% of Solomon and Head's (1982) estimate of 74 mW m^{-2} for the globally averaged heat flow on Venus. We therefore believe that it is reasonable to assume that Earth and Venus have comparable Nusselt numbers.

As Figures 9 to 12 show, viscosity model 2 at $Ra = 10^6$ provides a generally satisfactory explanation for the geoid and topography of the Equatorial Highlands. However, Table 2 shows that this model has a Nusselt number of

slightly less than 10, which on the basis of the preceding discussion is probably too small for Venus. Our results imply that viscosity model 3 can be excluded as a model for the mantle of Venus. Even at the rather low Ra of 10^5, corresponding to Nu = 7.5, we find a peak geoid anomaly of only 33 meters for viscosity model 3, less than half that observed at Atla, Beta, and Thetis.

On the other hand, for viscosity model 1 in the range of Ra between 10^7 and $3 \cdot 10^7$, we predict peak geoid anomalies of 70 to 90 meters and peak topographic uplifts of 3 to 3.5 km. The predicted Nu is 14 to 17, which overlaps our estimate of Earth's Nu. These results show that much of the geoid and topography observed in the Equatorial Highlands could be the result of uplift by mantle plumes. Although viscosity model 1 assumes that the mantle of Venus is isoviscous, it may also be possible to satisfy the observations with a viscosity model in which the upper mantle is a factor of several less viscous than the lower mantle.

Although the peak amplitudes of the geoid and topography are strong functions of Ra, the shapes of the model profiles depend only weakly on Ra. This can be quantified by considering the full width at half maximum (FWHM) of the model curves. For viscosity model 2 at $Ra = 10^6$, we find FWHM of 1800 km for the geoid profile and 1500 km for the topography profile. For comparison, a power-law projection of viscosity model 1 to $Ra = 10^7$ gives FWHM of 1600 km for the geoid and 1400 km for the topography. Thus, these two models differ in width by only 7 to 11%. Because of this, we believe that the viscosity model 2 results in Figures 9 to 12 provide a good estimate of how viscosity model 1 at $Ra = 10^7$ would fit the overall shapes of the observed geoid and topography profiles.

Discussion of Inferred Viscosity Profile

The foregoing discussion shows that a nearly isoviscous mantle is consistent with observations of the geoid and topography in the Equatorial Highlands. In this section, we show that such a viscosity model is also consistent with the long-wavelength admittance spectrum of Venus, as well as with the

slope of the geoid spectrum. In contrast, a model similar to viscosity model 3 has been shown to be consistent with the Earth's long-wavelength geoid (Hager and Richards, 1989; Hager and Clayton, 1989) and with the geoid and topography observed at terrestrial hotspot swells (Richards et al., 1988; KH). We discuss possible reasons for the differences in the viscosity profiles of Venus and Earth at the end of this section.

The Long-Wavelength Admittance Spectrum

Kiefer et al. (1986a) developed a model for the long-wavelength admittance spectrum of Venus and concluded that in order to fit the observed admittance spectrum, Venus could not have a low-viscosity asthenosphere. Subsequently, we showed that our original model had to be modified in two ways. First, all of the model admittance results in Figure 3 of Kiefer et al. (1986a) need to be multiplied by a factor of 3.3 (Bills, Kiefer, and Jones, 1987). This has the effect of allowing models in which the upper mantle viscosity is a factor of a few less than the lower mantle viscosity to satisfy the observed admittances.

A more important issue concerns the density contrast model used in these calculations. In the work of Kiefer et al. (1986a), we did not solve the energy equation to determine a thermal structure. Rather, we assumed *a priori* that the density contrasts associated with convection were independent of depth. This is a reasonable first approximation to the pipe-like structure of a mantle plume, but it neglects the structure of thermal boundary layers. With this assumption, we solved the incompressible equations of motion using the propagator matrix technique of Richards and Hager (1984). From the resulting flow field, we calculated the dynamic topographic uplift and geoid anomalies, and hence the admittance, as a function of spherical harmonic degree.

As shown by Jarvis and Peltier (1986) and Kiefer et al. (1986b), the thermal boundary layers have a spectrum that is dominated by the longest wavelengths, whereas within the interior of the convecting layer, the spectrum of the plume thermal structure has power distributed over many wavelengths. A correct parameterization of the boundary layer structure is important, because the upper thermal boundary layer makes a significant contribution to the dynamic topography but virtually no contribution to the long-wavelength

geoid. A precise analytic treatment of how this affects the model admittances is quantitatively difficult, but the general effect is to cause some flattening of the model curves at the lowest harmonic degrees.

In spite of these difficulties, the general conclusion of Kiefer et al. (1986a) about the viscosity profile of Venus is correct. As shown in Figure 3 of Kiefer et al. (1986a), Venus has an admittance spectrum that is positive at all resolved wavelengths, whereas a model using the Earth viscosity profile of Hager and Richards (1989) produces a band of negative admittances centered near degree 6. There are good reasons for believing that Earth has a negative admittance in this wavelength band. At spherical harmonic degrees 4 to 9, the Earth's geoid is dominated by positive geoid anomalies over subduction zones (e.g., Hager, 1984). As downwelling structures, subducting slabs should produce negative dynamic topography, which Hager and Clayton (1989) estimated to be about 400 meters in peak amplitude. Back-arc basins in the western Pacific are observed to be deeper than expected based on their age (Sclater et al., 1976; Watanbe et al., 1977), which is consistent with the expectation of negative dynamic topography. The combination of positive geoid anomalies and negative dynamic topography implies that the Earth's admittance is negative for degrees 4 to 9, consistent with the Earth model prediction of Kiefer et al. (1986a). The observation that the admittance spectrum of Venus is positive in this same wavelength range requires that Venus can not have an Earth-like, low viscosity zone in its asthenosphere and upper mantle. This supports the conclusion reached above based on our modeling of individual parts of the Equatorial Highlands of Venus.

Phillips (1990) has also recently concluded that Venus lacks a low viscosity asthenosphere. Phillips presented his results in terms of apparent compensation depth, but this quantity is interchangeable with the admittance used by Kiefer et al. (1986a). The work of Phillips therefore supports our previously presented conclusions about the viscosity profile of Venus (Kiefer et al., 1986a; Kiefer and Hager, 1988).

The Geoid Spectral Slope

A compact way to describe the magnitude of the geoid as a function of wavelength is to use the rms amplitude, σ_L, defined as

$$\sigma_L = \left(\frac{\sum_{M=0}^{L} (C_{LM}^2 + S_{LM}^2)}{2L+1} \right)^{0.5} . \quad (4)$$

In equation 4, C_{LM} and S_{LM} are the cosine and sine coefficients at harmonic degree L and order M. As shown in Figure 13, the long-wavelength rms geoid spectrum for Venus can be approximated by a power law of the form $\sigma_L \approx A \cdot L^{-1.5}$, where A is a constant. The power law fit shown in Figure 13 is based on spherical harmonic degrees 3 to 14. Degree 2 is omitted from the analysis because it is significantly depressed relative to the trend of the higher harmonics. Degrees 15 to 18 are omitted because of the possible effects of aliasing at these wavelengths (Bills et al., 1987). In contrast with Venus, the Earth's geoid spectrum is a somewhat steeper function of wavelength, with σ_L decaying as approximately $L^{-2.2}$ (Figure 14).

We believe that the different spectral slopes of the two planets may be related to their different viscosity profiles. At the longest wavelengths, the flow pattern essentially averages over the entire depth of the mantle and is not strongly sensitive to the presence of a shallow low-viscosity zone. Thus, at very long wavelengths, the geoid amplitudes should be comparable on Venus and Earth. Indeed, there is good agreement in the values of σ_L at degrees 3 and 4, although at degree 2, σ_L for Venus is only 40% of its terrestrial value. As one goes to increasingly higher harmonic degrees, or shorter wavelengths, the influence of a low viscosity asthenosphere will be felt more strongly by the flow field. As shown earlier, a low viscosity zone causes the geoid amplitude to decrease, so with increasing harmonic degree, the Earth's spectrum should increasingly fall below the geoid spectrum of Venus, as is observed. Although qualitative, we believe that this argument can help explain the difference in the spectral slopes of the two planets and further supports the claim that Venus lacks a low viscosity asthenosphere.

Comparison of the Viscosity Profiles of Venus and Earth

Based on the preceding discussion, it seems likely that Venus and Earth have significantly different mantle viscosity profiles, with Venus lacking the low viscosity asthenosphere that characterizes Earth. Although inclusion of effects such as temperature-dependent or stress-dependent rheology may alter our conclusions about the absolute viscosity profiles of the two planets, our conclusions about the relative differences between the two planets are probably robust.

The lack of a low viscosity zone on Venus may be a result of the mantle of Venus being drier than Earth's mantle. The possible importance of water in determining the rheology of Venus was first emphasized by Weertman (1979) in a discussion of viscous crustal flow. Chopra and Paterson (1981, 1984) and Karato et al. (1986) have shown that the presence of water in olivine rich materials substantially weakens the rheology in comparison with dry materials. Comparisons of laboratory data with our viscosity models is somewhat difficult, because the lab results are typically non-Newtonian (stress dependent), whereas our models use Newtonian rheology for computational simplicity. However, for a fixed differential stress level, the strain rates of "wet" samples are typically one to two orders of magnitude higher than for dry samples. This implies that the presence of water lowers the effective Newtonian viscosity by 1 to 2 orders of magnitude. As in all laboratory rheology studies, the strain rates used by Chopra and Paterson and by Karato et al. are about 10 orders of magnitude larger than the strain rates likely to characterize the mantles of Venus and Earth. We assume, however, that some water weakening of rheology will also occur at lower strain rates.

Chopra and Paterson (1984) estimated that only 100 ppm of water is necessary in order for the viscosity of dunite to be substantially altered by the water. Michael (1988) estimated that the Earth's upper mantle water content is between 100 and 450 ppm. This suggests that the Earth's mantle viscosity profile may be significantly affected by the presence of water. If the mantle of Venus is much drier than Earth's mantle, then the absence of a water weakening mechanism on Venus could explain the inferred lack of an upper mantle low viscosity zone. However, we do not rule out the possibility that other

mechanisms may contribute to the observed differences in the viscosity profiles of Venus and Earth.

One way that Venus's mantle could presently be dry is if Venus never accreted significant amounts of water from the solar nebula, as in the equilibrium condensation model of Lewis and Prinn (1984, Table 4.6). The likelihood of radial mixing in the solar nebula (Wetherill, 1986) implies that Venus should have accreted at least some water, although the initial water budgets of Earth and Venus need not have been the same.

Even if Venus and Earth initially accreted comparable amounts of water, the upper mantle of Venus could now be drier than Earth's upper mantle if Venus has lost water over geologic time. One possibility, proposed by Kaula (1990), is that water has been drained into the lower mantle of Venus. However, it is not obvious why this same process did not occur on Earth. An alternative possibility is that Venus has lost water to space. On Earth, water that is outgassed from the mantle can be bound into hydrous minerals and returned to the mantle at subduction zones. Because of the high surface temperature on Venus, the formation of hydrous minerals is inhibited (Nozette and Lewis, 1982). Outgassed water should therefore enter the atmosphere, where it can be photochemically dissociated. The hydrogen will escape to space, producing a permanent loss of water. If Venus had a hot, greenhouse atmosphere for most of its history, this process could have caused it to lose most of its initial water budget. The Pioneer Venus entry probe determined that the deuterium to hydrogen ratio (D/H) in the atmosphere of Venus is about 100 times the terrestrial value (Donahue et al., 1982). This result is consistent with the loss of substantial water from Venus, although Grinspoon (1987) argued that other interpretations of the D/H ratio are also possible. Assuming that the high D/H ratio on Venus is due to isotopic fractionation during escape of hydrogen to space, Donahue et al. (1982) estimated a minimum water loss that is equivalent to 0.3% of a terrestrial ocean mass. However, they also concluded that it would be "astonishing" if the water loss were not considerably larger than this lower limit, and suggested that the equivalent of a terrestrial ocean could have been lost. Hunten et al. (1989) concluded that Venus may have lost several ocean masses of water without violating the D/H ratio constraint. These results

suggest that loss of water may play a significant role in explaining the lack of an asthenosphere on Venus.

Summary and Conclusions

The four main parts of the Equatorial Highlands, Atla, Beta, Ovda, and Thetis Regiones, are each quasi-circular in planform, with characteristic horizontal sizes of 2000 to 3000 km, and reach peak elevations of 4 to 5 km above the mean planetary radius. These highland units are associated with large, positive geoid anomalies and with topographic valleys that are believed to be rift zones. Shield volcanoes have been documented in Beta Regio.

Although Airy-compensated crustal thickness variations can contribute to the high topography of the Equatorial Highlands, the average crustal thickness would have to be implausibly large in order for crustal thickness variations to be the dominant source of the observed geoid. Spreading centers have been proposed to exist in Ovda and Thetis, but presently available data do not necessarily require the existence of spreading centers in these areas. Even if spreading centers do exist in Ovda and Thetis, a cooling plate thermal model shows that no more than 20 to 30% of the observed topography and geoid could be related to the spreading centers. The large amplitudes of the geoid anomalies observed in the Equatorial Highlands requires the presence of substantial density anomalies within the convecting mantle.

In this paper, we consider the possibility that the Equatorial Highlands are the surface expressions of hot, upwelling mantle plumes. We have developed a series of mantle plume models using a cylindrical, axisymmetric finite element code and depth-dependent, Newtonian rheology. We scale our results by assuming whole mantle convection and that Venus and Earth have similar mantle heat flows. In order for the plume model to explain the observed geoid and topography in the Equatorial Highlands, we favor a model in which the Rayleigh number is about 10^7 and the viscosity of the asthenosphere and upper mantle is no more than a factor of a few less than the viscosity of the lower mantle. Our best model fits are for Beta Regio and Atla Regio. Mantle plumes

may also play significant roles in Thetis Regio and Ovda Regio, but the required models are more complicated than for Beta and Atla.

The shape of Venus's long-wavelength admittance spectrum and the slope of its geoid spectrum are both consistent with the lack of a low viscosity zone in the upper mantle of Venus. In contrast, models of the Earth's long-wavelength geoid require a substantial upper mantle low viscosity zone. The lack of an asthenosphere on Venus may be due to the mantle of Venus being drier than the Earth's mantle.

References

Banerdt, W.B., Support of Long-Wavelength Loads on Venus and Implications for Internal Structure, *J. Geophys. Res., 91,* 403-419, 1986.

Banerdt, W.B., and M.P. Golombek, Deformational Models of Rifting and Folding on Venus, *J. Geophys. Res., 93,* 4759-4772, 1988.

Baumgardner, J.R., Application of Supercomputers to 3-D Mantle Convection, in *The Physics of the Planets,* edited by S.K. Runcorn, pp. 199-231, John Wiley and Sons, New York, 1988.

Bercovici, D., G. Schubert, and G.A. Glatzmaier, Three-Dimensional Spherical Models of Convection in the Earth's Mantle, *Science, 244,* 950-955, 1989.

Bills, B.G., W.S. Kiefer, and R.L. Jones, Venus Gravity: A Harmonic Analysis, *J. Geophys. Res., 92,* 10,335-10,351, 1987.

Bills, B.G., and M. Kobrick, Venus Topography: A Harmonic Analysis, *J. Geophys. Res., 90,* 827-836, 1985.

Bindschadler, D.L., and E.M. Parmentier, Mantle Flow Tectonics and a Weak Lower Crust: Implications for Formation of Large-scale Features on Venus (abstract), *Lunar and Planetary Science, 20,* 78-79, 1989.

Black, M.T., M.T. Zuber, and D.C. McAdoo, Comparison of Observed and Predicted Gravity Profiles over Aphrodite Terra, Venus, submitted to *J. Geophys. Res.,* 1990.

Campbell, D.B., J.W. Head, J.K. Harmon, and A.A. Hine, Venus: Volcanism and Rift Formation in Beta Regio, *Science, 226,* 167-170, 1984.

Campbell, D.B., J.W. Head, A.A. Hine, J.K. Harmon, D.A. Senske, and P.C. Fisher, Styles of Volcanism on Venus: New Arecibo High Resolution Radar Data, *Science, 246,* 373-377, 1989.

Ceuleneer, G., M. Rabinowicz, M. Monnereau, A. Cazenave, and C. Rosemberg, Viscosity and Thickness of the Sub-Lithospheric Low-Viscosity Zone: Constraints from Geoid and Depth over Oceanic Swells, *Earth Planet. Sci. Lett., 89,* 84-102, 1988.

Chopra, P.N., and M.S. Paterson, The Experimental Deformation of Dunite, *Tectonophysics, 78,* 453-473, 1981.

Chopra, P.N., and M.S. Paterson, The Role of Water in the Deformation of Dunite, *J. Geophys. Res., 89,* 7861-7876, 1984.

Courtney, R.C., and R.S. White, Anomalous Heat Flow and Geoid Across the Cape Verde Rise: Evidence for Dynamic Support from a Thermal Plume in the Mantle, *Geophys. J. R. Astr. Soc., 87,* 815-867, 1986.

Crisp, J.A., Rates of Magma Emplacement and Volcanic Output, *J. Volcanol. Geotherm. Res., 20,* 177-211, 1984.

Crumpler, L.S., J.W. Head, and J.K. Harmon, Regional Linear Cross-Strike Discontinuities in Western Aphrodite Terra, Venus, *Geophys. Res. Lett., 14,* 607-610, 1987.

Crumpler, L.S., and J.W. Head, Bilateral Topographic Symmetry Patterns Across Aphrodite Terra, Venus, *J. Geophys. Res., 93,* 301-312, 1988a.

Crumpler, L.S., and J.W. Head, Split and Separated Topography on Earth's Seafloor: A Comparison to Bilateral Symmetry in Aphrodite Terra, Venus

(abstract), *Lunar and Planetary Science, 19,* 235-236, 1988b.

Daly, S.F., and A. Raefsky, On the Penetration of a Hot Diapir Through a Strongly Temperature-Dependent Viscosity Medium, *Geophys. J. R. Astr. Soc., 83,* 657-681, 1985.

Donahue, T.M., J.H. Hoffman, R.R. Hodges, and A.J. Watson, Venus was Wet: A Measurement of the Ratio of Deuterium to Hydrogen, *Science, 216,* 630-633, 1982.

Esposito, P.B., W.L. Sjogren, N.A. Mottinger, B.G. Bills, and E. Abbott, Venus Gravity: Analysis of Beta Regio, *Icarus, 51,* 448-459, 1982.

Glatzmaier, G.A., Numerical Simulations of Mantle Convection: Time-Dependent, Three-Dimensional, Compressible, Spherical Shell, *Geophys. Astrophys. Fluid Dynamics, 43,* 223-264, 1988.

Grimm, R.E., and S.C. Solomon, Limits on Modes of Lithospheric Heat Transport on Venus from Impact Crater Density, *Geophys. Res. Lett., 14,* 538-541, 1987.

Grimm, R.E., and S.C. Solomon, Viscous Relaxation of Impact Crater Relief on Venus: Constraints on Crustal Thickness and Thermal Gradient, *J. Geophys. Res., 93,* 11,911-11,929, 1988.

Grimm, R.E., and S.C. Solomon, Tests of Crustal Divergence Models for Aphrodite Terra, Venus, *J. Geophys. Res., 94,* 12,103-12,131, 1989.

Grinspoon, D.H., Was Venus Wet? Deuterium Reconsidered, *Science, 238,* 1702-1704, 1987.

Hager, B.H., Subducted Slabs and the Geoid: Constraints on Mantle Rheology and Flow, *J. Geophys. Res., 89,* 6003-6015, 1984.

Hager, B.H., Dynamics and Constitution of the Earth's Interior (abstract), *EOS, 70,* 1334, 1989.

Hager, B.H., and R.W. Clayton, Constraints on the Structure of Mantle Convection Using Seismic Observations, Flow Models, and the Geoid, in *Mantle Convection: Plate Tectonics and Global Dynamics* , edited by W.R. Peltier, Gordon and Breach, New York, pp. 657-763, 1989.

Hager, B.H., and M.A. Richards, Long-Wavelength Variations in Earth's Geoid: Physical Models and Dynamical Implications, *Phil. Trans. R. Soc. London A, 328,* 309-327, 1989.

Head, J.W., and L.S. Crumpler, Evidence for Divergent Plate-Boundary Characteristics and Crustal Spreading on Venus, *Science, 238,* 1380-1385, 1987.

Head, J.W., and L.S. Crumpler, Divergent Plate Boundary Characteristics and Crustal Spreading in Aphrodite Terra, Venus: A Test of Some Predictions, *Earth, Moon, and Planets, 44,* 219-231, 1989.

Herrick, R.R., B.G. Bills, and S.A. Hall, Variations in Effective Compensation Depth Across Aphrodite Terra, Venus, *Geophys. Res. Lett., 16,* 543-546, 1988.

Ho-Liu, P., B.H. Hager, and A. Raefsky, An Improved Method of Nusselt Number Calculation, *Geophys. J. R. Astr. Soc., 88,* 205-215, 1987.

Hunten, D.M., T.M. Donahue, J.C.G. Walker, and J.F. Kasting, Escape of Atmospheres and Loss of Water, in *Origin and Evolution of Planetary and Satellite Atmospheres,* edited by S.K. Atreya, J.B. Pollack, and M.S. Matthews, Univ. of Arizona Press, Tucson, pp. 386-422, 1989.

Jarvis, G.T., and W.R. Peltier, Lateral Heterogeneity in the Convecting Mantle, *J. Geophys. Res., 91,* 435-451, 1986.

Karato, S., M.S. Paterson, and J.D. Fitzgerald, Rheology of Synthetic Olivine Aggregates: Influence of Grain Size and Water, *J. Geophys. Res., 91,* 8151-8176, 1986.

Kaula, W.M., Venus: A Contrast in Evolution to Earth, *Science, 247,* 1191-1196, 1990.

Kaula, W.M., and R.J. Phillips, Quantitative Tests for Plate Tectonics on Venus, *Geophys. Res. Lett., 8,* 1187-1190, 1980.

Kiefer, W.S., A Reexamination of the Spreading Center Hypothesis for Ovda and Thetis Regiones, Venus, submitted to *Geophys. Res. Lett.,* 1990.

Kiefer, W.S., and B.G. Bills, Atla and Beta: Gravity Models of Venusian Volcanic Provinces (abstract), *EOS, 65,* 982, 1984.

Kiefer, W.S., M.A. Richards, B.H. Hager, and B.G. Bills, A Dynamic Model of Venus's Gravity Field, *Geophys. Res. Lett., 13,* 14-17, 1986a.

Kiefer, W.S., B.H. Hager, M.A. Richards, and B.G. Bills, Mantle Convection and Venus's Long-Wavelength Geoid (abstract), *EOS, 67,* 1194, 1986b.

Kiefer, W.S., and B.H. Hager, Mantle Plumes on Venus: A Model for the Equatorial Highlands and a Possible Connection with the Ovoids (abstract), *Lunar and Planetary Science, 19,* 601-602, 1988.

Kiefer, W.S., and B.H. Hager, Geoid Anomalies and Dynamic Topography from Convection in Cylindrical Geometry: Applications to Mantle Plumes on Earth and Venus, manuscript to be submitted to *Geophysical Journal,* 1990a.

Kiefer, W.S., and B.H. Hager, Mantle Downwelling and Crustal Convergence: A Model for Ishtar Terra, Venus, submitted to *J. Geophys. Res.,* 1990b.

Lerch, F.J., S.M. Klosko, G.B. Patel, and C.A. Wagner, A Gravity Model for Crustal Dynamics (GEM-L2), *J. Geophys. Res., 90,* 90, 9301-9311, 1985.

Lewis, J.S., and R.G. Prinn, *Planets and their Atmospheres: Origin and Evolution,* Academic Press, Orlando, Florida, 1984.

Machetel, P., M. Rabinowicz, and P. Bernardet, Three-Dimensional Convection in Spherical Shells, *Geophys. Astrophys. Fluid Dynamics, 37,* 57-84, 1986.

Masursky, H., E. Eliason, P.G. Ford, G.E. McGill, G.H. Pettengill, G.G. Schaber, and G. Schubert, Pioneer Venus Radar Results: Geology from Images and Altimetry, *J. Geophys. Res., 85,* 8232-8260, 1980.

McGill, G.E., S.J. Steenstrup, C. Barton, and P.G. Ford, Continental Rifting and the Origin of Beta Regio, Venus, *Geophys. Res. Lett., 8,* 737-740, 1981.

McKenzie, D., A. Watts, B. Parsons, and M. Roufosse, Planform of Mantle Convection Beneath the Pacific Ocean, *Nature, 288,* 442-446, 1980.

Michael, P.J., The Concentration, Behavior, and Storage of H_2O in the Suboceanic Upper Mantle: Implications for Mantle Metasomatism, *Geochimica et Cosmochimica Acta, 52,* 555-566, 1988.

Morgan, P., and R.J. Phillips, Hot Spot Heat Transfer: Its Application to Venus and Implications to Venus and Earth, *J. Geophys. Res., 88,* 8305-8317, 1983.

Nozette, S., and J.S. Lewis, Venus: Chemical Weathering of Igneous Rocks and Buffering of Atmospheric Composition, *Science, 216,* 181-183, 1982.

Olson, P., G. Schubert, and C. Anderson, Plume Formation in the D"-Layer and the Roughness of the Core-Mantle Boundary, *Nature, 327,* 409-413, 1987.

Parsons, B., and J.G. Sclater, An Analysis of the Variation of Ocean Floor Bathymetry and Heat Flow with Age, *J. Geophys. Res., 82, 803-827, 1977.*

Pettengill, G.H., E. Eliason, P.G. Ford, G.B. Loriot, H. Masursky, and G.E. McGill, Pioneer Venus Radar Results: Altimetry and Surface Properties, *J. Geophys. Res., 85,* 8261-8270, 1980.

Phillips, R.J., Convection-Driven Tectonics on Venus, *J. Geophys. Res., 95,* 1301-1316, 1990.

Phillips, R.J., and M.C. Malin, The Interior of Venus and Tectonic Implications, in *Venus,* edited by D.M Hunten, L. Colin, T.M. Donahue, and V.I. Moroz, pp. 159-214, Univ. of Arizona Press, Tucson, 1983.

Richards, M.A., and B.H. Hager, Geoid Anomalies in a Dynamic Earth, *J. Geophys. Res., 89,* 5987-6002, 1984.

Richards, M.A., and B.H. Hager, The Earth's Geoid and the Large-Scale Structure of Mantle Convection, in *The Physics of the Planets,* edited by S.K. Runcorn, pp. 247-272, John Wiley and Sons, New York, 1988.

Richards, M.A., B.H. Hager, and N.H. Sleep, Dynamically Supported Geoid Highs over Hotspots: Observation and Theory, *J. Geophys. Res., 93,* 7690-7708, 1988.

Robinson, E.M., B. Parsons, and S.F. Daly, The Effect of a Shallow Low Viscosity Zone on the Apparent Compensation of Mid-Plate Swells, *Earth Planet. Sci. Lett., 82,* 335-348, 1987.

Robinson, E.M., and B. Parsons, Effect of a Shallow Low-Viscosity Zone on the Formation of Midplate Swells, *J. Geophys. Res., 93,* 3144-3156, 1988.

Sandwell, D.T., and M.L. Renkin, Compensation of Swells and Plateaus in the North Pacific: No Direct Evidence for Mantle Convection, *J. Geophys. Res., 93,* 2775-2783, 1988.

Schaber, G.G., Venus: Limited Extension and Volcanism along Zones of Lithospheric Weakness, *Geophys. Res. Lett., 9,* 499-502, 1982.

Schubert, G., P. Olson, C. Anderson, and P. Goldman, Solitary Waves in Mantle Plumes, *J. Geophys. Res., 94,* 9523-9532, 1989.

Sclater, J.G., D. Karig, L.A. Lawver, and K. Louden, Heat Flow, Depth, and Crustal Thickness of the Marginal Basins of the South Philippine Sea, *J. Geophys. Res., 81,* 309-318, 1976.

Senske, D.A., and J.W. Head, Venus Equatorial Geologic Units (abstract), *Lunar and Planetary Science, 20,* 986-987, 1989.

Sjogren, W.L., R.J. Phillips, P.W. Birkeland, and R.N. Wimberly, Gravity Anomalies on Venus, *J. Geophys. Res., 85,* 8295-8302, 1980.

Sleep, N.H., Hotspots and Mantle Plumes: Some Phenomenology, *J. Geophys. Res., 95,* 6715-6736, 1990.

Solomon, S.C., and J.W. Head, Mechanisms for Lithospheric Heat Transport on Venus: Implications for Tectonic Style and Volcanism, *J. Geophys. Res., 87,* 9236-9246, 1982.

Sotin, C., D.A. Senske, J.W. Head, and E.M. Parmentier, Terrestrial Spreading Centers Under Venus Conditions: Evaluation of a Crustal Spreading Model for Western Aphrodite Terra, *Earth and Planetary Sci. Lett., 95,* 321-333, 1989.

Stofan, E.R., J.W. Head, D.B. Campbell, S.H. Zisk, A.F. Bogomolov, O.N. Rzhiga, A.T. Basilevsky, and N. Armand, Geology of a Rift Zone on Venus: Beta Regio and Devana Chasma, *Geol. Soc. Am. Bull., 101,* 143-156, 1989.

Surkov, Y.A., V.L. Barsukov, L.P. Moskalyeva, V.P. Kharyukova, and A.L. Kemurdzhian, New Data on the Composition, Structure, and Properties of Venus Rock Obtained by Venera 13 and Venera 14, *Proc. Lunar Planetary Sci. Conf. 14, J. Geophys. Res. (supplement), 89,* B393-B402, 1984.

Surkov, Y.A., L.P. Moskalyova, V.P. Kharyukova, A.D. Dudin, G.G. Smirnov, and S.Y. Zaitseva, Venus Rock Composition at the Vega 2 Landing Site, *Proc. Lunar Planetary Sci. Conf. 17, J. Geophys. Res. (supplement), 91,* E215-E218, 1986.

Surkov, Y.A., F.F. Kirnozov, V.N. Glazov, A.G. Dunchenko, L.P. Tatsy, and O.P. Sobornov, Uranium, Thorium, and Potassium in the Venusian Rocks at the Landing Sites of Vega 1 and 2, *Proc. Lunar Planetary Sci. Conf. 17, J. Geophys. Res., 92,* E537-E540, 1987.

Turcotte, D.L., A Heat Pipe Mechanism for Volcanism and Tectonics on Venus, *J. Geophys. Res., 94,* 2779-2785, 1989a.

Turcotte, D.L., Thermal Evolution of Mars and Venus Including Irreversible Fractionation (abstract), *Lunar and Planetary Science, 20,* 1138-1139, 1989b.

U. S. Geological Survey, *Altimetric and Shaded Relief Map of Venus,* Miscellaneous Investigations Series Map I-1324, 1981.

U. S. Geological Survey, *Topographic and Shaded Relief Maps of Venus,* Miscellaneous Investigations Series Map I-1562, 1984.

Watanbe, T., M.G. Langseth, and R.N. Anderson, Heat Flow in Back-Arc Basins of the Western Pacific, in *Island Arcs, Deep Sea Trenches, and Back-Arc Basins,* edited by M. Talwani and W.C Pitman, pp. 137-161, American Geophysical Union, Washington D.C., 1977.

Weertman, J., Height of Mountains on Venus and the Creep Properties of Rock, *Phys. Earth Planet. Int., 19,* 197-207, 1979.

Wetherill, G., Accumulation of the Terrestrial Planets and Implications Concerning Lunar Origin, in *Origin of the Moon,* edited by W.K. Hartmann, R.J. Phillips, and G.J. Taylor, pp. 519-550, 1986.

Zuber, M.T., Constraints on the Lithospheric Structure of Venus from Mechanical Models and Tectonic Surface Features, *Proc. Lunar Planetary Sci. Conf. 17, J. Geophys. Res. (supplement), 92,* E541-E551, 1987.

Zuber, M.T., and E.M. Parmentier, On the Relationship between Isostatic Elevation and the Wavelengths of Tectonic Surface Features on Venus, *Icarus, 85,* 290-308, 1990.

Table 1. Scaling Parameters

ρ_m	Mantle Density	3.3 gm cm^{-3}
g	Gravitational Acceleration	887 cm s^{-2}
α	Thermal Expansion Coefficient	$3 \cdot 10^{-5}$ $°C^{-1}$
ΔT	Vertical Temperature Contrast	1000 °C
d	Depth of Convecting Layer	2800 km
κ	Thermal Diffusivity	10^{-2} cm^2 sec^{-1}

Table 2. Model Results

	$Ra=10^6$	$5 \cdot 10^6$	10^7	$3 \cdot 10^7$
Viscosity Model 1				
Geoid	182	115	94	69
Topography	5.2	4.0	3.5	3.0
Nusselt Number	8.5	11.7	13.5	16.8
Viscosity Model 2				
Geoid	77	50	41	31
Topography	3.5	2.6	2.3	1.8
Nusselt Number	9.7	13.0	14.7	17.8
Viscosity Model 3				
Geoid	25	22	21	19
Topography	2.5	1.9	1.6	1.3
Nusselt Number	11.2	14.8	16.7	20.2

Geoid results are in meters and topographic uplifts are in kilometers. Both quantities are values at the surface along the axis of the upwelling plume. Nusselt numbers are volume averaged values. Results for $Ra = 10^6$ are from our finite element modeling and other values are based on power-law projections, as described in the text. Results are scaled using the quantities in Table 1. In order to facilitate comparison of geoid results with the spherical harmonic expansion of the geoid by Bills et al. (1987), only horizontal wavelengths longer than 1850 km are included in the geoid results tabulated here.

Figure 1. Topographic map of Venus, based on the spherical harmonic model of Bills and Kobrick (1985). The contour interval is 500 meters, with lows shaded. Cylindrical projection.

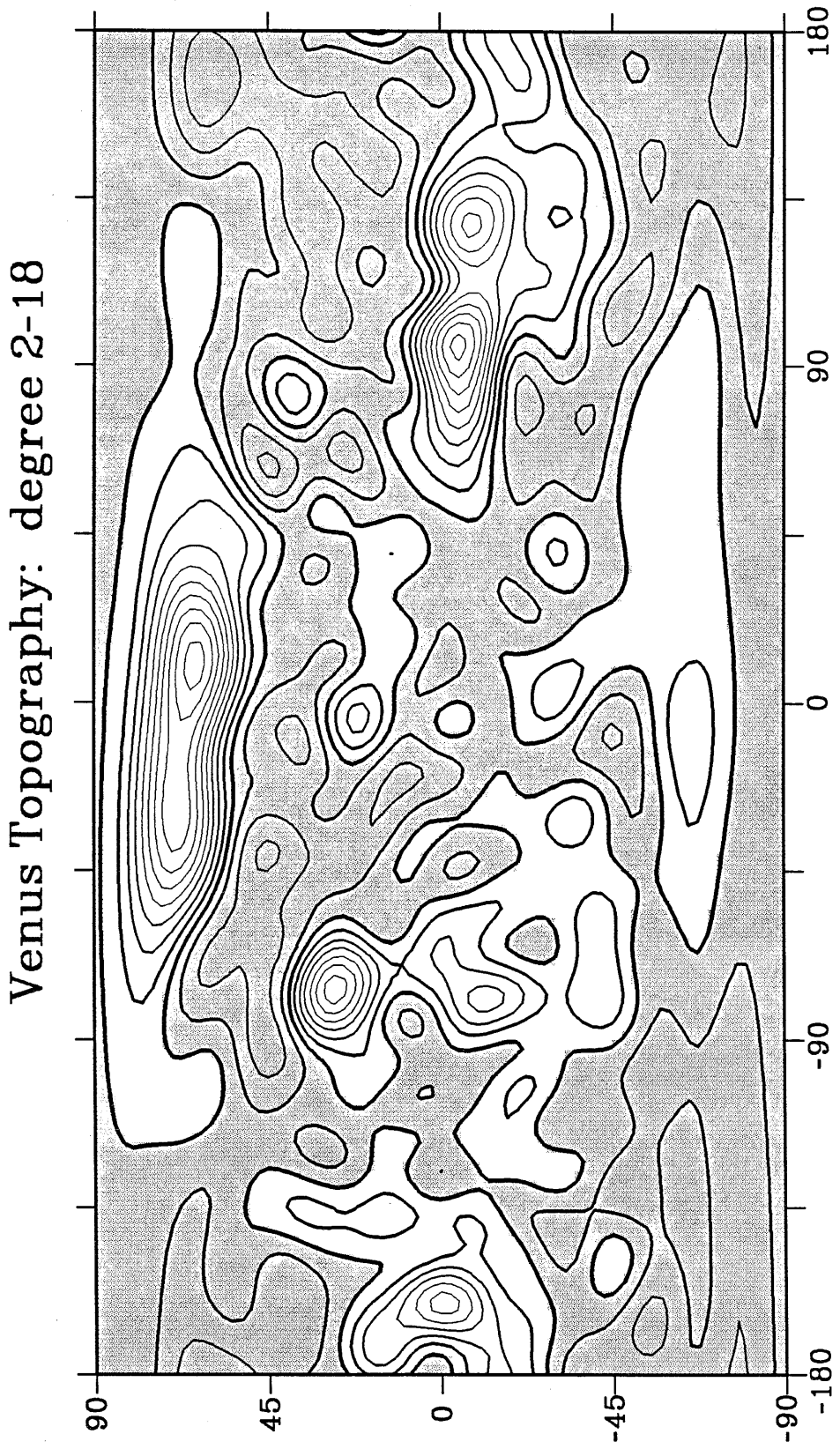
Venus Topography: degree 2-18
90
45
0
-45
-90
-180
-90
0
90
180
contour interval: 500 m

Figure 2. Geoid map of Venus, based on the spherical harmonic model of Bills, Kiefer, and Jones (1987). Contour interval is 10 meters.

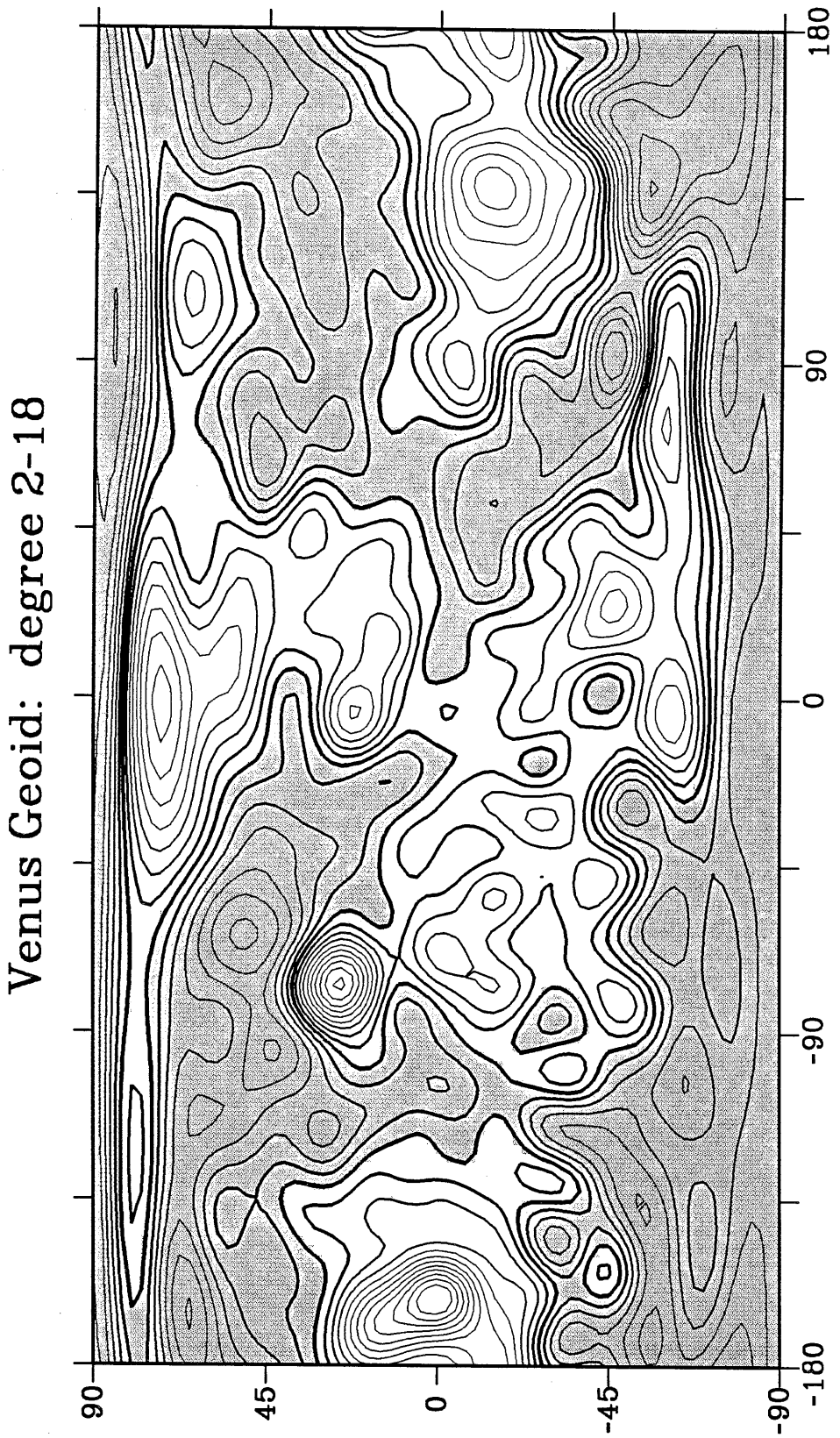
Venus Geoid: degree 2-18
90
45
0
-45
-90
-180
-90
0
90
180
contour interval: 10 m

Figure 3. Geoid map of Earth, based on the spherical harmonic model of Lerch et al. (1985). Contour interval is 10 meters.

Earth Geoid: degree 2-18

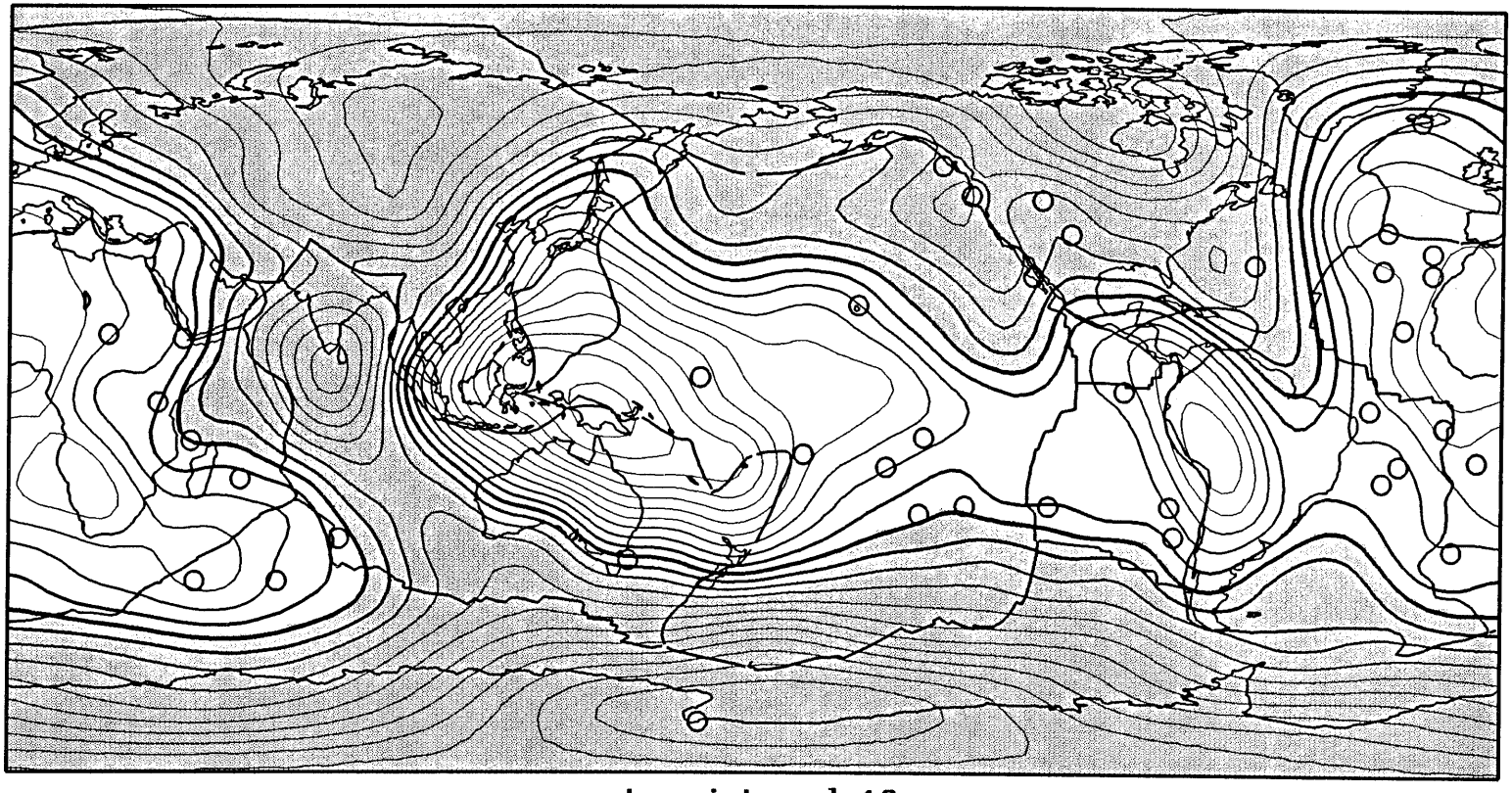

contour interval: 10 m

Figure 4. Temperature contours for a cylindrical plume at $Ra = 10^6$ using viscosity model 2 of Figure 6. The contour interval is 0.10 of the total temperature difference in the cylinder.

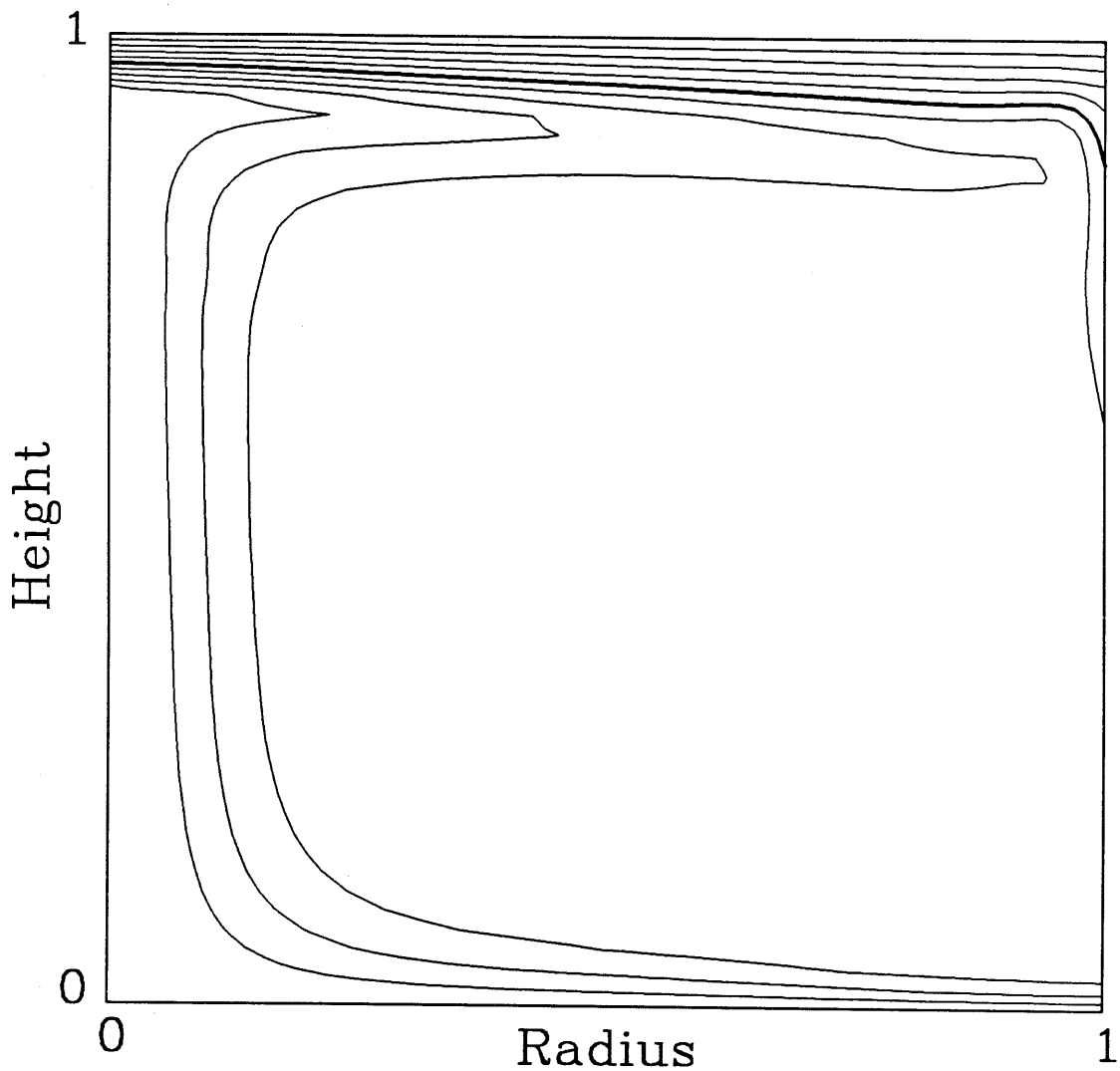
1
Height
0
0
Radius
1

Figure 5. Comparison of admittances for the convective model of Figure 4 (triangles) and for Pratt compensation at 100 km, 200 km, and 400 km depth. Although the convective admittances are defined only for wavelengths that are harmonics of the model cylinder, the results are connected by solid lines for ease of perceiving trends in the results. The very low admittance at a wavelength of 1400 km may not be significant, because for this particular model, both the geoid and the topography have very low power at this wavelength.

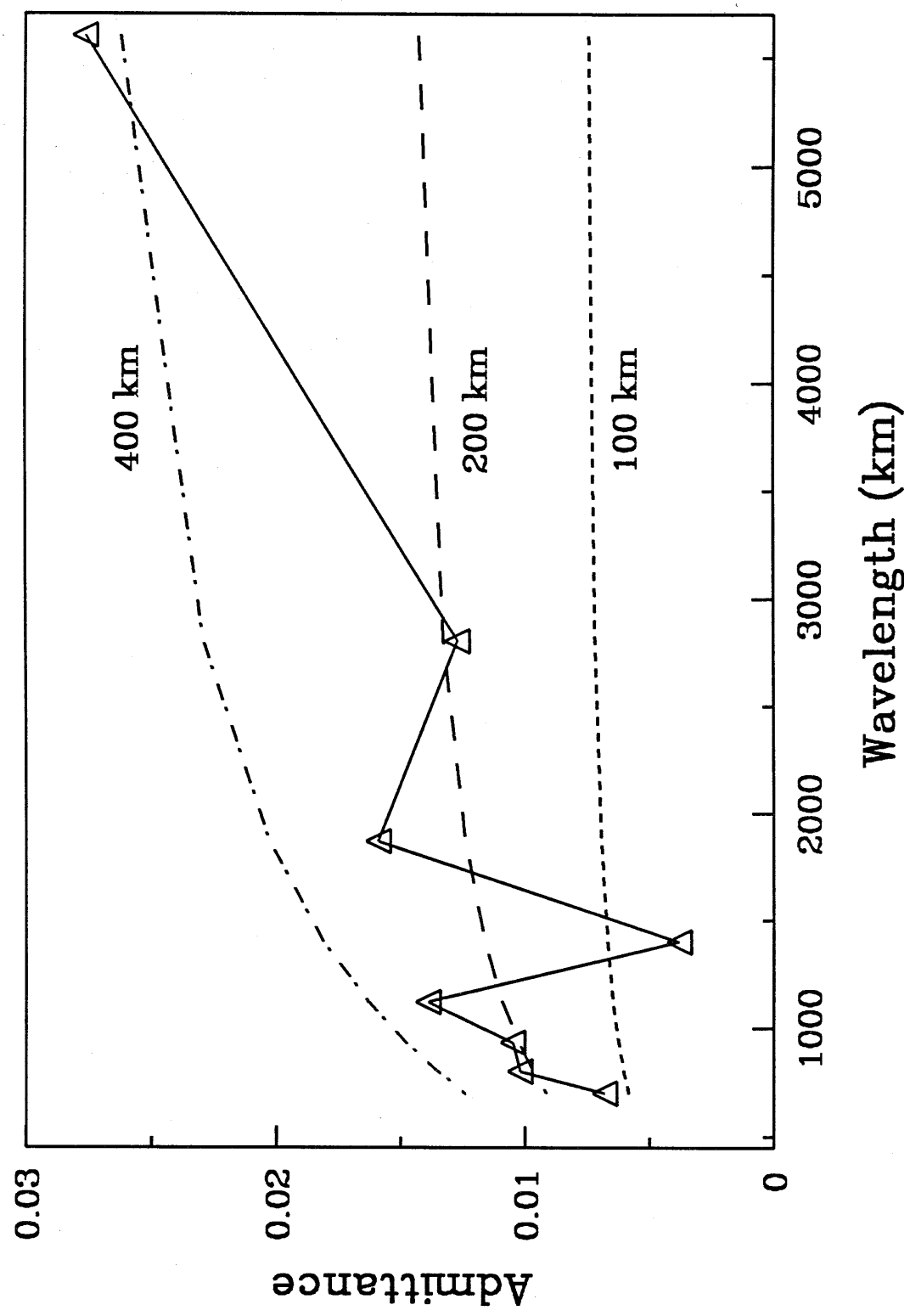
0.03
0.02
0.01
0
Admittance
1000
2000
3000
4000
5000
Wavelength (km)
400 km
200 km
100 km

Figure 6. Viscosity models used in this study. All viscosities are normalized relative to the lower mantle viscosity. a) Viscosity model 1. b) Viscosity model 2. c) Viscosity model 3.

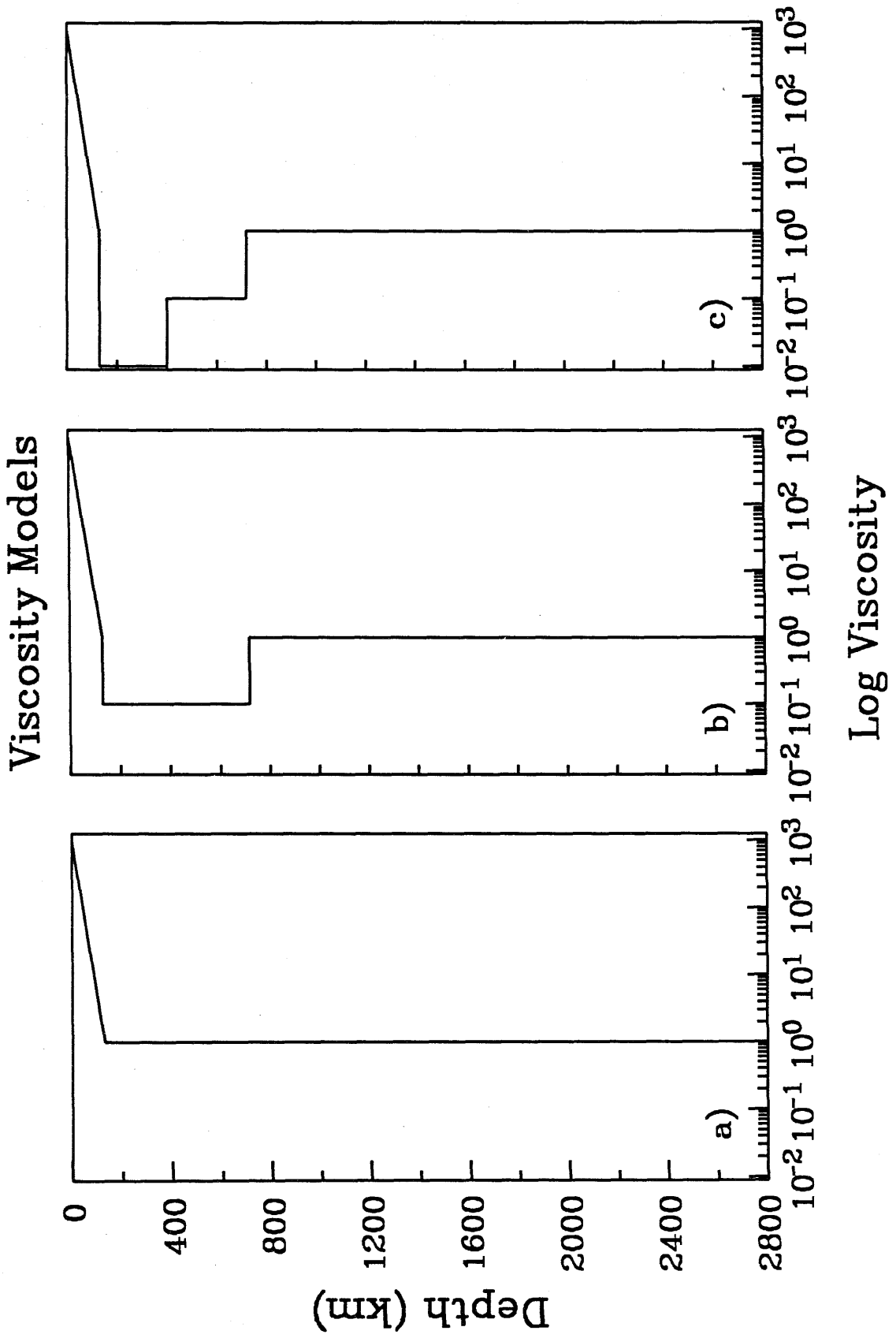
Viscosity Models
Depth (km)
0
400
800
1200
1600
2000
2400
2800
a)
b)
c)
10^{-2} 10^{-1} 10^{0} 10^{1} 10^{2} 10^{3}
Log Viscosity

Figure 7. Geoid anomalies and topographic uplifts versus distance from the upwelling axis for $Ra = 10^6$. Viscosity model 1 is shown in short dashed lines, viscosity model 2 is shown in long dashed lines, and viscosity model 3 is shown in dot-dashed lines. a) Geoid anomalies. b) Topographic uplifts.

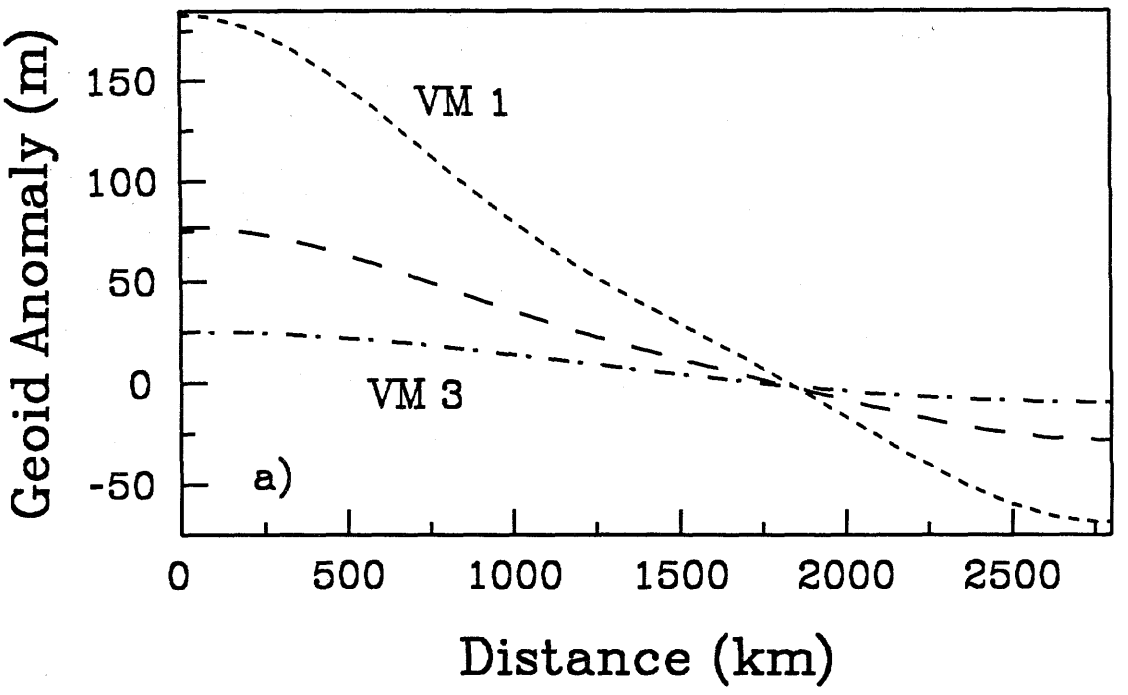
Geoid Anomaly (m)
150
100
50
0
-50
VM 1
VM 3
a)
0
500
1000
1500
2000
2500
Distance (km)

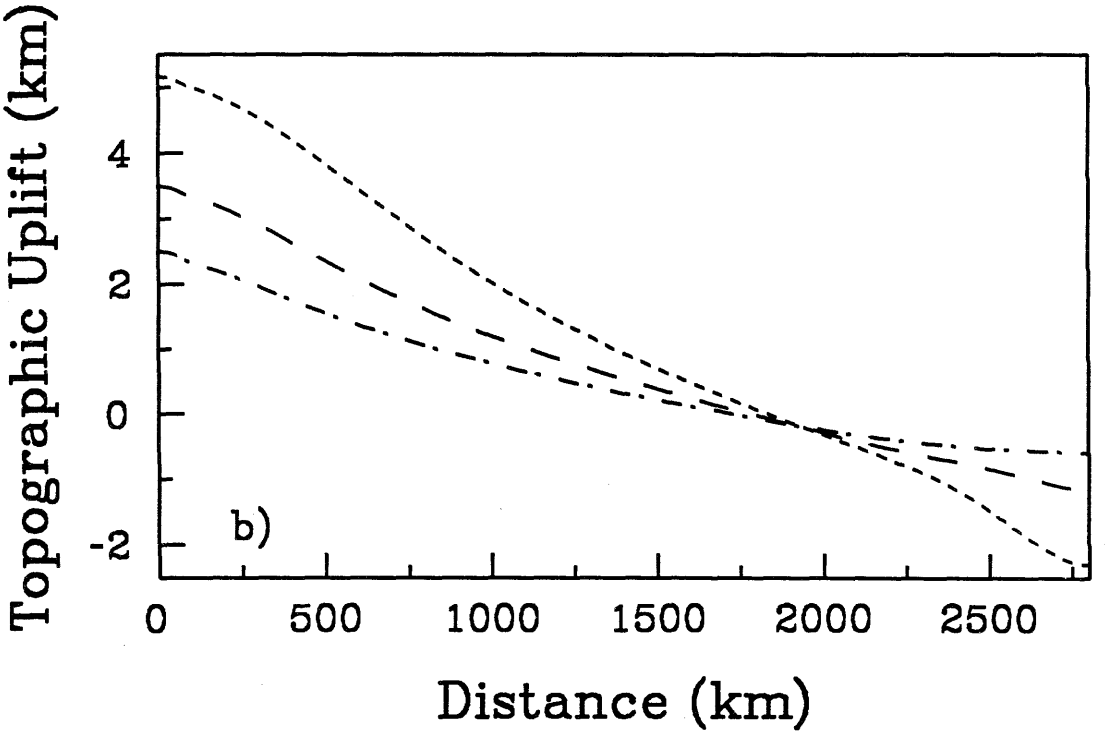
Topographic Uplift (km)
4
2
0
-2
b)
0
500
1000
1500
2000
2500
Distance (km)

Figure 8. Geoid anomalies and topographic uplifts versus distance from the upwelling axis for viscosity model 1. $Ra = 10^5$ is shown in short dashed lines, $Ra = 3 \cdot 10^5$ is shown in long dashed lines, and $Ra = 10^6$ is shown in dot-dashed lines. a) Geoid anomalies. b) Topographic uplifts.

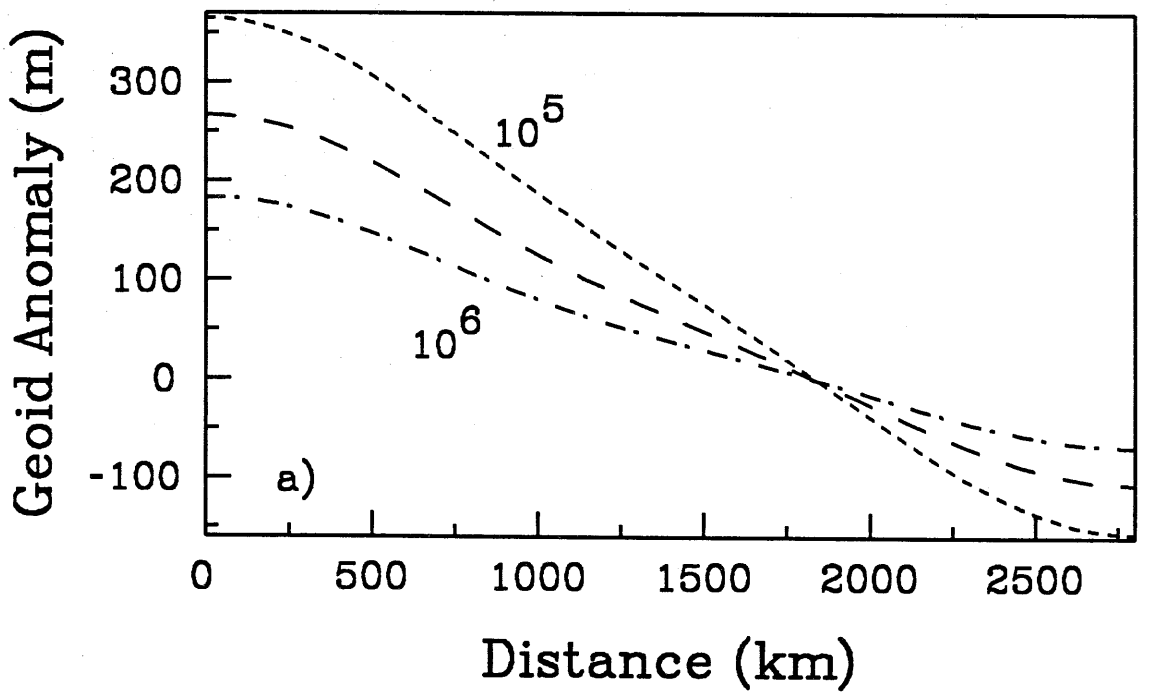
Geoid Anomaly (m)
300
200
100
0
-100
10^5
10^6
a)
0
500
1000
1500
2000
2500
Distance (km)

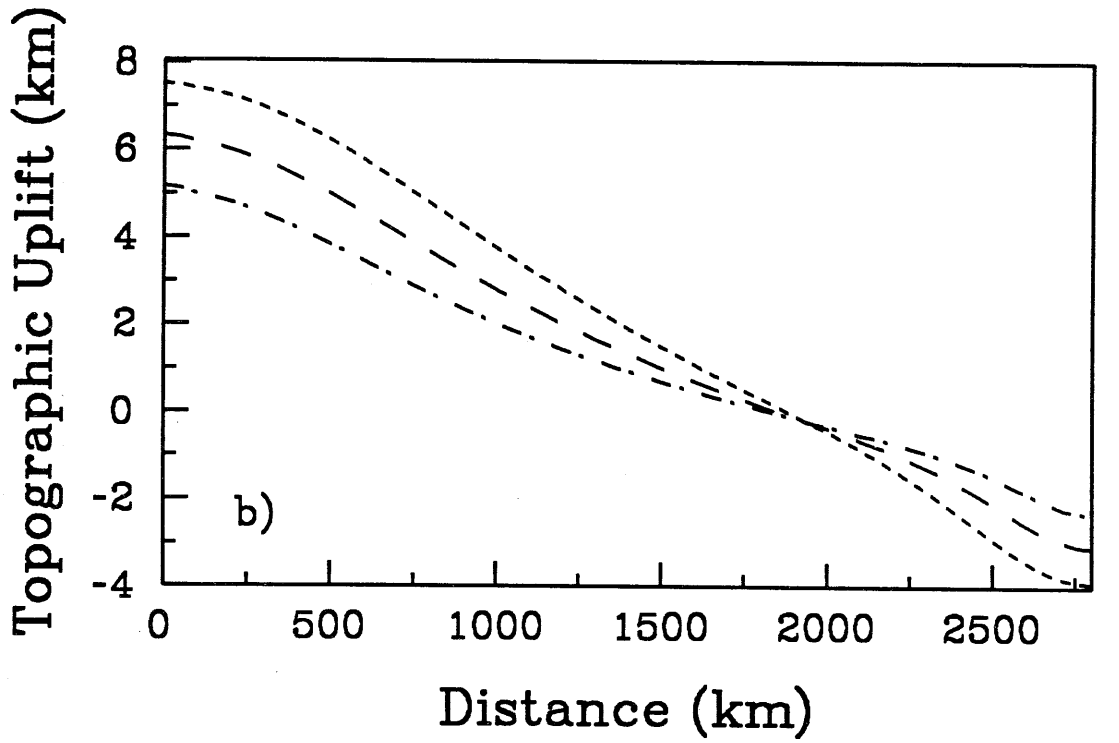
Topographic Uplift (km)
8
6
4
2
0
-2
-4
b)
0
500
1000
1500
2000
2500
Distance (km)

Figure 9. Comparison of model results with observations of Beta Regio. The solid lines are data and the other lines are the model results from Figure 7. a) Topography. b) Geoid anomalies.

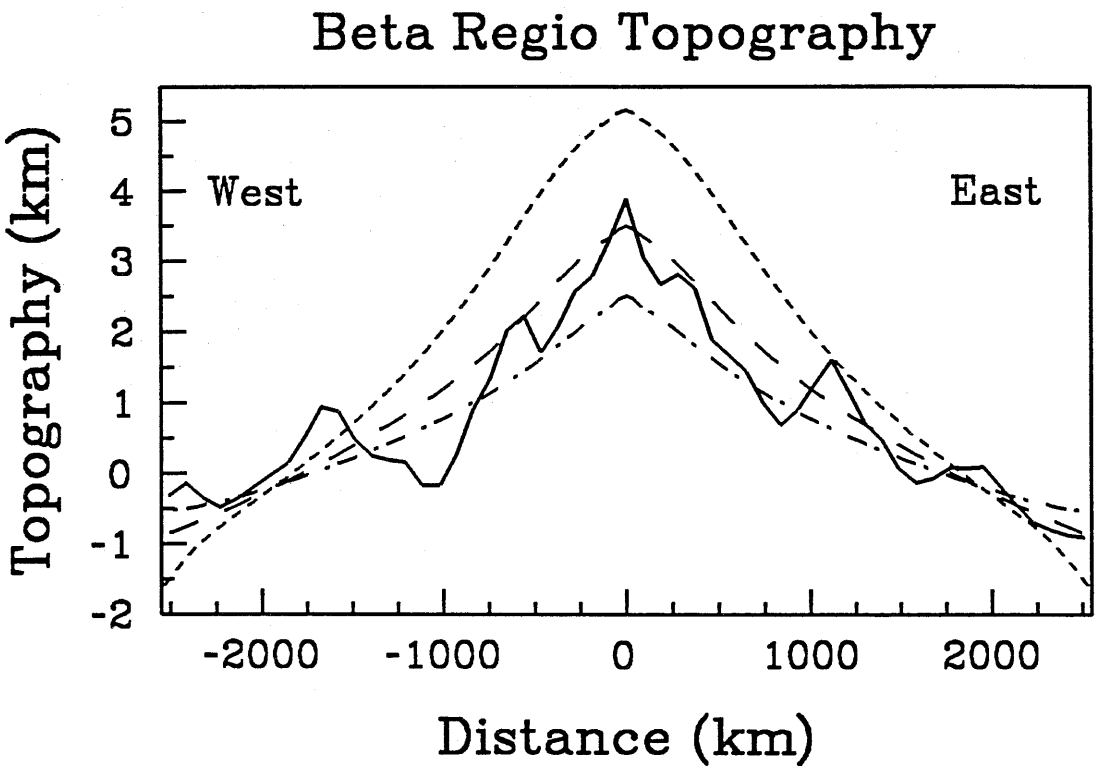
Beta Regio Topography
Topography (km)
5
4
3
2
1
0
-1
-2
West
East
-2000
-1000
0
1000
2000
Distance (km)

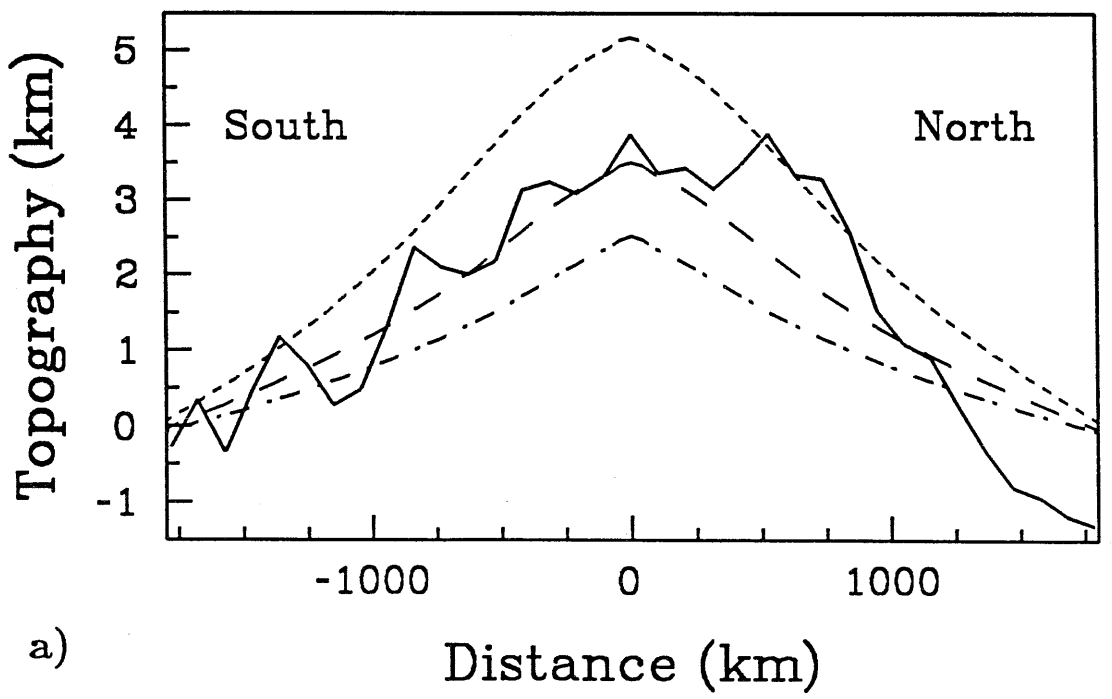
Topography (km)
5
4
3
2
1
0
-1
South
North
-1000
0
1000
Distance (km)

a)

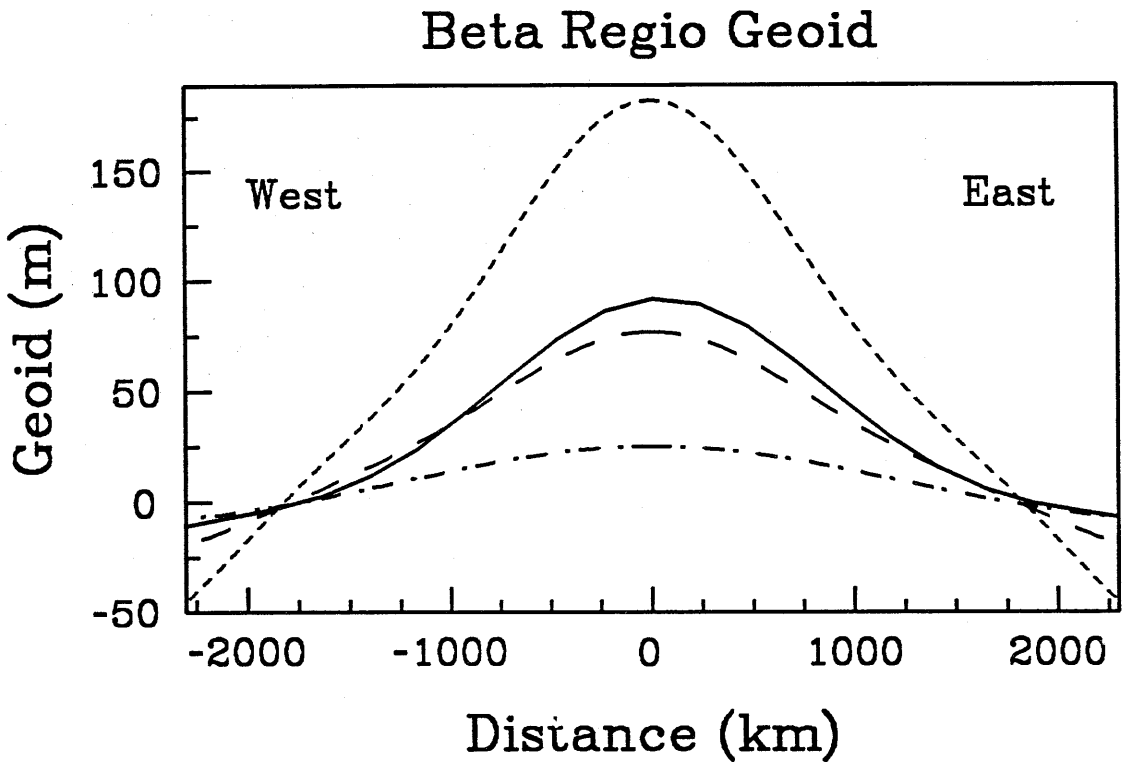
Beta Regio Geoid
West
East
150
100
50
0
-50
Geoid (m)
-2000
-1000
0
1000
2000
Distance (km)

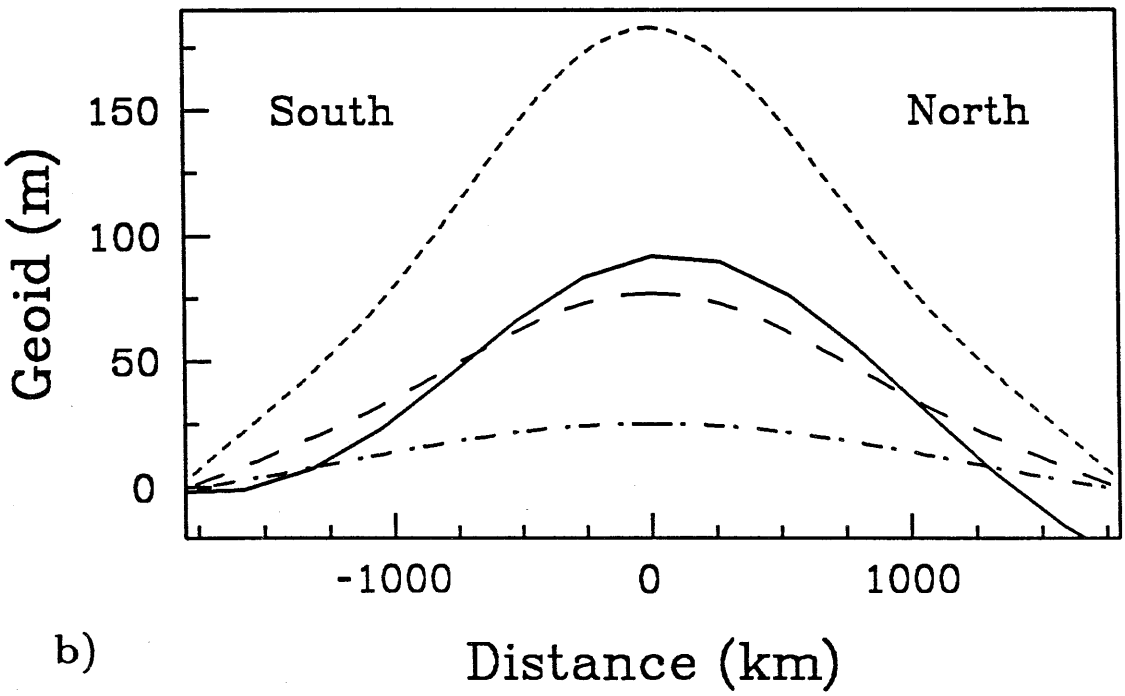
South
North
150
100
50
0
Geoid (m)
-1000
0
1000
Distance (km)

b)

Figure 10. Comparison of model results with observations of Atla Regio. The solid lines are data and the other lines are the model results from Figure 7. a) Topography. b) Geoid anomalies. c) Geoid anomalies as in Figure 10 b, except that model geoids have had 35 meters added to them. See text for explanation.

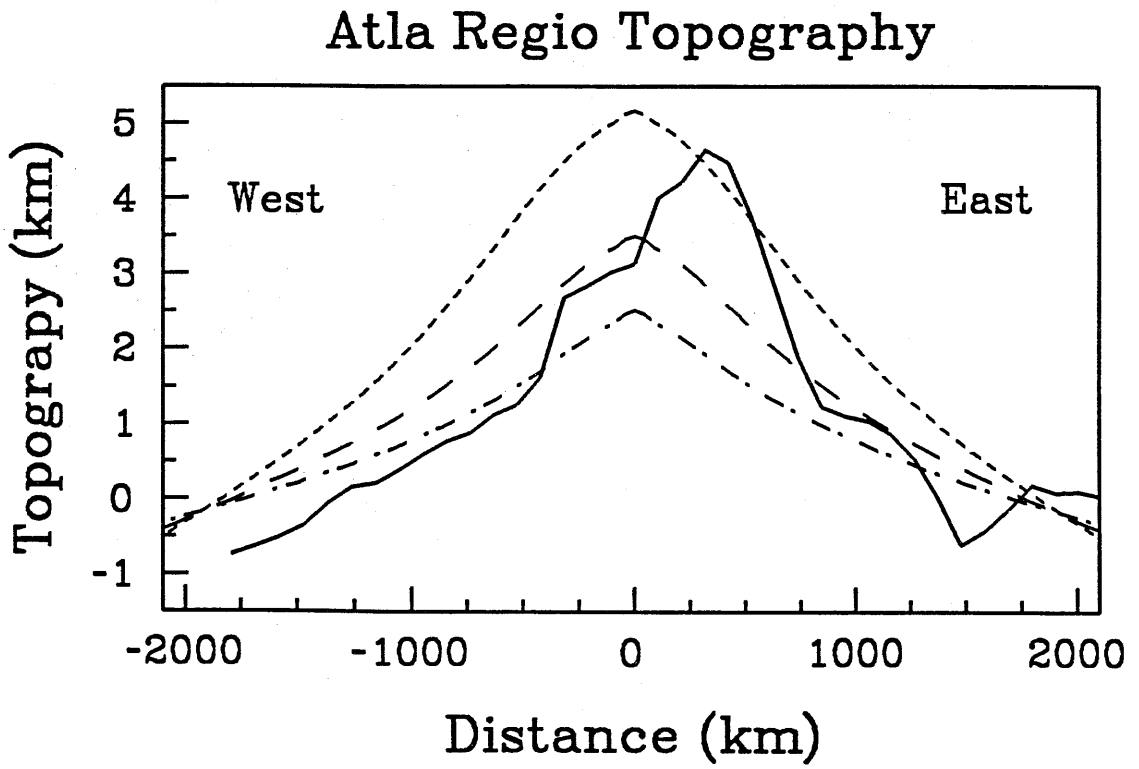
Atla Regio Topography
Topograpy (km)
5
4
3
2
1
0
-1
West
East
-2000
-1000
0
1000
2000
Distance (km)

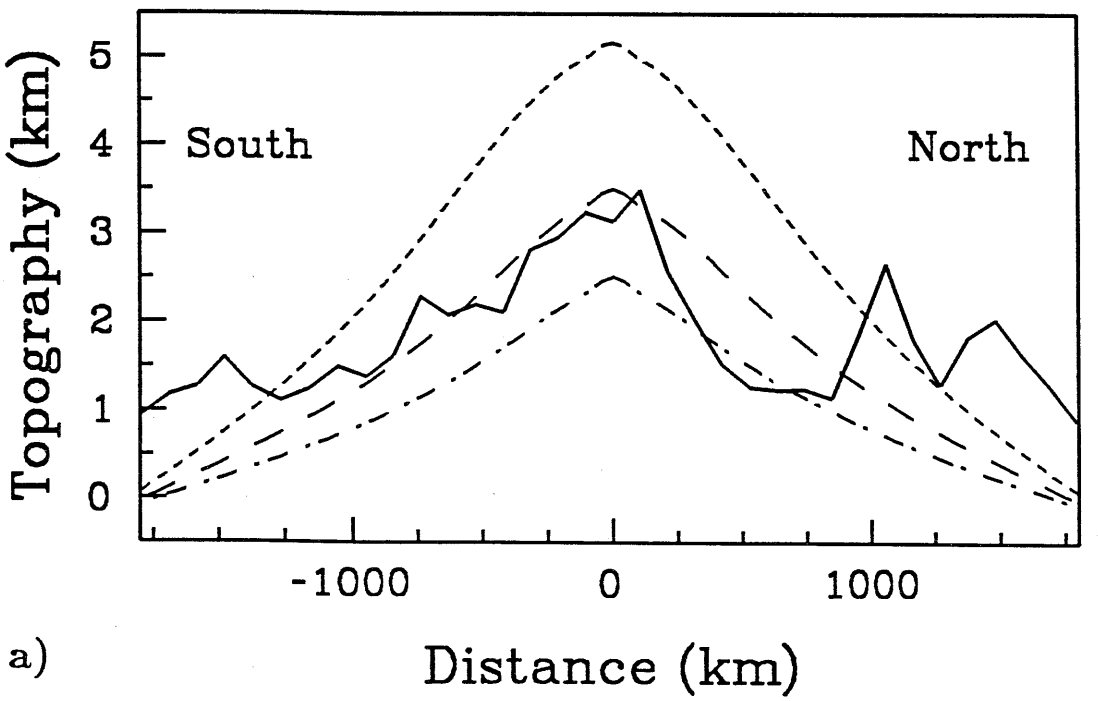
Topography (km)
5
4
3
2
1
0
South
North
-1000
0
1000
Distance (km)

a)

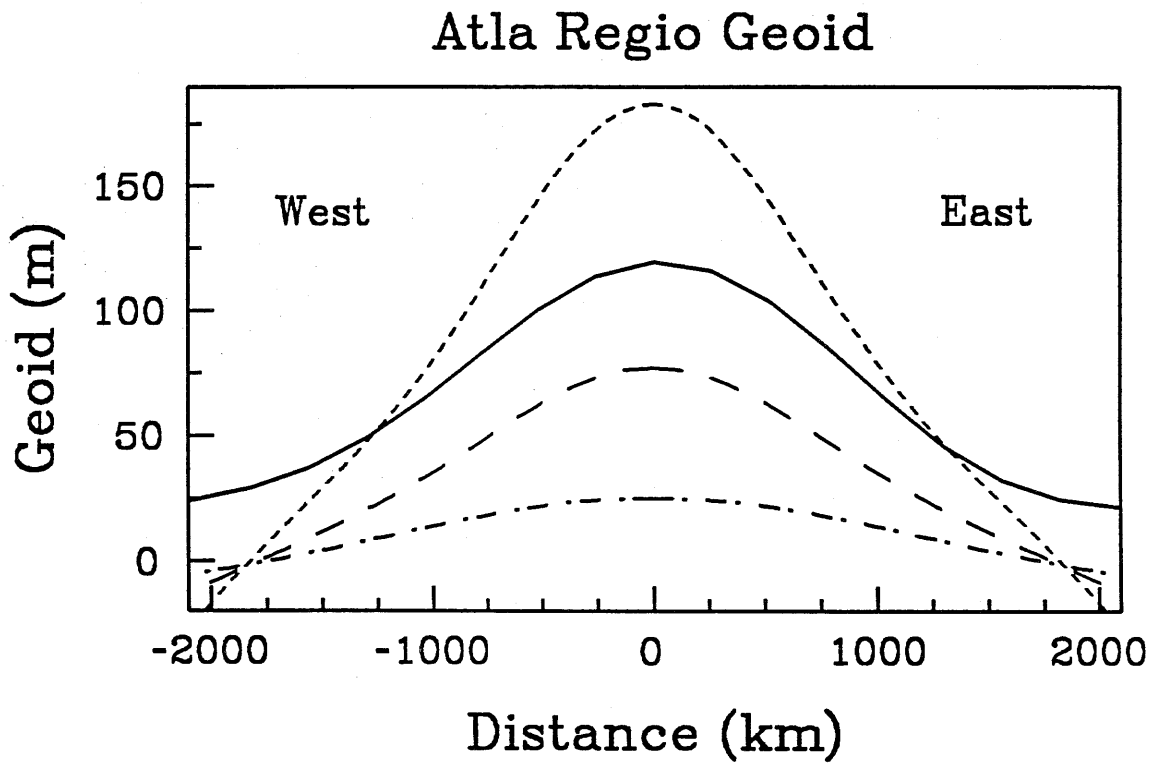
Atla Regio Geoid
West
East
Geoid (m)
150
100
50
0
-2000
-1000
0
1000
2000
Distance (km)

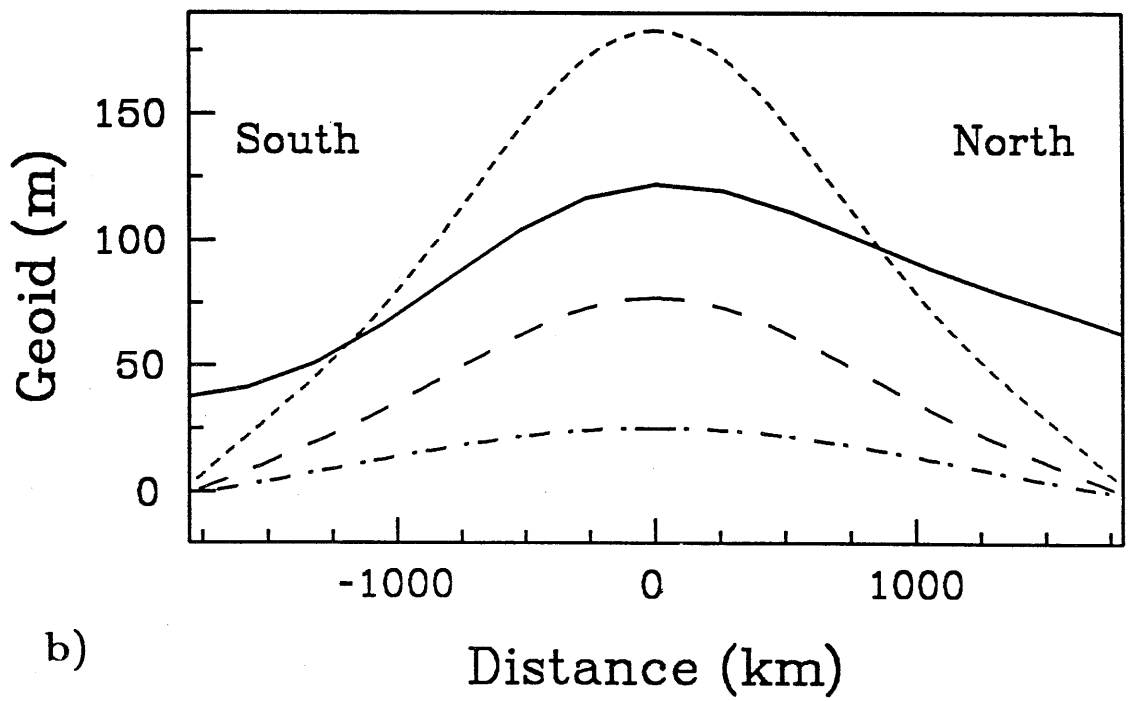
South
North
Geoid (m)
150
100
50
0
-1000
0
1000
Distance (km)

b)

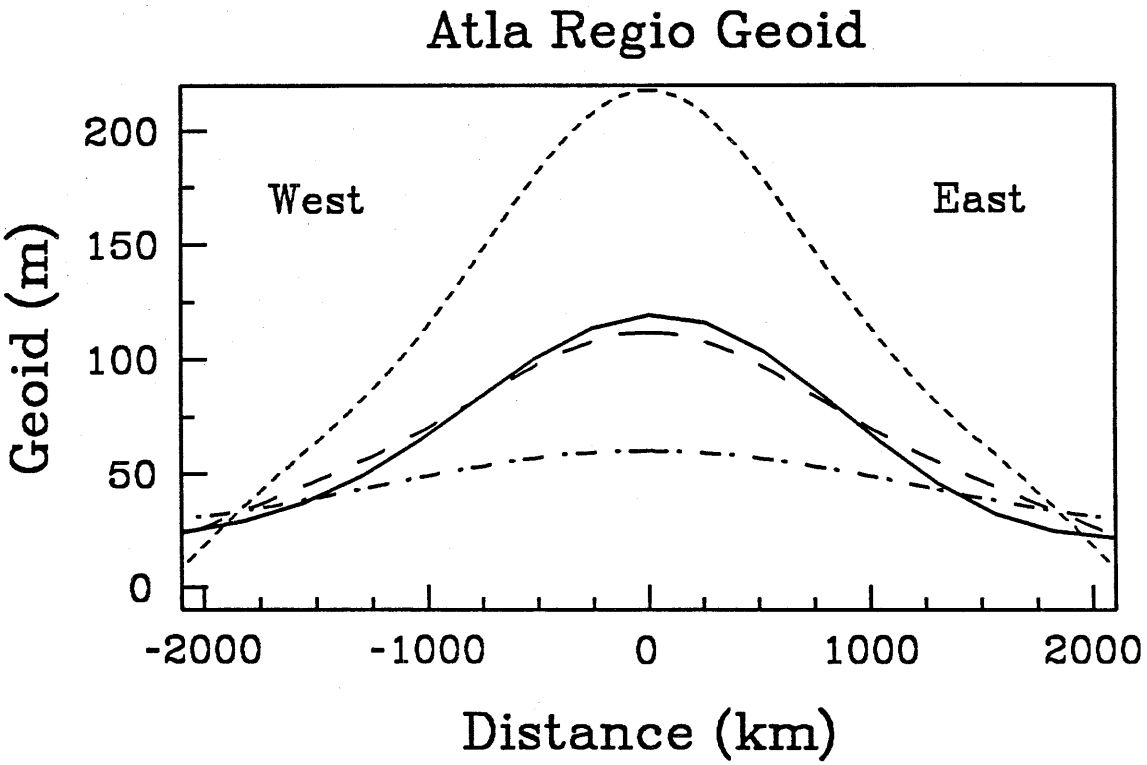
Atla Regio Geoid
West
East
Geoid (m)
200
150
100
50
0
-2000
-1000
0
1000
2000
Distance (km)

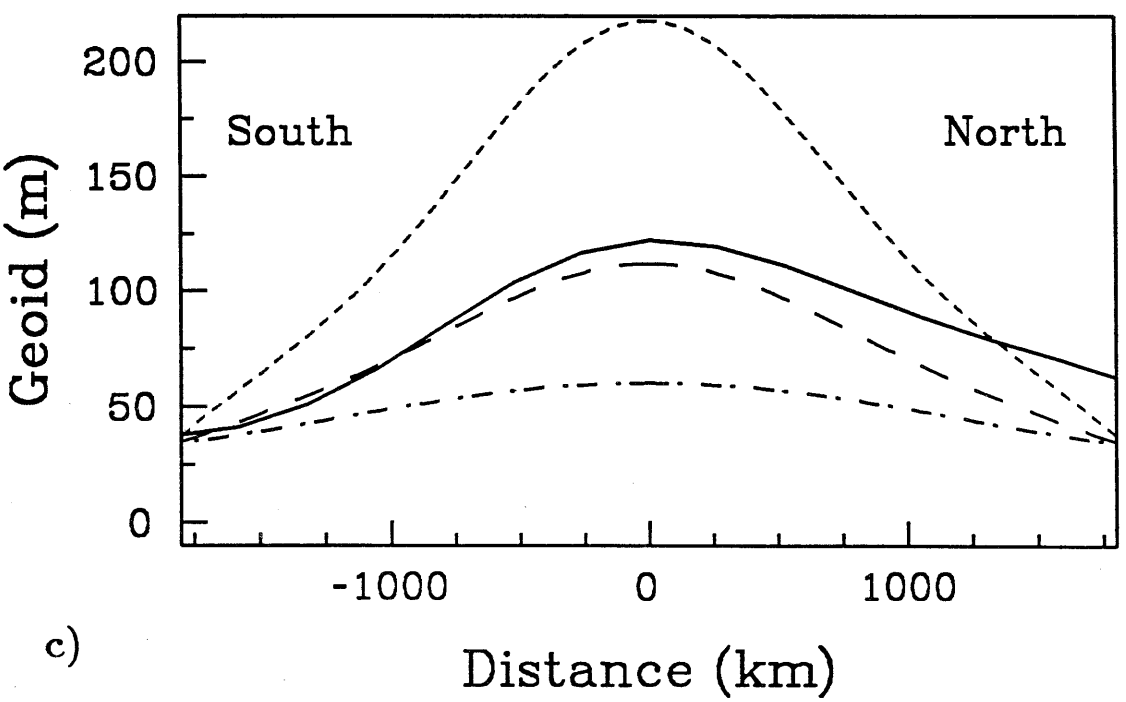
South
North
Geoid (m)
200
150
100
50
0
-1000
0
1000
Distance (km)

c)

Figure 11. Comparison of model results with observations of Thetis Regio. The solid lines are data and the other lines are the model results from Figure 7. a) Topography. b) Geoid anomalies.

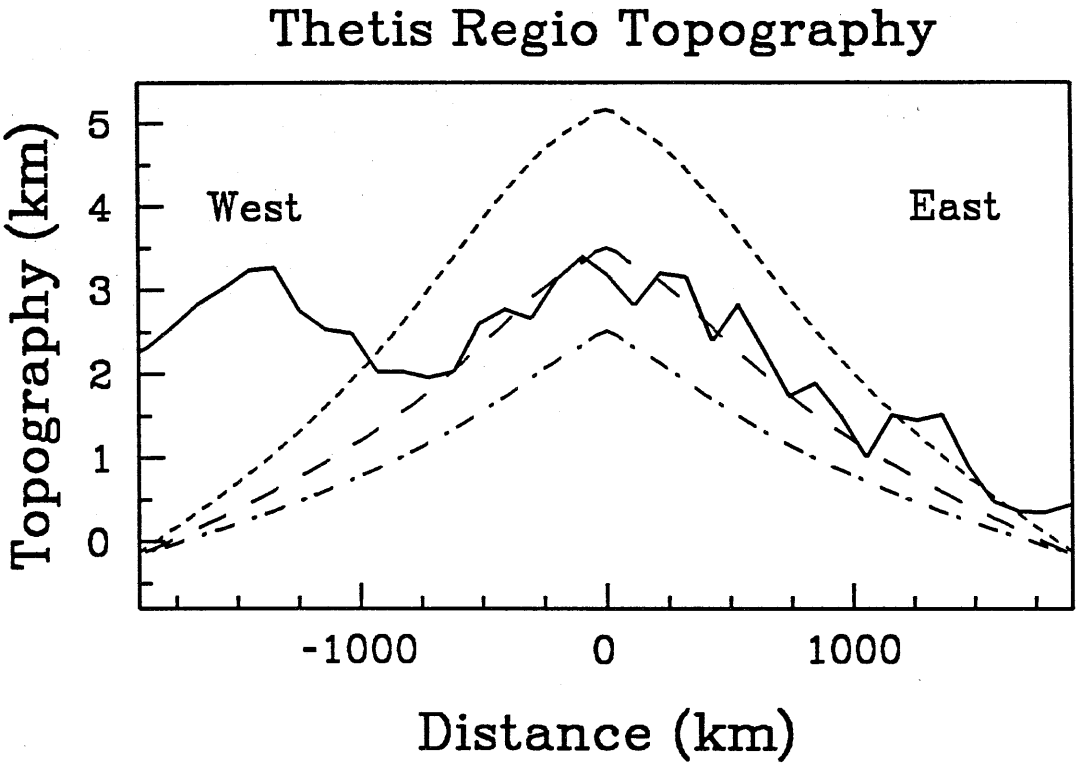
Thetis Regio Topography
Topography (km)
0
1
2
3
4
5
West
East
-1000
0
1000
Distance (km)

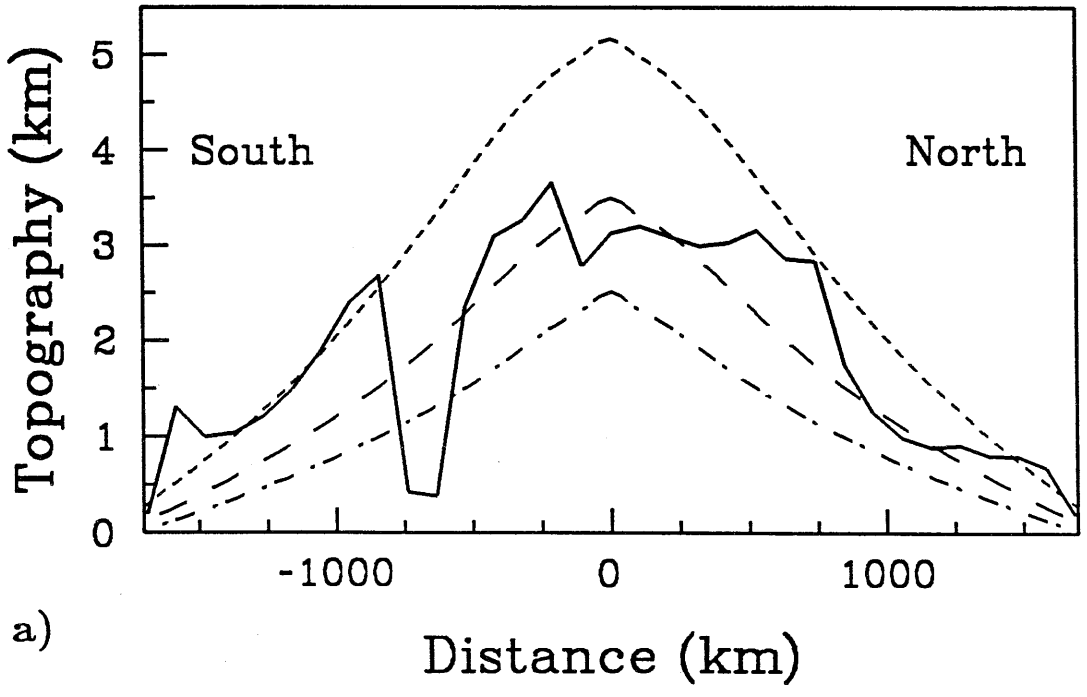
Topography (km)
0
1
2
3
4
5
South
North
-1000
0
1000
Distance (km)

a)

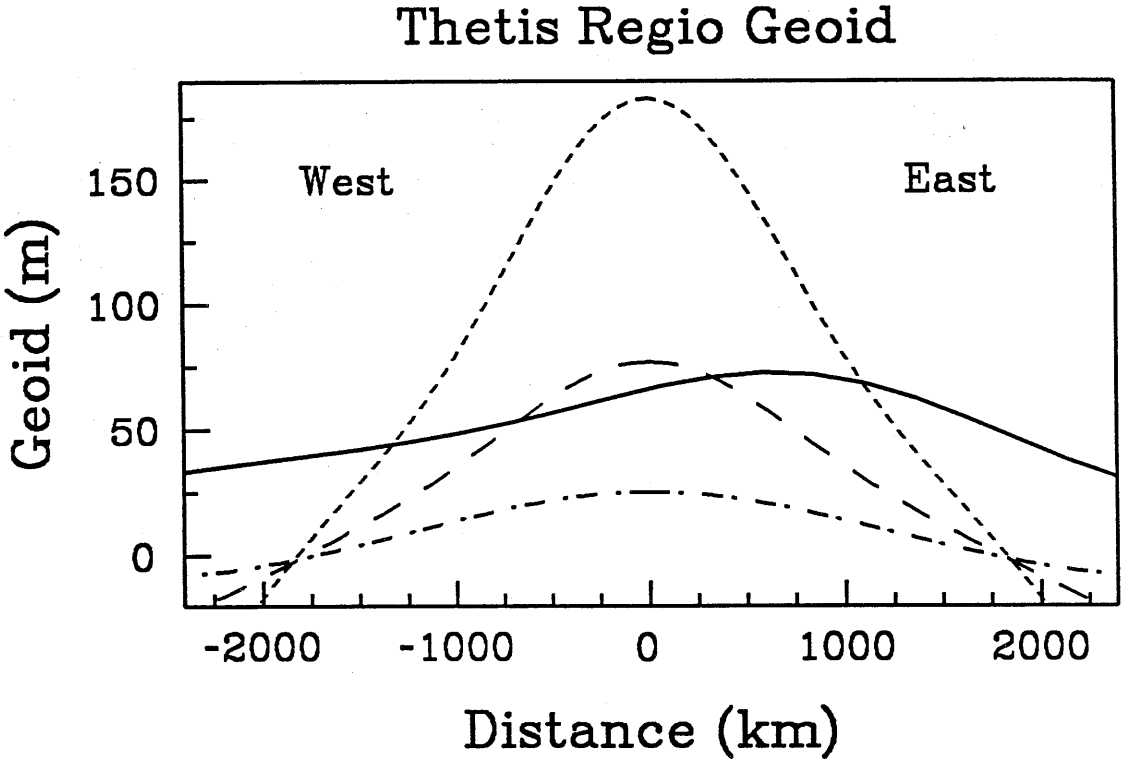
Thetis Regio Geoid
West
East
150
100
50
0
Geoid (m)
-2000
-1000
0
1000
2000
Distance (km)

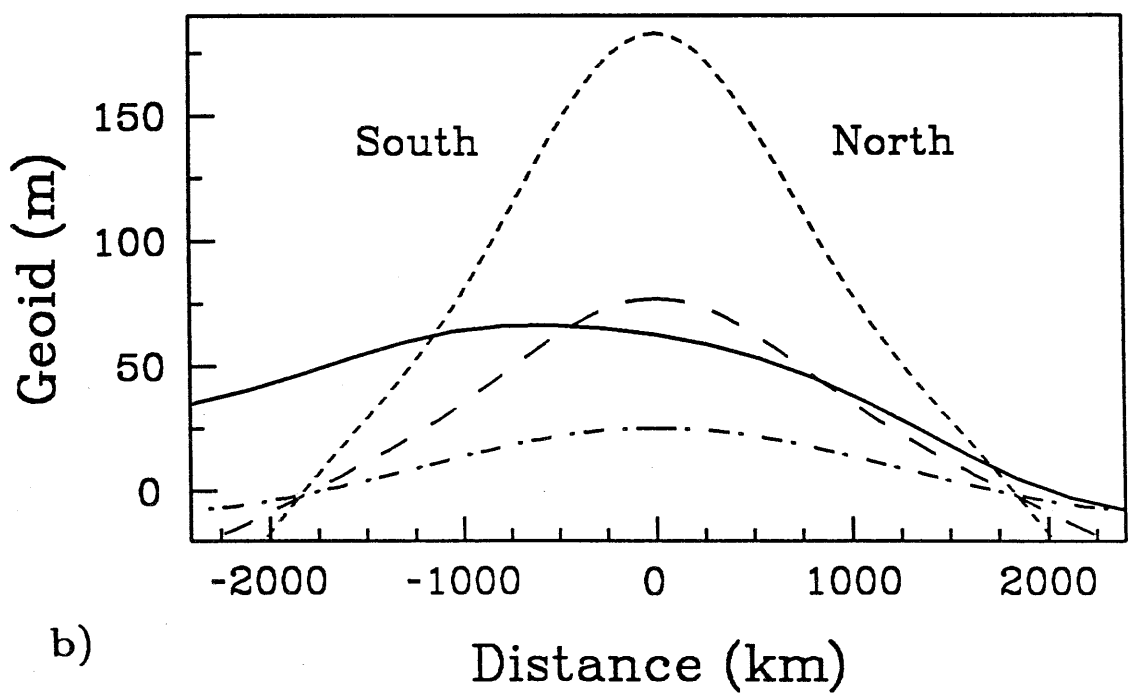
South
North
150
100
50
0
Geoid (m)
-2000
-1000
0
1000
2000
Distance (km)

b)

Figure 12. Comparison of model results with observations of Ovda Regio. The solid lines are data and the other lines are the model results from Figure 7. a) Topography. b) Geoid anomalies.

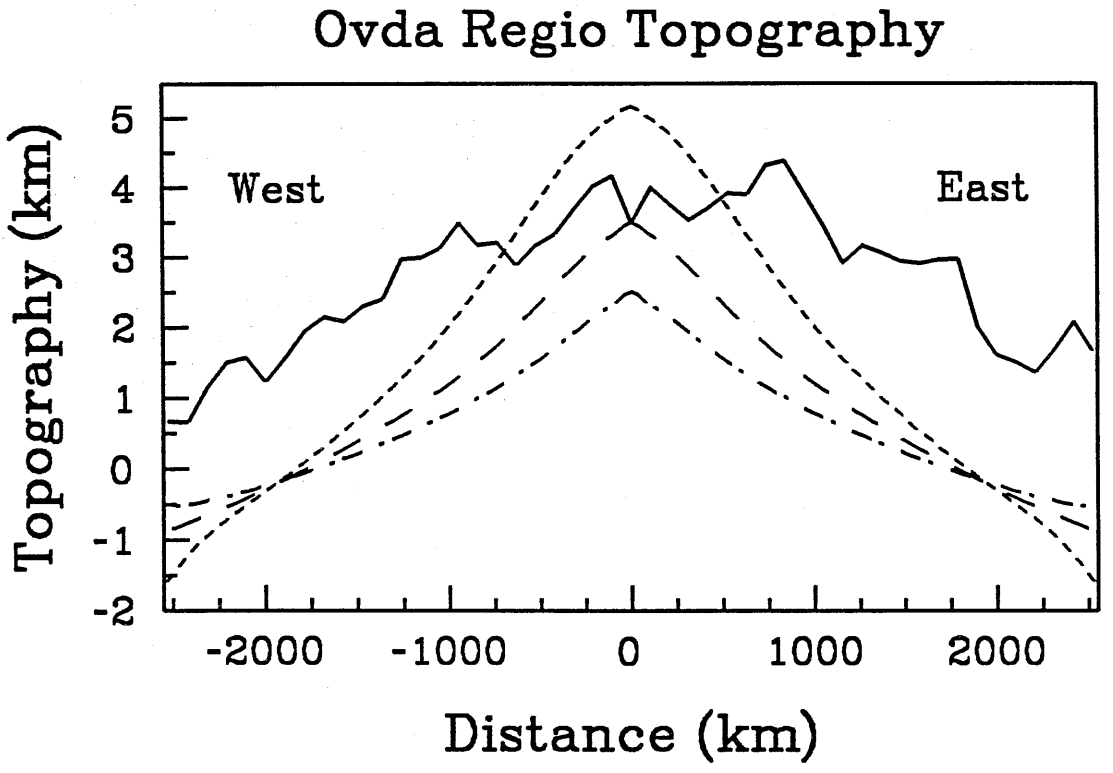
Ovda Regio Topography
Topography (km)
5
4
3
2
1
0
-1
-2
West
East
-2000
-1000
0
1000
2000
Distance (km)

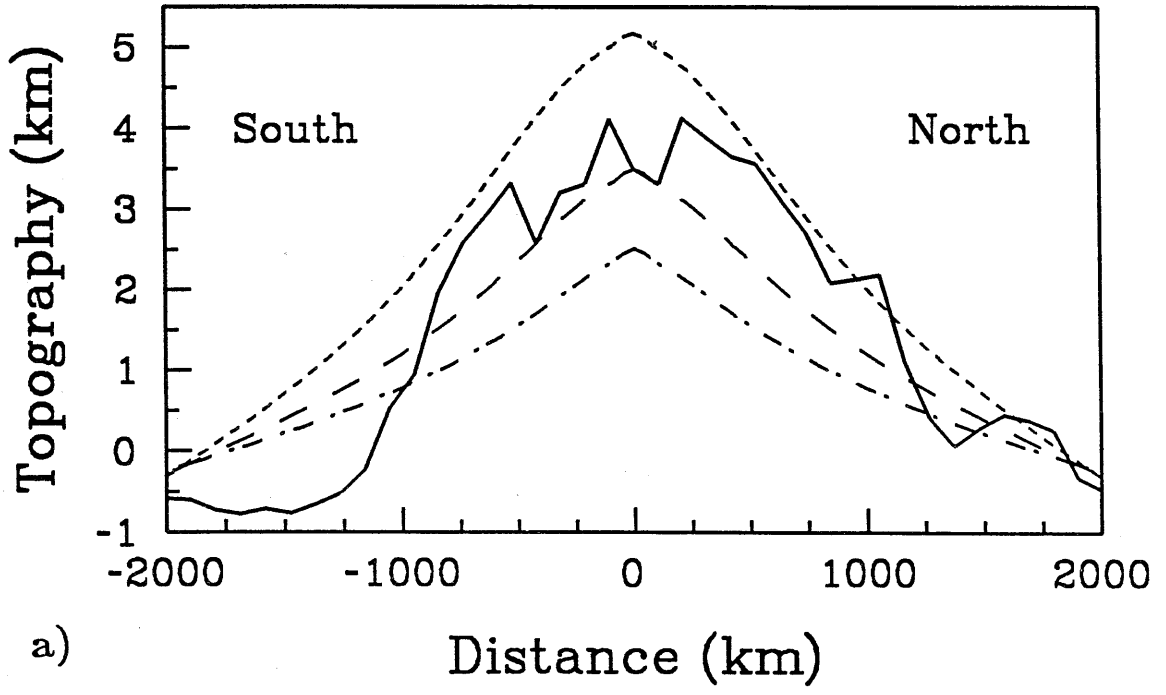
Topography (km)
5
4
3
2
1
0
-1
South
North
-2000
-1000
0
1000
2000
Distance (km)

a)

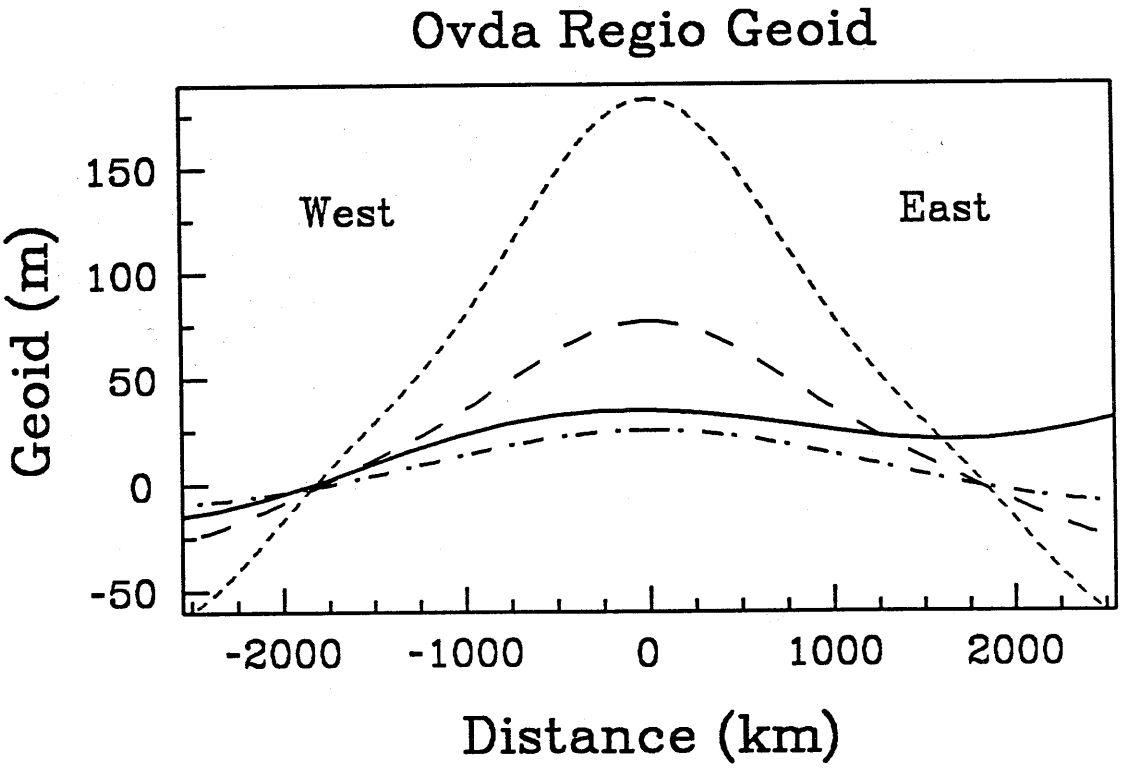
Ovda Regio Geoid
West
East
Geoid (m)
150
100
50
0
-50
-2000
-1000
0
1000
2000
Distance (km)

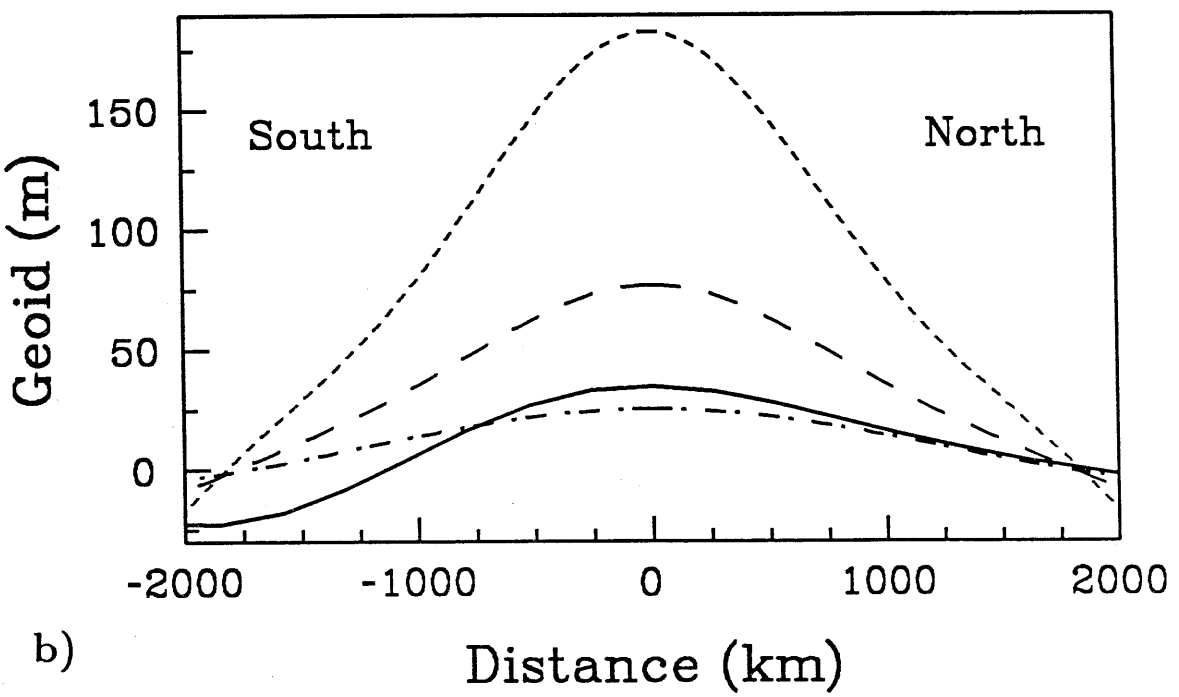
South
North
Geoid (m)
150
100
50
0
-2000
-1000
0
1000
2000
Distance (km)

b)

Figure 13. The RMS amplitude spectrum of the Bills et al. (1987) Venus geoid model. The solid line is the spherical harmonic model and the dashed line is a power law approximation to the spectrum, as described in the text.

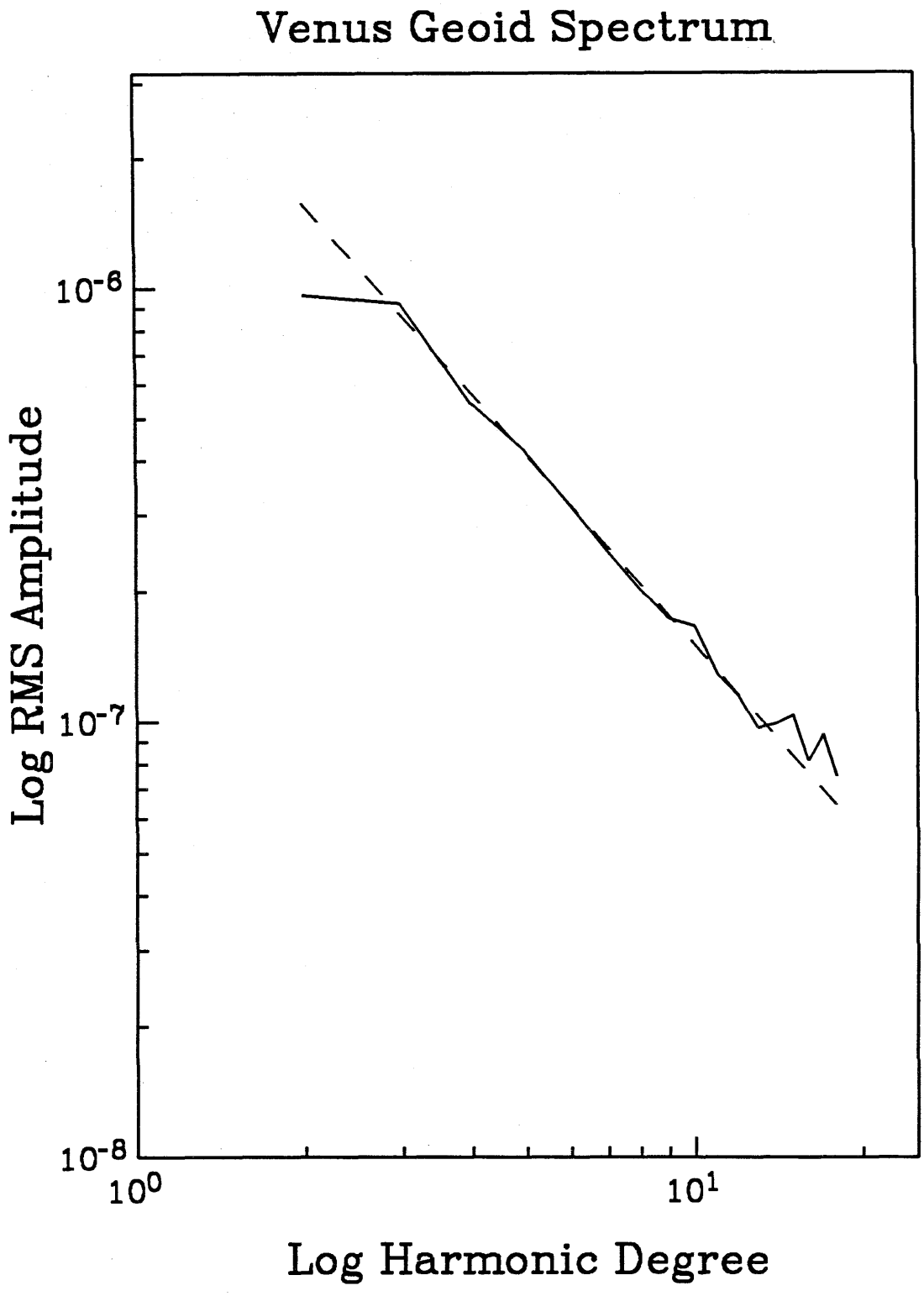
Venus Geoid Spectrum
Log RMS Amplitude
10^{-6}
10^{-7}
10^{-8}
10^{0}
10^{1}
Log Harmonic Degree

Figure 14. The RMS amplitude spectrum of the Lerch et al. (1985) Earth geoid model. The solid line is the spherical harmonic model and the dashed line is a power law approximation to the spectrum, as described in the text.

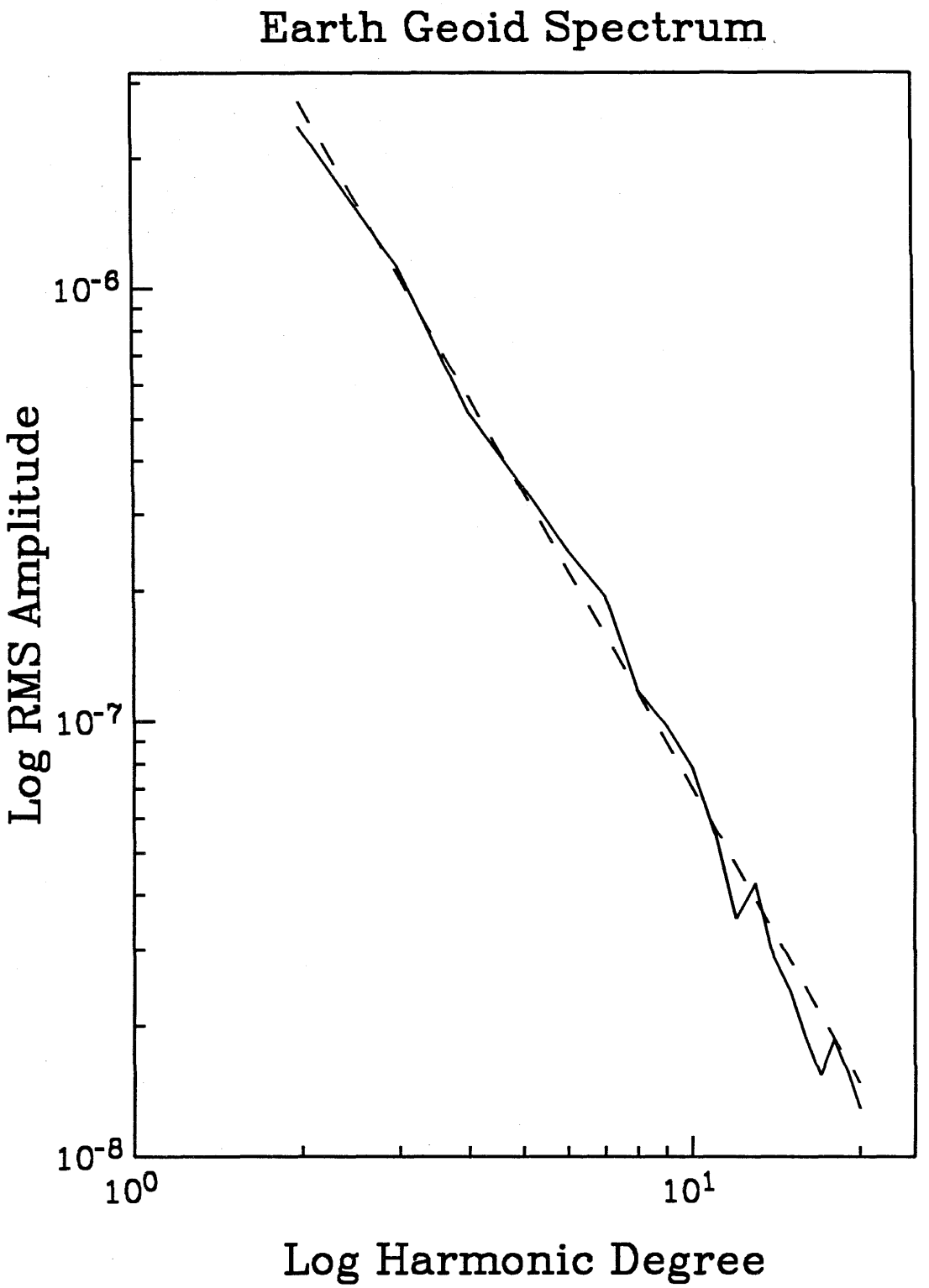
Earth Geoid Spectrum
Log RMS Amplitude
10^{-6}
10^{-7}
10^{-8}
10^{0}
10^{1}
Log Harmonic Degree

Chapter 3

A Reexamination of the Spreading Center Hypothesis for Ovda and Thetis Regiones, Venus

Walter S. Kiefer

Division of Geological and Planetary Sciences
California Institute of Technology
Pasadena, CA 91125

Accepted for Publication in
Geophys. Res. Lett.

Ovda Regio and Thetis Regio are two of the most prominent highland units on Venus. Crumpler, Head, and colleagues have advocated that Ovda and Thetis are terrestrial-type spreading centers (Crumpler et al., 1987; Crumpler and Head, 1988; Head and Crumpler, 1987; Sotin et al., 1989). Grimm and Solomon (1989) discussed several aspects of the spreading center model. I examine several other aspects of the spreading center model in this manuscript. I focus primarily on the possible relationship between the observed geoid and the hypothesized spreading centers. I also discuss possible weaknesses in the evidence advanced by Crumpler et al. (1987) for cross-strike discontinuities in the Ovda and Thetis regions.

Spreading Center Geoid Anomalies and Topography

Geoid and topography data provide one means of assessing the spreading center model. Although it is not possible to exclude the spreading center hypothesis on the basis of either geoid or topography alone, it is possible to set strict limits on the extent to which a spreading center can contribute to the observed geoid and topography. Both Head and Crumpler (1987) and Sotin et al. (1989) have acknowledged that other processes can contribute to the observed topography, focusing primarily on crustal thickening due to volcanic activity at hotspots. Sotin et al. showed that their model can also satisfy the observed gravity in Ovda, but they did not discuss the relative contributions of each part of their model to the total gravity anomaly. One of the purposes of this paper is to show that spreading centers, as an end member process, can account for no more than a small fraction of the observed geoid anomalies in Ovda and Thetis.

Terrestrial spreading centers are essentially uncorrelated with the long-wavelength geoid (Richards and Hager, 1988), whereas on Venus geoid and topography highs are strongly correlated (Kiefer et al., 1986; Bills et al., 1987). On Earth, the density anomalies associated with spreading centers occur primarily in the upper hundred kilometers of the mantle and produce only small long-wavelength geoid anomalies. Most of Earth's long-wavelength geoid is due to density anomalies at much greater depths in the mantle (Hager and

Richards, 1989). The lack of correlation between terrestrial spreading centers and the geoid implies that spreading centers are not closely related to upwelling from deep within the mantle. There are local exceptions to this general rule in places such as Iceland, which is formed by a mantle plume that happens to be located near a spreading center. The strong correlation of geoid and topography on Venus suggests that the Equatorial Highlands are related to deep convective structures.

Recently, Sotin et al. (1989) argued that there is also a strong correlation between spreading centers and gravity anomalies on Earth and cited work by Madsen et al. (1984) to support this claim. Madsen et al. examined gravity anomalies within 100 km of the crest of the East Pacific Rise, whereas the correlations addressed here concern much longer wavelengths ($\lambda > 2000$ km, Bills et al., 1987). Wavelengths of 100 to 200 km are not even detectable in PVO gravity data. Near periapse, the Doppler tracking of the PVO spacecraft was averaged over 5 second intervals, which corresponds to a sampling length of 40 km. The Nyquist condition therefore indicates that wavelengths as short as 80 km are theoretically resolvable, but in practice signal-to-noise ratio constraints prevent this theoretical limit from being achieved. Bills et al. (1987) estimated that the noise level in the PVO gravity data is 3 mgal. At short wavelengths, we can neglect the sphericity of Venus and use a planar approximation, so that gravity anomalies attenuate with altitude as $\exp(-2\pi d/\lambda)$, where d is the altitude of the spacecraft above the surface and λ is the horizontal wavelength of the gravity anomaly. The minimum detectable wavelength is a function of the amplitude of the anomaly at the surface, but for moderate amplitude anomalies, a good rule of thumb is that $\lambda \geq 3d$ is necessary for the anomaly to be detectable above the noise level. The PVO spacecraft was at an altitude of 250 to 350 km when over Ovda and Thetis, implying that only wavelengths longer than 750 to 1000 km are detectable. Thus, the discussion of short-wavelength correlations between spreading centers and gravity anomalies in Sotin et al. (1989) is not relevant to data presently available for Venus.

On Venus, the topographic relief of possible spreading centers is reduced substantially in comparison with Earth, both because of the lack of oceans on Venus and because the high surface temperature implies a thinner thermal

lithosphere. Kaula and Phillips (1981) estimated that the maximum difference in elevation between spreading centers and old lithosphere on Venus is only about 1.5 km. The plains of Venus, whose average elevation essentially corresponds to the mean planetary radius (MPR), are the appropriate comparison to old oceanic lithosphere on Earth. Ovda reaches a peak elevation of 5 km above MPR and Thetis reaches a peak of 4 km above MPR (U.S. Geological Survey, 1984), both substantially higher than expected for a spreading center. Thus, even if spreading centers exist in Ovda and Thetis, other mechanisms must still be invoked to explain 60 to 70 % of the peak topography in Ovda and Thetis.

Sotin et al. (1989) presented a model for the Ovda Regio gravity anomaly in which the observed gravity receives contributions both from thermal anomalies in the lithosphere that are associated with the spreading plates as well as from topographic variations that are due to regional variations in crustal thickness. Their model requires that the crust is about 30 km thick in central Ovda and 11 to 17 km thick on the northern and southern flanks. They suggested that the regional variations in crustal thickness are due to a sudden increase of 100 to 200 °C in the temperature of the mantle beneath Ovda, which would lead to increased magma production and a thicker crust. Such regional variations in upper mantle temperature would also contribute to topographic uplift and to the gravity anomaly, but these contributions are not included in the model of Sotin et al.

Sotin et al. (1989) and Black et al. (1990) used a cooling half-space thermal model out to ages of several hundred million years in performing their gravity modeling. Based on terrestrial experience, the half-space model overestimates the amount of thermal subsidence at large ages and consequently the gravity anomalies predicted by this model will also be too large. For example, Sotin et al. apply the half-space model out to ages of about 300 million years, implying a thermal lithosphere that exceeds 200 km in thickness. Unless Venus has a mean heat flow that is much less than Earth's, such a lithospheric thickness is not plausible. A better thermal model is the cooling plate model, in which the thermal lithosphere asymptotically approaches a maximum thickness. For the cooling plate model, Sandwell and Schubert (1980) gave the

relationship for N(t), the geoid height as a function of plate age, t. Rather than calculate a detailed profile of geoid height versus age (or distance) to compare with observations, I simply calculate the peak geoid anomaly created by a cooling plate by calculating the difference in the geoid at t=0 and at $t \rightarrow \infty$. I find that

$$\Delta N = N(t=0) - N(t \rightarrow \infty)$$
$$= \frac{2\pi G L^2}{g} \left(\frac{\rho_m^2 \alpha^2 (T_m - T_s)^2}{8(\rho_m - \rho_s)} + \frac{1}{6} \rho_m \alpha (T_m - T_s) \right). \quad (1)$$

In equation 1, G is the gravitational constant, g is the gravitational acceleration (887 cm sec^{-2}), L is the plate thickness as $t \rightarrow \infty$, and α is the thermal expansion coefficient ($3 \cdot 10^{-5}$ $°C^{-1}$). T_s and T_m are the temperatures of the surface and the mantle and ρ_m is the mantle density (3.3 gm cm^{-3}). ρ_s is the density of the material overlying the solid surface. For Venus, ρ_s is the atmospheric density and is effectively 0, but it would be the density of water for oceanic regions on Earth. Following Kaula and Phillips (1981), I assume $L \approx 100$ km and $T_m - T_s \approx 1000$ °C, which implies $\Delta N \approx 8$ meters. This calculation treats Venus as a flat planet rather than as a sphere. The effect of sphericity is to decrease this value further (Hager, 1983). For comparison, the degree 18 spherical harmonic geoid of Bills et al. (1987) gives a peak geoid anomaly of 35 meters at Ovda and 73 meters at Thetis. Thus, most of the geoid anomalies observed in Ovda and in Thetis must be due to density anomalies that are unrelated to a spreading center thermal structure.

If we consider a spreading center on Venus with the maximum possible topographic uplift of 1.5 km (Kaula and Phillips, 1981) and 8 meters of geoid, then following Sotin et al. (1989), we can calculate the required crustal thickness on the assumption that the remaining topography and geoid are due to Airy compensated crustal thickness variations. Ovda Regio has a peak elevation of 5 km (U.S. Geological Survey, 1984) and a peak geoid anomaly of 35 meters (Bills et al., 1987), so the Airy model must account for 3.5 km of topography and 27 meters of geoid. I estimate an admittance (the ratio of geoid to topography) of F = 0.0077 and estimate an Airy compensation depth, D, using equation 4 of Kiefer et al. (1986). This calculation is only approximate because

this relationship is for a single wavelength, whereas the admittance calculated here contains many wavelengths. Nevertheless, the resulting compensation depth estimates yield some insight into the nature of processes that may be operating in Ovda and Thetis.

Assuming a crustal density of $\rho_c = 2.8$ gm cm^{-3} and a wavelength of 4000 km (spherical harmonic degree 10), the isostatic compensation depth in Ovda must be about D = 60 km if the Airy mechanism is to account for all of the geoid and topography that is not explained by the spreading center thermal model. This estimate of the required crustal thickness is about twice that of Sotin et al. (1989). My result differs from Sotin et al. because the cooling plate model, which is more realistic, produces a smaller geoid than the half-space model used by Sotin et al. Consequently, my calculations require a larger geoid anomaly from the crustal thickening model and lead to larger values of D. Herrick et al. (1988) gave an estimate of Ovda's compensation depth that is similar to that derived here.

A number of workers have estimated that the crustal thickness in the northern plains of Venus is at most 30 km (Zuber, 1987; Banerdt and Golombek, 1988; Grimm and Solomon, 1988; Zuber and Parmentier, 1990; Kiefer and Hager, 1990b; Chapter 4). If the spreading center hypothesis is correct, then at least some of these northern plains were formed by the Aphrodite spreading system. Sotin et al. (1989) estimated that the crustal thickness which could be produced by possible spreading centers on Venus is probably less than 30 km. Both of these considerations suggest that the crustal thickness in Ovda can not be as large as the 60 km estimated above, implying that the Airy model and the spreading center model together can not fully explain the observed geoid anomaly in Ovda Regio. I therefore believe that at least some of the Ovda geoid anomaly is related to density anomalies within the mantle of Venus, as in the mantle plume model of Kiefer and Hager (1990a; Chapter 2). However, because of the approximate nature of the Airy isostasy calculation described above, the possibility that the required compensation depth is somewhat less than 60 km can not be ruled out. This leaves open the possibility that all of the Ovda Regio geoid anomaly is due to density anomalies within the crust and lithosphere.

Thetis Regio has a peak elevation of 4 km (U.S. Geological Survey, 1984) and a peak geoid anomaly of 73 meters (Bills et al., 1987). If the Airy model is applied to Thetis, it must account for 2.5 km of topography and 65 meters of geoid. This implies an admittance $F = 0.026$ and a required compensation depth $D = 230$ km, which is much larger than any reasonable estimate of the lithospheric thickness on Venus. The Airy model can not plausibly account for most of the geoid anomaly observed in Thetis Regio. Most of the Thetis geoid anomaly must therefore be related to density anomalies within the mantle. The mantle plume models of Kiefer and Hager (1990a) can explain much of the observed topography as well as the amplitude of the observed geoid anomaly. However, the observed geoid anomaly is broader than predicted by a simple plume model.

Cross-Strike Discontinuities

Crumpler et al. (1987) mapped a set of seven parallel linear features, which they termed cross-strike discontinuities (CSDs), in Ovda and Thetis. They characterized the CSDs as 2000 to 4000 km in length and 100 to 200 km in width, with an average separation between CSDs of several hundred km. The CSDs strike at about $N20^0W$, at a high angle to the approximately East-West strike of the long axes of Ovda and Thetis. They proposed that the CSDs are analogous to terrestrial oceanic transform fault zones or fracture zones. This proposal was motivated in part by an assertion that substantial lateral offsets can be observed across the CSDs, but the evidence for such offsets is not obvious.

For each CSD, Crumpler et al. cited between 3 and 6 features in the Pioneer Venus Orbiter (PVO) altimetry as structures that helped to define the trend of the CSD. They characterized these topographic features as troughs, truncated ridges, linear boundaries, and "displaced contour lines." Many of the topographic features that Crumpler et al. tabulated in their Table 1 represent small changes in the trends of individual contour lines. Unfortunately, many of these features are of uncertain validity. The PVO altimeter had a vertical uncertainty of 200 meters and a measurement footprint of about 20 km on a

side near periapse (Pettengill et al., 1980). However, because the measurements are widely spaced, the effective resolution of the resulting topographic maps (U.S. Geological Survey, 1984) is more like 50 to 100 km in the Equatorial region. Because of these resolution limitations, some of the small-scale topographic features that Crumpler et al. used to identify CSDs, particularly "displaced contours," may in fact be products of the contouring procedures used in compiling the topographic maps rather than true features on the surface of Venus.

Even if the topographic maps accurately reflect the small-scale structure, it is not clear that some of the features identified by Crumpler et al. are useful in identifying linear tectonic zones. For example, they cited a "displaced contour" at 8° S, 95° E, on CSD 3. This marks the head of a trough that strikes to the southwest. They cited "truncated ridges" at 5° S, 138° E and at 9° S, 139° E as support for the location of CSD 7. These two points help define the northwest and southeast walls of a trough that strikes North-Northeast. On CSD 4, they cited a trough at 5° N, 95° E. This point is on the northern rim of a trough whose orientation meanders somewhat. In the location where the CSD crosses the trough, the trough strikes approximately East-West. The orientations of these troughs are all quite different from the proposed North-Northwest striking CSDs.

Crumpler et al. also used two East-West altimetry profiles obtained by Arecibo. These profiles represent the topography averaged over 10 km (East-West) by 100 km (North-South) regions, with a vertical uncertainty of 100 to 150 meters. Crumpler et al. presented such data for 3 of their 7 CSDs. CSD 2 lies along the western wall of a trough in the Arecibo altimetry. This profile shows a small blip near 74° E, which Crumpler et al. identified as the location of the CSD. However, this blip is less than 100 meters deep, less than the stated vertical resolution of the profile. The base of the trough is actually about 100 km east of CSD 2. The other two CSDs for which data are given are topographically lower than the surrounding terrain by several hundred meters to a kilometer. However, several other topographic depressions of comparable amplitude also exist in the Arecibo altimetry profiles but were not identified as CSDs.

The third data set used by Crumpler et al. was PVO synthetic aperture radar (SAR) imagery, which mapped small-scale surface roughness at a horizontal resolution of 20 to 30 km. They characterized the CSDs as regions of distinct gradients or abrupt changes in radar brightness. In most cases, the SAR data in their Figure 2 does not appear to strongly correlate with the locations of the proposed CSDs. However, it is possible that other representations of the SAR data may show linear features more clearly. The two most prominent CSDs in the PVO SAR data are CSDs 2 and 5. However, these two CSDs are on the western and eastern margins of Ovda Regio, where the elevation changes rapidly. There is a known correlation between radar brightness and elevation on Venus (e.g., Head et al., 1985). It seems possible that at least some of the radar brightness gradients identified in the vicinities of CSDs 2 and 5 may be related to this global elevation-dependent pattern rather than to the supposed transform fault zones.

The foregoing considerations suggest that the Crumpler et al. (1987) CSD hypothesis can not be considered conclusive at the present time. Magellan data will hopefully provide clear evidence for either the existence or non-existence of the CSDs.

If Magellan provides evidence for the existence of the CSDs, this would significantly strengthen the case for some type of crustal divergence in Ovda and Thetis. However, this would not necessarily mean that the CSDs are transform faults and that terrestrial style plate tectonics is operating on Venus (Grimm and Solomon, 1989). The key feature of plate tectonics is the existence of **rigid** plate motions, at least in oceanic regions. In terrestrial continents, deformation is often distributed over broad zones that are hundreds or thousands of kilometers in dimension, and the language of plate tectonics can not be readily applied (Molnar, 1988). The differing tectonic styles of oceanic plates and continents reflect their differing rheologies: the oceanic lithosphere is strong, whereas regions of thick continental crust lead to a weak continental lithosphere that is incapable of behaving rigidly over long distances. The high surface temperature on Venus means that the mechanical lithosphere should be relatively thin and weak. Tectonic deformation on Venus may therefore occur in a diffuse or broadly distributed style. There is substantial evidence for such

diffuse deformation in places such as the Ishtar Terra mountain belts, the Atalanta Planitia ridge belts, and in the various tessera units (e.g., Basilevsky et al., 1986). On the other hand, there is not yet any compelling evidence for rigid lithospheric motions on Venus. Unless Magellan imagery provides evidence for rigid motions, use of plate tectonics nomenclature such as "transform fault" or "spreading center" may be inappropriate to describe features whose mechanical behavior may be quite different from terrestrial plate tectonic structures.

If Magellan data confirm the existence of CSDs, then a detailed comparison of their structure with the structure of oceanic transform fault zones may indicate the extent to which rigid lithospheric motions occur on Venus. One apparent difference between the CSDs and terrestrial transform fault zones is their widths. Crumpler et al. (1987) characterized the CSDs as being 100 to 200 km wide. In contrast, oceanic transform fault valleys are typically less than 20 km wide and the fault zone itself may be only a few kilometers across (Fox and Gallo, 1986). Transform fault valleys tend to be deepest at nodal basins where they cross the spreading center axis (Fox and Gallo, 1986). If Magellan obtains sufficiently high resolution altimetry data, the CSDs should be examined to see if they have the same behavior. The style and distribution of tectonic and volcanic features within the discontinuity zones should also be compared with observations of such features in well studied transform fault zones.

Summary

In this paper, I have shown that spreading centers as an end member process can explain at most only a small fraction of the observed geoid anomalies in Ovda and Thetis. Spreading centers can also account for no more than about a third of the observed topography in these areas. Given that both the geoid and the topography in these areas must be dominated by processes other than spreading centers, the case for possible crustal spreading must ultimately rest on geologic evidence, such as that which Magellan will hopefully provide.

References

Banerdt, W.B., and M.P. Golombek, Deformational Models of Rifting and Folding on Venus, *J. Geophys. Res., 93,* 4759-4772, 1988.

Basilevsky, A.T., A.A. Pronin, L.B. Ronca, V.P. Kryuchkov, A.L. Sukhanov, and M.S. Markov, Styles of Tectonic Deformations on Venus: Analysis of Venera 15 and 16 Data, *Proc. Lunar and Planetary Sci. Conf. 16, J. Geophys. Res. (supplement), 91* D399-D411, 1986.

Bills, B.G., W.S. Kiefer, and R.L. Jones, Venus Gravity: A Harmonic Analysis, *J. Geophys. Res., 92,* 10,335-10,351, 1987.

Black, M.T., M.T. Zuber, and D.C. McAdoo, Comparison of Observed and Predicted Gravity Profiles over Aphrodite Terra, Venus, submitted to *J. Geophys. Res.,* 1990.

Crumpler, L.S., J.W. Head, and J.K. Harmon, Regional Linear Cross-Strike Discontinuities in Western Aphrodite Terra, Venus, *Geophys. Res. Lett., 14,* 607-610, 1987.

Crumpler, L.S., and J.W. Head, Bilateral Topographic Symmetry Patterns Across Aphrodite Terra, Venus, *J. Geophys. Res., 93,* 301-312, 1988.

Fox, P.J., and D.G. Gallo, The Geology of North Atlantic Transform Plate Boundaries and their Aseismic Extensions, in *The Geology of North America, Vol. M, The Western North Atlantic Region,* edited by P.R. Vogt and B.E. Tucholke, Geological Society of America, pp. 157-172, 1986.

Grimm, R.E., and S.C. Solomon, Viscous Relaxation of Impact Crater Relief on Venus: Constraints on Crustal Thickness and Thermal Gradient, *J. Geophys. Res., 93,* 11,911-11,929, 1988.

Grimm, R.E., and S.C. Solomon, Tests of Crustal Divergence Models for Aphrodite Terra, Venus, *J. Geophys. Res., 94,* 12,103-12,131, 1989.

Hager, B.H., Global Isostatic Geoid Anomalies for Plate and Boundary Layer Models of the Lithosphere, *Earth Planet. Sci. Lett., 63,* 97-109, 1983.

Hager, B.H., and M.A. Richards, Long-Wavelength Variations in Earth's Geoid: Physical Models and Dynamical Implications, *Phil. Trans. R. Soc. London A, 328,* 309-327, 1989.

Head, J.W., A.R. Peterfreund, J.B. Garvin, and S.H. Zisk, Surface Characteristics of Venus Derived from Pioneer Venus Altimetry, Roughness, and Reflectivity Measurements, *J. Geophys. Res., 90,* 6873-6885, 1985.

Head, J.W., and L.S. Crumpler, Evidence for Divergent Plate-Boundary Characteristics and Crustal Spreading on Venus, *Science, 238,* 1380-1385, 1987.

Herrick, R.R., B.G. Bills, and S.A. Hall, Variations in Effective Compensation Depth Across Aphrodite Terra, Venus, *Geophys. Res. Lett., 16,* 543-546, 1988.

Kaula, W.M., and R.J. Phillips, Quantitative Tests for Plate Tectonics on Venus, *Geophys. Res. Lett., 8,* 1187-1190, 1980.

Kiefer, W.S., M.A. Richards, B.H. Hager, and B.G. Bills, A Dynamic Model of Venus's Gravity Field, *Geophys. Res. Lett., 13,* 14-17, 1986.

Kiefer, W.S., and B.H. Hager, A Mantle Plume Model for the Equatorial Highlands of Venus, to be submitted to *J. Geophys. Res.,* 1990a.

Kiefer, W.S., and B.H. Hager, Mantle Downwelling and Crustal Convergence: A Model for Ishtar Terra, Venus, submitted to *J. Geophys. Res.,* 1990b.

Madsen, J.A., D.W. Forsyth, and R.S. Detrick, A New Isostatic Model for the East Pacific Rise Crest, *J. Geophys. Res., 89,* 9997-10,015, 1984.

Molnar, P., Continental Tectonics in the Aftermath of Plate Tectonics, *Nature, 335,* 131-137, 1988.

Pettengill, G.H., E. Eliason, P.G. Ford, G.B. Loriot, H. Masursky, and G.E. McGill, Pioneer Venus Radar Results: Altimetry and Surface Properties, *J. Geophys. Res., 85,* 8261-8270, 1980.

Richards, M.A., and B.H. Hager, The Earth's Geoid and the Large-Scale Structure of Mantle Convection, in *The Physics of the Planets,* edited by S.K. Runcorn, pp. 247-272, John Wiley and Sons, New York, 1988.

Sandwell, D., and G. Schubert, Geoid Height Versus Age for Symmetric Spreading Ridges, *J. Geophys. Res., 85,* 7235-7241, 1980.

Sotin, C., D.A. Senske, J.W. Head, and E.M. Parmentier, Terrestrial Spreading Centers Under Venus Conditions: Evaluation of a Crustal Spreading Model for Western Aphrodite Terra, *Earth and Planetary Sci. Lett., 95,* 321-333, 1989.

U. S. Geological Survey, *Topographic and Shaded Relief Maps of Venus,* Miscellaneous Investigations Series Map I-1562, 1984.

Zuber, M.T., Constraints on the Lithospheric Structure of Venus from Mechanical Models and Tectonic Surface Features, *Proc. Lunar Planetary Sci. Conf. 17, J. Geophys. Res. (supplement), 92,* E541-E551, 1987.

Zuber, M.T., and E.M. Parmentier, On the Relationship between Isostatic Elevation and the Wavelengths of Tectonic Surface Features on Venus, *Icarus, 85,* 290-308, 1990.

Chapter 4

Mantle Downwelling and Crustal Convergence: A Model for Ishtar Terra, Venus

Walter S. Kiefer[1] and Bradford H. Hager[2]

[1] Division of Geological and Planetary Sciences
California Institute of Technology
Pasadena, CA 91125

[2] Department of Earth, Atmospheric, and Planetary Science
Massachusetts Institute of Technology
Cambridge, MA 02139

Submitted to J. Geophysical Research

Because of the similarity in size between Venus and Earth, comparisons of the two planets should yield insights into the nature of tectonic processes on large terrestrial planets. The Ishtar Terra region of Venus contains the highest known topography on the planet, as well as distinctive tectonic units. As a result, understanding the processes that formed Ishtar is important to our understanding of tectonic processes on Venus.

In this paper, we develop a model for the origin and evolution of Ishtar Terra. We begin by reviewing a variety of observations that can be used as modeling constraints. We then examine several possible models and show that the most plausible model is one in which Ishtar is a zone of crustal convergence over a region of mantle downwelling. We develop a simple fluid mechanical model for this crustal convergence and show that this places constraints on the thickness of the crust in the Ishtar region. On the basis of this flow model, we suggest a possible origin for some of the deformation observed in Fortuna Tessera. We also discuss possible origins for the volcanic activity observed in Ishtar Terra.

Observational Constraints

Models for the formation and evolution of Ishtar Terra can be constrained with a variety of observations. These include topography, gravity, tectonism, volcanism, and crater density.

Topography

The major structural elements of Ishtar Terra are identified in Figure 1. Topographic profiles of selected parts of Ishtar are shown in Figure 2. These topographic profiles are based on Pioneer Venus Orbiter (PVO) altimetry observations (Pettengill et al., 1980; USGS, 1984). The topographic data used in Figures 1 and 2 were obtained in digital form from the Lunar and Planetary Institute's Geophysical Data Facility. The topography is referenced to a mean planetary radius (MPR) of 6052 km (Bills and Kobrick, 1987).

Ishtar Terra is centered on Lakshmi Planum, a 1500 km wide oblong to irregularly shaped plateau with an average elevation of 3 to 3.5 km. To the south, Lakshmi is bounded by a steep, sloping escarpment, Vesta Rupes. In turn, Vesta is bounded on the south by the basin Sedna Planitia, which has an elevation of about -1 km (Figure 2a). Lakshmi is surrounded on the west, north, and east by the mountain belts Akna Montes, Freyja Montes, and Maxwell Montes. Akna and Freyja are each about 300 km wide, 700 to 1000 km long, and reach elevations of about 6 km (Figure 2b). Maxwell Montes is 500 km wide, 1000 km long, and reaches an elevation of about 10 km. To the east of Maxwell, Fortuna Tessera lies between 1 and 5 km elevation, with a general decrease in elevation to the east (Figure 2c). Maxwell Montes is by far the highest known topography on Venus. Outside of Ishtar Terra, the highest elevation known on Venus is approximately 6 km in Atla Regio (USGS, 1984).

Gravity

Like most highland regions on Venus, Ishtar Terra has a large positive gravity anomaly associated with it. In the eighteenth degree spherical harmonic expansion of Bills et al. (1987), the peak geoid anomaly at Ishtar is over 60 meters. In addition to the main gravity anomaly over Ishtar, there is also a significant anomaly extending to the southeast of Ishtar, which has been studied in more detail using individual PVO gravity profiles by Sjogren et al. (1984) and by Janle and Jannsen (1984). Sjogren et al. found that they could not explain the southern gravity anomaly using their isostatically compensated topography model, suggesting that there is an additional source of excess mass at depth. They suggested that it may be analogous to the gravity anomalies observed at terrestrial subduction zones. They modeled the southern anomaly as a disk of radius 1000 km, centered at 51.5° North and 8° West, with a surface density of 100 kg cm^{-2}. If this surface density contrast is due to colder than normal temperatures uniformly distributed throughout a 100 km thick lithosphere, then it corresponds to a lithospheric temperature that is about 100° C colder than normal. Janle and Jannsen suggested that the southern anomaly is due either to cold, dense, downwelling lithosphere or to high density volcanic intrusives. They favored the downwelling lithosphere interpretation on the basis that it seemed more consistent with the observed tectonics.

Tectonism

A variety of tectonic structures can be seen in radar images of the Ishtar Terra region. Interpretations of tectonic features are based on two distinct radar data sets, ground-based data obtained by the Arecibo Radio Observatory (Campbell et al., 1983; Stofan et al., 1987) and orbital data obtained by Venera 15 and 16 (Barsukov et al., 1986; Basilevsky et al., 1986), which provide complementary information. The Arecibo data have a horizontal resolution of 1 to 3 km and were obtained using a radar wavelength of 12.6 cm at an incidence angle of 60 to 70 degrees from the vertical. The Venera data have a horizontal resolution of 1 to 2 km and were obtained at a radar wavelength of 8 cm and an incidence angle of 10 degrees. At the large incidence angles obtained in the Arecibo data, the strength of the reflected radar signal is strongly dependent on the surface roughness on a horizontal scale comparable to the radar wavelength, but relatively insensitive to topographic slopes at much longer wavelengths. On the other hand, at the small incidence angles in the Venera data, the strength of the radar backscatter is a strong function of the topographic slope at wavelengths much longer than the radar wavelength (Elachi, 1987, Sec. 6.1). The Venera radar system illuminated the surface to the west of the spacecraft ground track, so that radar bright surfaces represent predominantly east-facing slopes and radar dark surfaces represent predominantly west-facing slopes. Bindschadler and Head (1989a, Figure 5) provide a good illustration of this concept.

The dominant tectonic structures observed in the Ishtar region are the banded structures observed in the Akna, Freyja, and Maxwell Montes mountain belts. These structures were first mapped in Arecibo radar imagery as regions of high radar backscatter, and hence high small-scale roughness (Campbell et al., 1983). The Arecibo data reveal a series of parallel, linear, radar bright bands, separated from one another by regions of lower radar backscatter. The individual bands are typically 10 to 20 km wide and up to several hundred km long. They are found in all three of the major mountain units in Ishtar, and in each case, the radar bright bands strike in a direction parallel to the long axis of the mountain topography. Venera 15 and 16 radar imagery also show parallel sets of radar bright and radar dark bands within the

mountain belts, indicating the presence of significant topographic slopes on horizontal scales of meters to tens of meters (Barsukov et al., 1986; Basilevsky et al., 1986). Bindschadler and Head (1989a) suggested that the correlation of high topographic slopes and high small-scale roughness may be due to downslope mass wasting, which would produce debris piles at the base of topographic slopes and hence lead to enhanced levels of small-scale roughness. They referred to this process as "tectonic weathering."

The linearity of the banded structures, their great length, and their tendency to parallel the dominant topographic trends all strongly suggest that they are of tectonic origin. Clearly, the type of stress that produced the banded terrain provides a key constraint on models for the formation of Ishtar Terra. As Solomon and Head (1984) pointed out, the banded terrain could in principle be of either extensional or compressional origin.

Several different research groups (e.g., Solomon and Head, 1984; Basilevsky et al., 1986; Crumpler et al., 1986; Head, 1990) have used a variety of morphological observations to favor a compressional origin for the mountain belts. One argument for compression in the mountain belts is a structure in Akna Montes which appears to be a partially overthrust crater (Crumpler et al., 1986).

In some places the radar bright bands wrap around and merge with adjacent bands (Solomon and Head, 1984). On Earth, such band closures are striking both in radar images (Arvidson et al., 1988) and air photos of the Appalachian mountains and are due to the differential erosion of sedimentary layers in plunging anticlines and synclines. Solomon and Head (1984) therefore interpreted the existence of band closures as indicating a compressive origin for the Ishtar bands. Although some examples of band closure can be seen both in Arecibo and in Venera imagery, they seem to be relatively rare considering the total areal extent of the mountain belts. This may in part be a resolution effect. As Arvidson et al. (1988) showed, band closure in the Appalachians is hard to detect at a radar resolution of 1 to 2 km but is easily detected at a resolution of 200 to 300 meters. Magellan may therefore provide much stronger evidence for band closure. However, even if the mountain belts are of

compressive origin, it is not obvious that Magellan should detect many examples of band closures. On Venus, the lack of liquid water implies that the erosion rate is low in comparison with Earth, so sedimentary layers may not be common. Of course, layers of basalt flows could be folded to form the banded terrain, but in the absence of significant erosion it is not clear that they would produce a radar signature comparable to that observed for the Appalachian mountains.

Observations of possible asymmetric structures in the radar bright bands have also been used as an argument for compressive deformation. Markov (1986) and Pronin (1986) have both noted that in Akna Montes, the banded structures are asymmetrically shaped, with short, steep east-facing slopes and more gentle west-facing slopes. In western-most Maxwell Montes, they found the opposite situation, with steeper dipping slopes to the west. Markov (1986, Figure 3) suggested that these asymmetric ridges formed by the emplacement of a series of thrust sheets, with the individual thrust faults dipping away from Lakshmi Planum. Crumpler et al. (1986) argued that the asymmetry of the Akna ridges resembles that of lunar mare ridges and hence favored a compressive origin for the Akna ridges. However, there are several possible difficulties with these interpretations. Both Basilevsky (1986) and Pronin (1986) noted that in central and eastern Maxwell Montes, the eastern faces of the mountain ridges commonly appear steeper than their west faces, contrary to Markov's preferred thrusting model. A more general difficulty is that details of the ridge asymmetry may be distorted by the viewing geometry. Because the Venera radar illumination is from the East, east-facing slopes will appear foreshortened relative to west-facing slopes (Elachi, 1987, Figure 6-29). Thus, a symmetric ridge could appear asymmetric in a radar image. If Magellan is able to obtain radar imagery of Ishtar viewed both from the east and from the west, this potential ambiguity could be resolved and a definitive determination of possible ridge asymmetry could be made.

Another type of deformation that has been suggested to occur in the mountain belts is strike-slip faulting. Vorder Bruegge et al. (1986) mapped 9 structures in Maxwell Montes that they termed cross-strike discontinuities, or CSDs. Based on matching patterns of radar bright and dark material, they

concluded that the CSDs were right-lateral strike-slip faults, with individual displacements of 20 to 120 km and a total displacement of 540 km across all 9 CSDs. They carried out a hypothetical retro-deformation of these strike-slip offsets and concluded that Maxwell Montes once had a surface planform similar to the current planforms of Akna and Freyja Montes. Their model thus provides a possible explanation for the observed differences in the current planforms of Maxwell and Akna. However, given that the bright and dark bands in Maxwell have a quasi-periodic spacing, it is not clear that one can uniquely define a preferred set of offsets along the proposed CSDs, or even that any offset is necessary at all. For example, the boundary between radar bright material in Maxwell and radar dark material to the northwest is an approximately linear structure at the present time (Vorder Bruegge et al., 1986, Figure 1a). However, in their retro-deformation (their Figure 1c), this boundary is split into four separate segments, with a total offset of about 200 km, implying that the current linearity of this border is merely coincidental. We therefore regard the strike-slip deformation hypothesis as an interesting but unproven idea. Crumpler et al. (1986) proposed the existence of both left- and right-lateral strike-slip faults in Akna and Freyja Montes. As in the case of Maxwell Montes, it is not clear that one can adequately define a preferred strike-slip offset in these regions on the basis of current data.

In contrast with the banded structures observed in the mountain belts, most of Lakshmi Planum is an area of moderate, relatively uniform radar backscattering in Venera imagery, with little evidence of tectonic deformation (Barsukov et al., 1986, Figure 8). Most of Lakshmi is radar dark in Arecibo imagery, indicating a surface that is smooth at a scale of 10 cm (Campbell et al., 1983; Stofan et al., 1987). There are two major exceptions to the general lack of tectonic structures in Lakshmi. One is a set of lineaments located near the eastern margin of Lakshmi, between Longitudes 355° and 0° near 62° North Latitude. Venera data shows about 6 such lineaments, each 100 to 150 km long and striking North-Northwest (Barsukov et al., 1986, Figure 8). These features have the radar signature expected of topographic valleys, and hence may be graben, indicating possible extensional deformation. In Arecibo data, these structures show levels of radar backscatter that are higher than the adjacent

plateau but not as high as in the mountain belts (Campbell, 1983; Stofan et al., 1987). This implies that the lineaments are regions of moderate small-scale roughness. The second major tectonic structure on Lakshmi is an elevated region near 345° Longitude and 65° North Latitude that has been dissected by a closely spaced set of ridges and groves. Basilevsky et al. (1986) indicated that this structure has been embayed by material from the surrounding plateau, indicating that it is relatively old. A smaller patch of what may be similar material is visible in Venera data near 328° Longitude, 72° North Latitude.

South of Lakshmi Planum is the structurally complex Vesta Rupes, which forms the transition zone between the high plateau of Lakshmi and the lowland plains to the south. In the northern part of Vesta, Venera data shows a 50 to 100 km wide belt of ridges and groves that strike in a direction which approximately parallels the contact between Lakshmi and Vesta. These ridges and grooves are up to 100 km in length and have a characteristic spacing of 10 to 15 km. Further south in Vesta, towards lower topographic elevations, the ridges and grooves become much shorter and the terrain takes on a more chaotic appearance (Basilevsky et al., 1986). In Arecibo imagery (Stofan et al., 1987), Vesta Rupes is relatively radar bright, indicating substantial small-scale roughness. The distribution of radar bright and radar dark regions is structurally complex, but there is a tendency for structures to parallel the Lakshmi Planum margin. The various structures observed in both the Arecibo and the Venera data are probably tectonic in origin, but it is unclear if they represent folding or faulting and if the deformation is extensional or compressional.

A final group of terrains in the Ishtar region that are probably related to tectonic processes are the tessera. Tessera, sometimes also referred to as parquet terrain, are characterized by multiple sets of intersecting ridges and groove systems. The ridges and grooves have characteristic spacings of 10 to 25 km and are observed to intersect at a variety of angles. Tessera units are widespread in the portion of Venus imaged by Veneras 15 and 16 (Basilevsky et al., 1986; Sukhanov, 1986). Various models for the formation of tessera were discussed by Bindschadler and Head (1989b). In the Ishtar region, the largest tessera unit occurs in Fortuna Tessera, to the east of Maxwell Montes. Smaller tessera units are observed adjacent to Akna Montes, Freyja Montes, and portions of Vesta

Rupes (Barsukov et al., 1986; Basilevsky et al., 1986). We discuss the nature of tectonic processes that may have operated in Fortuna Tessera more completely in a later section.

Volcanism

The Ishtar Terra region contains a number of features of probable volcanic origin. Two such features, Colette and Sacajawea, occur in Lakshmi Planum and have been described by Barsukov et al. (1986), Stofan et al. (1987), and Magee and Head (1988a). Both are elliptical depressions; Colette is 80 by 120 km in size and Sacajawea is 140 by 280 km. PVO altimetry indicates that both structures have depths of 1 to 1.5 km relative to Lakshmi Planum (USGS, 1984). In Venera 15 and 16 radar imagery, Colette is surrounded by a sharply defined set of lineaments that are roughly concentric with the main rim. A series of sinuous, radar bright regions, with typical widths of 10 to 20 km and lengths of 100 to 300 km, are oriented radial to Colette and are probably lava flows. These flow structures, together with Colette's elliptical shape, suggest that Colette is probably a volcanic caldera. In Arecibo radar imagery, Colette is quite bright, indicating a surface that is rough on a horizontal scale of 10 cm. Sacajawea is located about 500 km east-southeast of Colette. In Venera imagery, Sacajawea is much less distinct than Colette and lacks obvious flow features. In Arecibo imagery, Sacajawea shows some radar bright segments but is not as prominent as Colette. Despite the lack of distinctive volcanic features, Sacajawea's elliptical planform favors a volcanic rather than an impact origin. Its relatively muted appearance probably indicates that it is older than Colette.

In addition to Colette and Sacajawea, much of the rest of Lakshmi's surface may also be of volcanic origin. Magee and Head (1988b) reported the presence of a number of domes and cones that they consider to be volcanic. These structures have a wide range of sizes, from a few kilometers up to 75 km, and are sometimes observed to have summit pits. The location of many of these features appears to be structurally controlled. Magee and Head also suggested that the Lakshmi Planum plains are probably a series of lava flows. In some cases, they identified plains units with specific source regions. In other cases, specific sources could not be identified, but the plains were nevertheless

suggested to be volcanic on the basis of observed embayment relationships. In northwest Ishtar, near the junction of Akna and Freyja Montes, Gaddis and Greeley (1989) described a basin that is 200 by 250 km in size and has a maximum depth of about 1.5 km relative to its surroundings. They suggested that this structure may be volcanic, but diagnostic landforms are difficult to identify and the origin of this basin must be considered as uncertain at the present time.

Cleopatra Patera is a 100 km diameter circular structure that occurs on the east flank of Maxwell Montes. In comparison with its surroundings, Cleopatra is radar dark both in Arecibo imagery (Campbell et al., 1983) and in Venera imagery (Barsukov et al., 1986), indicating that the floor of Cleopatra is relatively smooth both at a scale of order 10 cm and at a scale of several meters. Cleopatra is clearly superimposed on the banded terrain in Maxwell Montes, indicating that it is younger than the banded terrain. Cleopatra's origin has been somewhat controversial. Ivanov et al. (1986) suggested that Cleopatra is a double ring impact structure. Basilevsky and Ivanov (1990) concluded that Cleopatra might be either an impact crater or a volcanic caldera and asserted that in either case it is morphologically unusual. Schaber et al. (1987a) advanced a number of arguments in favor of a volcanic origin of Cleopatra, the most persuasive of which involve Cleopatra's topographic relief. Venera 16 altimetry shows that Cleopatra has two distinct floor levels. The inner floor is quite flat and 2 to 2.5 km deep relative to the rim. The outer floor is somewhat rougher and only about 1 to 1.5 km deep. Cleopatra is much deeper than expected for a 100 km impact crater on Venus. Based on a gravity scaling of Pike's (1980) depth-diameter relationship for lunar impact craters, a depth of only about 0.8 km is expected. Venera altimetry data for two other Venus craters in the size range 100 to 140 km diameter, Cochran and Klenova, show that both are only 0.7 to 0.8 km deep. Moreover, the substantial difference in elevation between inner and outer floors is unlike the behavior expected for double ring impact basins. On the other hand, these topographic relationships are quite consistent with a volcanic caldera. Basilevsky and Ivanov (1990) argued that Cleopatra's depth could be consistent with an impact origin if the layer of impact breccia that normally occurs on the floor of

an impact crater somehow managed to escape from Cleopatra, but their proposed mechanisms for accomplishing this are not convincing. On the basis of Schaber et al.'s topographic arguments, we believe that Cleopatra is probably a volcanic structure.

Cratering Age

A final constraint on models for Ishtar is its age. Basilevsky et al. (1987) identified about 12 features in Ishtar that they regarded as probable impact structures. Most of these are in Basilevsky et al.'s morphological freshness class 2 and have well defined rims. Some of the larger ones also have central peaks. These structures are unambiguously impact features. On the other hand, the more degraded class 3 features are harder to identify reliably. Some of these features might well turn out to be volcanic structures in higher resolution Magellan imagery. None of the impact craters observed in Ishtar have the radar bright rim deposits observed in fresh, morphologic class 1 craters elsewhere on Venus.

In order to estimate the cratering age of a planetary surface, one must know both the observed crater density and the cratering rate. Unfortunately, both quantities are in dispute for Venus. For crater diameters $D \geq 8$ km, Basilevsky et al. (1987) gave an average crater density of $1.2 \cdot 10^{-6}$ km^{-2} for the $1.15 \cdot 10^{8}$ km^{2} surveyed by Venera 15 and 16. Although their Figure 17 shows that Ishtar's crater density is somewhat higher than for their survey area as a whole, they concluded that the statistical uncertainties in their data are large enough that Ishtar's crater density is indistinguishable from the crater density of the entire survey area. On the other hand, Plaut and Arvidson (1988) and Burba (1989) argued that regional variations in crater density can be statistically distinguished in the Venera data and that Ishtar's crater density is perhaps twice the average value. Because Magellan will obtain radar imagery with a resolution approaching an order of magnitude higher than Venera, it may be possible to identify many additional small craters. This could improve the crater density statistics and therefore might provide a definitive resolution to this debate. On the other hand, the dense atmosphere of Venus inhibits the formation of small impact craters, so if a dense atmosphere has existed for

most of the history of Venus, then there may not be many small impact craters present.

Basilevsky et al. (1987) combined their estimate of Venus's crater density, together with a scaled version of Hartmann et al.'s (1981) lunar cratering flux, to estimate an average age for Venus's surface of nearly 1 billion years. Schaber et al. (1987b,c), on the other hand, favored a much younger average age, of order 100 to 200 million years, although they conceded that an average age of 400 to 500 million years is possible. These two contrasting estimates differ primarily in their choice of cratering flux. The Hartmann et al. flux represents an average over the last 3.3 billion years. Schaber et al. based their estimates on the Earth's Phanerozoic cratering record along with estimates of the cratering rate due to currently observed Earth and Venus crossing asteroids. This gives a significantly higher cratering flux and hence a younger average age. Combining the uncertainties in both the crater density and the cratering flux, Ishtar may range in age from 100 million years to as much as 1 to 2 billion years.

Models for the Origin of Ishtar Terra

Models for the formation of Ishtar's high topography can be divided into two main classes. One class are thermal models, in which Ishtar's topography is supported by high temperatures in the lithosphere or in the mantle beneath Ishtar. This class of models can be further subdivided into two sub-classes, active mantle upwelling and lithospheric delamination. Basilevsky (1986) and Pronin (1986) have suggested that a convective upwelling is centered under Lakshmi Planum. Pressure release melting would occur within the upwelling, accounting for the observed volcanism in Lakshmi. They also suggested that the radial outflow of material away from Lakshmi would produce a zone of crustal convergence and compressive deformation that could explain the mountain belts observed in Ishtar. The mechanism for localizing the crustal convergence in the region of the currently observed mountain belts was not specified by these workers. Presumably, it must involve the existence of convective downwellings near the mountain belts. Basilevsky suggested that the convective

downwelling would occur in the lowland basin Atalanta Planitia, but this is 6000 km away from Ishtar and downwelling in Atalanta could not create a localized zone of crustal convergence within the current mountain belts.

Upwelling mantle plumes are now widely accepted as the cause of Beta Regio and perhaps other parts of the Equatorial Highlands (McGill et al., 1981; Morgan and Phillips, 1983; Kiefer et al., 1986; Kiefer and Hager, 1988; Banerdt, 1986). We have modeled these mantle plumes using finite element techniques and have shown that the plume model can quantitatively account for the observed topography and geoid anomalies in the Equatorial Highlands (Kiefer and Hager, 1988, 1990a; Chapter 2). The plume model is also consistent with evidence for shield volcanism and rifting in the Equatorial Highlands. However, if the upwelling plume model is applicable to features such as Beta Regio, then the strong contrast in tectonic styles between Beta and Ishtar make it unlikely that Ishtar was formed by an upwelling plume. Our finite element models show that the surface topography over a rising mantle plume has a dome-like shape, although this can be modified by volcanic activity and by rift-zone formation. This is consistent with the topography of Beta Regio and other features in the Equatorial Highlands but inconsistent with the flat plateau surface in Lakshmi Planum. Also, the upwelling model predicts extensional deformation near the upwelling. As summarized above, there is some evidence for extensional deformation in Ishtar, but it is minor in comparison to the observed compression. In contrast, extensional rifting dominates in the Equatorial Highlands (McGill et al., 1981; Schaber, 1982; Campbell et al., 1984; Stofan et al., 1989). Finally, it is difficult to account for the observed mountain belts in the context of a plume model. No such structures are observed near Beta Regio or other likely plume sites in the Equatorial Highlands.

A second thermal mechanism for creating Ishtar's high topography is lithospheric delamination, in which the cold thermal boundary layer is detached from the surface and replaced by hot mantle material. As discussed by Morgan and Phillips (1983), if the lithosphere's thermal structure is approximated as a simple linear geotherm and if complete delamination occurs, then

the predicted uplift is

$$\delta h = 0.5\, l\, \alpha \Delta T\,, \qquad (1)$$

where δ h is the uplift due to delamination, l is the lithospheric thickness prior to delamination, α is the volumetric thermal expansion coefficient, and ΔT is the temperature contrast across the lithosphere. Kaula and Phillips (1981) used boundary layer theory to estimate $l \approx 100$ km and $\Delta T \approx 1000$ K for Venus. Adopting these values and $\alpha = 3 \cdot 10^{-5}$ per degree yields an estimate of $\delta h \approx 1.5$ km, which is not adequate to explain the observed height of either Lakshmi Planum or the surrounding mountain belts. Moreover, an isolated, elevated plateau is in deviatoric tension relative to its surroundings (Bott and Kusznir, 1979), and thus lithospheric delamination acting alone could not produce the observed compressive deformation. It is possible, however, that lithospheric delamination has played some role, in combination with other mechanisms, in producing Ishtar's observed topography.

A second class of models for Ishtar invoke variations in crustal thickness as an explanation for the high topography. One mechanism for producing lateral variations in crustal thickness is volcanism. Clearly, volcanism has occurred in Ishtar and has probably contributed to crustal thickening. However, volcanic construction, like lithospheric delamination, would lead to extensional deformation of the high topography, and thus cannot be the sole mechanism responsible for forming Ishtar. It is also possible to create lateral variations in crustal thickness by tectonic processes. This is illustrated schematically in Figure 3, which shows a zone of crustal convergence and thickening overlying a region of downwelling mantle. The mantle flow entrains crustal material and causes it to pile up over the downwelling. Because the crust is less dense than the mantle, isostasy requires that the region of thick crust will be topographically higher than its surroundings. Although the mantle downwelling illustrated in Figure 3 is symmetric about a vertical plane, the downwelling could also have an asymmetric structure, as is the case for terrestrial subduction zones. An axisymmetric downwelling can be ruled out, because with such a downwelling geometry, the azimuthal normal stress, $\tau_{\phi\phi}$, is more compressive than the radial normal stress, τ_{rr}. This implies mountain belts that are radial

to the center of the downwelling, whereas the observed mountain belts are approximately concentric about Lakshmi Planum.

The crustal convergence model can produce both the crustal thickening needed to explain Ishtar's high topography and the horizontal compression necessary to explain the tectonics, and we therefore favor it as the dominant mechanism in the origin of Ishtar Terra. Similar models have been advocated by other workers (Morgan and Phillips, 1983; Banerdt, 1986; Bindschadler and Parmentier, 1989; Vorder Bruegge and Head, 1989; Head, 1990). The Tibetan Plateau and Himalaya Mountains provide a terrestrial analog. Like Lakshmi Planum, Tibet is a high, flat plateau surrounded on several sides by mountain belts. Moreover, Lakshmi and Tibet have similar horizontal dimensions. The mean elevation of Tibet is 5 km (Bird, 1978), somewhat higher than Lakshmi, whereas the peak elevation in the Himalayas, 9 km, is somewhat less than the peak elevation in Maxwell Montes. The overall similarity between the two regions supports the crustal convergence model for Ishtar Terra.

Nevertheless, it seems likely that other mechanisms also played a role in the formation of Ishtar Terra. As noted above, volcanism has undoubtedly contributed to Ishtar's formation. Lithospheric delamination may also have occurred. Houseman et al. (1981) modeled the thermal evolution of the mantle underlying terrestrial continental convergence zones. In such an environment, the cold thermal boundary layer may become detached from the surface layer and sink into the mantle on a timescale that may be as short as 10 million years. England and Houseman (1989) recently argued that such a delamination event may be necessary to explain the development of normal faults in the Tibetan plateau within the last 5 million years. Houseman et al.'s delamination time scale should also be applicable to Venus, so given Ishtar's estimated cratering age in excess of 100 million years, it seems likely that Ishtar has experienced one or more delamination events during its history. If most or all of the mantle lithosphere delaminates during one of these events, then the base of the crust will be exposed to temperatures of order 1400 °C. This is one possible cause of volcanic activity in Ishtar Terra.

Viscous Crustal Flow Due to Topographic Gradients

The high surface temperature on Venus allows viscous flow of crustal materials to occur at relatively shallow depths (Weertman, 1979; Smrekar and Phillips, 1988). In this section, we develop a simple model of viscous flow in Venus's crust and the coupling of this flow to flow in the mantle. This work was presented in abstract form by Kiefer and Hager (1990b). The basic model is shown in Figure 4a. Variations in topographic height, h, are assumed to be due to isostatically compensated variations in crustal thickness. Viscous flow within the crust is driven both by a basal velocity, v_o, which is imposed by the mantle flow field, as well as by lateral pressure gradients within the crust that are associated with topographic gradients. Figure 4b considers a possible later stage in the evolution of the viscous crustal flow and will be discussed in greater detail later.

We assume that the horizontal planform of the flow has a sheet-like or planar structure, with no variation along strike, thus allowing us to neglect the out-of-plane component of velocity. Although this assumption is certainly not applicable to Ishtar Terra as a whole, the observed topographic contours suggest that is a reasonable approximation in some regions, for example in Fortuna Tessera. The topographic profiles shown in Figure 2 show that the regions of high topography are in excess of 1000 km in lateral extent. As we will show later, the thickness of the crust is likely to be significantly less than 100 km. Because the horizontal length scale is so much larger than the vertical length scale, on average the horizontal flow velocity, v_x, should be much larger than the vertical flow velocity, v_z. We therefore set $v_z = 0$ and solve only for v_x. With these two approximations, we have a one dimensional problem and it is possible to derive an analytic solution for the flow, even when using a non-Newtonian rheology.

We choose a coordinate frame in which z increases from the surface downward. The depth of the crust-mantle interface, D_{max}, is determined from the Airy isostasy condition:

$$D_{max} = D + h\left[1 + \frac{\rho_c}{(\rho_m - \rho_c)}\right], \tag{2}$$

where h is the topographic height relative to mean planetary radius, D is the reference crustal thickness when h=0, and ρ_c and ρ_m are the densities of the crust and mantle. The solution takes the form

$$v_x(z) = v_o + \int_{D_{max}}^{z} \frac{\partial v_x}{\partial z'}\, dz' = v_o + 2 \int_{D_{max}}^{z} \dot{\epsilon}_{xz}(z')\, dz' \quad (3)$$

where $\dot{\epsilon}_{xz}$ is the shear strain-rate. The integral is carried out in the direction of decreasing z because the velocity boundary condition is imposed at the base of the crust, at $z = D_{max}$. The shear-strain rate can also be written as

$$\dot{\epsilon}_{xz} = A\, \tau^{n-1}\, \tau_{xz} \exp\left(\frac{-E}{RT(z)}\right), \quad (4)$$

where τ_{xz} is the shear stress, τ is the second stress invariant, R is the gas constant, T(z) is the temperature at depth z, and A, E, and n are rheological parameters that depend on the type of material. Over the depth range of interest in this problem, the effects of pressure on the rheology can be ignored. Given our assumption that $v_z = 0$, it is clear that $\frac{\partial v_z}{\partial z} = 0$. The continuity equation then requires that $\frac{\partial v_x}{\partial x} = 0$, so that the deviatoric normal stresses τ_{xx} and τ_{zz} must both equal zero.

At the summit of the mountain range, the topographic gradient and hence the pressure gradient that drives the viscous flow change sign. The crustal flow driven by the pressure gradient therefore goes to zero at the summit and will take on non-zero values of opposite sign on the two sides of the summit. Clearly, in this region $\frac{\partial v_x}{\partial x}$ is not zero. Indeed, as shown in Figure 4b and as discussed more fully later, it is possible that v_z is the dominant velocity component in the summit region, so that models of the crustal flow in the vicinity of the mountain belts must explicitly solve the coupled momentum equations for both v_x and v_z. For a temperature- and stress-dependent rheology such as that given in equation 4, the two dimensional flow problem is analytically intractable and must be analyzed using numerical techniques. However, in locations which are substantial distances from the mountain belt summits, it is a

reasonable approximation to assume that $\frac{\partial v_x}{\partial x} = 0$. Similar approximations are made in other geologic flow problems, for example in analytic boundary layer models of mantle convection. We return to this issue when we discuss specific applications below. With these approximations, the only stress in the problem is τ_{xz}, and the stress invariant in equation 4 can simply be replaced by τ_{xz}. Combining equations 3 and 4, we have

$$v_x(z) = v_o + 2 \int_{D_{max}}^{z} A(\tau_{xz}(z'))^n \exp\left(\frac{-E}{RT(z')}\right) dz' \quad . (5)$$

We determine τ_{xz} from the horizontal momentum equation,

$$-\frac{\partial P}{\partial x} + \frac{\partial \tau_{xx}}{\partial x} + \frac{\partial \tau_{xz}}{\partial z} = 0 \, . \quad (6)$$

However, because $\tau_{xx} = 0$, equation 6 reduces to $\frac{\partial \tau_{xz}}{\partial z} = \frac{\partial P}{\partial x}$, and hence

$$\tau_{xz}(z) = z\frac{\partial P}{\partial x} + C \, . \quad (7)$$

We assume that the lateral pressure gradient arises from lateral variations in the height of isostatically compensated topography, so that

$$\frac{\partial P}{\partial x} = \rho_c \, g \, \frac{\partial h}{\partial x} \, , \quad (8)$$

where $\frac{\partial h}{\partial x}$ is the topographic slope and g is the gravitational acceleration. The constant C in equation 7 is determined from the free-slip condition, $\tau_{xz} = 0$ at the surface. The free-slip surface condition is satisfied if equations 7 and 8 are combined and rewritten as

$$\tau_{xz}(z) = \rho_c \, g \, \frac{\partial h}{\partial x} z \, . \quad (9)$$

Together, equations 5 and 9 constitute the desired solution to the problem. In practice, we carry out the integral in equation 5 numerically using a trapezoid rule, typically using a step size $dz = 0.5$ km. A test calculation using $dz = 0.1$ km changed the calculated velocities by only 0.2 %.

The rheological law (equation 4) requires that we specify temperature as a function of depth in the crust. Neglecting the possible contributions of lateral advection and shear heating to the thermal structure, T(z) satisfies the vertical heat conduction equation,

$$k\frac{\partial^2 T}{\partial z^2} + H(z) = 0, \tag{10}$$

where k is the thermal conductivity and H is the volumetric heat generation rate due to radiometric heating of the crust. Following Sclater et al. (1980), we assume that the radioactive heating decays with depth as

$$H(z) = H_o \exp(\frac{-z}{\lambda}) . \tag{11}$$

One boundary condition is that $T(0) = T_s$, where T_s is a specified surface temperature. The other boundary condition is that the surface heat flow, q(0), is given by

$$q(0) = k\frac{\partial T}{\partial z}\Big|_{z=0} = q_b + \int_0^{D_{max}} H_o \exp(\frac{-z}{\lambda})dz$$

$$= q_b + H_o\lambda\left[1 - \exp(\frac{-D_{max}}{\lambda})\right]. \tag{12}$$

Equation 12 is simply a statement of conservation of energy, where q_b is the heat flow from the mantle into the crust and D_{max} is the total crustal thickness as defined in equation 2. With these boundary conditions, T(z) takes the form

$$T(z) = T_s + \left[\frac{q_b}{k} - \frac{H_o\lambda}{k}\exp(\frac{-D_{max}}{\lambda})\right]z$$

$$+ \frac{H_o\lambda^2}{k}\left[1 - \exp(\frac{-z}{\lambda})\right]. \tag{13}$$

Equation 13 shows that T(z) depends on four different combinations of thermal parameters: T_s, $\frac{q_b}{k}$, $\frac{H_o}{k}$, and λ. We assume that T_s is the atmospheric temperature at the surface, given by the relationship

$$T_s = 737\,K - 7.7\,K/km * h . \tag{14}$$

In equation 14, 737 K is the surface temperature at MPR and 7.7 K km^{-1} is the observed atmospheric lapse rate (Seiff, 1983). The crustal convergence hypothesis assumes that Ishtar is a region of cold, downwelling mantle and hence should have relatively low heat flow. We adopt a nominal value of $q_b = 25$ mW m^{-2} based on observations of reduced heat flow in terrestrial shield regions (Sclater et al., 1980, Table 8). We have no information on the crustal composition in the Ishtar region, so we assume that Venera and Vega lander observations in the equatorial regions of Venus can also be used to characterize the Ishtar region. Although we have no direct knowledge of the mineralogy of Venus's crust, major element analyses obtained by X-ray fluorescence spectroscopy at 3 landing sites are consistent with a basaltic composition (Surkov et al., 1984, 1986). We therefore use laboratory data for diabase to estimate both the thermal conductivity and the rheological parameters needed in our model. Clark's (1966) compilation of thermal conductivities gives k for diabase in the range 2.09-2.35 W m^{-1} K^{-1} in the temperature range 273 K to 673 K. Clark's data shows some tendency for decreasing k as T increases, reflecting the decreasing efficiency of phonon transport with increasing temperature. However, at still higher temperatures, such as those which characterize Venus's crust, the radiative contribution to thermal conductivity becomes increasingly important (Solomon et al., 1981, Sec. 9.4.2). We adopt a nominal value of $k = 2.5$ W m^{-1} K^{-1}, which leads to a nominal value of $\frac{q_b}{k} = 10$ K km^{-1}. This is probably a lower bound on the geothermal gradient at Ishtar and hence our estimates of the temperature in Venus's lower crust will also be lower bounds. The temperature dependence in equation 5 then implies that our velocity estimates will also be lower bounds.

The abundances of the radioactive elements K, U, and Th have been measured at 5 near-equatorial sites by gamma ray spectroscopy. Four sites, Veneras 9 and 10 and Vegas 1 and 2, give similar results, with average abundances of 0.41% K, 0.6 ppm U, and 2.0 ppm Th (Surkov et al., 1987). For our assumed crustal density of 2.8 gm cm^{-3}, this corresponds to a volumetric heating rate of $H_o = 3.6 \cdot 10^{-7}$ W m^{-3}. The Venera 8 lander measured substantially higher radioactive abundances, corresponding to $H_o = 1.5 \cdot 10^{-6}$ W m^{-3} (Surkov et al.,

1987). Because our model assumes that crustal material undergoes net convergence, we assume that λ changes in proportion to the total amount of crustal thickening. Thus, if we use λ' to denote the value prior to crustal thickening and λ to denote the value after crustal thickening, the two quantities are related by

$$\lambda = \lambda' \left(\frac{D_{max}}{D} \right), \tag{15}$$

where D and D_{max} are defined as before. On Earth, values of λ' can be estimated from reduced heat flow data. Sclater et al. (1980, Table 8) give data for a number of continental heat flow provinces, with λ' ranging from 4.5 to 16 km. We therefore adopt a nominal value of $\lambda' = 10$ km. This implies that $\frac{H_o \lambda'}{k}$ has a nominal value of 1.4 K km^{-1}. Figure 5 shows a geotherm calculated using equation 13 and the nominal thermal parameters described above. This model is initialized with h=3 km and D=20 km, corresponding to a total crustal thickness of $D_{max} = 40$ km. The surface temperature is 714 K, the basal temperature is 1145 K, and the surface heat flow is 31 mW m^{-2}.

Parameter Studies

As the foregoing discussion shows, crustal flow velocities depend on the values of a number of parameters. In this section we present the results of a series of parameter studies in order to show quantitatively how the flow is affected by various parameter values. In a later section, we apply the model to observations of Fortuna Tessera and show that it places constraints on the maximum allowed crustal thickness.

The results of the parameter sensitivity studies are shown in Figures 6, 7, and 8. In each of the panels of these figures, the solid line represents the same reference model. The parameters used in this model are summarized in Table 1. In each figure, we vary a single parameter and hold the other parameters fixed. The figures show flow velocities, v_x, as a function of depth. We have set the basal velocity $v_o = 0$, so that the flow velocity simply represents the flow of crustal material down-slope. We consider the effect of non-zero basal velocities in a later section. Because a free-slip surface is assumed, the velocity profile is

a monotonic function of depth and reaches its maximum velocity at the surface. Depth is expressed relative to MPR, so that negative depth corresponds to topography above MPR. Crustal thickness is specified in terms of its reference value in the plains, D in Figure 4a. For the assumed value of h=3 km, D=20 km corresponds to a total crustal thickness of $D_{max} = 40$ km.

One class of model parameters are the rheological law constants, A, E, and n, that are needed in equation 4. Given the evidence cited earlier for a basaltic composition crust on Venus, we assume a diabase rheology. Two sets of laboratory determinations of the diabase flow law are available. Shelton and Tullis (1981) give $A = 8.8 \cdot 10^{-8}$ bar^{-n} sec^{-1}, $E = 260$ kJ mole^{-1}, and $n = 3.4$. Caristan (1982) gives $A = 5.45 \cdot 10^{-5}$ bar^{-n} sec^{-1}, $E = 276$ kJ mole^{-1}, and $n = 3.05$. The reason for the very large difference in the value of A from the two sets of experiments is unclear. It could be due to differences in the composition of the samples used by the two experimental groups, or it may simply represent the real uncertainty in the value of A. Figure 6 shows the resulting flow velocities as a function of depth for these two rheological laws. Our reference model is shown as the solid line and uses the Shelton and Tullis flow law. It gives a peak flow velocity of 4 cm year^{-1}, whereas the Caristan model reaches a much larger peak velocity of 100 cm year^{-1}.

Our philosophy is to choose material constants conservatively, so that the resulting flow velocities will be lower bounds. In the work that follows, we therefore make use of the Shelton and Tullis flow law unless otherwise indicated. Grimm and Solomon (1988) pointed out that the compositions reported by the Venera landers are closer to the composition of Caristan's experimental samples than they are to the samples used by Shelton and Tullis. As a result, Grimm and Solomon favored the use of Caristan's rheology in their crater relaxation calculations. If this reasoning is correct, then the actual flow velocities could be more than an order of magnitude larger than calculated in this paper.

A second class of model parameters involve the topographic height, h, the topographic gradient, $\frac{\partial h}{\partial x}$, and the crustal thickness, expressed in terms of either D or D_{max}. Figure 7 shows the effects of varying these parameters. In

Figure 7a, we fix D = 20 km and vary the value of $\frac{\partial h}{\partial x}$. As shown in equations 5 and 9, the outflow velocity is a strongly increasing function of topographic gradient. The peak velocity increases from 0.4 cm year^{-1} for a surface slope of $\frac{\partial h}{\partial x} = 0.2°$ to 16 cm year^{-1} for a slope of $\frac{\partial h}{\partial x} = 0.6°$, a factor of $3^{3.4}$. Figure 7b examines the effects of varying crustal thickness. We fix $\frac{\partial h}{\partial x} = 0.4°$ and vary D from 15 to 25 km, corresponding to D_{max} from 35 to 45 km. The outflow velocity increases rapidly with increasing crustal thickness, from 0.7 cm year^{-1} at $D_{max} = 35$ km to 20 cm year^{-1} at $D_{max} = 45$ km. This is due in part to the fact that the shear stress is an increasing function of depth (equation 9). More important, however, is the effect of increasing temperature with depth, which causes an exponential increase in velocity.

The third important class of parameters are those that affect the crust's thermal structure. Increasing the value of $\frac{q_b}{k}$, $\frac{H_o}{k}$, or λ' leads to increased interior temperatures and hence to higher flow velocities. Figure 8 shows the effects of varying $\frac{q_b}{k}$. Reducing $\frac{q_b}{k}$ from its nominal value of 10 K km^{-1} to 8 K km^{-1} decreases the flow velocity to 0.6 cm year^{-1}. Increasing $\frac{q_b}{k}$ to 12 K km^{-1} gives a peak flow velocity of 23 cm year^{-1}. If H_o is increased from its nominal value to the Venera 8 value of $1.5 \cdot 10^{-6}$ W m^{-3}, the outflow velocity increases from its nominal value of 4 cm year^{-1} to 46 cm year^{-1}. On the other hand, if we assume no crustal heating, $H_o = 0$, then the peak outflow velocity is reduced to 1.7 cm year^{-1}. The value of λ' has only a modest effect on the calculated flow velocities. Increasing λ' to 15 km increases the peak outflow velocity to 5.8 cm year^{-1}; decreasing λ' to 5 km decreases the peak outflow velocity to 2.4 cm year^{-1}. The limiting case $\lambda' \rightarrow \infty$ corresponds to a uniform distribution of radioactive elements within the crust. For the other parameters of our nominal model, this corresponds to a basal temperature of 1220 K and a surface heat flow of 39 mW m^{-2} and has a peak outflow velocity of 25 cm year^{-1}.

Surface Boundary Condition: Free-slip versus Rigid

In the preceding discussion, we assumed that the entire crust behaved viscously and that the surface boundary condition is free-slip, or zero shear stress. Strictly speaking, this boundary condition is appropriate because Venus's atmosphere is incapable of exerting a significant shear on the crust. With these assumptions, Figures 6 to 8 show that v_x can reach large values at the surface. However, with a temperature of order 700 K, Venus's near-surface region has a very high effective viscosity and may be more properly treated as a plastic medium rather than a viscous medium. At greater depths and higher temperatures, of course, the crust will behave viscously. The near-surface layer can exert a shear stress on the portion of the crust that flows, so that a free-slip boundary is no longer appropriate. If the plastic layer is continuous across the surface, the appropriate outer surface boundary condition is a rigid boundary, $v_x = 0$.

We have modeled the effects of a strong surface layer using a modification of the formulation described above. Because most of the shear strain occurs near the base of the crust, where the viscosity is low, for the purpose of calculating a flow velocity profile it does not matter whether the near-surface is treated as a plastic or viscous medium, and we therefore continue to assume that the rheological law given by equation 4 applies to the entire crust. The important point is that the surface boundary condition has been changed from $\tau_{xz} = 0$ to $v_x = 0$. In this case, the integration constant in equation 7 can no longer be determined analytically. Instead, it is determined by combining equations 5, 7, and 8 and iteratively searching for a value of C that satisfies the boundary condition. A rigid surface substantially reduces the flow velocities relative to the free-slip case. If we use a rigid top with the parameter values given in Table 1, we find that the peak flow velocity is only $2 \cdot 10^{-3}$ cm year^{-1} and is reached near a depth of 30 km. In contrast, with these same parameters and a free-slip top, we found a peak flow velocity of 4 cm year^{-1} (Figure 6, solid line). If we increase D to 60 km (corresponding to a total crustal thickness of $D_{max} = 80$ km), we get the result shown in Figure 9. In this case, the peak flow velocity is 22 cm year^{-1} and is reached near a depth of 70 km. As Figure

7b shows, a comparable flow velocity is reached in the free-slip top case when D is only about 25 km. The general form of the velocity profile shown in Figure 9 is similar to that found by Webb and Stevenson (1987) in their study of subsidence of volcanic features on Io.

If the strong outer portion of the crust is not horizontally continuous, but instead fails because its yield stress is exceeded in some places, then the condition $v_x = 0$ is no longer appropriate as a surface boundary condition. Such failure zones would result in a region of crust cut by a series of faults. These failure zones would effectively decouple the various segments of unbroken crust from one another. Within each segment of strong crust, the flow velocity is determined by the average topographic, rheologic, and thermal parameters for that segment of crust. Differences in flow velocity between various segments of crust are accommodated by horizontal extension or compression within the fault zones. In this situation, profiles of flow velocity should resemble those shown for free-slip tops in Figures 6 to 8. An appropriate analogy can be made to the motion of lithospheric plates on Earth. If the Earth's outer layer were horizontally continuous, we would not expect to see plate motion at the Earth's surface. However, both spreading centers and subduction zones behave as weak zones that decouple the various plates from one another, allowing the observed plate velocities to occur.

As we discussed earlier, there is substantial evidence for tectonic deformation in Ishtar Terra, particularly in the mountain belts and the tessera. Although some of this may represent folding, faulting has undoubtedly occurred as well. Presumably at least some of these faults penetrate to the base of the plastic layer, and thus could have created weak zones within the crust. We therefore believe that the results obtained for the free-slip top boundary are a more accurate description of the crustal flow than the results obtained for a rigid top boundary. Nevertheless, we include the rigid boundary results here for completeness.

Applications of the Crustal Flow Model

Until now, we have assumed that the basal velocity, v_o, is zero, which implies that the crustal flow is entirely down-slope. However, if a large enough basal velocity is applied, then there can be a net movement of crustal material up the topographic slope. This net up-slope crustal flow is required if Ishtar is to be formed by the crustal convergence mechanism. In this section we examine the required magnitude of v_o and show that this places constraints on the maximum allowed crustal thickness.

In order to determine the minimum value of v_o required to build Ishtar, we calculate the volume flux, Q, of material through a vertical plane,

$$Q = \int_0^{D_{max}} v_x(z)\, dz \quad , \tag{16}$$

where v_x is the flow velocity given by equation 5. We define the no net flux velocity, v_{NF}, such that $Q = 0$ when $v_o = v_{NF}$. Because velocities are taken to be positive down-slope, we must have $v_{NF} < 0$. Our hypothesis is that Ishtar formed as a result of crustal convergence, which requires that $Q < 0$. Clearly, for $Q < 0$, we must have $v_o < v_{NF} < 0$.

An example is shown in Figure 10. The flow law and thermal parameters used in this calculation are given in Table 1. For this calculation, we have used $h = 3.1$ km and $\frac{\partial h}{\partial x} = 0.41°$. These values differ slightly from those in Table 1 and were chosen to be representative of Fortuna Tessera, as discussed below. With these model parameters, the peak flow velocity is $v_x(0) - v_o = 5.6$ cm year^{-1} and the no net flux velocity is $v_{NF} = -5.2$ cm year^{-1}. Figure 10 illustrates the resulting velocity profile. Near the base of the crust, the flow is up-slope (negative flow velocity), whereas the near-surface material is flowing down-slope at a velocity of 0.4 cm year^{-1}. If we had chosen $v_o < -5.2$ cm year^{-1}, then net up-slope transport would have occurred.

As shown in Figure 4, the crustal flow pattern is likely to vary over time as Ishtar is built up. In the early stages of Ishtar's formation, the topography will be low and hence the pressure gradient will be small. As shown in Figure

4a, during this period, the crustal flow will be directed up the topographic gradient at all depths within the crust. Later, as the topography increases, the increasing pressure gradient will cause the near-surface layer to flow downslope, although the material near the base will continue to flow up-slope in response to the applied basal velocity. This is the situation illustrated in Figures 4b and 10. The complete circulation pattern clearly requires a region of vertical flow to connect the incoming basal flow with the outgoing near-surface flow. As shown in Figure 4b, we suggest that this vertical flow occurs in the vicinity of the mountain belts. v_z is likely to be significant over a horizontal distance of order the crustal thickness. At greater distances from the mountain belts, the flow should be predominantly horizontal, as we assumed in deriving the flow solution. There must also be some mechanism for accommodating the crustal outflow at the base of the topographic slope. We assume that this occurs in some way, although with our present knowledge of the geology of Venus it may be premature to identify specific regions where this occurs.

We can use the calculated magnitude of v_{NF} as a discriminant to determine what combinations of model parameters are allowed. Of course, we do not know what the actual basal velocity is in the Ishtar Terra region, but it is possible to place bounds on the allowed value of v_o. The basal velocity is determined by the convective velocity in Venus's mantle. Because Venus and Earth are of comparable size and are likely to have similar total heat sources, convective velocities in the two mantles should also be comparable. On Earth, plate velocities presently range up to about 10 cm year^{-1} (Minster and Jordan, 1978). We therefore adopt $v_o < 20$ cm year^{-1} as a conservative upper bound on the allowed basal velocity. For a given set of model parameters, including topographic slope, crustal thickness, flow law, and thermal parameters, we calculate the required value of v_{NF}. If the absolute magnitude of v_{NF} is greater than 20 cm year^{-1}, then net up-slope transport of crustal material is impossible and we conclude that the given set of model parameters is inconsistent with a crustal convergence origin for Ishtar Terra. On the other hand, if v_{NF} is less than 20 cm year^{-1}, then net up-slope transport of crustal material can occur and the given set of model parameters is consistent with a crustal convergence origin for Ishtar. This logic is similar in some ways to that of Grimm and

Solomon (1988), who placed bounds on allowed crustal conditions based on their viscous relaxation models for impact craters on Venus.

We have calculated v_{NF} for a range of possible model parameters. In these calculations, we have used values of h and $\frac{\partial h}{\partial x}$ that are appropriate for a portion of Fortuna Tessera between Longitudes 19° and 29° and North Latitudes 61° to 66°, a region which is approximately 500 km by 500 km in size. In this region, PVO altimetry (USGS, 1984) shows that the topographic contours run predominantly North-South, although this does break down in the southeast corner of the study region. We therefore expect the crustal flow to have a sheet-like structure, with predominantly East-West flow velocities. This sheet-like flow satisfies one of the assumptions made by our flow model. As Figure 2c shows, the topographic elevation falls from 4.7 km at 65° North, 19° East to 1.5 km at 65° North, 29° East. We therefore use as average values h = 3.1 km and $\frac{\partial h}{\partial x} = 0.41°$ in the following calculations. The topographic slope will of course vary locally about this average value. Our calculated flow velocities should be regarded as an average value for the entire region. Our study region is located 700 to 1150 km away from the summit of Maxwell Montes, a distance which we assume is large enough so that we can safely neglect the details of possible vertical flow in the summit region.

The results of our Fortuna Tessera flow modeling are presented in Figure 11. The various curves in Figure 11 show the value of v_{NF} as a function of crustal thickness for various choices of flow law and thermal parameters. In these calculations, we have set h = 3.1 km and $\frac{\partial h}{\partial x} = 0.41°$, as discussed above. Except as indicated below, the thermal parameters and flow law parameters used are as given in Table 1.

Figure 11a shows the effects of various flow law parameters on the required basal velocity. The crustal thickness is expressed in terms of the reference thickness in the plains surrounding Ishtar, D in Figure 4a. As discussed above, v_{NF} must always be negative, so the velocities shown in Figure 11 actually refer to the absolute magnitude of v_{NF}. One way of interpreting Figure 11 is to consider a particular value of the basal velocity, in which case the various

curves set upper limits on the crustal thickness for which net crustal convergence is possible. For example, if the basal velocity is assumed to be 20 cm year^{-1}, then for the Shelton and Tullis (1981) diabase flow law (solid line), we must have D $<$ 25 km in order for net crustal convergence to occur. For this rheology and basal velocity, if D $>$ 25 km is assumed, then net up-slope transport of crustal material does not occur, and Ishtar Terra could not have formed by means of crustal convergence. If we assume a smaller basal velocity of 10 cm year^{-1}, then for the Shelton and Tullis flow law, we must have D $<$ 22 km in order for net crustal convergence to be possible. As discussed above, convective flow in Venus's mantle controls the value of v_o, with 20 cm year^{-1} as a generous upper bound on its allowed magnitude. Nevertheless, in Figure 11 we show results for basal velocities as large as 50 cm year^{-1} to make the point that even assuming extremely large values of v_o does not permit substantial increases in the allowed maximum value of D. For example, with the Shelton and Tullis flow law and $v_o = 50$ cm year^{-1}, D $<$ 28 km is necessary for net crustal convergence to be possible. Because the Caristan flow law is much softer than the Shelton and Tullis flow law, it places tighter restrictions on the allowed values of D(long-dashed line). For $v_o = 20$ cm year^{-1}, it requires D $<$ 15 km in order for net crustal convergence to be possible.

Because laboratory experiments must be performed at strain rates that are 5 to 10 orders of magnitude higher than are found in typical geological applications, large extrapolations are necessary in applying laboratory results to geologic modeling. As a result, while we regard the laboratory flow laws as guides to the possible viscous behavior of rocks, we also consider the effects of perturbations to the flow law parameters from their laboratory values. Thus, the short-dashed line in Figure 11a, labeled "S&T A/10", is for an arbitrary decrease by a factor of 10 in the Shelton and Tullis value for the pre-exponential viscosity constant, A. For this stiffer flow law, net crustal convergence is possible at $v_o = 20$ cm year^{-1} provided that D $<$ 33 km. On the other hand, if the Shelton and Tullis value of A is arbitrarily increased by a factor of 10 (dot-dashed line, labeled "S&T 10xA"), then D $<$ 18 km in order for net crustal convergence to occur.

The effects of changing the temperature dependence of the viscosity law can be addressed either by varying E or by varying the thermal parameters. In Figure 11b, we use the nominal Shelton and Tullis flow law parameters and consider the effects of changing the value of basal heat flow. The solid line uses our nominal value of $\frac{q_b}{k} = 10$ K km^{-1} and is identical to the solid line in Figures 11a. Decreasing $\frac{q_b}{k}$ increases the viscosity at depth and hence allows net crustal convergence to occur with thicker crusts. Thus, for $v_o = 20$ cm year^{-1}, $\frac{q_b}{k} = 6$ K km^{-1} requires D $<$ 44 km, while $\frac{q_b}{k} = 8$ K km^{-1} requires that D $<$ 32 km. For $\frac{q_b}{k} = 12$ K km^{-1}, we must have D $<$ 19 km, while $\frac{q_b}{k} = 15$ K km^{-1} requires that D $<$ 14 km in order for net crustal convergence to be possible.

In summary, if Ishtar Terra formed by crustal convergence, then for our nominal set of model parameters, the reference crustal thickness, D, must be less than 25 km. Increasing the allowed basal velocity above its nominal upper bound of 20 cm year^{-1} only increases the allowed value of D by 2 to 3 km. There are 3 ways in which our nominal model could be altered to permit larger values of D. One way would be to decrease the assumed values of $\frac{q_b}{k}$ and $\frac{H_o}{k}$, which would lead to colder interior temperatures and hence allow net crustal convergence for larger values of D. The conductive heat flux could be reduced by assuming that most of the heat transport in the lithosphere is transported magmatically in "heat pipes" (Turcotte, 1989). Turcotte's model requires a global average magma flux of 200 km^3 year^{-1}, which is more than an order of magnitude higher than Earth's observed magma flux. On the basis of a model for the resurfacing of impact craters, Grimm and Solomon (1987) estimated an upper limit of 2 km^3 year^{-1} for extrusive volcanism on Venus. Thus, if Turcotte's model is correct, virtually all magma on Venus must form intrusive structures, with less than 1% occurring as extrusive eruptions. On Earth, extrusive eruptions are typically 10 to 20% of the total volume of magmatic activity (Crisp, 1984). There is no obvious reason why extrusive volcanism

should be so much less likely on Venus than on Earth, and we therefore doubt that the heat pipe mechanism is as effective as Turcotte has suggested. Thus, we consider it unlikely that the geothermal gradient in the Ishtar region is significantly colder than our model geotherm. If anything, the real geotherm is likely to be hotter than in our model, requiring that D be less than 25 km for net crustal convergence to be possible.

A second way in which the upper bound on D could be increased is if the flow law is substantially stiffer than we assumed. As noted earlier, we have used the stiffest of the available diabase flow laws in performing our modeling. The pre-exponential constant, A, would have to be changed by more than an order of magnitude, in order to change our bound on D by more than 10 km.

A final possibility is that the surface behaves as a rigid boundary rather than as a free-slip boundary. For our nominal model parameters and a rigid top, net crustal convergence is possible for $D < 50$ km. However, as noted above, we think it is unlikely that Venus's surface behaves as a rigid boundary.

Discussion of Crustal Flow Models

It has long been recognized that viscous crustal flow is likely to be important on Venus, and a variety of attempts to model this process have been previously presented by other researchers. The first was Weertman (1979), who estimated vertically-averaged strain rates for flow away from an isostatically compensated elevated region on Venus. Assuming a dry quartzite rheology, he found a maximum total crustal thickness of 26 km for the elevated region. This thickness corresponds to D_{max} in our model and is about 20 km less than the upper limit that we found in the preceding section. There are several reasons for the differences between our results and Weertman's results. Weertman's criterion for determining the maximum allowed crustal thickness was that the vertically averaged strain rate must be less than 10^{-17} sec^{-1} in order for the elevated crustal block to survive for 10^9 years. Unlike our model, Weertman did not allow for a basal velocity to be imposed by the mantle on the crust. Because a non-zero basal velocity can resist the tendency of the high topography to spread, our model allows a larger value of D. Also, Weertman used a geothermal gradient of 15.2 K km^{-1}, which is larger than we use in our

nominal model. This also contributes to the differences in the the two sets of results.

Solomon et al. (1982) presented a model of the viscous relaxation of impact basins that used a constant Newtonian viscosity layer overlying an inviscid halfspace. With this simplified rheological structure, they solved both for the vertical flow velocity as well as one horizontal flow velocity. Stephens et al. (1983) applied this same model to the viscous relaxation of Ishtar Terra. They found that in the absence of dynamic support of topography, Maxwell Montes would decay to negligible relief in less than 1 billion years, although they cautioned that this is probably an upper limit because of uncertainties in what average viscosity should be assigned to their viscous layer.

Grimm and Solomon (1988) generalized the Solomon et al. (1982) relaxation model to include a series of horizontal layers, thus allowing the inclusion of temperature-dependent, and hence depth-dependent, viscosity. This model is formulated in terms of Newtonian rheology, although they have attempted to include stress-dependent rheology in an approximate way by estimating a volume-averaged effective stress from their initial topographic distribution and using this stress to evaluate an effective Newtonian viscosity. Bindschadler and Parmentier (1987, 1989) have also considered relaxation models with depth-dependent Newtonian viscosity. They have focused both on estimating time scales for viscous relaxation and on determining the distribution of tectonic features expected in a viscously relaxed terrain.

The only prior model of viscous relaxation on Venus to fully incorporate stress-dependent rheology is that of Smrekar and Phillips (1988), who considered a one-dimensional flow model, solving only for v_x as a function of depth. They estimated the minimum crustal thickness necessary for viscous crustal flow to occur on Venus, whereas we have attempted to place bounds on the maximum allowed crustal thickness. As a test of our numerical code, we have also performed several of the calculations reported in Smrekar and Phillips, with generally good agreement.

The bound on crustal thickness that we derived above, $D < 25$ km, can be compared with several independent estimates of crustal thickness on Venus.

Zuber (1987), Banerdt and Golombek (1988), and Zuber and Parmentier (1990) have used the spacing of tectonic features on Venus to place bounds on the crustal and lithospheric structure. They noted that in many places on Venus, there are two characteristic length scales for the spacing of tectonic structures, 10 to 20 km and 100 to 300 km. They suggested that these characteristic spacings are determined by the thicknesses of elastic layers in Venus's lithosphere. The shorter spacing is due to an elastic zone in Venus's upper crust, while the larger spacing is related to an elastic layer in the sub-crustal lithosphere. The requirement that an elastic layer exists beneath the crust, together with reasonable limits on the geothermal gradient, places an upper limit on the thickness of the crust. Zuber (1987) and Zuber and Parmentier (1990) found that $D < 30$ km, while Banerdt and Golombek (1988) found $D < 15$ km.

Grimm and Solomon (1988) have used models of the viscous relaxation of impact craters to place an upper bound on crustal thickness. They assumed that when first formed, impact craters on Venus have a topographic profile that can be determined by gravity scaling from observations of lunar craters. They allowed this profile to relax viscously for 50 to 500 million years. This range of relaxation times was chosen based on bounds on the average age of Venus's surface inferred from crater densities. Grimm and Solomon compared the depth-diameter ratios for their relaxed model craters with Venera 15 and 16 observations of large craters. They concluded that the average crustal thickness must be less than 20 km or else the relaxed craters would be shallower than observed. Grimm and Solomon used a volume-averaged effective stress to evaluate an effective Newtonian viscosity for their flow calculations. This procedure tends to overestimate the viscosity and hence underestimate the flow velocity in high stress regions. However, as relaxation proceeds, the declining topographic amplitude leads to smaller stresses and higher effective viscosities. Grimm and Solomon did not update their effective stress estimate as the calculation proceeded, so their results overestimate the rate of relaxation during the later stages of relaxation. These two effects must offset one another to some extent. It is not clear how they alter the inferred bounds on crustal thickness, but it seems unlikely that the net change will be very large.

Thus, the bounds that we infer on crustal thickness appear to be generally consistent with those inferred in the earlier work of Zuber (1987), of Banerdt and Golombek (1988), of Grimm and Solomon (1988), and of Zuber and Parmentier (1990). Although each of these models makes assumptions that may be questioned, we find the general concordance of results to be encouraging. We therefore suggest that 25 to 30 km is a likely upper limit to the crustal thickness in the plains of Venus.

In contrast with this estimate of crustal thickness, an Airy isostasy model for Ishtar's gravity anomaly leads to an estimated crustal thickness of 150 km (Sjogren et al., 1984). For any reasonable geothermal gradient, a 150 km thick crust must contain a region near its base that is partially or entirely molten. This material will have a very low viscosity resulting in large viscous flow velocities. Under these circumstances, it would be impossible to maintain the observed topographic relief in Ishtar Terra for geologically significant periods of time. This is true whether one chooses a free-slip or rigid surface boundary condition. We therefore conclude that the crust cannot be as thick as the Airy isostasy model suggests.

This does not mean that the Airy model does not apply to the Ishtar region, but it does require that other processes be occurring as well. Because shallowly compensated topography does not produce much long-wavelength geoid, most of Ishtar's geoid anomaly must be related to density anomalies within the mantle beneath Ishtar. Hager (1984) showed that in order to produce a large positive geoid anomaly over a region of downwelling mantle, the viscosity in the upper part of the mantle must be significantly less than the viscosity deeper in the convecting layer. Grimm and Phillips (1990) recently advanced similar arguments. However, we have shown elsewhere that both the global admittance spectrum and the geoid anomalies observed for features such as Beta Regio and Atla Regio are best fit if Venus's mantle is nearly isoviscous (Kiefer et al., 1986; Kiefer and Hager, 1988, 1990a; Chapter 2). One possible way out of this apparent paradox would be to assume that the upper mantle on Venus is about one order of magnitude less viscous than its lower mantle. With this type of viscosity structure, inclusion of temperature-dependent rheology in the calculations of mantle flow could alter the coupling of mantle flow

stresses with the surface in such a way that the geoid could be positive over both upwelling and downwelling regions (Richards et al., 1988). Although this model is qualitatively consistent with the existence of positive geoid anomalies both at Ishtar and in the Equatorial Highlands, it is not yet known if it can quantitatively explain the observed geoid amplitudes and shapes. Clearly, developing a model for the Ishtar geoid anomaly will provide an important additional test of the crustal convergence model.

Anderson (1980, 1981) and Kaula (1990) have also favored a relatively thick crust on Venus. They argued that because basalt is less dense than mantle material, it can not be recycled back into the mantle. Thus, in this model the crustal thickness increases with time until the basalt enters the eclogite stability field. Eclogite is denser than upper mantle material and is therefore able to sink into the mantle. Anderson and Kaula therefore concluded that thickness of Venus's crust is controlled by the depth to the basalt-eclogite phase boundary, which Anderson estimated to occur at 100 to 170 km depth. As described above, crustal thicknesses of this magnitude are inconsistent with the observation that substantial topography exists on Venus. The models of Anderson and of Kaula overlook the possibility that positively buoyant basalt can be recycled into the mantle if it is attached to a sufficient quantity of cold, negatively buoyant mantle. Because crust can be recycled into the mantle in regions of mantle downwelling, it may be possible for Venus to maintain an equilibrium crustal thickness that is much less than that predicted by arguments involving the basalt-eclogite phase transition. The possibility of crustal recycling on Venus has not yet been quantitatively modeled but is clearly an issue that should be studied further.

Extensional Deformation in Fortuna Tessera?

Within Fortuna Tessera, there is an unusual type of tessera, termed the Chevron Tessera by Vorder Bruegge and Head (1989). At a horizontal scale of 10 km, they characterized the Chevron Tessera as being similar in appearance to other tessera units, with intersecting sets of ridges and grooves. At a

horizontal scale of 100 to 200 km, on the other hand, they described the Chevron Tessera as having a disrupted or buckled appearance. Although tessera units are common on Venus, the large-scale disruption observed in the Chevron Tessera is not known to exist in tessera units elsewhere on Venus. Vorder Bruegge and Head proposed that the Chevron Tessera formed by the collision and compressional deformation of a series of distinct crustal blocks.

While substantial compressive deformation has probably occurred within Fortuna Tessera, several features within the Chevron Tessera may be indicative of extensional deformation. An examination of a mosaic of Venera 15 and 16 radar imagery (USGS, 1989) reveals that the structures that define the individual blocks within the Chevron Tessera are often parallel pairs of lineaments. These lineament pairs have characteristic spacings of a few tens of kilometers and characteristic lengths of a few hundred kilometers. They have a range of orientations. Some strike North-northwest, for example Lasdona Chasma near 70° N, 37° E. Others strike nearly due North, for example Morana Chasma near 70° N, 25° E. Still others strike North-northeast, for example Hina Chasma near 65° N, 22° E. Typically, the western lineament of a given pair is radar bright, indicating predominantly east-facing slopes, whereas the eastern lineament is radar dark, indicating predominantly west-facing slopes. Thus, these lineament pairs have the radar signature expected of a topographic valley. One possible explanation for these valleys is that they are graben and hence formed by extensional deformation.

Extensional deformation within Fortuna Tessera has been previously advocated by Sukhanov (1986) and by Kozak and Schaber (1989). Sukhanov argued that many of the features described above are graben and that the structure of Fortuna Tessera formed entirely by the flow of crustal material down the topographic slope. In his view, there is a plume-like upwelling under Ishtar, and the flow of mantle material away from Ishtar Terra serves to enhance the downslope flow of the crust. In contrast, the mantle flow pattern sketched in Figure 3 is directed in toward Ishtar, with downwelling occurring under Ishtar. Kozak and Schaber argued that a large North-South rift zone occurs in the central to eastern part of the Chevron Tessera, which they claimed is a portion of a global rift system on Venus. While we believe that there may be some extensional

deformation in Fortuna Tessera, we see no reason to connect this into a global tectonic system such as that advocated by Kozak and Schaber.

As we showed in Figure 10, in some circumstances it is possible for the near-surface layer to be flowing down the topographic slope even though the crust as a whole may be undergoing net up-slope transport. We speculate that the apparent graben which we described above may be related in some way to this down-slope flow of the near-surface crust, although we cannot model the deformation in detail using the one-dimensional flow model. We noted earlier that it is likely that the Ishtar region has undergone one or more delamination episodes. If such a delamination event occurred beneath Fortuna Tessera, then the crust in this region would be subjected to a sudden increase in the basal heat flux, q_b. The magnitude of the increase in q_b will depend on the extent to which the sub-crustal lithosphere is thinned during delamination. As shown in Figure 8, increasing q_b causes the down-slope flow velocity to increase. The enhanced heat flow will decline with time as the thermal boundary layer forms again by conductive cooling and by lateral advection, and thus the down-slope flow velocity will also decline with time following the delamination event. Thus, Fortuna Tessera may have been subjected to alternating periods of net up-slope and net down-slope flow, and this may have played a role in the formation of the distinctive Chevron Tessera landforms.

Mechanisms for the Origin of Volcanism in Ishtar Terra

We now consider possible mechanisms for producing the volcanism observed in Ishtar Terra. Mantle upwelling cannot account for the observed topography and tectonics of Ishtar, so pressure-release melting can be ruled out as a magma generating mechanism at Ishtar. On Earth, island arc volcanism shows that magma can also be generated in regions of mantle downwelling. However, it seems likely that magma generation in either an oceanic subduction zone or a continental collision zone requires the presence of water as an aqueous phase (Wyllie, 1988). Hydrous minerals undergo dehydration reactions when

exposed to sufficiently high temperature, providing the source of the necessary aqueous phase in terrestrial subduction zone volcanism. On Venus, however, the high surface temperature will inhibit the formation of hydrous mineral phases. For example, Nozette and Lewis (1982) found that for a nominal atmospheric water mixing ratio of 10^{-4}, tremolite is only stable at elevations of more than about 9 km above MPR, and hence could only form near the summit of Maxwell Montes. In the absence of hydrous phases, it seems unlikely that Earth-like subduction zone volcanism can occur on Venus.

There are at least two other mechanisms that could contribute to the volcanism observed in Ishtar. One is basal melting of the crust. As initially noted by Anderson (1980), if Venus's crust is thick enough and the geothermal gradient is large enough, then the temperature near the base of the crust can exceed the basalt solidus, producing a partial melt. We note that for our nominal thermal model and the upper limit crustal thickness inferred from our flow model, we never find a crustal temperature that exceeds the basalt solidus as given by Anderson's phase diagram. Indeed, as we discussed above, we doubt that the base of the crust can generally be at its solidus, because in that case, the viscosity would be quite low and viscous flow would be so rapid that it would be impossible to support differences in topographic elevation for geologically significant periods of time. It therefore seems unlikely that Colette and Sacajawea can be due to basal melting of Lakshmi Planum. It may be possible, however, for localized zones of basal melting to occur if q_b or H_o are larger than in our nominal thermal model. Maxwell Montes has the highest topography in Ishtar and hence must have the deepest crustal root. If basal melting occurs anywhere on Venus, Maxwell is the most likely location at which it might occur. This could help explain the formation of Cleopatra Patera.

As discussed above, lithospheric delamination can also lead to volcanism. If multiple delamination events have occurred, then volcanism in Ishtar may have had an episodic history. Following a delamination event, there would be a burst of volcanic activity that would gradually decay as the crust cooled. A later delamination episode could then lead to renewed volcanism. It is possible that the differing amounts of degradation observed at Colette and Sacajawea could be due to these structures forming during different delamination events.

Summary and Conclusions

In this paper, we have presented a model for Ishtar Terra that accounts for most of Ishtar's observed features. Ishtar is probably a zone of crustal convergence overlying a region of downwelling mantle. This convergence explains the predominance of compressive tectonics and leads to a region of thickened crust, which explains the observed high topography. Volcanism in Ishtar is probably related both to heating of the crust under Lakshmi Planum during delamination events and to basal melting of the crustal roots underlying the mountain belts.

We have developed models of the crustal flow in the Ishtar region. For reasonable upper limits on the mantle flow velocity, we find that the crust in the plains surrounding Ishtar cannot be more than about 25 km thick. This result is in good agreement with independent estimates of crustal thicknesses on Venus that other research groups have made based on modeling of the spacing of tectonic features and of impact crater relaxation. On the other hand, our upper limit on crustal thickness is much less than that inferred from Airy isostasy models of Ishtar's gravity anomaly. In general, Venus's crust cannot be so thick that its base is partially or entirely molten, or else it would be impossible to support the observed topography for geologically significant periods of time. It may, however, be possible for isolated regions of basal melting of the crust to exist either in regions of very thick crust or of high heat flow. Our model requires that substantial density anomalies exist within the mantle beneath Ishtar, but we have not modeled this in detail.

Although we treat Ishtar as a crustal convergence zone, our crustal flow models indicate that under some circumstances there can be outflow of crustal material in the near-surface region. This suggests the possibility that there may be some extensional deformation within Ishtar Terra, which could explain possible graben in Fortuna Tessera and Lakshmi Planum. Because of the one-dimensional nature of our crustal flow model, we cannot presently define the details of the flow field in the vicinity of the mountain belts. This will be the subject of a later investigation.

References

Anderson, D.L., Tectonics and Composition of Venus, *Geophys. Res. Lett., 7,* 101-102, 1980.

Anderson, D.L., Plate Tectonics on Venus, *Geophys. Res. Lett., 8,* 309-311, 1981.

Arvidson, R.E., M. Schulte, R. Kwok, J. Curlander, C. Elachi, J.P. Ford, and R.S. Saunders, Construction and Analysis of Simulated Venera and Magellan Images of Venus, *Icarus, 75,* 163-181, 1988.

Banerdt, W.B., Support of Long-Wavelength Loads on Venus and Implications for Internal Structure, *J. Geophys. Res., 91,* 403-419, 1986.

Banerdt, W.B., and M.P. Golombek, Deformational Models of Rifting and Folding on Venus, *J. Geophys. Res., 93,* 4759-4772, 1988.

Barsukov, V.L., A.T. Basilevsky, G.A. Burba, N.N. Bobinna, V.P. Kryuchkov, R.O. Kuzmin, O.V. Nikolaeva, A.A. Pronin, L.B. Ronca, I.M. Chernaya, V.P. Shaskina, A.V. Garanin, E.R. Kushky, M.S. Markov, A.L. Sukhanov, V.A. Kotelnikov, O.N. Rzhiga, G.M. Petrov, Y.N. Alexandrov, A.I. Sidorenko, A.F. Bogomolov, G.I. Skrypnik, M.Y. Bergman, L.V. Kudrin, I.M. Bokshtein, M.A. Kronrod, P.A. Chochia, Y.S. Tyuflin, S.A. Kadnichansky, and E.L. Akim, The Geology and Geomorphology of the Venus Surface as Revealed by the Radar Images Obtained by Veneras 15 and 16, *Proc. Lunar and Planetary Sci. Conf. 16, J. Geophys. Res. (supplement), 91,* D378-D398, 1986.

Basilevsky, A.T., Structure of Central and Eastern Areas of Ishtar Terra and Some Problems of Venusian Tectonics, *Geotectonics, 20,* 282-288, 1986.

Basilevsky, A.T., A.A. Pronin, L.B. Ronca, V.P. Kryuchkov, A.L. Sukhanov, and M.S. Markov, Styles of Tectonic Deformations on Venus: Analysis of Venera 15 and 16 Data, *Proc. Lunar and Planetary Sci. Conf. 16, J. Geophys. Res. (supplement), 91,* D399-D411, 1986.

Basilevsky, A.T., B.A. Ivanov, G.A. Burba, I.M. Chernaya, V.P. Kryuchkov, O.V. Nikolaeva, D.B. Campbell, and L.B. Ronca, Impact Craters of Venus: A Continuation of the Analysis of Data from the Venera 15 and 16 Spacecraft, *J. Geophys. Res., 92,* 12,869-12,901, 1987.

Basilevsky, A.T., and B.A. Ivanov, Cleopatra Crater on Venus: Venera 15/16 Data and Impact/Volcanic Origin Controversy, *Geophys. Res. Lett., 17,* 175-178, 1990.

Bills, B.G., W.S. Kiefer, and R.L. Jones, Venus Gravity: A Harmonic Analysis, *J. Geophys. Res., 92,* 10,335-10,351, 1987.

Bills, B.G., and M. Kobrick, Venus Topography: A Reappraisal (abstract), *Lunar and Planetary Science, 18,* 71-72, 1987.

Bindschadler, D.L., and J.W. Head, Characterization of Venera 15/16 Geologic Units from Pioneer Venus Reflectivity and Roughness Data, *Icarus, 77,* 3-20, 1989a.

Bindschadler, D.L., and J.W. Head, Models of Venus Tectonics: Evaluation and Application to Tessera Terrain (abstract), *Lunar and Planetary Science, 20,* 76-77, 1989b.

Bindschadler, D.L., and E.M. Parmentier, Tectonic Features Due to Gravitational Relaxation of Topography (abstract), *Lunar and Planetary Science, 18,* 75-76, 1987.

Bindschadler, D.L., and E.M. Parmentier, Mantle Flow Tectonics and a Weak Lower Crust: Implications for Formations of Large-scale Features on Venus (abstract), *Lunar and Planetary Science, 20,* 78-79, 1989.

Bird, P., Initiation of Intracontinental Subduction in the Himalaya, *J. Geophys. Res., 83,* 4975-4987, 1978.

Bott, M.H.P., and N.J. Kusznir, Stress Distributions Associated with Compensated Plateau Uplift Structures with Application to the Continental Splitting Mechanism, *Geophys. J. R. Astr. Soc., 56,* 451-459, 1979.

Burba, G.A., Crater Density in the Northern Part of Venus: Areal and Topographic Patterns (abstract), *Lunar and Planetary Science, 20,* 123-124, 1989.

Campbell, D.B., J.W. Head, J.K. Harmon, and A.A. Hine, Venus: Identification of Banded Terrain in the Mountains of Ishtar Terra, *Science, 221,* 644-647, 1983.

Campbell, D.B., J.W. Head, J.K. Harmon, and A.A. Hine, Venus: Volcanism and Rift Formation in Beta Regio, *Science, 226,* 167-170, 1984.

Caristan, Y., The Transition from High Temperature Creep to Fracture in Maryland Diabase, *J. Geophys. Res., 87,* 6781-6790, 1982.

Clark, S.P., Thermal Conductivity, *Handbook of Physical Constants, Geological Society of America Memoir 97,* 459-482, 1966.

Crisp, J.A., Rates of Magma Emplacement and Volcanic Output, *J. Volcanol. Geotherm. Res., 20,* 177-211, 1984.

Crumpler, L.S., J.W. Head, and D.B. Campbell, Orogenic Belts on Venus, *Geology 14,* 1031-1034, 1986.

Elachi, C., *Introduction to the Physics and Techniques of Remote Sensing,* John Wiley and Sons, New York, 1987.

England, P., and G. Houseman, Extension During Continental Convergence, with Application to the Tibetan Plateau, *J. Geophys. Res., 94,* 17,561-17,579, 1989.

Gaddis, L.R., and R. Greeley, Volcanism in NW Ishtar Terra, Venus (abstract), *Lunar and Planetary Science, 20,* 319-320, 1989.

Grimm, R.E., and R.J. Phillips, Gravity Anomalies and the Geodynamics of Lakshmi Planum (abstract), *Lunar and Planetary Science, 21,* 437-438, 1990.

Grimm, R.E., and S.C. Solomon, Limits on Modes of Lithospheric Heat Transport on Venus from Impact Crater Density, *Geophys. Res. Lett., 14,* 538-541, 1987.

Grimm, R.E., and S.C. Solomon, Viscous Relaxation of Impact Crater Relief on Venus: Constraints on Crustal Thickness and Thermal Gradient, *J. Geophys. Res., 93,* 11,911-11,929, 1988.

Hager, B.H., Subducted Slabs and the Geoid: Constraints on Mantle Rheology and Flow, *J. Geophys. Res., 89,* 6003-6015, 1984.

Hartmann, W.K., R.G. Strom, S.J. Weidenschilling, K.R. Blasius, A. Woronow, M.R. Dence, R.A.F. Grieve, J. Diaz, C.R. Chapman, E.M. Shoemaker, and K.L. Jones, Chronology of Planetary Volcanism by Comparative Studies

of Planetary Cratering, pp. 1049-1127 in *Basaltic Volcanism on the Terrestrial Planets,* Pergamon Press, New York, 1981.

Head, J.W., Formation of Mountain Belts on Venus: Evidence for Large-Scale Convergence, Underthrusting, and Crustal Imbrication in Freyja Montes, Ishtar Terra, *Geology, 18,* 99-102, 1990.

Houseman, G.A., D.P. McKenzie, and P. Molnar, Convective Instability of a Thickened Boundary Layer and its Relevance for the Thermal Evolution of Continental Convergent Belts, *J. Geophys. Res., 86,* 6115-6132, 1981.

Ivanov, B.A., A.T. Basilevsky, V.P. Kryuchkov, and I.M. Chernaya, Impact Craters of Venus: Analysis of Venera 15 and 16 Data, *Proc. Lunar and Planetary Sci. Conf. 16, J. Geophys. Res. (supplement), 91,* D413-D430, 1986.

Janle, P., and D. Jannsen, Tectonics of the Southern Escarpment of Ishtar Terra from Observations of Morphology and Gravity, *Earth, Moon, and Planets, 31,* 141-155, 1984.

Kaula, W.M., and R.J. Phillips, Quantitative Tests for Plate Tectonics on Venus, *Geophys. Res. Lett., 8,* 1187-1190, 1981.

Kaula, W.M., Venus: A Contrast in Evolution to Earth, *Science, 247,* 1191-1196, 1990.

Kiefer, W.S., M.A. Richards, B.H. Hager, and B.G. Bills, A Dynamic Model of Venus's Gravity Field, *Geophys. Res. Lett., 13,* 14-17, 1986.

Kiefer, W.S., and B.H. Hager, Mantle Plumes on Venus: A Model for the Equatorial Highlands and a Possible Connection with the Ovoids (abstract),

Lunar and Planetary Science, 19, 601-602, 1988.

Kiefer, W.S., and B.H. Hager, A Mantle Plume Model for the Equatorial Highlands of Venus, to be submitted to *J. Geophys. Res.,* 1990a.

Kiefer, W.S., and B.H. Hager, Crustal Convergence and Mantle Downwelling in the Ishtar Terra Region of Venus (abstract), *Lunar and Planetary Science, 21,* 629-630, 1990b.

Kozak, R.C., and G.G. Schaber, New Evidence for Global Tectonic Zones on Venus, *Geophys. Res. Lett., 16,* 175-178, 1989.

Magee, K.P., and J.W. Head, Colette and Sacajawea: Characterization, Comparison, and Interpretation of Major Caldera Structures on Lakshmi Planum (abstract), *Lunar and Planetary Science, 19,* 711-712, 1988a.

Magee, K.P., and J.W. Head, Lakshmi Planum: A Distinctive Highland Volcanic Province (abstract), *Lunar and Planetary Science, 19,* 713-714, 1988b.

Markov, M.S., Structural Ensembles in the Northern Belt of Deformations on Venus and Possible Mechanisms for their Development, *Geotectonics, 20,* 306-313, 1986.

McGill, G.E., S.J. Steenstrup, C. Barton, and P.G. Ford, Continental Rifting and the Origin of Beta Regio, Venus, *Geophys. Res. Lett., 8,* 737-740, 1981.

Minster, J.B., and T.H. Jordan, Present-day Plate Motions, *J. Geophys. Res., 83,* 5331-5354, 1978.

Morgan, P., and R.J. Phillips, Hot Spot Heat Transfer: Its Application to Venus and Implications to Venus and Earth, *J. Geophys. Res., 88,* 8305-8317, 1983.

Nozette, S., and J.S. Lewis, Venus: Chemical Weathering of Igneous Rocks and Buffering of Atmospheric Composition, *Science, 216,* 181-183, 1982.

Pettengill, G.H., E. Eliason, P.G. Ford, G.B. Loriot, H. Masursky, and G.E. McGill, Pioneer Venus Radar Results: Altimetry and Surface Properties, *J. Geophys. Res., 85,* 8261-8270, 1980.

Pike, R.J., *Geometric Interpretation of Lunar Craters,* U. S. Geological Survey Professional Paper 1046-C, 1980.

Plaut, J.J., and R.E. Arvidson, Comment on "Impact Craters of Venus: A Continuation of the Analysis of Data from the Venera 15 and 16 Spacecraft" by A. T. Basilevsky et al., *J. Geophys. Res., 93,* 15,339-15,340, 1988.

Pronin, A.A., The Structure of Lakshmi Planum, an Indication of Horizontal Asthenospheric Flow on Venus, *Geotectonics, 20,* 271-281, 1986.

Richards, M.A., B.H. Hager, and N.H. Sleep, Dynamically Supported Geoid Highs over Hotspots: Observation and Theory, *J. Geophys. Res., 93,* 7690-7708, 1988.

Schaber, G.G., Venus: Limited Extension and Volcanism Along Zones of Lithospheric Weakness, *Geophys. Res. Lett., 9,* 499-502, 1982.

Schaber, G.G., R.C. Kozak, and H. Masursky, Cleopatra Patera on Venus: Venera 15/16 Evidence for a Volcanic Origin, *Geophys. Res. Lett., 14,* 41-44, 1987a.

Schaber, G.G., E.M. Shoemaker, and R.C. Kozak, Is the Venusian Surface Really Old? (abstract), *Lunar and Planetary Science, 18,* 874-875, 1987b.

Schaber, G.G., E.M. Shoemaker, and R.C. Kozak, The Surface Age of Venus: Use of the Terrestrial Cratering Record, *Solar System Research, 21,* 89-94, 1987c.

Sclater, J.G., C. Jaupart, and D. Galson, The Heat Flow Through Oceanic and Continental Crust and the Heat Loss of the Earth, *Rev. Geophys. Space Phys., 18,* 269-311, 1980.

Shelton, G., and J. Tullis, Experimental Flow Laws for Crustal Rocks (abstract), *EOS, 62,* 396, 1981.

Sjogren, W.L., B.G. Bills, and N.A. Mottinger, Venus: Ishtar Gravity Anomaly, *Geophys. Res. Lett., 11,* 489-491, 1984.

Smrekar, S., and R.J. Phillips, Gravity-Driven Deformation of the Crust on Venus, *Geophys. Res. Lett., 15,* 693-696, 1988.

Solomon, S.C., T.J. Ahrens, P.M. Cassen, A.T. Hsui, J.W. Minear, R.T. Reynolds, N.H. Sleep, D.W. Strangway, and D.L. Turcotte, Thermal Histories of the Terrestrial Planets, pp. 1129-1234 in *Basaltic Volcanism on the Terrestrial Planets,* Pergamon Press, New York, 1981.

Solomon, S.C., S.K. Stephens, and J.W. Head, On Venus Impact Basins: Viscous Relaxation of Topographic Relief, *J. Geophys. Res., 87,* 7763-7771, 1982.

Solomon, S.C., and J.W. Head, Venus Banded Terrain: Tectonic Models for Band Formation and their Relationship to Lithospheric Thermal

Structure, *J. Geophys. Res., 89,* 6885-6897, 1984.

Stephens, S.K., S.C. Solomon, and J.W. Head, On the Age of Venus Highland Topography: Constraints from the Viscous Relaxation of Relief (abstract), *Lunar and Planetary Science, 14,* 747-748, 1983.

Stofan, E.R., J.W. Head, and D.B. Campbell, Geology of the Southern Ishtar Terra/Guinevere and Sedna Planitae Region on Venus, *Earth, Moon, and Planets, 38,* 183-207, 1987.

Stofan, E.R., J.W. Head, D.B. Campbell, S.H. Zisk, A.F. Bogomolov, O.N. Rzhiga, A.T. Basilevsky, and N. Armand, Geology of a Rift Zone on Venus: Beta Regio and Devana Chasma, *Bull. Geol. Soc. Am., 101,* 143-156, 1989.

Sukhanov, A.L., Parquet: Regions of Areal Plastic Dislocations, *Geotectonics, 20,* 294-305, 1986.

Surkov, Y.A., V.L. Barsukov, L.P. Moskalyeva, V.P. Kharyukova, and A.L. Kemurdzhian, New Data on the Composition, Structure, and Properties of Venus Rock Obtained by Venera 13 and Venera 14, *Proc. Lunar and Planetary Sci. Conf. 14, J. Geophys. Res. (supplement), 89,* B393-B402, 1984.

Surkov, Y.A., L.P. Moskalyova, V.P. Kharyukova, A.D. Dudin, G.G. Smirnov, and S.Y. Zaitseva, Venus Rock Composition at the Vega 2 Landing Site, *Proc. Lunar and Planetary Sci. Conf. 17, J. Geophys. Res. (supplement), 91,* E215-E218, 1986.

Surkov, Y.A., F.F. Kirnozov, V.N. Glazov, A.G. Dunchenko, L.P. Tatsy, and O.P. Sobornov, Uranium, Thorium, and Potassium in the Venusian Rocks at the Landing Sites of Vega 1 and 2, *Proc. Lunar and Planetary Sci.*

Conf. 17, J. Geophys. Res. (supplement), 92, E537-E540, 1987.

Turcotte, D.L., A Heat Pipe Mechanism for Volcanism and Tectonics on Venus, *J. Geophys. Res., 94,* 2779-2785, 1989.

U.S. Geological Survey, *Topographic and Shaded Relief Maps of Venus,* Miscellaneous Investigations Series Map I-1562, 1984.

U.S. Geological Survey, *Maps of Part of the Northern Hemisphere of Venus,* Miscellaneous Investigations Series Map I-2041, 1989.

Vorder Bruegge, R.W., J.W. Head, and D.B. Campbell, Cross Strike Discontinuities on Maxwell Montes, Venus: Evidence for Large-Scale Strike-Slip Faulting (abstract), *Lunar and Planetary Science, 17,* 917-918, 1986.

Vorder Bruegge, R.W., and J.W. Head, Fortuna Tessera, Venus: Evidence of Horizontal Convergence and Crustal Thickening, *Geophys. Res. Lett., 16,* 699-702, 1989.

Webb, E.K., and D.J. Stevenson, Subsidence of Topography on Io, *Icarus, 70,* 348-353, 1987.

Weertman, J., Height of Mountains on Venus and the Creep Properties of Rock, *Phys. Earth Planet. Interiors, 19,* 197-207, 1979.

Wyllie, P.J., Magma Genesis, Plate Tectonics, and Chemical Differentiation of the Earth, *Rev. Geophys., 26,* 370-404, 1988.

Zuber, M.T., Constraints on the Lithospheric Structure of Venus from Mechanical Models and Tectonic Surface Features, *Proc. Lunar and Planetary Sci. Conf. 17, J. Geophys. Res. (supplement), 92,* E541-E551, 1987.

Zuber, M.T., and E.M. Parmentier, On the Relationship between Isostatic Elevation and the Wavelengths of Tectonic Surface Features on Venus, *Icarus, 85,* 290-308, 1990.

Table 1. Reference Model Parameters

v_o	Basal Velocity	0 cm year^{-1}
h	Topographic Height (relative to MPR)	3 km
$\frac{\partial h}{\partial x}$	Topographic Gradient	0.4°
D	Reference Crustal Thickness	20 km
ρ_c	Crustal Density	2.8 gm cm^{-3}
ρ_m	Mantle Density	3.3 gm cm^{-3}
$\frac{q_b}{k}$	Basal Heating Thermal Gradient	10 K km^{-1}
$\frac{H_o}{k}$	Crustal Heating Parameter	0.14 K km^{-2}
λ'	Radioactive Element e-folding Depth	10 km
A	Viscosity Law Constant	$8.8 \cdot 10^{-8}$ bar^{-n} sec^{-1}
E	Viscosity Activation Energy	260 kJ mole^{-1}
n	Viscosity Stress Exponent	3.4

Figure 1. Map of features in the Ishtar Terra region. Regions whose elevation is below mean planetary radius are shaded in dark gray; regions between 0.0 and 2.8 km are shaded in light gray. Regions between 2.8 and 4.0 km elevation are unshaded. Regions above 4.0 km are shaded with diagonal lines. Within Maxwell Montes, the 6.0 and 8.0 km contour levels are also shown. The solid lines mark the locations of topographic profiles shown in Figure 2. Note that the full extent of Akna and Freyja Montes is not shown in this map because the Pioneer Venus altimetry used to construct the map only extends to about 74° North Latitude.

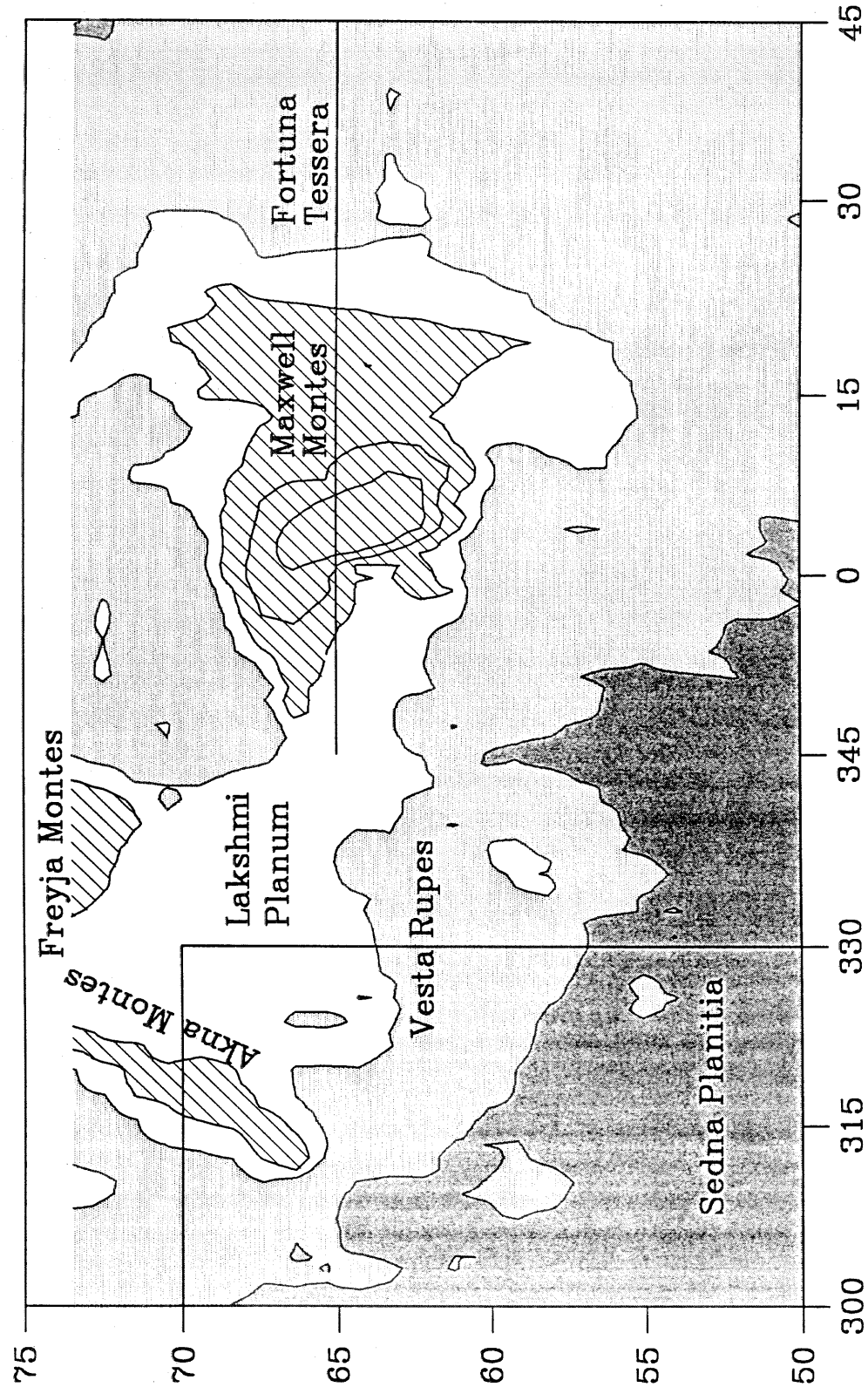
Fortuna Tessera
Maxwell Montes
Freyja Montes
Lakshmi Planum
Vesta Rupes
Akna Montes
Sedna Planitia
75
70
65
60
55
50
300
315
330
345
0
15
30
45

Figure 2. Topographic profiles across selected parts of Ishtar Terra.

a) North-South profile along Longitude 330° from 50° to 70° North Latitude. Profile extends from Sedna Planitia, up Vesta Rupes, and into Lakshmi Planum.

b) East-West profile along 70° North Latitude from 290° to 330° West Longitude. Profile extends from Mnemosyne Regio, over Akna Montes, and into Lakshmi Planum.

c) East-West profile along 65° North Latitude from 15° West to 60° East Longitude. Profile extends from Lakshmi Planum, over Maxwell Montes, and into Fortuna Tessera.

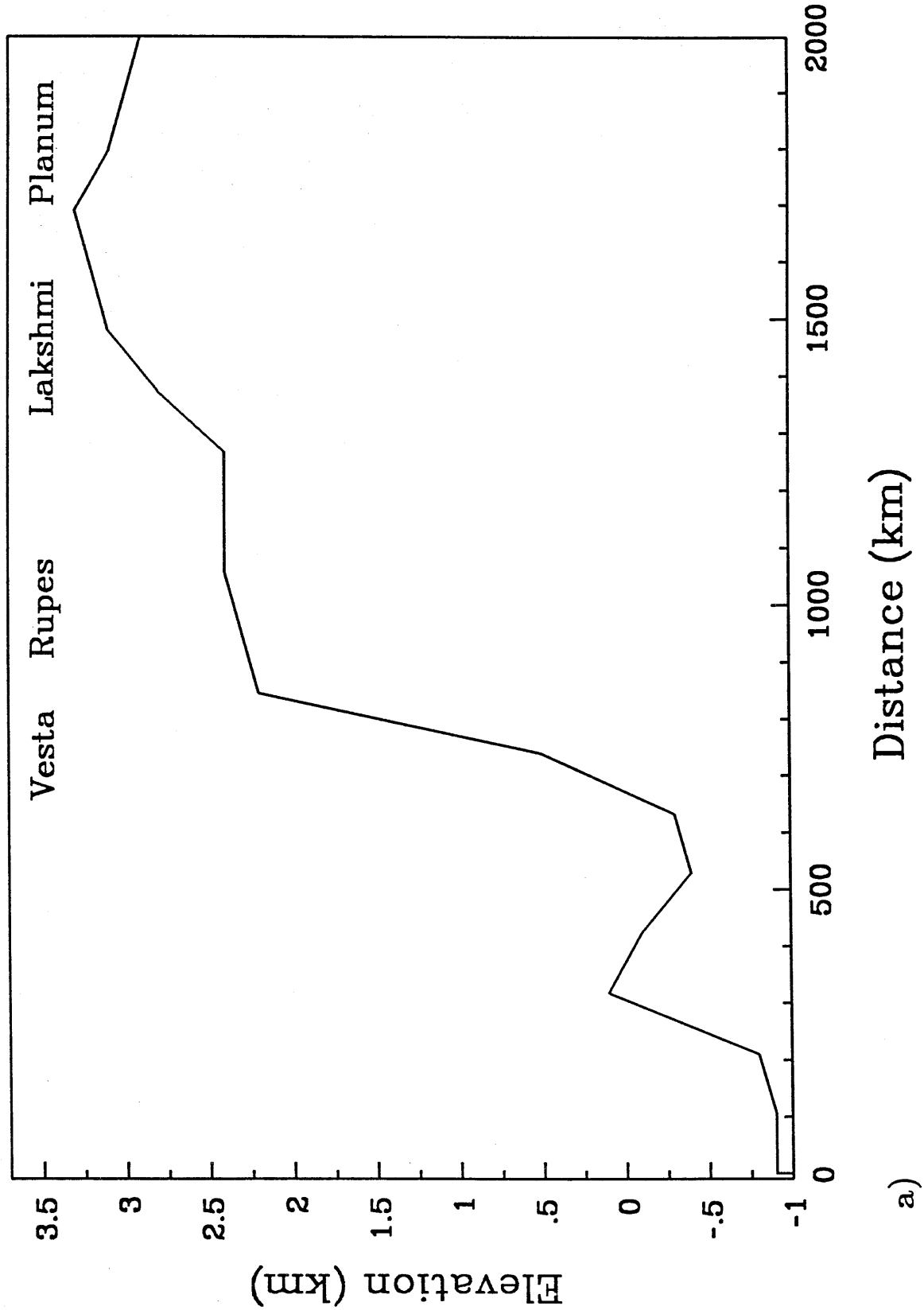
Vesta Rupes Lakshmi Planum
Elevation (km)
3.5
3
2.5
2
1.5
1
.5
0
-.5
-1
0
500
1000
1500
2000
Distance (km)

a)

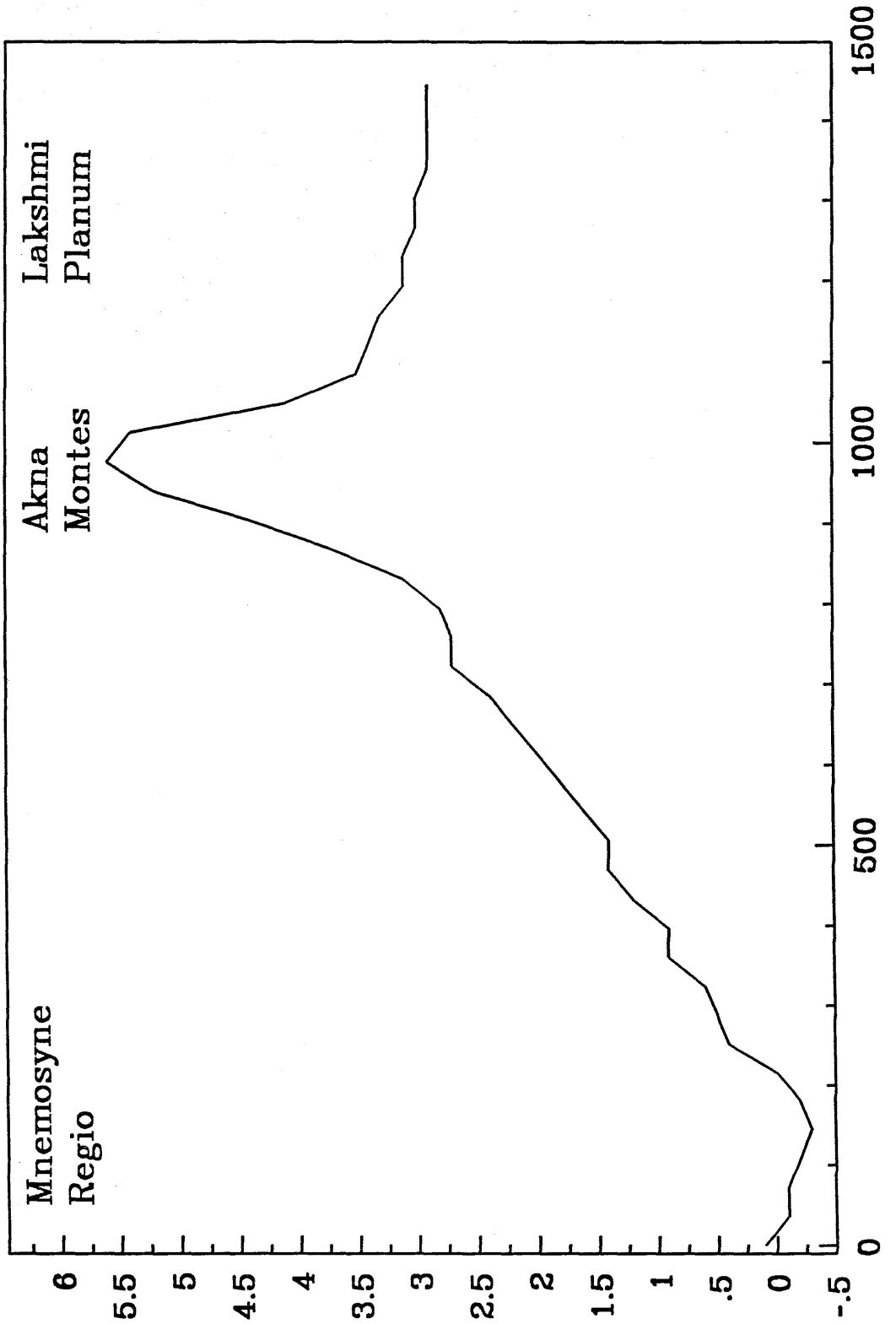
Mnemosyne
Regio
Akna
Montes
Lakshmi
Planum
Elevation (km)
6
5.5
5
4.5
4
3.5
3
2.5
2
1.5
1
.5
0
-.5
0
500
1000
1500
Distance (km)

b)

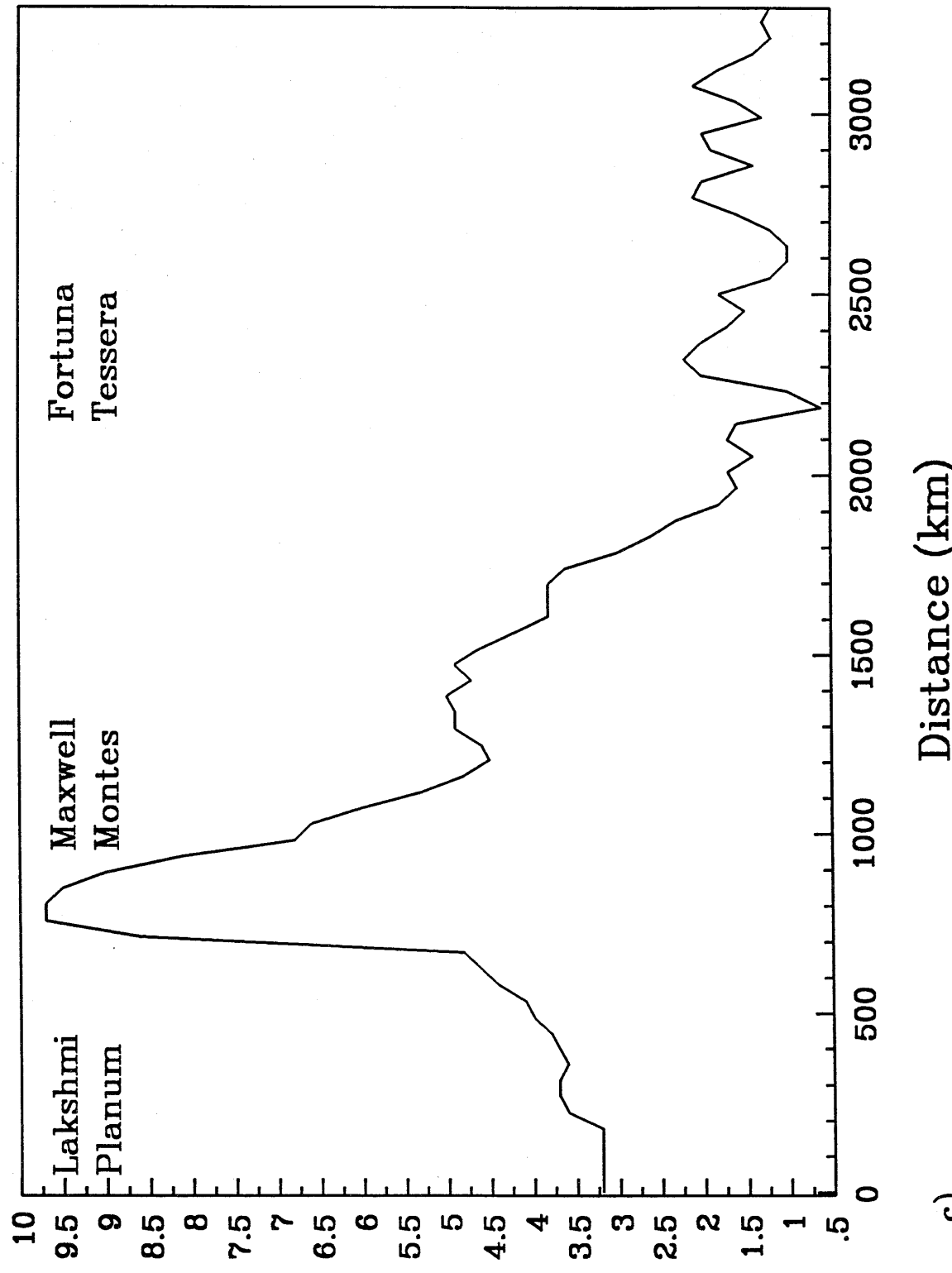
Lakshmi
Planum
Maxwell
Montes
Fortuna
Tessera
Elevation (km)
Distance (km)
10
9.5
9
8.5
8
7.5
7
6.5
6
5.5
5
4.5
4
3.5
3
2.5
2
1.5
1
.5
0
500
1000
1500
2000
2500
3000

c)

Figure 3. Schematic illustration of our crustal convergence model for Ishtar Terra. Downwelling flow in the mantle creates a zone of crustal thickening, and hence of high topography, over the downwelling.

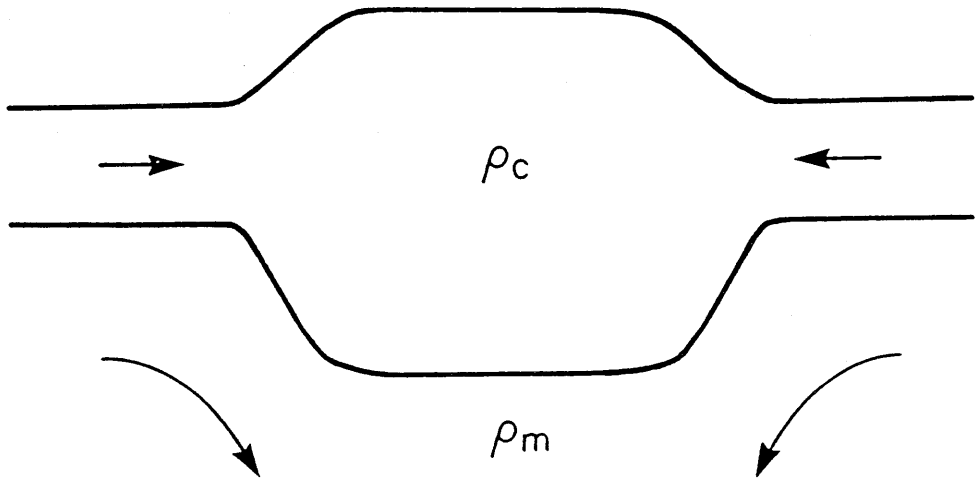
ρ_c
ρ_m

Figure 4. a) Schematic illustration of the viscous crustal flow model. Crustal flow is driven both by pressure gradients due to gradients in isostatically compensated topography, as well as by a basal velocity, V_o, imposed by convective flow in the mantle. The reference crustal thickness in the plains, away from regions of crustal thickening, is D.

b) A possible later stage of viscous crustal flow, with inflow near the base and outflow near the surface. The transition of material from inflow to outflow is accommodated by a region of predominantly vertical flow under the mountain belts.

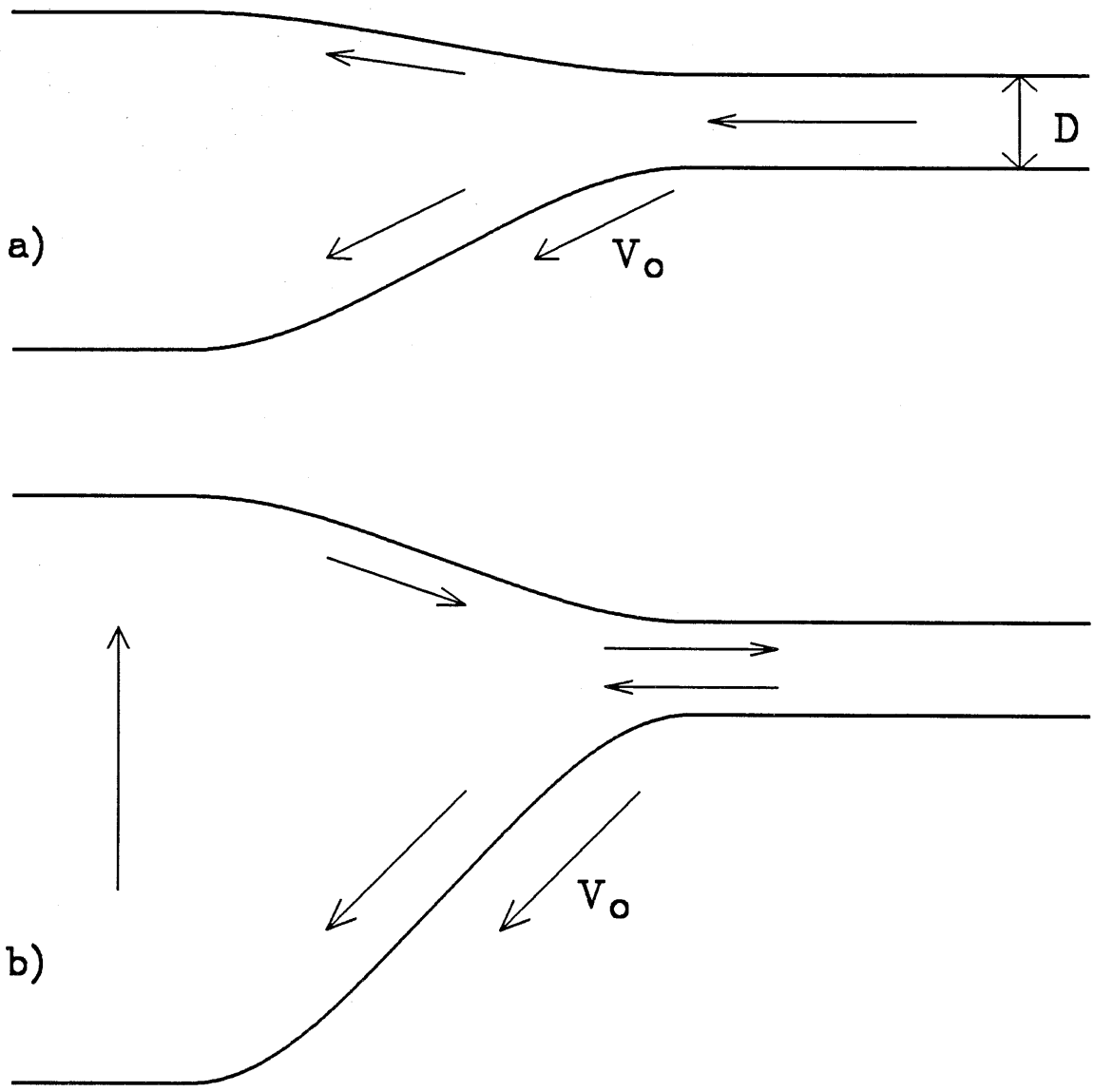
D
a)
V_o
b)
V_o

Figure 5. Geotherm versus depth for the reference model given in Table 1. The surface temperature is 714 K, the temperature at the base of the crust is 1145 K, and the total surface heat flow is 31 mW m^{-2}.

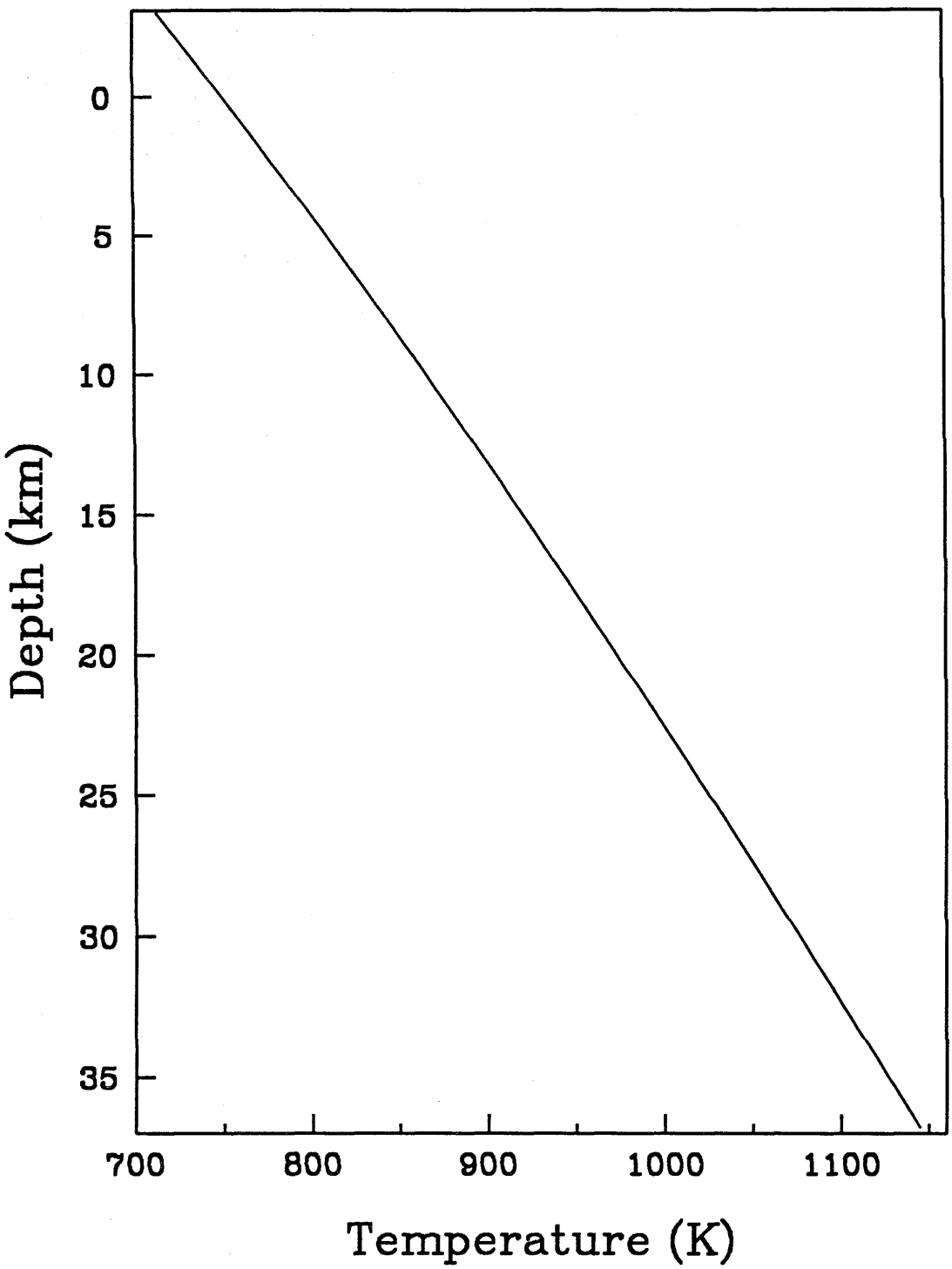
0
5
10
15
20
25
30
35
Depth (km)
700
800
900
1000
1100
Temperature (K)

Figure 6. Profiles of horizontal flow velocity versus depth. The solid line uses the Shelton and Tullis (1981) diabase flow law. The dashed line uses the diabase flow law of Caristan (1982). All other model parameters are as given in Table 1.

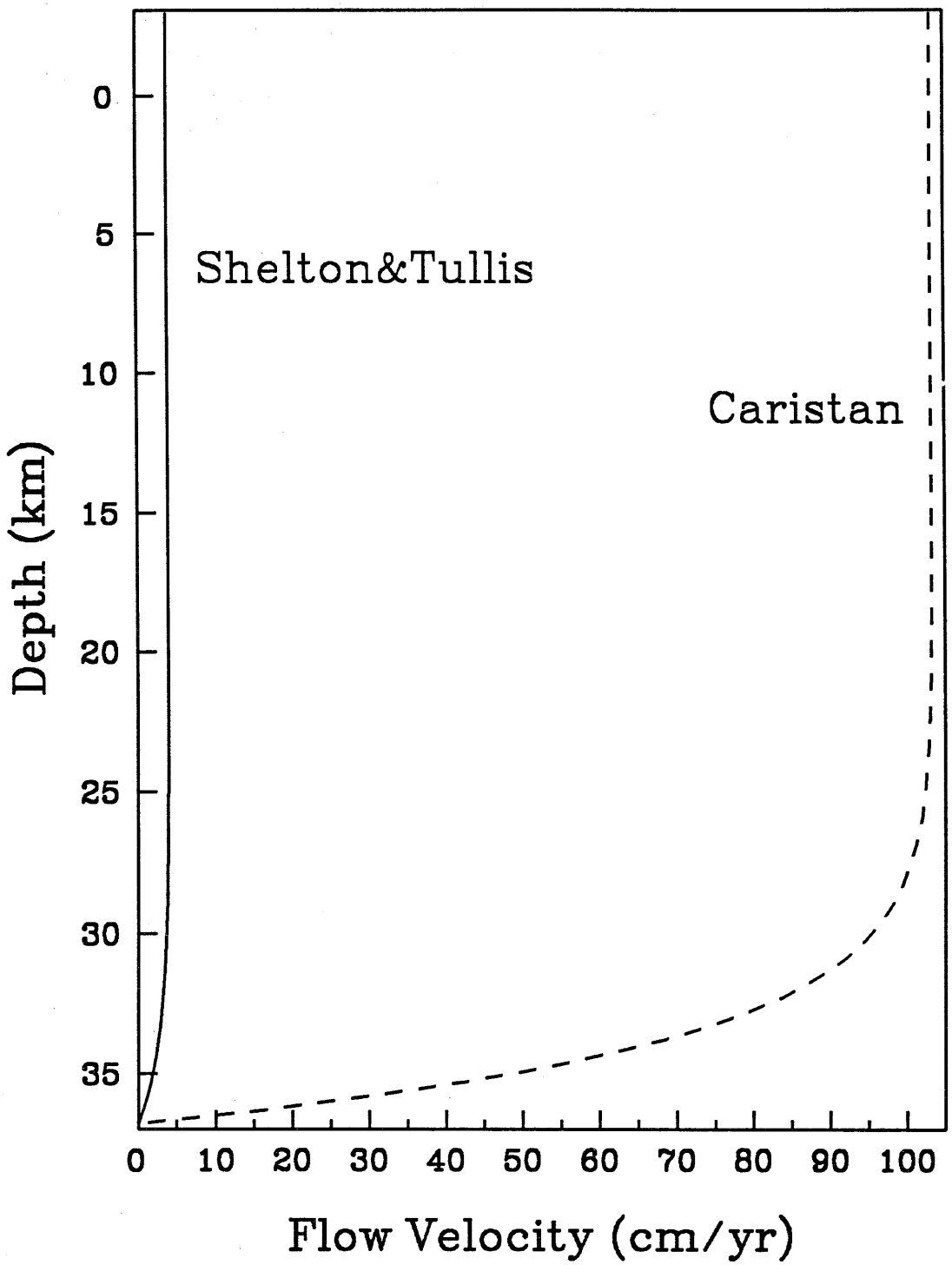
Shelton&Tullis
Caristan
Depth (km)
0
5
10
15
20
25
30
35
0
10
20
30
40
50
60
70
80
90
100
Flow Velocity (cm/yr)

Figure 7. a) Effect on flow velocity of changing surface slope. The dot-dash line has surface slope 0.2°, the solid line has surface slope 0.4°, and the dashed line has surface slope 0.6°. All other model parameters are as given in Table 1.

b) Effect on flow velocity of changing crustal thickness. The dot-dash line has D=15 km, the solid line has D=20 km, and the dashed line has D=25 km. These values correspond to total crustal thicknesses (D_{max}) of 35, 40, and 45 km respectively. Other model parameters are as in Table 1.

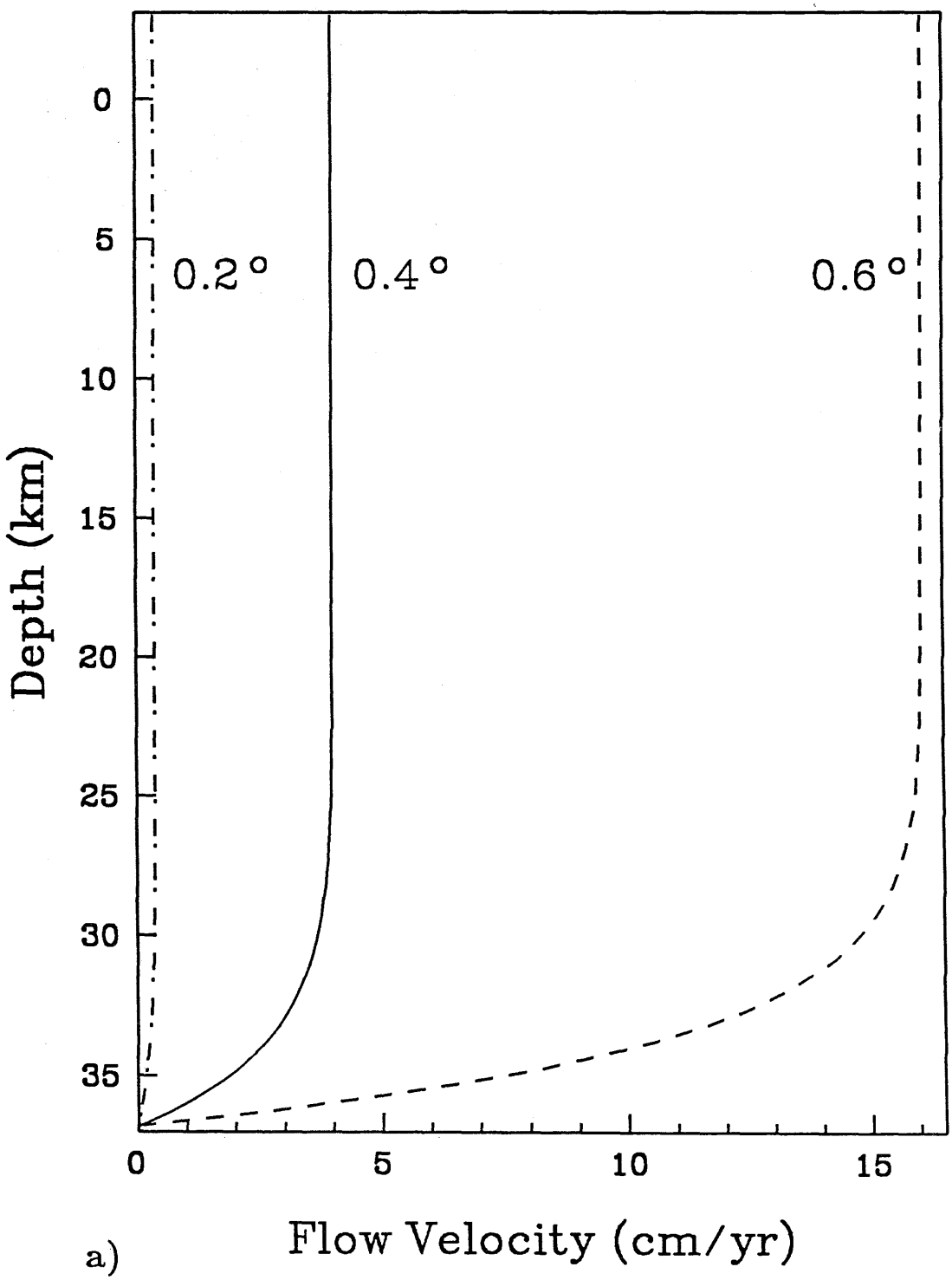

a)

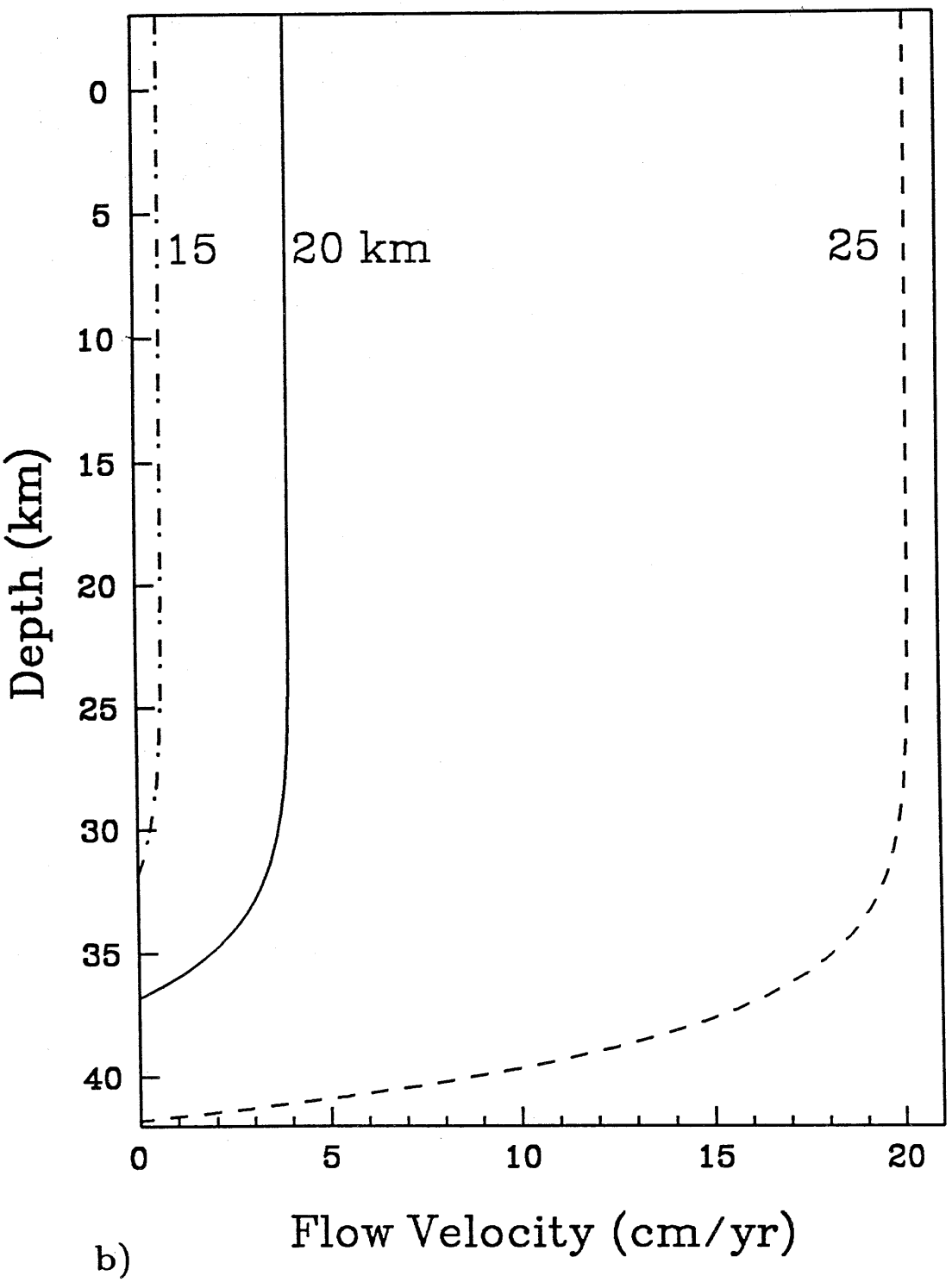
15
20 km
25
Depth (km)
0
5
10
15
20
25
30
35
40
0
5
10
15
20
Flow Velocity (cm/yr)

b)

Figure 8. Effect on flow velocity of changing basal heating. Values of $\frac{q_b}{k}$ are 8 K km^{-1} for the dot-dash line, 10 K km^{-1} for the solid line, and 12 K km^{-1} for the dashed line. Other model parameters are as in Table 1.

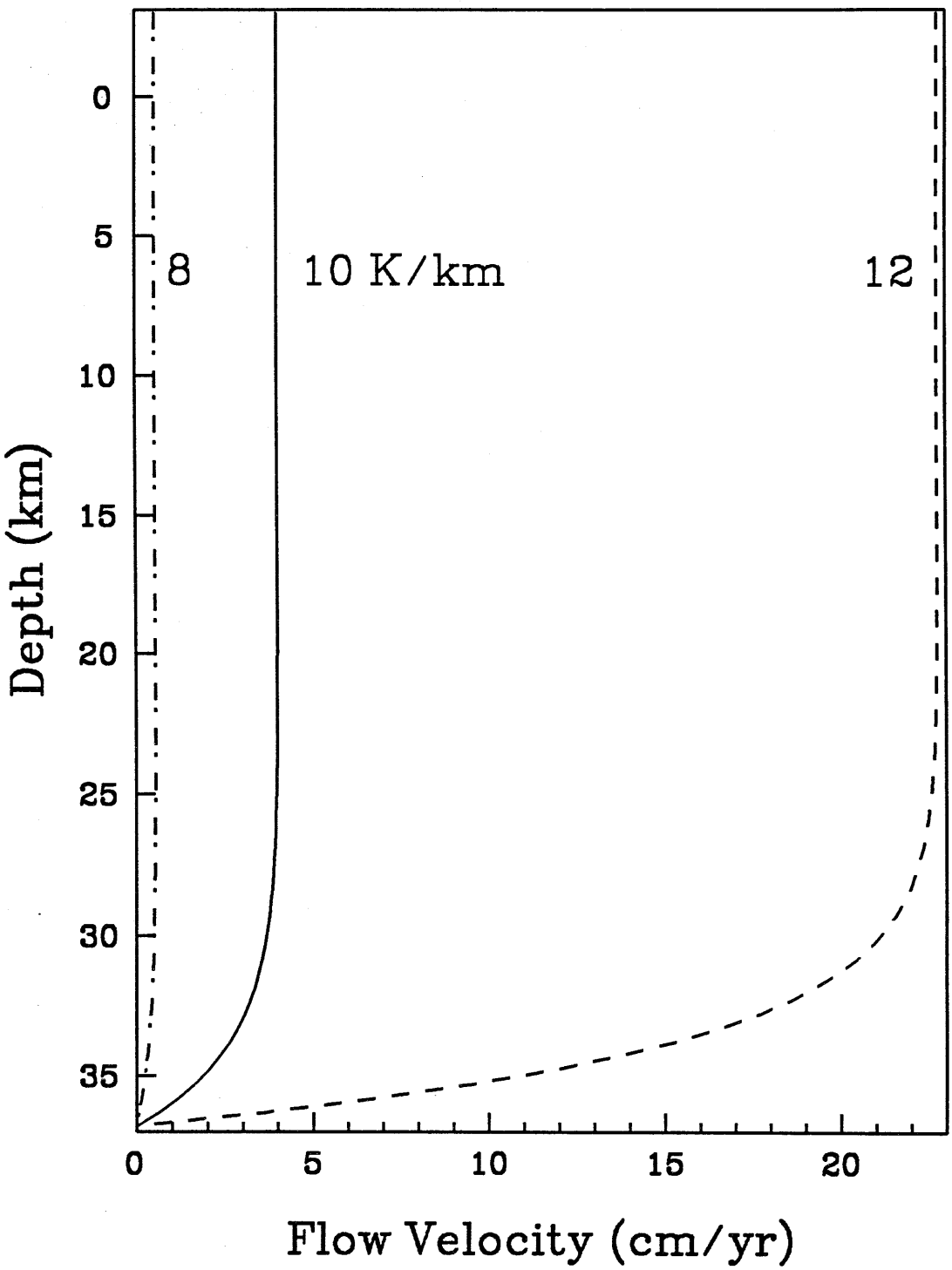
8
10 K/km
12
Depth (km)
0
5
10
15
20
25
30
35
0
5
10
15
20
Flow Velocity (cm/yr)

Figure 9. Horizontal flow velocities for a model with a rigid top boundary. All model parameters are the same as in Table 1 except that the reference crustal thickness is D=60 km.

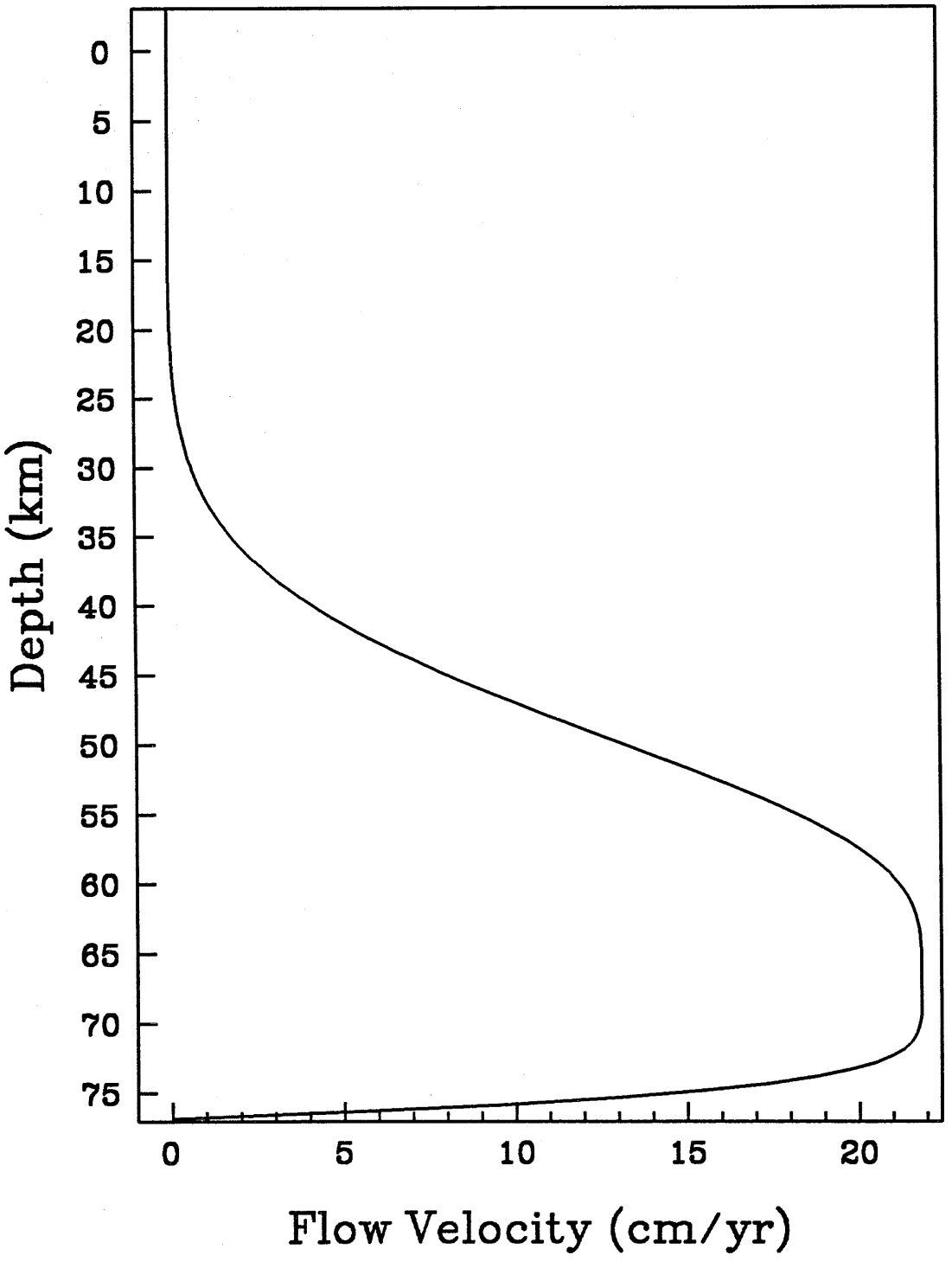
Depth (km)
0
5
10
15
20
25
30
35
40
45
50
55
60
65
70
75
0
5
10
15
20
Flow Velocity (cm/yr)

Figure 10. An example of a no net flux velocity profile. The topographic slope, $\frac{\partial h}{\partial x} = 0.41°$, and the mean topographic elevation, h=3.1 km, are adopted as mean values for Fortuna Tessera. The thermal parameters and flow law are as given in Table 1. Positive flow velocities indicate downslope flow and negative velocities indicate upslope flow. The basal velocity of -5.2 cm $year^{-1}$ was chosen using equation 16 so that the net horizontal mass flux through the total crustal column is 0. Note that most of the crust is flowing downslope at a velocity of about 0.4 cm $year^{-1}$ and that upslope flow occurs only near the base of the crust.

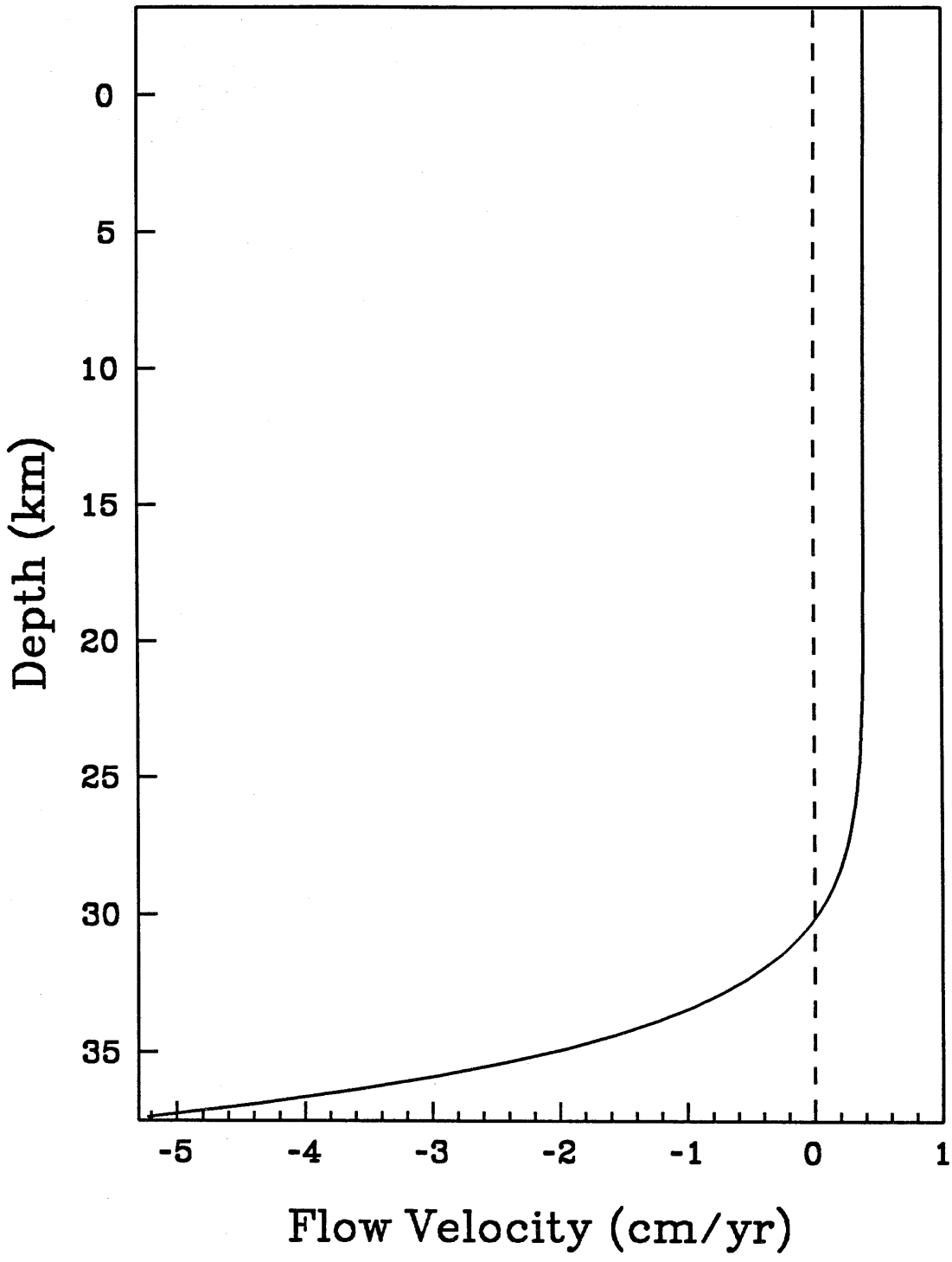
0
5
10
15
20
25
30
35
Depth (km)
-5
-4
-3
-2
-1
0
1
Flow Velocity (cm/yr)

Figure 11. Upper limits on crustal thickness as a function of the magnitude of the allowed basal velocity. The topographic elevation and topographic slope are representative of Fortuna Tessera, as discussed in the text. Except as indicated below, other model parameters are as given in Table 1. Crustal thickness limits are expressed in terms of D, the reference crustal thickness in the plains away from regions of crustal thickening.

a) Effects of varying the flow law parameter, A. The solid line is for the nominal A value of Shelton and Tullis (1981). The short dashed line is for A a factor of 10 less than given by Shelton and Tullis. The dot-dash line is for A a factor 10 larger than given by Shelton and Tullis. The long dashed line is for Caristan's (1982) diabase flow law.

b) Effects of varying the basal heating parameter, $\frac{q_b}{k}$. The solid line is for 10 K km^{-1}. The other models are 6 K km^{-1}, long dashed line; 8 K km^{-1}, dot-dashed line; 12 K km^{-1}, short dashed line; and 15 K km^{-1}, double-dashed line.

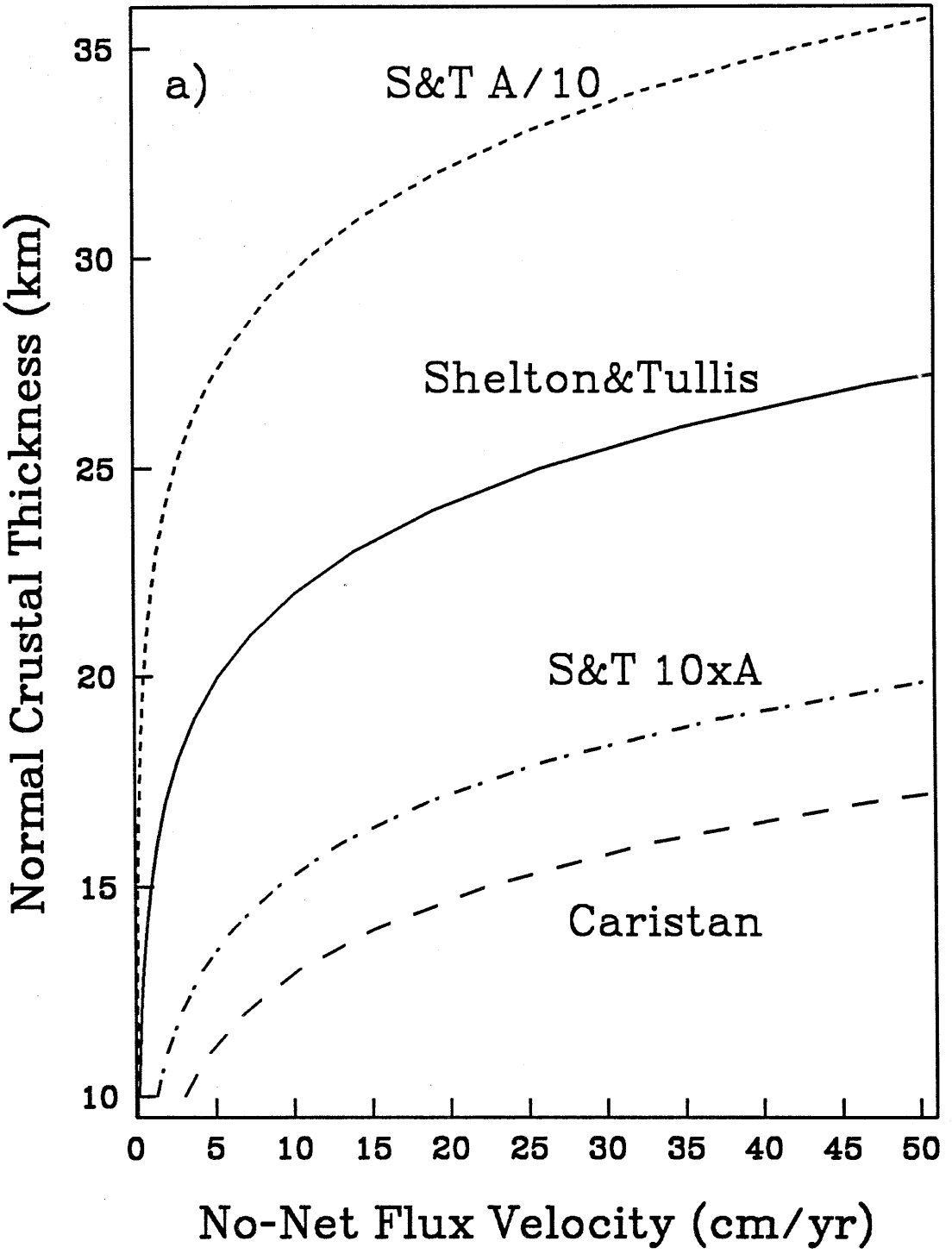
a)
S&T A/10
Shelton&Tullis
S&T 10xA
Caristan
Normal Crustal Thickness (km)
No-Net Flux Velocity (cm/yr)
10
15
20
25
30
35
0
5
10
15
20
25
30
35
40
45
50

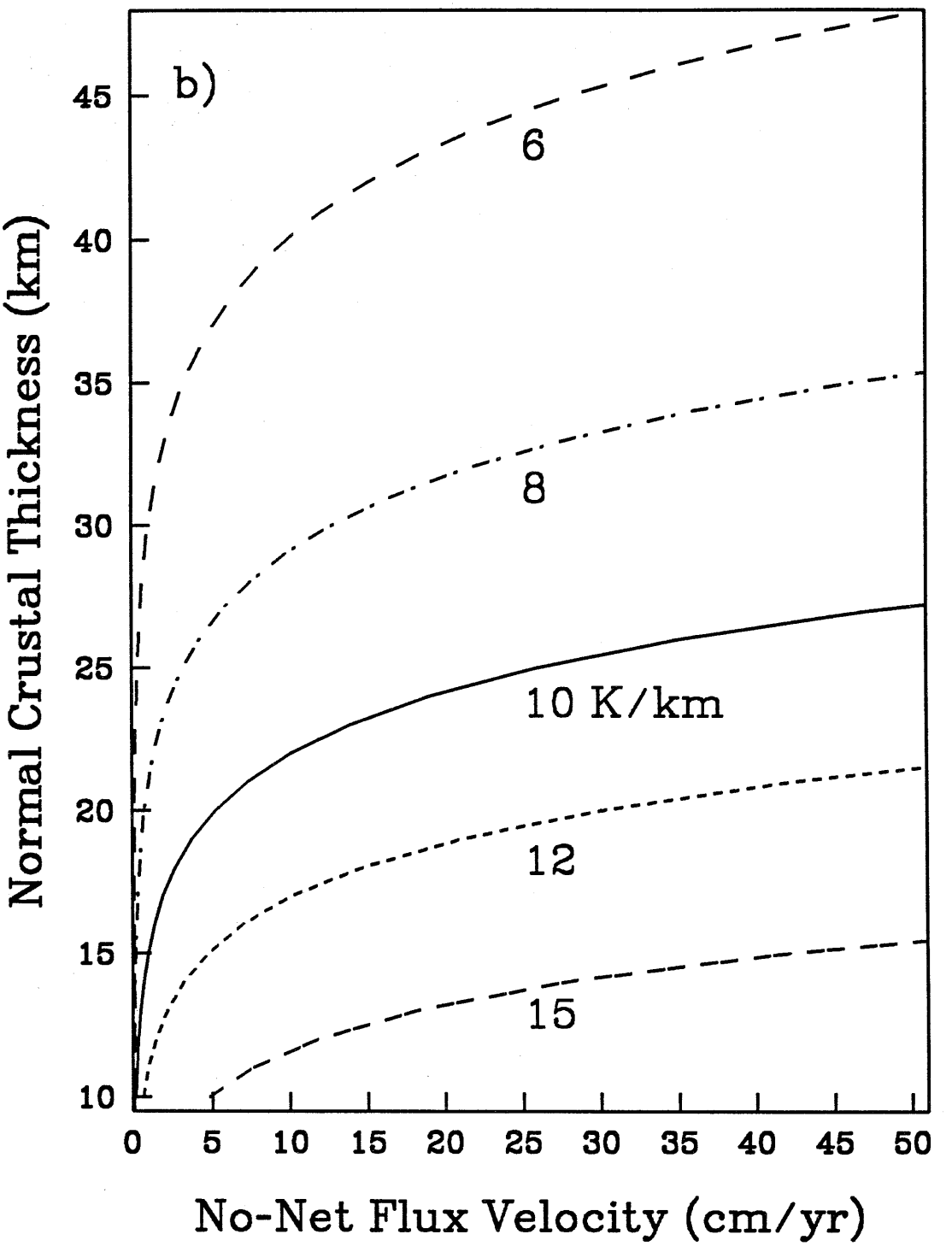
b)
6
8
10 K/km
12
15
Normal Crustal Thickness (km)
No-Net Flux Velocity (cm/yr)
10
15
20
25
30
35
40
45
0
5
10
15
20
25
30
35
40
45
50